MODELLING, ANALYSIS AND OPTIMISATION OF CANTILEVER PIEZOELECTRIC ENERGY HARVESTERS

RUPESH PATEL

MEng (Mechanical Engineering)

The University of Nottingham

Thesis submitted to The University of Nottingham

for the degree of Doctor of Philosophy

DECEMBER 2012

ABSTRACT

Over the last decade there has been a growing increase in research in the field of vibrational energy harvesting – devices which convert ambient vibrational energy into electrical energy. The major application area for such devices is as power sources for wireless sensors, thereby replacing currently used batteries which suffer from a finite lifespan and pose environmental issues during disposal. The vast majority of designs are cantilever beams comprising of piezoelectric layers having coverage identical to the substrate layer. It is evident from the literature that rudimentary work has been performed on design optimisation, with reliable and extensive parametric studies on geometry, especially piezoelectric layer coverage, being overlooked. As a result of this, outcomes from previous research are yet to be seen in designs for practical applications.

In this work a versatile linear model is developed which can accurately predict the performance of cantilever piezoelectric energy harvesters. An integral part of the model uses a transfer matrix method to accommodate the difference in structural dynamics of both uniform and non-uniform structures with model validation provided through extensive experimental work. The linear model developed is used to carry out parametric studies on the geometry of three distinct energy harvester cases thereby providing comprehensive knowledge on key variables and geometrical changes which can improve performance. In one of the cases examined, an improvement in performance of over 100% is predicted by solely altering piezoelectric layer coverage. However, the load resistance, i.e. electrical condition, has a significant effect on the trends in generated power which led to work directed toward harvester optimisation in a more realistic electrical scenario.

Investigation on harvester geometry whilst utilising an electrical scenario comprising of an energy storage medium is undertaken in this work. The developed model ensures the effects of electro-mechanical coupling remain and provides a solid basis from which users can readily apply model extensions through inclusion of further electrical components to resemble practical circuitry. Theoretically, for all examined case studies, improvements in performance were realised through alterations to piezoelectric layer dimensions with the most notable result indicating an improvement of over 200% during optimisation of piezoelectric layer length. In conjunction to theoretical findings, outcomes of extensive experimental work are provided in order to highlight the accuracy and reliability of the presented theoretical models in both electrical scenarios. Variation in mechanical damping magnitude plays a pivotal role throughout experimental testing and is one key factor in explaining why devices comprising of shorter piezoelectric layers have high performance.

A methodology behind unbiased design comparisons is also provided in this work, and involves comparing devices with identical fundamental frequencies. The reasoning behind this approach is to allow for each device to perform as efficiently as possible in the same excitation scenario. Systematic alterations to multiple geometric parameters are used to achieve this. Geometric parameters such as the substrate thickness are observed to provide adequate frequency control. Using this approach, performance improvements from adjustments to piezoelectric coverage still remain.

The occurrence of non-linearity in piezoelectric materials is a widely known phenomena and so lastly, a more robust model is provided which incorporates material and geometric non-linearity. This model is useful in determining dynamical responses of uniform and non-uniform piezoelectric energy harvesters when subjected to moderate-to-high acceleration levels. A thorough validation of the theoretical model is achieved using extensive experimental data obtained from a range of samples. For the harvester composition tested in this work, the occurrence of mild non-linearity at base acceleration levels as low as 1 m.s^{-2} is witnessed with softening behaviour causing the resonant frequency to decrease with base acceleration. In order to avoid reduced efficiency in the final application, the prediction of possible frequency shifts is vital during the design process.

ACKNOWLEDGEMENTS

This dissertation would not have been possible without the guidance and help of several individuals who, in one way or another, contributed and extended their valuable assistance throughout the duration of this study.

First and foremost, it is with tremendous gratitude that I acknowledge the continual help and support of my supervisors, Dr Stewart McWilliam and Prof Atanas A. Popov. The patience they have shown during encountered obstacles, along with the inspiration and expertise they provided will not be forgotten. The completion of this work would not have been possible without their recommendations and assurances.

I would also wish to thank Dr Adam Clare. Insightful yearly review discussions, in addition to his guidance and knowledge regarding experimental work were invaluable.

My family who supported me emotionally, financially (and on numerous occasions, nutritionally!) deserve special recognition. I am indebted to them and it gives me great pleasure in acknowledging Ma, Dad, Mum, Pritesh, Hiran, Amit, Priya, Urwi, big and small Foi, and the two Fugis. Thank you all for everything you have done for me over the years.

A special thank you must also be accredited to Dina Makar. I cannot find words to express my gratitude to her for the willingness shown and motivation provided throughout the writing period. Her continuous moral support, advice and guidance, both personally and professionally, will always be remembered.

Finally, my numerous colleagues and friends in the ITRC building who provided encouragement and frequent relief during my 4 years in the office must be mentioned. There are just too many to name individually here, but I thank you all for the happy memories.

CONTENTS

NOMENCLATURE

A_e	Electrode area
A_p	Cross-sectional area of piezoelectric layer
A_s	Cross-sectional area of substrate layer
b_{tip}	Width of tip mass
b_p	Width of piezoelectric layer
b_s	Width of substrate layer
C_p	Piezoelectric internal capacitance
C_s	Storage capacitance
$C_1 - C_{14}$	Time independent constants for non-linear model
c_g	Centre of gravity of tip mass
D	Electric displacement
d	Tip mass offset distance
d_{31}	Piezoelectric material constant
E_{field}	Electric field strength
E_p	Young's modulus of piezoelectric material
E_s	Young's modulus of substrate material
H	Heaviside function
I_G	Inertia of tip mass
I_p	Second moment of area for piezoelectric layer
I_s	Second moment of area for substrate layer
i	Current
L	Overall beam length
L_{tip}	Length of tip mass
$\mathcal{L}$	System Lagrangian
M	Internal moment
m	Mass per unit length
m_{tip}	Mass of tip mass
Q	Mechanical forcing
q	Electric charge

P	Dissipated power
R	Electro-mechanical coupling (1)
R_{load}	Load resistance
s	Arc length
T	Kinetic energy of system
t	Time
t_{tip}	Thickness of tip mass
t_p	Thickness of piezoelectric layer
t_{pc}	Distance between neutral axis and centre of piezoelectric layer
t_s	Thickness of substrate layer
U	Potential energy of system
$\mathbf{U}$	Transfer matrix
$\mathbf{U_{tm}}$	Transfer matrix for the tip mass
u	Longitudinal deflection
V	Voltage
V_{th}	Diode bridge threshold voltage
V_0	Peak voltage
v	Transverse deflections (non-linear model)
W	Normalised eigenvectors
$\mathcal{W}$	External work on system
w	Transverse deflection (linear model)
w_b	Base displacement
w_{rel}	Beam displacement relative to the base
x	Position along beam
x_1	Length from clamp to piezoelectric layer
x_2	Length of piezoelectric layer
x_3	Length from piezoelectric layer to free end
$\overline{y}$	Neutral axis location from bottom of structure
Y_0	Amplitude of base excitation
y	Distance from the neutral axis

α	1st constant for proportional damping
β	2nd constant for proportional damping
δ	Dirac function
δ_{rq}	Kronecker delta function
ϵ	Electro-mechanical coupling
η	Generalised modal co-ordinates
γ	Mechanical damping ratio
μ_1	1st piezoelectric non-linear coefficient

μ_2	2nd piezoelectric non-linear coefficient
μ_{s1}	Substrate non-linear coefficient
ω	Frequency of excitation
ω_q	Natural frequency
ϕ	Electro-mechanical coupling (2)
ρ	Beam curvature
ρ_{tip}	Density of tip mass material
ρ_p	Density of piezoelectric material
ρ_s	Density of substrate material
σ	Stress
ε	Strain
ε_{33}^S	Permittivity at constant strain

CHAPTER 1

INTRODUCTION AND LITERATURE REVIEW

1.1 Introduction

Over the last decade there has been a rapid growth in research within the field of energy harvesting. Another well documented trend is the continual increase in applications for wireless sensors – used in, for example, structural health monitoring and condition monitoring. The classic sources of power for these sensors were batteries. However, they have a finite lifespan and therefore must be replaced periodically. In the near future, the cost of maintaining and replacing these batteries is seen to be impractical. A more pressing concern is the environmental impact caused by creating and disposing of such power sources. For these reasons there is an urgent need for an alternative, or at least a supplementary, power supply.

'Energy harvester' is the term given to a device which converts forms of otherwise wasted energy into useful energy – usually electrical. Devices which utilise ambient energy sources such as light, thermal and vibrational are widely reported in literature and are seen as possible replacements/supplements to batteries. In this chapter a flavour of literature in the field of vibrational energy harvesting will be presented with particular emphasise on piezoelectric energy harvesters. Capabilities of current devices and possible target applica-

tions, along with associated limitations and areas of design improvement, will be detailed to the reader.

This chapter is arranged in the following manner. Initially, information on the three vibration based energy harvesting methods (piezoelectric, electromagnetic and electrostatic) is provided, culminating in reasoning behind why piezoelectric transduction will be the transduction method of choice. Following this, further details will be provided on piezoelectric energy harvesters in terms of both design and operational mode. Performance levels of previously manufactured devices, including those targeted at specific applications will be provided. A substantial quantity of information is then supplied on limitations to the conventional design (rectangular cantilever beam comprising of combinations of piezoelectric and non-piezoelectric material) including information on the various methods which make progress towards tackling key issues. Issues such as the dependency of energy harvester performance on excitation frequency and their poor performance in low excitation frequency scenarios will be addressed here. The next section will consider parametric studies and optimisations for the conventional design. Methodologies, utilised models and results from previous research will be detailed and discussed. In the penultimate section, information regarding the non-linear modelling of energy harvesting systems, more-so systems comprising of piezoelectric material, is provided including reasons behind the importance of this modelling approach.

Throughout the chapter, gaps and shortcomings in existing research will be identified. Those which are to be addressed in this thesis are outlined in the final section. Also provided here will be motivations behind this research in the form of objectives, and details on differentiation with respect to existing work. Lastly an overview of the thesis is provided, by means of a chapter to chapter breakdown.

1.2 Energy harvesting methods

1.2.1 Introduction

Numerous technologies exist which allow for the harvesting of otherwise wasted energy. Examples include solar energy harvesting [17], thermal energy harvesting [9] and vibrational energy harvesting [76]. A solar energy harvesting device which is in direct sunlight offers the greatest power densities – 15 μW.mm^{-3}. However, if the same device was used on a cloudy day a power density of only 0.15 μW.mm^{-3} is achievable. The performance of such a device is further reduced if it is used indoors, for example, if used in an office a power density of only 0.006 μW.mm^{-3} is expected. As a comparison, devices with a volume of 1000 mm^3, which utilise piezoelectric materials to harvest energy from vibrations, offer power densities of approximately 0.25 μW.mm^{-3} [84]. Figure 1.1 shows how solar and vibrational energy harvesting compare to conventional batteries in terms of power density and lifespan. It is immediately clear that for long-term applications battery power is inadequate.

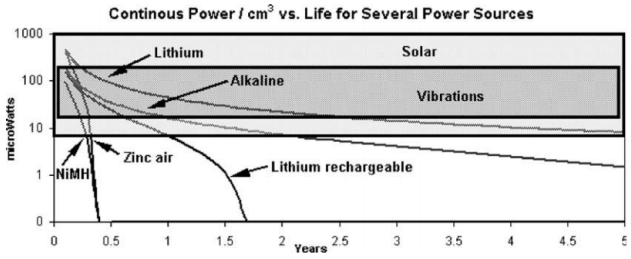

Figure 1.1: Comparison of power from solar, vibrations and various batteries [84].

Although the solar cell has the highest energy density its use in particular applications, i.e. inside the tyre of a vehicle [51], is infeasible and here ambient vibrations are the most attractive source of power. Vibrational energy harvesters make use of an electromechanical transducer and the three most conventional types are piezoelectric, electromagnetic and electrostatic. A number of review papers, providing comprehensive information on vibrational energy harvesting, have been released by various research groups – Sodano *et al.* [89], Beeby *et al.* [10], Mitcheson *et al.* [65] and Cook-Chennault *et al.* [21]. More specifically for piezoelectric energy harvesting, the reader is directed to compendium in the

form of two recent books, Energy Harvesting Technologies [76] and Piezoelectric Energy Harvesting [30]. In the following sections, a brief overview of the three vibrational energy harvesting transduction methods is provided.

1.2.2 Electromagnetic transduction

Electromagnetic devices utilise Faraday's law of induction which states the induced electromotive force in any closed circuit is equal to the time rate of change of the magnetic flux through the circuit. This can be achieved by either moving a coil through a fixed magnetic field or by changing the orientation of the magnetic field in the proximity of a fixed coil. The latter is often preferred as the magnet is usually attached to a resonating cantilevered beam, and also acts as a tip mass to lower the natural frequency of the system. Kulkarni *et al.* [48] designed, fabricated and tested micro-fabricated electromagnetic generators. The authors compared the performance of both moving coil, volume of 106 mm^3, and moving magnet, volume of 150 mm^3, configurations. One moving coil generator was designed to operate at 7400 Hz, the frequency of an industrial fan. However, due to generator size, small imperfections during manufacture caused a large shift in fundamental frequency. Issues such as this, and issues relating to energy harvester performance are discussed in Section 1.4. For prototype A (see Figure 1.2(a)), a maximum power of 0.418 μW was obtained at a frequency of 8080 Hz with a source acceleration of 3.9 $m.s^{-2}$. The moving mass generator (see Figure 1.2(b)) produced a maximum power output of 0.584 μW at a frequency of 60 Hz and source acceleration of 8.829 $m.s^{-2}$. The experiments showed that the resonating magnet assembly performs better at low frequencies and the fabrication of this device can be achieved with greater accuracy.

1.2.3 Electrostatic transduction

The concept behind electrostatic transduction is that of a variable capacitor – two conductors, which move relative to one another, are separated by a dielectric. There are three different configurations for electrostatic transducers – in-plane overlapping, in-plane gap closing and out-of-plane gap closing (see Figure 1.3). Each configuration has its merits

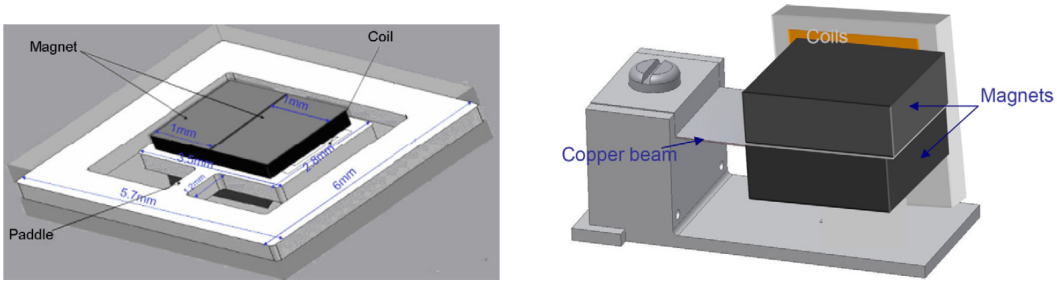

(a) Prototype A – resonating coil

(b) Prototype C – resonating mass

Figure 1.2: Schematic for electromagnetic generator [48].

and flaws. The in-plane overlapping generator has the smallest parasitic damping ratio but also has the least maximum capacitance. The out-of-plane gap closing generator has the greatest maximum capacitance but in addition possesses the largest mechanical damping. The in-plane gap closing generator also has a large maximum capacitance but requires mechanical stops to prevent the capacitor plates from touching one another. Chiu *et al.* [18] designed and fabricated MEMS in-plane gap closing electrostatic harvesters with theoretical calculations estimating, for a generator area of 80 mm^2, an output power of 0.2 μW is possible.

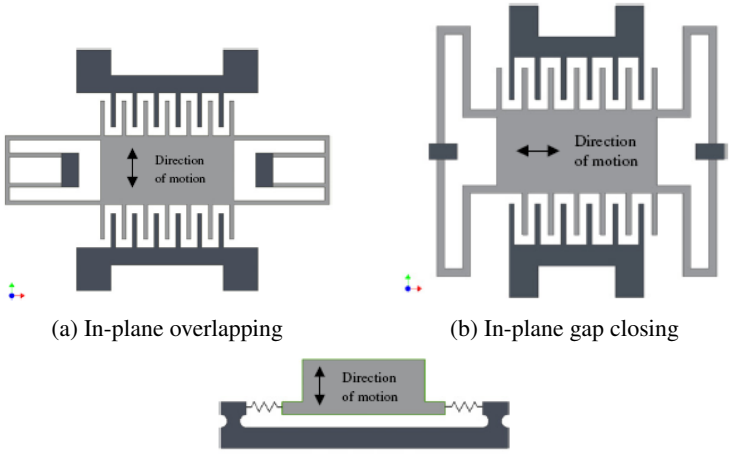

(a) In-plane overlapping

(b) In-plane gap closing

(c) Out-of-plane gap closing

Figure 1.3: Different configurations of electrostatic transducers [10].

Mitcheson *et al.* [64] classify vibrational energy harvesters into three categories – velocity-damped resonant generator (VDRG), coulomb-damped resonant generator (CDRG) and coulomb-force parametric generator (CFPG). Piezoelectric and electromagnetic devices

fall into the VDRG category and electrostatic devices into the remaining two. The authors investigate how each type of generator will perform in different operating conditions and with different geometries, see Figure 1.4. It is clear that if the generator is tuned to the natural frequency of the source, and the amplitude of the input force is large compared to the space envelope, then the VDRG has best performance. On the other hand if the source frequency is less than half of the natural frequency the non-resonant CFPG produces the greatest power. This is an indication of the importance in being familiar with the application characteristics for which the generator is being designed.

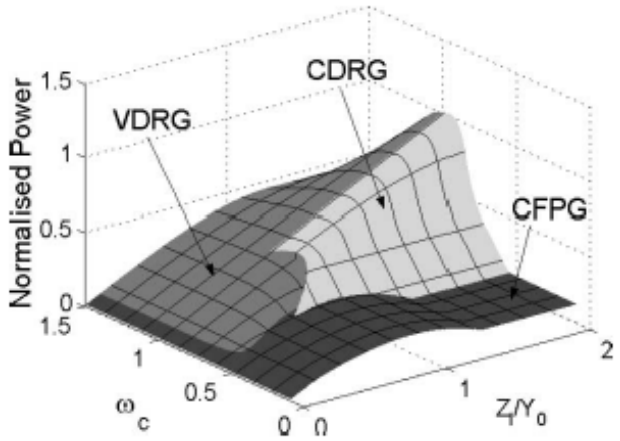

Figure 1.4: A power comparison for the three categories of generator. ω_c is the ratio between the source and natural frequency, Z_l represents the space envelope and Y_0 represents the magnitude of input acceleration [64].

1.2.4 Piezoelectric transduction

Roundy *et al.* [83] state that, the piezoelectric transducer provides maximum practical energy density. Practical energy density refers to what is achievable with current materials and manufacturing processes. Piezoelectric transducers can have an energy density of up to 35.4 μJ.mm^{-3} compared to 4 μJ.mm^{-3} for electrostatic transducers and 24.8 μJ.mm^{-3} for electromagnetic transducers. Piezoelectric energy harvesting in the focus of this thesis.

Piezoelectricity is the ability of particular crystalline materials to produce an electric potential when they experience stresses. The effect was first defined in 1880 by Jacques Curie and Pierre Curie. There are two types of piezoelectricity, namely, direct and converse.

Converse piezoelectricity is used to describe the phenomenon where applying a voltage across the material induces mechanical strain. Direct piezoelectricity produces a voltage across the material when it is put under stress. This effect is utilised in piezoelectric vibrational energy harvesting devices. A procedure known as poling is required in order for material to exhibit piezoelectric properties. Poling is achieved by applying a strong electric field across the material at a temperature slightly below the Curie temperature with the material becoming anisotropic (Figure 1.5(b)). The direction of the applied field will determine the orientation of both mechanical and electrical axes. The process permanently changes the dimensions of the structure, however once the electric field has been removed the orientation of the dipoles remains and the material will exhibit piezoelectric properties (Figure 1.5(c)).

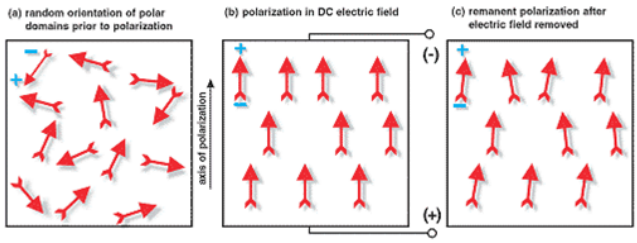

Figure 1.5: Steps in poling a piezoelectric material [6].

Various configurations for piezoelectric energy harvesters have been reported in the literature. One of the simplest structures is a unimorph energy harvester, see Figure 1.6. It consists of a single layer of piezoelectric material bonded to a layer of non-piezoelectric material, referred to as the 'substrate layer', in a cantilever arrangement. Electrodes, which collect generated charge, are bonded to the top and bottom surfaces of the piezoelectric material. For small scale applications the dimensions of energy harvesters are naturally small and the fundamental frequency of the beam resonators are high. The fundamental frequency can be reduced through the inclusion of additional mass, referred to as a tip/proof mass, at the free end of the beam.

Mechanical and electrical symbols and relations will be presented in tensor form. The tensor indices are defined thus: index 1 refers to the x-direction i.e. parallel to the beam length, and index 3 refers to the y-direction i.e. perpendicular to beam length, through the

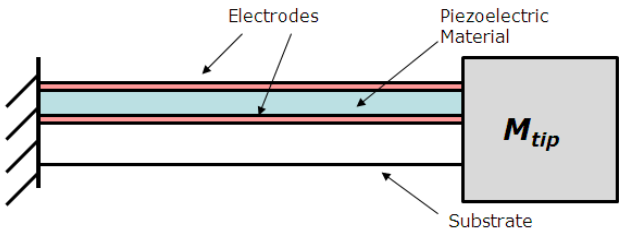

Figure 1.6: Schematics of unimorph piezoelectric energy harvester.

thickness of the material. Magnitude of the electrical coefficients relating to piezoelectric material are dependant on the direction of both applied stress and electric displacement. As an example the piezoelectric constant d_{31} concerns stress applied in the x-direction (1) and electric displacement in the y-direction (3); the latter occurring as a result of electrode design/position. For comprehensive information on tensor notation the reader is directed to the IEEE Standard on Piezoelectricity [1]. Piezoelectric material can be used to harvest energy through various modes of operation. The direction of load applied to the cantilever beam in relation to the electric displacement, electrode location, will determine which mode of operation is utilised. The d_{31} mode of operation has previously been defined. The d_{33} operational mode describes situations where the electric field is parallel to the applied stress. Both cases are represented visually in Figure 1.7.

(a) d_{31} mode (b) d_{33} mode

Figure 1.7: Schematic of configurations representing two operational modes (σ – applied stress).

The voltage produced by a harvester operating in the d_{33} mode, theoretically, is much higher due to the magnitude of the coefficients, refer to Table 1.1. Table 1.1 also indicates the importance of material selection. Lead zirconate titanate (PZT) has piezoelectric coefficients of far greater magnitude, however, polyvinylidene fluoride (PVDF) is more flexible and less susceptible to fracture failure. Another reason behind an expected increase in the output voltage for the d_{33} operational mode is as increase in distance between electrode pairs.

Jeon *et al.* [42] fabricated and tested a device which utilises the d_{33} mode, see Fig-

Table 1.1: Coefficients of common piezoelectric materials [10].

Property	PZT-5H	PZT-5A	$BaTIO_3$	PVDF
d_{33} (pC/N)	593	374	149	-33
d_{31} (pC/N)	-274	-171	78	23
Relative permittivity	3400	1700	1700	12

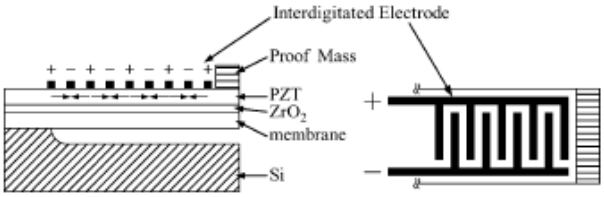

Figure 1.8: Schematic of piezoelectric device designed to operate in the d_{33} mode [42].

ure 1.8. Although the authors state the device will generate twenty times more voltage than a similar dimensioned device operating in the d_{31} mode, they provide no comparison results. For a source frequency of 13.9 kHz, 1.01 μW was delivered to a 5.2 MΩ load by a thin film of PZT with dimensions 0.17 mm $\times$ 0.26 mm $\times$ 0.00048 mm. Another stated advantage of a d_{33} mode harvester is that, since an interdigitated top electrode is used, a bottom electrode is not required hence the fabrication process becomes cheaper. This however is debatable when devices on the macro-scale are concerned.

1.3 Devices targeted for practical application

In addition to published literature on the power output of fabricated devices, several authors have also targeted their devices for particular applications. One novel application is using energy harvesting to power wireless keyboards. Wacharasindhu and Kwon [99] designed, fabricated and tested a hybrid device consisting of both electromagnetic and piezoelectric transducers. Their device is designed so it can be integrated underneath the keys on a keyboard. The piezoelectric aspect of the design contributed the most power – for optimal load resistances, a maximum power output of 40.8 μW was generated by the piezoelectric transducer and 1.15 μW by the electromagnetic transducer. The authors stated that, with some design modifications, a skilled typist typing over forty words a minute would be capable

of generating roughly 3460 μW. Bai and Yang [8], who investigated using solar cells as the power source for wireless keyboards, state the power requirements of modern wireless keyboards is approximately 1540 μW.

Metzger *et al.* [62] investigated the feasibility of using vibrational energy harvesting to power RFID tags for cold chain monitoring. The term 'cold chain' relates to the distribution of goods, i.e. pharmaceuticals, at a desired temperature level. Cold chain monitoring ensures the goods are kept at the required temperature during transit [46]. RFID, radio frequency identification, tags are found in numerous applications, two examples being goods tracking and environmental condition monitoring. There are three types of RFID tags namely passive, semi-passive and active. The power source used to supply the tag determines the tag categorisation. Passive RFID tags obtain their power from radio frequency energy emitted by the source. Active tags use an internal power source, conventional lithium ion battery, whereas semi-passive tags use a combination of an on-chip battery and radio frequency energy. Active tags have numerous advantages over the passive type, for example they have the ability to provide continuous power to on-board electronic and communication circuitry. Passive tags can only transmit and collect data when in proximity to the source greatly reducing their operation range. A RFID tag equipped with a temperature sensor requires approximately 27 μW to function adequately. Although the generator presented in [62] only produces 0.73 μW the authors state that continuous monitoring is not required so the power requirements of the sensor can be reduced. Additionally through design optimisation, not preformed by the authors, improvements in output power are likely to be realised.

Another possible application area is condition monitoring; for example in power plants, oil refineries, chemical plants, vehicles and aeroplanes to name but a few. Companies such as Perpetuum and Ferro Solutions design, manufacture and sell devices for this purpose. Perpetuum [70] offers a wireless sensor for industrial condition monitoring. The device can be used to continuously monitor machine performance; it has a maximum power output of 5000 μW for an acceleration of $0.1g$ at 120 Hz. Ferro Solutions [34] are currently selling energy harvesters which have a maximum power output of 10800 μW for an accel-

eration of $0.1g$ at 60 Hz. The downside of such devices is their space envelope, in the order of 100's of mm, making them impractical in smaller scale applications.

Reducing the size of sensors allows them to become less intrusive which is particularly attractive in human applications. The lithium battery, which is the current power source for the majority of sensors, is the component which takes up the most space. The power consumption of wireless sensors has been reducing due to more efficient electronics and less power demanding data transmitters. One example is a product available from MicroStrain [63]. It is a wireless thermocouple system which only requires a power of 300 μW for a data rate of 1 sample per minute.

The development of an alternative or secondary energy source for pacemakers has been a topic of interest for many years. The main driving force behind this research is to eliminate the necessity to replace the pacemaker battery. There are an estimated 350,000 patients worldwide and the majority of pacemakers are powered by a lithium-iodine battery which lasts 7-10 years. After this period the patient must undergo another operation causing unnecessary anxiety, stress and risk. One of the main components of a pacemaker is the pulse generator which contains the output circuit, sensing circuit and the timing circuit. In 1960, the energy this component required to function was 675 μJ and in 1990 it was down to 3-6 μJ [13]. Continuous development of circuit components and lead design reduce power consumption hence increase the possibility of using energy harvesters to solely power pacemakers. Various designs have already been presented to harvest energy from inside the body. As an example, Tashiro *et al.* [95] use an electrostatic generator to harness ventricular wall motion. The type of capacitor used was out-of-plane gap closing, and the mean output power was measured to be 36 μW.

Renaud *et al.* [81] have presented work on harvesting energy for human limb motion. Due to the low frequencies present in this application the researchers designed an impact-based energy harvester. Findings from experimental work indicted rotating the device at a frequency of 1 Hz was able to generate 47 μW. If the device was shaken via hand movement at a frequency and amplitude of approximately 10 Hz and 100 mm one can expect a power

of over 600 μW across an optimum resistive load.

Wischke *et al.* [104] investigated the feasibility in using piezoelectric energy harvesters as a power source for wireless sensors in traffic tunnels. Testing in the field showed vibration levels on tunnel walls were insufficient to provide the required power magnitude however, vibrations present on railway sleepers would suffice. Conclusions also suggested applications in tunnels for trains as opposed to road traffic is feasible. Due to fluctuations observed in source frequency a arrayed device was fabricated, further details on such methods can be found in Section 1.4, with a space envelope of 41 mm $\times$ 36 mm $\times$ 11 mm. 270 μJ of energy was required to power the electrical interface and this was producible by 204 out of the 444 trains which passed through the tunnel. The average energy per train was calculated at 395 μJ and so with smart energy storage solutions energy requirements to monitor every train passing can be met. On a much larger scale (final device to have a length of 30 m), Mutsuda *et al.* [66] are attempting to design a piezoelectric energy harvesting structure which will extract power from ocean energy. The feasibility of this technology on such large scales and in an ocean environment remains unclear however current work is being targeted at improvement and optimisation of the overall floating structure. A prototype with a space envelope of 2200 mm $\times$ 1550 mm $\times$ 1200 mm has been manufactured and tested in a water tank with results indicating a power density of 18.36 μW.mm^2. In the final design, with the materials currently used, each 30 m device is hypothesised to generate $\approx$5 kW.

This brief overview of past work indicates the diversity in vibration energy harvesting applications. Magnitudes of power achievable by devices are at a practical level and are sufficient, particularly in applications such as condition monitoring through the use of wireless sensors. Novelty and the detailed optimisation of current designs is the next step to achieve further improvements in energy harvester performance.

1.4 Improvements and optimisations

1.4.1 Dependency on excitation frequency

There are numerous limitations which need to be addressed in order to improve performance and robustness of energy harvesting devices. Firstly and probably most importantly, is the fact that maximum power extraction requires matching the resonant frequency of the generator to the frequency of the input signal. In most applications however, the dominant frequency of the source is not constant but actually random. This is a major limitation on the number of applications in which vibrational energy harvesting can be used. Also, the manufacturing process by which the generator is made must be carefully controlled thus increasing production cost. As energy harvesters become smaller the effects of dimensional imperfections, on for example the natural frequencies and mode shapes, magnifies. Additionally, the desire for low mechanical damping, and hence associated small bandwidths, enhances the issue of resonant frequency dependency.

Roundy *et al.* [83] published a paper on general techniques for sustaining high power outputs over wider frequency ranges. One of the techniques mentioned is frequency tuning, which can be split into two categories – active and passive. Active tuning involves continuous monitoring of the power output and altering the natural frequency of the device accordingly to maintain power maximised. Passive tuning refers to a mechanism by which only occasional monitoring and natural frequency alterations occur. Active tuning mechanisms require a power source to function hence reduce the overall power output from the generator. Roundy *et al.* [83] state that if the generator is modelled as a second-order system, active tuning will never improve power output and passive tuning is the recommended approach. A patent published by Churchill and Arms [19] provides techniques for passive and active tuning. For an active tuning situation the authors use a movable mass to continuously alter the fundamental frequency of their device. Movement is achieved via a rack and pinion as shown in Figure 1.9(a). Passive tuning can be achieved using magnets attached to the mass and the enclosure. Adjusting the distance between magnets will alter beam stiffness through which the fundamental frequency of the device is controlled, see Figure 1.9(b).

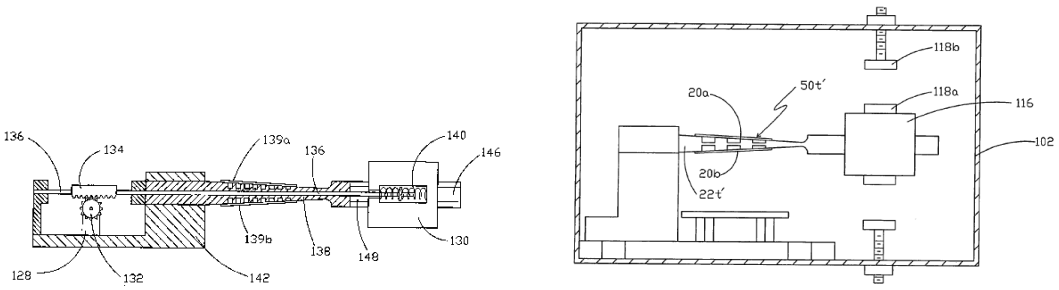

(a) Active tuning (b) Passive tuning

Figure 1.9: Methods of fundamental frequency tuning [19].

One method for reducing the dependency of a vibrational energy harvesting system on excitation-resonant frequency matching is to use arrays of cantilevered beams each with unique fundamental frequencies. This technique is well documented in both journal papers and patents. Liu *et al.* [49] use an array of three cantilevers each with different resonant frequencies to improve system bandwidth by a factor a three. Shahruz [86] has published numerous papers on beam arrays and has derived a model showing the intensity at which beam vibration is reduced when the individual cantilevers are treated as a coupled system. Priya and Myers [77] were issued a patent on a design employing multiple cantilevered beams, shown in Figure 1.10. Through the use of arrays oriented in three directions their design improves the overall power output from vibrations in a random plane with random frequency. Although such arrayed designs appear appealing, they drastically reduce the overall power density of an energy harvesting device.

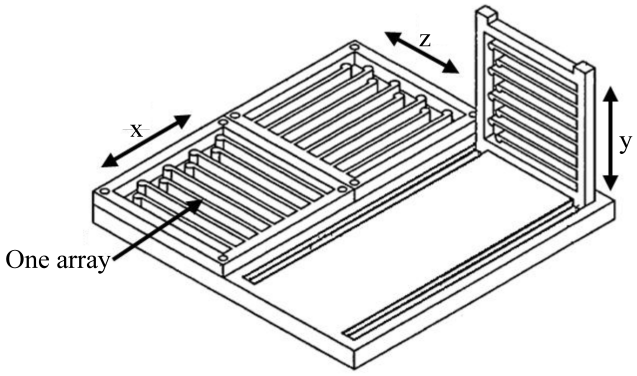

Figure 1.10: An array of cantilevers to increase device bandwidth [77].

Another method for reducing natural frequency dependency is to introduce non-linearity into the system. Mann and Sims [54] use magnetic levitation to achieve this, see

Figure 1.11(a). Their device possesses the ability to harvest reasonable amounts of energy over a much wider bandwidth when compared to the conventional linear harvester. Maximum power for a non-linear device no longer occurs close to the fundamental frequency so the group have derived a mathematical expression to find the frequency at which maximum power is produced (details on non-linear modelling with regards to energy harvester can be found in Section 1.6). The downside to their design is that non-linearity can only be engaged when the input signal has very large amplitude; this issue results from high levels of mechanical damping present in their device. It is clear from Figure 1.11(b) that for low levels of excitation, producing low velocity oscillations, the device behaves in a linear manner. Once the input excitation exceeds a 'threshold level', the system behaviour is non-linear and bandwidth is seen to increase.

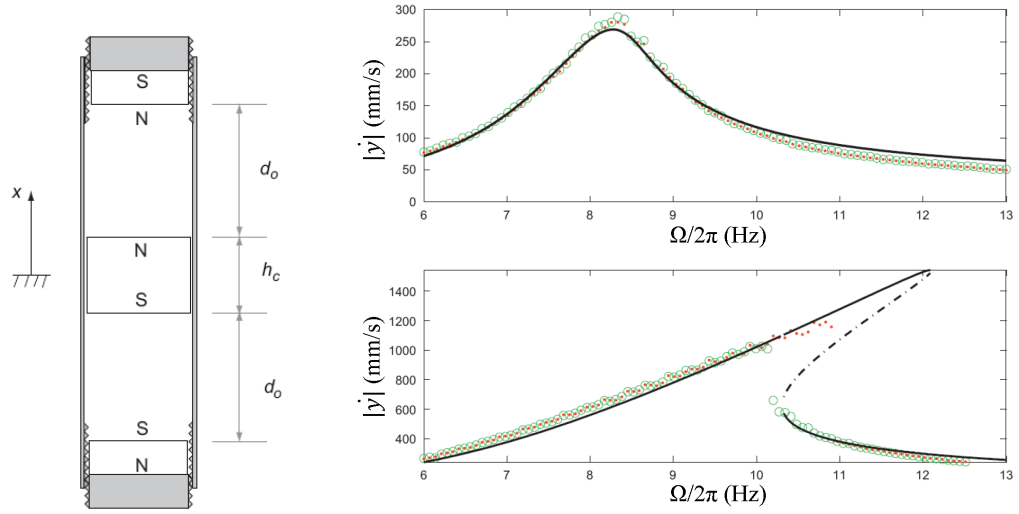

(a) Schematic of the non-linear harvester

(b) Graphical comparison between linear and non-linear device behaviour

Figure 1.11: Design of a device capable of utilising non-linear phenomena [54].

McInnes *et al.* [61] recently published a paper on using non-linear stochastic resonance to enhance the performance of energy harvesters. Stochastic resonance can be applied to a clamped-clamped beam by compressing and relaxing the structure in an oscillatory manner. The authors found that stochastic resonance can indeed produce superior power levels even though the forcing mechanism to compress the beam will require some electric energy. However, the overall structure is thought to be complicated and costly to manufacture and the authors did not perform experiment works to verify theoretical findings.

For further information on increasing the operating range of vibration energy harvesters the reader is referred to a review published by Zhu *et al.* [107].

1.4.2 Situations with low excitation frequency

Inspired to harvest energy from low frequency applications Veryst Engineering [98] designed a method to increase source frequency, also known as frequency-up conversion – allowing easier matching between source and resonant frequencies. Veryst Engineering is working on an electromagnetic device but a similar concept can be applied to piezoelectric generators. Their design decouples the input motion from the elastic component, thereby using said input motion as a mechanical energy accumulator. Work done by input motion is stored in a spring until a prescribed compression is reached. The spring is then released exciting the magnet to oscillate with a higher frequency.

Kulah has carried out significant research in this area; Kulah and Najafi [47] have designed, fabricated and tested a device which uses frequency-up conversion. Their generator, shown in Figure 1.12(a), is a hybrid device containing both electromagnetic and piezoelectric components. Magnets attached to the cantilever tips are attracted to magnets bonded to a diaphragm resonating with ambient vibrations. During the diaphragm vibratory motion the magnets will catch and release causing the cantilevers, comprising of piezoelectric material, to resonant at much greater frequencies, see Figure 1.12(b). From an ambient frequency of 25 Hz a resonant frequency of 15 kHz for the cantilever is possible. For a single cantilever with dimensions 0.5 mm $\times$ 0.4 mm $\times$ 0.015 mm their theoretical maximum power output was 3.97 μW.

Carman and Lee [14] released a patent containing a section on frequency-up conversion. Rather than harmonically exciting the cantilever base, a separate structure near the free end of the beam is excited, see Figure 1.13. When this displaces and releases the cantilever tip, the beam is allowed to vibrate with a higher frequency. An issue with such designs is that generator longevity may drastically reduce due to contact at the tip. Further information regarding patents tackling issues with the conventional piezoelectric energy harvester

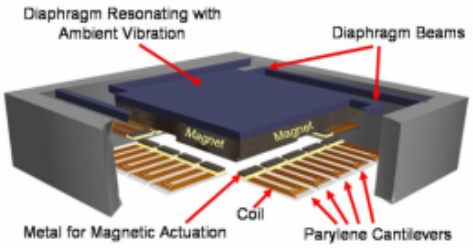

(a) Schematic of frequency-up device on the micro-scale

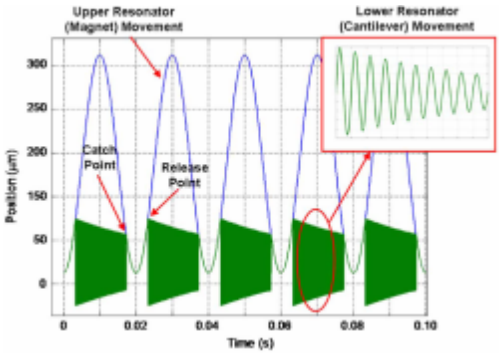

(b) Movements of low-frequency top plate and the high-frequency cantilevers

Figure 1.12: Design of a device utilising the frequency-up conversion method [47].

design can be found in a publication by Patel *et al.* [69].

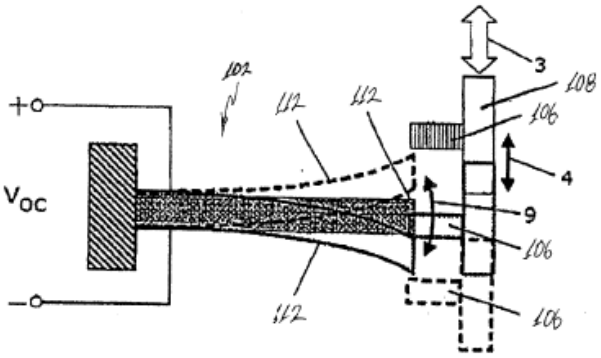

(a) Schematic of a frequency-up device

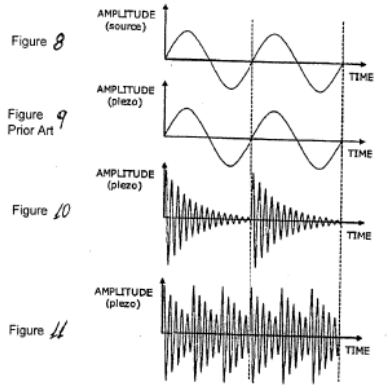

(b) Graphs showing how the device will cause an increase in the frequency

Figure 1.13: Design of a device utilising the frequency-up conversion method [14].

1.4.3 Strain distribution

As previously outlined the most common design for piezoelectric energy harvesters is a cantilevered beam with, depending on scale, a proof mass attached to the free end. Advantages of this design included the ability of the system to experience large deflections, hence strain, for relatively small input amplitudes and the simplicity allows easy integration with MEMS fabrication processes. One drawback however is that the piezoelectric material does not experience uniform strain; maximum strain occurs at the root of the cantilever whereas little or no strain at the tip – the design is therefore inefficient. Goldschmidtboeing and Woias [39]

investigated the effect of using tapered cantilever beams. Their results showed that although the efficiency of triangular beams is comparable to rectangular beams the triangular beams can withstand higher excitation amplitudes hence produce superior maximum power outputs in extreme operating conditions.

For a beam modelled using the Euler-Bernoulli method, strain throughout the beam thickness is dependent on the distance from the neutral axis. As this distance increases the strain increases, an optimisation which inevitably requires a thick stiff beam. Zheng *et al.* [106] have designed and developed an analytical model for symmetric air space cantilevers, see Figure 1.14, to overcome this problem. The piezoelectric beams do indeed experience higher strains and hence improved power outputs are expected. Akin to many novel designs the added complexity increases manufacturing costs and probability of failure, hence why the conventional cantilever configuration is often used.

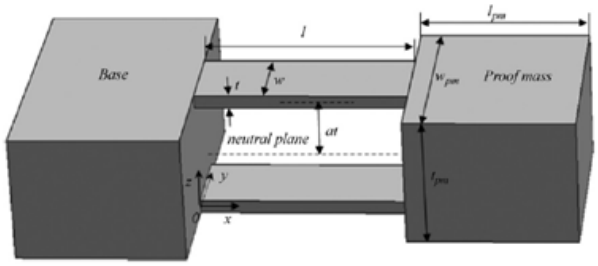

Figure 1.14: Schematic of a symmetrically air spaced cantilever [106].

1.4.4 Electrical circuits

Prior to this section improvements on only the structural aspects of a system have been outlined. However, research is also been carried out in relation to optimisations and improvements on the electrical side. The most basic electrical circuit for energy harvesting is to directly connect the energy harvester to an electrical load. In the vast majority of practical applications this is ill-advised for three key reasons. Firstly, direct current is required to power the electrical components as opposed to the alternating current generated by a piezoelectric element under harmonic excitation. Secondly, the magnitude of energy supplied by the harvester is often insufficient to directly power electronic components. Thirdly,

the vibration source is likely to be intermittent and so discontinuous power generation may result in the requirement of energy at a time it is not available. To overcome these issues and increase the flexibility of piezoelectric energy harvesters, in terms of possible applications, it is necessary to store the generated energy in for example a capacitor or battery [90]. Figure 1.15 shows a basic method for achieving this and consists of a diode bridge for rectification, a capacitor for energy storage and a resistor representing an electrical load.

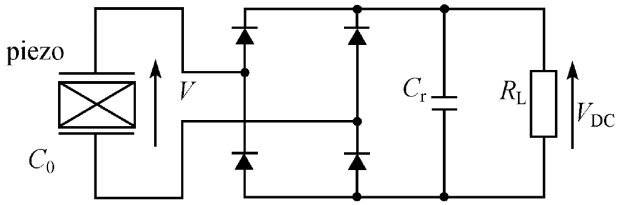

Figure 1.15: Basic method for accumulating and storing generated energy [78].

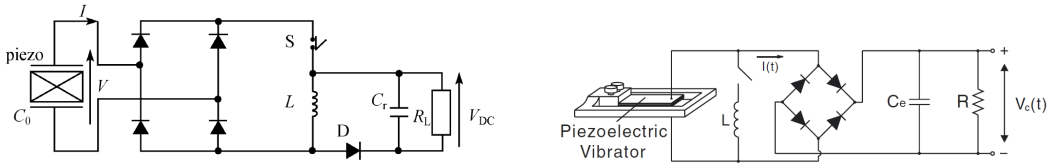

(a) Synchronous charge extraction [78].

(b) Synchronised switch harvesting on inductor [88]

Figure 1.16: Schematic of circuits which provide improved energy harvester outputs.

Methods such as synchronous charge extraction (SCE – Figure 1.16(a)) or synchronised switch harvesting on inductor (SSHI – Figure 1.16(b)) can be used to improve the overall performance of piezoelectric energy harvesting systems. Both methods utilise switches and inductors in order to synchronise mechanical vibrations with the extraction of energy. The operation of SCE is thus; the switch remains open until voltage across the piezoelectric material is at its maximum, at this point the switch is closed and the piezoelectric capacitor transfers energy to the inductor. Lastly, once charge across the piezoelectric material becomes zero the switch opens allowing the flow of energy from the inductor to the storage capacitor and electrical load. In the SSHI case, the switch is closed when peak displacements are realised allowing the inductor and piezoelectric layer to act as an oscillator. Once voltage inversion has taken place the switch is reopened. The main effect of SSHI is a voltage magnification from the inversion process corresponding to an optimisation in the transfer of energy [88]. A comparison study between various methods was performed by

Qiu *et al.* [78] with the outcome indicating that (when supplying power to an optimum load) SSHI can improve power levels by a factor of 7 over the basic energy storage circuit, Figure 1.15.

1.5 Parametric studies and previous models used for such studies

From work presented in Section 1.4 it is clear that a great deal of literature is available on novel designs and techniques for improving the performance of energy harvesters. Fewer works however can be found on the optimisation of the classical cantilever design through understanding the effects of geometric parameters on performance. Gao *et al.* [36] carried out one such study and their results showed that voltage per unit force can be increased by reducing the length ratio between piezoelectric and substrate layers, see Figure 1.17(a) (i.e. for a fixed substrate layer length, a shortening of piezoelectric layer length will benefit the voltage generated). Issues with their model include the omission of electrical aspects and excitation provided by pre-displacement at the tip, see Figure 1.17(b). It is fundamentally known that the electrical load, to which the harvester is connected, influences the system both mechanically in terms of resonant frequency and electrically in terms of voltage, power etc. This is likely to alter the observed trends, therefore [36] does not provide confident predictions regarding optimisation. In the majority of applications, energy harvesters are likely to be excited through base motion rather than displacement at the tip and this is also likely to affect presented trends.

Shen *et al.* [87] attempted to optimise a micro-scaled energy harvester design by altering parameters such as tip mass size. Findings showed that a larger tip mass is beneficial to performance, however this statement is inaccurate due to significant changes in fundamental frequency between designs. If the original device is designed for a certain operating frequency, changes to the tip mass size would produce an inefficient design. These fluctuations in fundamental frequency during optimisation processes are widely observed in past literature and it is thought the procedure used by many during design optimisation is

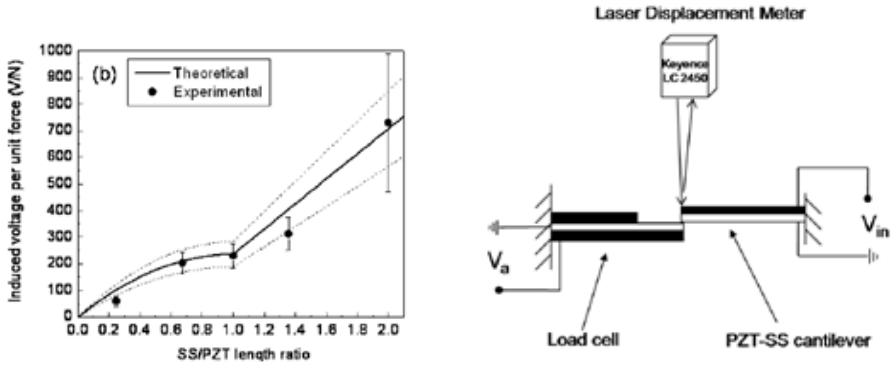

(a) Graphical representation of results obtained

(b) Schematic of experimental setup

Figure 1.17: Parametric study on the length ratio of a cantilever piezoelectric energy harvester [36].

flawed. A fair comparison should ensure fundamental frequency remains constant across the whole design range. In addition to this, the model used while estimating the performance of designs in [87] is overly simplified with an inaccurate account of electro-mechanical coupling. Reliable modelling of the harvesting device is essential in order to accurately estimate power outputs. Over the last 15 years numerous researchers have developed models to predict the performance of energy harvesting devices. One of the earliest models for estimating power generated by an energy harvester was proposed by William and Yates in 1996 [103]. They, like many who followed, represent the energy harvester as a single degree of freedom system based on a resonant second-order mass, spring, damper model. This is a good representation of an electromagnetic system but falls short when used to represent a cantilever piezoelectric device. Firstly, electrical properties of the piezoelectric material are not considered and secondly, electro-mechanical coupling is not proportional to velocity, as is the case in an electromagnetic harvesting system. However, basic models can be used with correction factors which incorporate these missing effects as shown by Erturk and Inman [28]. More accurate linear models, specifically for cantilever piezoelectric harvesters, have been developed by Daniel Inman's group at Virginia Tech. Sodano *et al.* [90] used the Rayleigh-Ritz procedure for estimating the power output from a cantilever mounted piezoelectric generator. Experiments were undertaken to validate the model and a good correlation with analytical results was obtained. Erturk and Inman [27] developed a distributed-parameter electromechanical model for energy harvesters. Validation was also completed by the authors with theoretical results in good agreement with experimental data [29]. For further

information on the modelling of piezoelectric energy harvesters the interested reader is directed to the two books previously suggested, namely Energy Harvesting Technologies [76] and Piezoelectric Energy Harvesting [30].

Zhu *et al.* [108] use a coupled piezoelectric-circuit finite-element model to determine the effects of various parameters on energy harvester performance. The authors show that, if both piezoelectric and substrate lengths are equal, an increase in power is achievable by using a shorter overall beam length, see Figure 1.18(a). This observation is thought to be inaccurate since their estimation of power was incorrectly normalised. While undertaking such parametric studies the base acceleration should be kept constant. However, Zhu *et al.* keep base displacement constant instead. This produces results which are highly dependent on the resonant frequency of the system from the relation $acc = Y\omega^2$. By observing variations in frequency with changes to beam length, Figure 1.18(b), one can appreciate the previous statement.

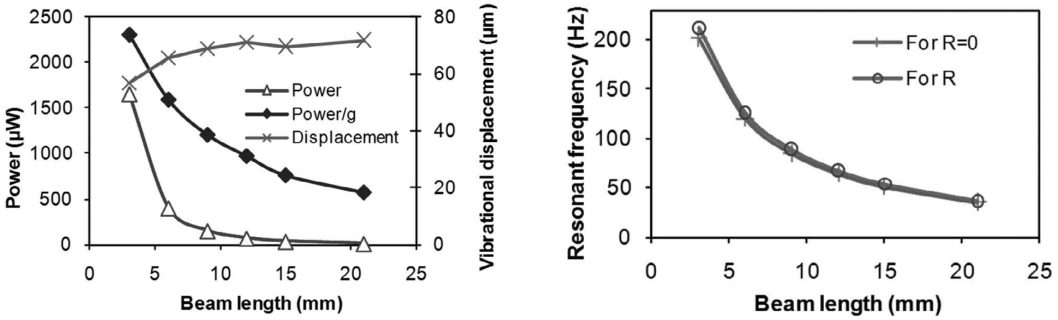

(a) Trend in power and displacement while increasing beam length

(b) Trend in frequency while increasing the beam length

Figure 1.18: Results from a parametric study performed by Zhu *et al.* while investigating beam length [108].

Bourisli and Al-Ajmi [12] theoretically attempt the optimisation of piezoelectric layer coverage, in various modes of vibration, on the electro-mechanical coupling coefficient. Findings show that reduced piezoelectric layer lengths are beneficial in terms of the electro-mechanical coupling coefficient magnitude. However, it is believed that sole optimisation of one system variable will not necessarily provide an optimum energy harvester design, i.e. one with maximum power generating capabilities. It was also shown that piezoelectric layer position is important when harvesting energy from higher modes of vibration due to

the presence of strain nodes causing charge cancellation. Similar conclusions have been made by Erturk [26] who proposed the use of segmented electrodes to overcome this issue.

Friswell and Adhikari [35] theoretically investigate the influence of sensor shape through modifications to electrode layer coverage (both substrate and piezoelectric layers assumed to remain identical in size). Through competing influences of capacitance and electro-mechanical coupling findings suggest improvements in performance are likely to occur by reduced electrode coverage. They also conclude that a rectangular electrode shape is beneficial over a triangular shape. One criticism is that results from only one load resistor magnitude are presented. Although several researchers have attempted the optimisation of cantilever piezoelectric energy harvesters directly connected to a load resistance, fewer work can be found on optimisation in more realistic electrical scenarios. Due to the intricate coupling between electrical and mechanical aspects present in a piezoelectric energy harvesting system, the electrical scenario is expected to play an important role in determining an optimum design. A recent publication by Wang and Wu [100] presents the optimisation of piezoelectric material length and location in a capacitor charging scenario. In addition to the development of a theoretical model, experimental work was also preformed, with discrepancies in the region of 7%. The device under consideration was 600 mm in length with findings showing a piezoelectric layer of 140 mm in length attached to the clamped end provides optimum efficiency when excited at 4.77 Hz. One drawback with their findings includes excitation provided at the cantilever tip as opposed to its base. Although Wang and Wu claim the optimum design has the stated piezoelectric length, it is believed that this outcome is due to a matching between resonant and excitation frequencies. During their optimisation procedure, excitation frequency remained constant, resulting in the expectancy of maximum efficiency to occur for a tuned design – the authors of [100] agree with this issue stating optimised design is dependant on excitation frequency. Tanaka *et al.* [93] have carried out experimental work on the optimisation of rectangular cantilever piezoelectric energy harvesters through changes to piezoelectric layer length. Findings showed that power output saturates at approximately 70% coverage (when harvester are connected to a 1 MΩ load) with longer lengths showing little or no benefit. Tests were also performed on the charging of capacitors and concluded in the device with the longest piezoelectric layer

length providing maximum charge. From their device dimensions one would expect small fluctuations in fundamental frequency. However, presented plots showed a large spread in the fundamental frequency of devices indicating inadequate control during sample manufacture. Along with a lack of clarity in the experimental procedure, this leads to doubt on the validity of the conclusions.

This flavour of work on optimisation indicates great potential in improving the conventional cantilever design whereby both piezoelectric and substrate lengths are identical. The majority of work in this design optimisation area is solely theoretically based with a clear lack of published material on the validation of findings through experimental testing. Detailed work, both theoretical and experimental, demonstrating the reliability of optimisation predictions, is yet to be undertaken. Several aims of this thesis will attempt to fill such gaps and provide the reader with detailed knowledge on how geometric parameter changes affect key variables responsible for energy harvester performance. From this, reliable optimisations of piezoelectric cantilever energy harvester can be performed confidently without the necessity of extensive, costly, experimental work.

1.6 Non-linear modelling with emphasis given to non-linearity in piezoelectric energy harvesters

The energy harvester models used during various parametric studies outlined in the previous section share a similarity whereby linear behaviour assumptions are made. This is not often applicable, particularly in practical scenarios where moderate-to-high levels of acceleration are expected, suggesting a limitation to the observations made from previous parametric studies. In addition to the level of excitation resulting in non-linear behaviour, as was mentioned in Section 1.4.1, non-linearity can be intentionally introduced into an energy harvesting system in order to increase the operational bandwidth of a device. Ramlan *et al.* [79] analytically investigate the effects of introducing non-linearity to a system via spring hardening. They find the bandwidth over which energy can be harvested is increased and dependant on several factor – damping ratio, the degree of non-linearly and the input ac-

celeration. In the ideal case, maximum power output for such a generator however, is only slightly larger when compared to the conventional linear harvester. Similar research, on both theoretical modelling and experimental work, whereby non-linearity is introduced to the system intentionally, by the use of for example magnets, can be found in [23, 32, 33, 85] to name but a few.

Scenarios where non-linearity is not introduced for increasing bandwidth but naturally exists is now considered. Non-linearity is inherent in vibrating beams undergoing large displacements (geometric non-linearity) and also when certain materials are involved in the composition of the energy harvesting device (material non-linearity) – particularly associated with piezoelectric material. As derived by Joshi [44], non-linear constitutive equations for piezoelectric material can be used to define material non-linear behaviour. Use of such equations with, in some case, the inclusion of geometric non-linearity can readily be found for devices utilising piezoelectric materials for actuation [7, 11, 16, 40, 50] with few works available in relation to energy harvesting devices [52, 91].

The prime importance of correctly modelling non-linear behaviour in piezoelectric energy harvesting devices is related to shifts in resonant frequency, refer to Figure 1.11. Since the performance of an energy harvester is intrinsically linked to the matching of excitation frequency and resonant frequency, knowledge on the extent to which non-linearities affect resonant frequency is essential. The presence of geometric non-linearities will give rise to a 'hardening' phenomenon whereby resonant frequency increases, in contrast to any reductions in resonant frequency resulting from material non-linearities. In addition to these phenomena, it is also known that the magnitude of mechanical damping increases with excitation [105], which naturally reduces the efficiency of energy harvesting devices. For these reasons, the non-linear modelling of piezoelectric energy harvesters is seen to be an important area of research which requires greater attention, more-so when considering parametric studies and optimisations. It is also worth mentioning the importance of design for application. A universal energy harvester design suited to a wide range of applications is impractical due to the heavy dependency of performance on frequency. Rather, one must modify the design (i.e. through tweaking of dimensions or material choices) in accordance

to vibration characteristics available in the application environment.

1.7 Motivation and thesis overview

1.7.1 Research objectives

This thesis will aim to fill some fundamental gaps in research observed within the field of piezoelectric vibrational energy harvesting. Reliable validated models for conventional piezoelectric energy harvesters are common in the literature. In this thesis, model extensions are attempted to efficiently simulate the behaviour of non-uniform piezoelectric energy harvesters. This will allow for detailed optimisations of energy harvester geometry, particularly in terms of piezoelectric layer coverage and size. As outlined in Section 1.5, research has previously been carried out on geometry optimisations. However, the transfer of reported findings onto designs targeted at applications is yet to be seen. It is believed this results from a lack of confidence in previous finding particularly when it comes to detailed explanations and robust experimental verifications. This thesis will attempt to show which geometric optimisations should be considered during energy harvester design and justifications provided via both explanatory and experimental means.

Linear theoretical models are known to be limited when the representation of a piezoelectric energy harvesting system is concerned. To tackle this issue the development of a non-linear model, for uniform and non-uniform energy harvesters, is attempted in this thesis. Two forms of non-linearity (geometric and material) will be considered. In addition to extensions in the mechanical side of modelling, more realistic electrical scenarios will be considered and modelled as there is a distinct lack of literature on harvester geometry optimisation in such cases. Assessing the performance of various configurations while charging a capacitor, with the objective of determining how best to optimise harvester geometry, is desired. Through extensive experimental works the theoretical findings from various developed models will be validated, providing confidence in the models and their use during future design for application procedures. One further objective of this research is to determine a methodology by which harvester designs can be compared in an unbiased manner as

this is seen to be a key limitation in the manner in which past work was conducted.

1.7.2 Research contributions

Work undertaken and presented in this thesis can be differentiated from existing works in the following manner:

- Derived analytical expressions will be utilised while performing parametric studies on device geometry rather than relying on finite element packages. This approach is believed to greatly reduce computational time with negligible detrimental effects on the accuracy of results.

- Geometric optimisation of energy harvesters of various size and composition will be presented which will provide the reader with knowledge regarding how best to maximise key parameters in various design cases.

- Optimisation of energy harvesters in a more realistic electrical scenario, i.e. one in which generated energy is stored in a capacitor, will also be considered. Throughout the thesis, along with theoretical findings, the reader will be presented with results from detailed experimental work with one chapter highlighting and tackling issues with vibration testing and associated influences on model validation.

- A methodology by which unbiased comparison studies between harvester designs can be undertaken is also provided to the reader. This is seen as essential in the determination of an optimum design with past work failing to address this issue.

- The derivation and detailed validation of a non-linear model for piezoelectric energy harvesters, both uniform and non-uniform, will also be presented. For the purposes of performance studies this is of particular interest partly due to the sensitivity of harvester performance on excitation frequency. Although devices consisting of piezoelectric material are known to exhibit material non-linearity at moderate excitation levels, non-linear models are yet to be seen in the piezoelectric energy harvester optimisation field of research.

1.7.3 Approach

The layout of this thesis is as follows:

Chapter 2

Initially, the development of a linear model from which mechanical and electrical behaviour can be extracted is required. This model must encompass an accurate representation of the effect of alterations to piezoelectric layer dimensions and converge. Influences of such changes, both mechanically, in terms of structure dynamics, and electrically, in terms of output charge, will require careful consideration. Predictions of natural frequencies and mode shapes for non-uniform structures are vital along with estimations on variations in damping magnitude with geometrical changes. The emphasise in Chapter 2 is to provide derivations and details on such a linear model along with the presentation of preliminary results.

Chapter 3

Chapter 3 investigates how various geometric parameters, i.e. piezoelectric layer coverage, affect the performance of piezoelectric energy harvesters. Using the theoretical model developed in Chapter 2, the harvester geometry is optimised for three distinct cases. These cases – two macro-scale (one of which is a thin film flexible device) and one micro-scale – are considered throughout the thesis. The influence of device size and composition on the optimisation process and optimised design are discussed. Additionally, findings/trends reported by other researchers, outlined in Section 1.5, will be revisited and compared with those generated by the current model. Also, comparisons between unimorph and bimorph devices are included in order to determine which of the two configurations has superior performance capabilities.

Chapter 4

In Chapter 4 the theoretical model is validated through detailed experimental works. A procedure for sample manufacture is outlined along with testing methodology. Initially, individual uniform and non-uniform energy harvesters are considered, followed by attempts to validate trends between piezoelectric length and generated voltage. The effects of testing conditions, i.e. consistency in clamping, and variations in mechanical damping during

testing are considered closely and discussed in detail.

Chapter 5

Chapters 2, 3 and 4 are based on devices connected to load resistors of varying magnitude. In Chapter 5, a more realistic electrical scenario comprising of a capacitor for energy storage is considered. A theoretical model is developed analytically and then implemented in SIMULINK® . This SIMULINK® model forms a basis from which further extensions to electrical aspects can be made readily. Geometry optimisation of devices, for the three distinct cases, is investigated whilst simulating the charging of a capacitor. A resistor representing electrical losses, which is also essential for validation purposes, is included in the theoretical model. Lastly, validation of the SIMULINK® model, in terms of both individual harvesters and the trends in piezoelectric layer length vs. performance, is presented through further experimental work.

Chapter 6

Preforming parametric studies on device geometry with a varying fundamental frequency between harvester designs is seen to be a major problem. This is tackled in Chapter 6 with presentation of a multi-geometric-parameter-alteration approach. Options and justifications for good control parameters in fundamental frequency control are discussed. Theoretical results are presented and analysed while investigating piezoelectric layer dimensions for three distinct cases.

Chapter 7

In the penultimate chapter, a theoretical model to predict the performance of a piezoelectric energy harvester taking into account non-linear effects is developed. Two forms of non-linearity are considered, namely material and geometric. Validation of the model through extensive experimental work, on uniform and non-uniform harvesters, will also be presented. Whilst subjecting the devices to excitation conditions which induce non-linear behaviour, the effect of piezoelectric layer coverage on device performance is investigated. Comparisons of the trends obtained here with those produced using the linear model developed in Chapter 2 are also made, and any differences are discussed.

Chapter 8

Chapter 8 provides an overview and discussion of the findings. Also included are details on areas in which further work can be undertaken.

CHAPTER 2

THEORETICAL MODELLING OF CANTILEVER PIEZOELECTRIC ENERGY HARVESTERS

2.1 Introduction

In this chapter an analytical model for the performance of a cantilever piezoelectric vibrational energy harvester is developed. The Erturk and Inman [27] model is used as a basis for the linear energy harvester model derived in this thesis. The model has been extended in both mechanical and electrical aspects. This chapter looks into extensions in mechanical system aspects where effects of altering the length and width of piezoelectric material are incorporated. A transfer matrix model [71] is adopted which allows for accurate predictions of the natural frequencies and mode shapes of the structure. The transfer matrix method makes use of exact beam functions and can be utilised efficiently to model both uniform and non-uniform harvester configurations. Altering the piezoelectric layer length will also have an affect on mechanical damping. An assumption of proportional damping is made which allows the mechanical damping ratio to change in correspondence to natural frequency while performing parametric studies.

Equations incorporating the effects of a rigid tip mass, offset from the cantilever free end,

will also be derived and included in the model. Tip masses are used on energy harvesters to reduce and tune fundamental frequency and improve strain distribution along a cantilever structure.

The objectives of this chapter are as follows:

- Develop a model for a unimorph energy harvester which allows length and position of the piezoelectric layer to be altered.
  - Incorporate proportional damping as a way to alter mechanical damping ratio with harvester topology.
  - Derive transfer matrix model for a non-uniform cantilever beam.
- Extend model to incorporates a tip mass whilst also considering the offset distance between the tip mass centre of gravity and the beam tip.
- Develop model for a bimorph energy harvester.

Initially, equations which govern the response of the harvester are derived for a unimorph energy harvester, Sections 2.2.1 to 2.2.3. Following this, a transfer matrix model, for modal information, is created, Section 2.2.4. The dynamic effects and energy harvester performance differences of adding a tip mass to the system are considered in Section 2.3. An additional piezoelectric layer is added in the last section, Section 2.4, allowing theoretical simulations of bimorph energy harvesters. The electrical scenario considered in this chapter consists solely of a load resistor. Voltage generated and power dissipated across the resistor can be used as performance measures. In Chapter 5 energy harvesters connected to storage capacitors are modelled and simulated.

2.2 Unimorph energy harvester

A unimorph piezoelectric energy harvester is considered in this section, see Figure 2.1. It consists of piezoelectric material perfectly bonded to a lower substrate layer. Only cantilever structures are considered in these works. Cantilevers (i.e. clamped-free boundary

conditions) provide relatively high strain in materials per unit forcing in comparison to other boundary conditions i.e. pinned-free (which is also harder to realise in practical situations). The derived model will take into account effects of piezoelectric material not covering the full substrate length. In Figure 2.1, x_2 refers to the piezoelectric material length, x_1 is the offset distance of piezoelectric material from the clamped end and x_3 is the distance from the end of the piezoelectric material to cantilever tip. Upper and lower surfaces of the piezoelectric layer are fully coated with electrode material, e.g. screen-printed silver, whose thickness is assumed negligible along with adhesive layer thickness. Adhesive layer effects, for example, reducing overall structure stiffness and sliding between individual layers are negligible and will not be considered in the following derivation.

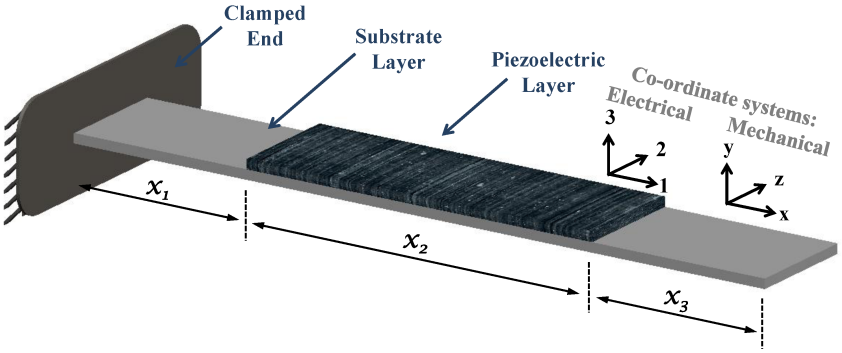

Figure 2.1: Example of a unimorph energy harvester.

2.2.1 Mechanical equation of motion

The unforced transverse vibration of an undamped beam is given by [20]:

$$\frac{\partial^2 M(x,t)}{\partial x^2} + m(x)\frac{\partial^2 w(x,t)}{\partial t^2} = 0\,, \tag{2.1}$$

where $w(x,t)$ is the transverse deflection, $M(x,t)$ is the internal moment of the beam cross-section and $m(x)$ is the mass per unit length. Note the consideration of a Euler-Bernoulli beam whereby rotary inertia effects and shear deformation are ignored by assuming the beam is long and slender. The conventional method for transferring vibrational energy to the beam structure is through base excitation. For the purposes of analysis it is convenient

to express the flexural displacement, $w(x,t)$, of the beam as follows:

$$w(x,t) = w_{\text{rel}}(x,t) + w_b(x,t) \ . \tag{2.2}$$

where $w_{\text{rel}}(x,t)$ is the beam displacement relative to the base and $w_b(x,t)$ the displacement of the base.

The following piezoelectric constitutive equations are used to describe the electromechanical coupling properties for the piezoelectric material [1], viz.:

$$\sigma_{11}^p = E_p \varepsilon_{11}^p - E_p d_{31} (E_{\text{field}})_3 \ , \tag{2.3}$$

$$D_3 = E_p d_{31} \varepsilon_{11}^p + \varepsilon_{33}^S (E_{\text{field}})_3 \ , \tag{2.4}$$

where σ is the stress and D the electric displacement. E, ε and E_{field} represents the Young's modulus, strain and electric field strength, respectively. d_{31} is the piezoelectric material constant (units C.N^{-1}) and ε_{33}^S is the permittivity at constant strain (units F.m^{-1}). As defined in Section 1.2.4, index 3 refers to the y-direction i.e. through the thickness of the material, and index 1 refers to the x-direction i.e. parallel to the beam length. In addition, subscript 'p' refers to the piezoelectric material. Assuming the electric field is uniform throughout the constant piezoelectric material thickness, t_p, then $(E_{\text{field}})_3(t)$ can be expressed as:

$$(E_{\text{field}})_3 = -\frac{V(t)}{t_p} \ , \tag{2.5}$$

where $V(t)$ is voltage across the piezoelectric layer electrodes. The constitutive equation for the substrate material is used to relate stress and strain, viz.:

$$\sigma_{11}^s = E_s \varepsilon_{11}^s \ , \tag{2.6}$$

where, subscript 's' refers to the substrate material.

The internal moment, $M(x,t)$, which appears in Equation 2.1 can be expressed as:

$$M(x,t) = -\int_{h_a}^{h_b} \sigma_{11}^{s} b_s y \mathrm{d}y - \int_{h_b}^{h_c} \sigma_{11}^{p} b_p y \mathrm{d}y \ , \tag{2.7}$$

where b_s and b_p are the widths of the substrate and piezoelectric layers, which are assumed to be constant along the beam length. The terms h_a, h_b and h_c are defined in Figure 2.2 and are dependant on the position of the neutral axis, $\overline{y}$. The position of the neutral axis is given by:

$$\overline{y} = \frac{{t_s}^2 b_s + {t_p}^2 n b_p + 2 t_s t_p n b_p}{2(t_s b_s + t_p n b_p)} \ , \tag{2.8}$$

where n is the constant ratio of the piezoelectric Young's modulus to the substrate Young's modulus (E_p/E_s).

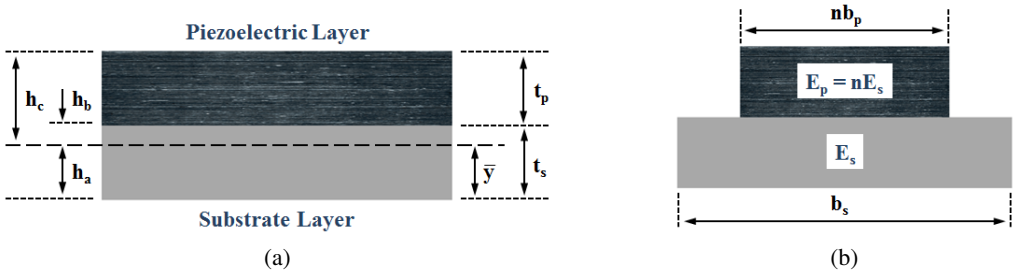

Figure 2.2: Cross-sectional view of unimorph energy harvester.

The strain in the beam can be approximated as follows:

$$\varepsilon(x,t) = -y \frac{\partial^2 w_{\text{rel}}(x,t)}{\partial x^2} \ . \tag{2.9}$$

where y is the distance from the neutral axis.

Using Equations (2.3), (2.6) and (2.9) in Equation (2.7), the internal moment can be expressed as:

$$M(x,t) = E_s I_s \frac{\partial^2 w_{\text{rel}}(x,t)}{\partial x^2} + E_p I_p \frac{\partial^2 w_{\text{rel}}(x,t)}{\partial x^2} + \epsilon V(t) \ . \tag{2.10}$$

I_s and I_p are expressions for the second moment of area and ϵ is an electromechanical

coupling term, viz.:

$$I_s = \frac{b_s}{3}\left[\left(t_s - \overline{y}\right)^3 - \left(-\overline{y}\right)^3\right], \tag{2.11}$$

$$I_p = \frac{b_p}{3}\left[\left(t_p + t_s - \overline{y}\right)^3 - \left(t_s - \overline{y}\right)^3\right], \tag{2.12}$$

$$\epsilon = -\frac{E_p b_p d_{31}}{2t_p}\left[\left(t_p + t_s - \overline{y}\right)^2 - \left(t_s - \overline{y}\right)^2\right]. \tag{2.13}$$

As opposed to the Erturk and Inman model [27], Heaviside functions are now introduced and carried throughout the derivation. Since parametric studies on geometry will inevitably affect the length and position of piezoelectric material, Heaviside functions are used to limit the contribution of the finite length piezoelectric layer on the overall moment. Using this approach the internal moment can be expressed as:

$$M(x,t) = EI(x)\frac{\partial^2 w_{\text{rel}}(x,t)}{\partial x^2} + \epsilon V(x,t)\,, \tag{2.14}$$

where $EI(x)$ is the flexural rigidity defined as:

$$EI(x) = E_s I_s + E_p I_p\big[H(x - x_1) - H(x - x_1 - x_2)\big]\,, \tag{2.15}$$

and $V(x,t)$ is defined as:

$$V(x,t) = V(t)\big[H(x - x_1) - H(x - x_1 - x_2)\big]\,. \tag{2.16}$$

A similar approach can be used to represent the mass term in Equation (2.1), and using Equation (2.14), Equation (2.1) can be expressed as follows:

$$\frac{\partial^2}{\partial x^2}\left[EI(x)\frac{\partial^2 w_{\text{rel}}(x,t)}{\partial x^2} + \epsilon V(x,t)\right] + m(x)\frac{\partial^2 w_{\text{rel}}(x,t)}{\partial t^2} = m(x)\frac{\partial^2 w_b(t)}{\partial t^2}\,, \tag{2.17}$$

where $m(x)$ is defined by:

$$m(x) = \rho_s A_s + \rho_p A_p \big[H(x - x_1) - H(x - x_1 - x_2)\big] \ . \tag{2.18}$$

The mechanical behaviour of a piezoelectric beam is governed by Equation (2.17) and can be analysed using classical modal analysis techniques. Using this approach the beam deflection, $w_{\text{rel}}(x,t)$, is expressed as an infinite sum of products of normalised eigenvectors, $W_r(x)$, and time dependant generalised co-ordinates, $\eta_r(t)$, viz.:

$$w_{\text{rel}}(x,t) = \sum_{r=1}^{\infty} W_r(x)\eta_r(t) \ , \tag{2.19}$$

where 'r' refers the mode number. Using Equation (2.19) in Equation (2.17) gives:

$$\frac{\partial^2}{\partial x^2}\left[EI(x)\sum_{r=1}^{\infty} W_r''(x)\eta_r(t) + \epsilon V(x,t)\right] + m(x)\sum_{r=1}^{\infty} W_r(x)\ddot{\eta}_r(t) = m(x)\ddot{w}_b(t) \ . \tag{2.20}$$

In this expression $()''$ refers to the second derivative with respect to longitudinal position, and $\ddot{()}$ refers to the second derivative with respect to time.

As a result of multiplying Equation (2.20) by $W_q(x)$ and integrating over the beam length, it can be shown that:

$$\ddot{\eta}_q(t) + {\omega_q}^2\eta_q(t) + \epsilon\int_0^L W_q(x)\frac{\partial^2 V(x,t)}{\partial x^2}\mathrm{d}x = \ddot{w}_b(t)\int_0^L m(x)W_q(x)\mathrm{d}x \ , \tag{2.21}$$

where the following orthogonality conditions have been used:

$$\int_0^L W_q(x)m(x)W_r(x)\mathrm{d}x = \delta_{rq} \qquad\qquad r,q = 1,2,3,..... \tag{2.22}$$

$$\int_0^L W_q(x)\Big(EI(x)W_r''(x)\Big)''\mathrm{d}x = {\omega_q}^2\delta_{rq} \qquad\qquad r,q = 1,2,3,..... \tag{2.23}$$

δ_{rq} is the Kronecker delta function which is unity when $r = q$, and zero otherwise. ω_q is

the undamped natural frequency of the q^{th} mode, and is considered in Section 2.2.4.

The voltage term appearing in Equation (2.21) can be manipulated by introducing the Dirac function [68], $\delta(x)$, as the derivative of the Heaviside function, i.e.

$$\begin{aligned}\epsilon \int_0^L W_q(x) \frac{\partial^2 V(x,t)}{\partial x^2} \mathrm{d}x =& \epsilon \int_0^L W_q(x) V(t) \big[H''(x-x_1) - H''(x-x_1-x_2)\big] \\ =& \epsilon \int_0^L W_q(x) V(t) \big[\delta'(x-x_1) - \delta'(x-x_1-x_2)\big] \\ =& \epsilon V(t) \big[W_q'(x_1+x_2) - W_q'(x_1)\big] \ . \end{aligned} \tag{2.24}$$

Using Equation (2.24) in (2.21) gives:

$$\ddot{\eta_q}(t) + {\omega_q}^2 \eta_q(t) + \epsilon V(t) \Big[W_q'(x_1+x_2) - W_q'(x_1)\Big] = \ddot{w}_b(t) \int_0^L m(x) W_q(x) \mathrm{d}x \ . \tag{2.25}$$

Equation (2.25) provides the modal response of a piezoelectric beam subjected to base excitation. Note that damping is currently not present in this equation and will be included in the following section.

2.2.1.1 Proportional damping

Some form of damping must be included in the system due to the presence of energy dissipation in all real situations. It is mathematically convenient to assume proportional damping [97], such that the damping matrix can be expressed as:

$$[C] = \alpha[M] + \beta[K] \ , \tag{2.26}$$

where α and β are constants and can be obtained from experimental data, see Chapter 4, and $[M]$ and $[K]$ are the mass and stiffness matrices of the structure respectively. Consider the following damped equation of motion for a beam (found in any vibrations text book i.e.

Weaver *et al.* [101]):

$$[M]\ddot{\boldsymbol{w}}_{\text{rel}} + [C]\dot{\boldsymbol{w}}_{\text{rel}} + [K]\boldsymbol{w}_{\text{rel}} = \boldsymbol{F}(t) \ , \tag{2.27}$$

where $\mathbf{F}(t)$ is an arbitrary forcing. Using Equation (2.19) for the beam deflection in Equation (2.27) provides the following:

$$[M]\sum_{r=1}^{\infty} W_r(x)\ddot{\eta}_r(t) + [C]\sum_{r=1}^{\infty} W_r(x)\dot{\eta}_r(t) + [K]\sum_{r=1}^{\infty} W_r(x)\eta_r(t) = \boldsymbol{F}(t) \ . \tag{2.28}$$

Modal decoupling and the modal orthogonality conditions can be used on Equation (2.28) along with Equation (2.26), allowing Equation (2.28) to be written as:

$$\ddot{\eta}_q(t) + \left(\alpha + {\omega_q}^2\beta\right)\dot{\eta}_q(t) + {\omega_q}^2\eta_q(t) = W_q(x)\boldsymbol{F}(t) \ . \tag{2.29}$$

If $W_q(x)$ is normalised with respect to the mass matrix, which will be the case, see Section 2.2.4, the following modal relations apply when obtaining Equation (2.29):

$$\begin{aligned} {W_q}^T[M]W_q &= 1 \ , \\ {W_q}^T[K]W_q &= {\omega_q}^2 \ . \end{aligned} \tag{2.30}$$

Introduction of the modal damping ratio, γ [101], provides the following relationship:

$$\alpha + {\omega_q}^2\beta = 2\gamma_q\omega_q \ . \tag{2.31}$$

Proportional damping is useful as it incorporates changes in mechanical damping magnitude with changes in energy harvester geometry due to differences in the fundamental frequency of configurations. Introducing modal damping in Equation (2.25) allows for the complete modal behaviour of the energy harvester to be predicted using:

$$\ddot{\eta}_q(t) + 2\gamma_q\omega_q\dot{\eta}_q(t) + {\omega_q}^2\eta_q(t) + \epsilon V(t)\Big[W_q'(x_1 + x_2) - W_q'(x_1)\Big] = \ddot{w}_b(t)\int_0^L m(x)W_q(x)\mathrm{d}x \ . \tag{2.32}$$

This equation, which now includes a contribution from mechanical damping, will be used in conjunction with an electrical equation derived in Section 2.2.2 to fully describe electro-mechanical behaviour of a piezoelectric cantilever energy harvester.

2.2.2 Electrical equation

In this section an expression for the electrical output (voltage) of the system is derived. Initially the piezoelectric cantilever is connected to a load resistor, as is shown Figure 2.3. The power dissipated through various load resistors will be investigated later to compare the performance of different harvester designs, Chapter 3. Also, in Chapter 5, a more realistic electrical scenario is investigated.

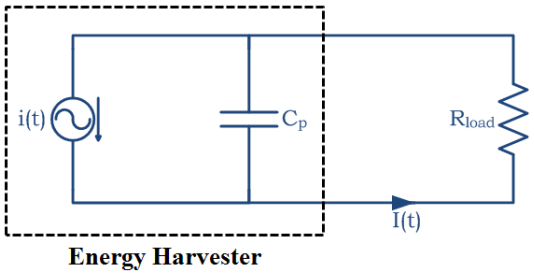

Figure 2.3: Electrical representation of energy harvester connected to a resistor.

Using Equations (2.5) and (2.9) in Equation (2.4) the 2nd piezoelectric constitutive equation can be expressed as:

$$D_3(x,t) = -E_p d_{31} t_{pc} \frac{\partial^2 w_{\text{rel}}(x,t)}{\partial x^2} - \frac{\varepsilon_{33}^S}{t_p} V(t) \ , \tag{2.33}$$

where t_{pc} is the distance between the neutral axis, $\overline{y}$, and the piezoelectric material centre. The generated charge, $q(t)$, can be calculated using a form of Gauss's Law, by integrating electric displacement over the electrode area, A_e, viz.:

$$q(t) = \iint_{A_e} D_3(x,t) \mathrm{d}A_e \ . \tag{2.34}$$

The current generated by the energy harvester, $i(t)$, is the time derivative of charge and

composed of a contribution from vibratory beam motion and static capacitance of the piezoelectric material.

$$i(t) = -\int_{x_1}^{x_1+x_2} E_p d_{31} t_{pc} b_p \frac{\partial^3 w_{\text{rel}}(x,t)}{\partial x^2 \partial t} \mathrm{d}x - C_p \frac{\partial V(t)}{\partial t} \ , \tag{2.35}$$

where C_p refers to the piezoelectric internal capacitance:

$$C_p = \frac{\varepsilon_{33}^S b_p x_2}{t_p} \ . \tag{2.36}$$

As previously mentioned, the harvester is connected to a load resistor, R_{load}, and in this case Ohm's Law can be used in conjunction with Equations (2.19) and (2.35) to obtain the following differential equation for voltage generated:

$$C_p \frac{\partial V(t)}{\partial t} + \frac{V(t)}{R_{\text{load}}} = \sum_{q=1}^{\infty} -E_p d_{31} t_{pc} b_p \left[\frac{\partial W_q(x)}{\partial x} \right]_{x_1}^{x_1+x_2} \dot{\eta}_q(t) \ . \tag{2.37}$$

Equation (2.37) indicates the voltage generated by the piezoelectric layer is dependent on the modal response of the beam, mode shape, internal capacitance, load resistance and mechanical and electric properties of the material.

2.2.3 Coupled model

The derived mechanical and electrical equations (Equations (2.32) and (2.37)) are coupled equations, and in this section the coupled response is obtained. Assuming the base motion is harmonic, the voltage generated is also harmonic and the base excitation and voltage generated can be expressed as follows:

$$w_b(t) = Y_0 \mathrm{e}^{\mathrm{i}\omega t} \ , \tag{2.38}$$

$$V(t) = V_0 \mathrm{e}^{\mathrm{i}\omega t} \ , \tag{2.39}$$

where Y_0 is the amplitude of the base excitation, V_0 is the peak voltage, ω is the frequency of excitation and t is time. All studies in this thesis will consider excitation close to the fun-

damental frequency of the energy harvester design; because peak performance is achieved. For this reason, only the first vibration mode is considered in what follows. Inserting Equations (2.38) and (2.39) into the modal equation of motion, Equation (2.32), and setting the mode number q to 1 provides:

$$\ddot{\eta_1}(t) + 2\gamma_1\omega_1 + {\omega_1}^2\eta_1(t) = \Big(Q_1 - R_1V_0\Big)\mathrm{e}^{\mathrm{i}\omega t} \,, \tag{2.40}$$

where Q_1 and R_1 are the mechanical forcing and electromechanical coupling terms respectively, defined by:

$$Q_1 = -Y_0\omega^2 \int_0^L m(x)W_1(x)\mathrm{d}x \,, \tag{2.41}$$

$$R_1 = \epsilon\Big[W_1'(x_1 + x_2) - W_1'(x_1)\Big] \,. \tag{2.42}$$

Assuming the particular solution for the modal co-ordinate is $\eta_1(t) = \eta_1 e^{i\omega t}$ the solution to Equation (2.40) can be expressed as:

$$\eta_1(t) = \left[\frac{Q_1 - R_1V_0}{\Big({\omega_1}^2 - \omega^2\Big) + \Big(2\gamma_1\omega_1\omega\Big)\mathrm{i}}\right]\mathrm{e}^{\mathrm{i}\omega t} \,. \tag{2.43}$$

Using Equation (2.43) in Equation (2.37) yields:

$$V(t) = \left[\frac{\dfrac{Q_1\phi_1\mathrm{i}\omega}{\Big({\omega_1}^2 - \omega^2\Big) + \Big(2\gamma_1\omega_1\omega\Big)\mathrm{i}}}{\dfrac{R_1\phi_1\mathrm{i}\omega}{\Big({\omega_1}^2 - \omega^2\Big) + \Big(2\gamma_1\omega_1\omega\Big)\mathrm{i}} + \left(\mathrm{i}\omega + \dfrac{1}{C_pR_{\text{load}}}\right)}\right]\mathrm{e}^{\mathrm{i}\omega t} \,, \tag{2.44}$$

where ϕ_1 is a second electro-mechanical coupling term defined by:

$$\phi_1 = -\frac{E_pd_{31}t_{pc}b_p}{C_p}\Big[W_1'(x_1 + x_2) - W_1'(x_1)\Big] \,. \tag{2.45}$$

The power dissipated, $P(t)$, in a load resistor is readily calculated using the relation $P(t) = V^2(t)/R_{\text{load}}$. Using Equation (2.43) in Equation (2.19), the beam displacement is

given by:

$$w_{\text{rel}}(x,t) = W_1(x)\left[\frac{Q_1 - R_1 V_0}{\left({\omega_1}^2 - \omega^2\right) + \left(2\gamma_1\omega_1\omega\right)\mathrm{i}}\right]\mathrm{e}^{\mathrm{i}\omega t}\,. \tag{2.46}$$

Equation (2.44) will be used throughout Chapter 3 for performance comparisons of harvesters with various geometries, and in Chapter 4 where model validation through experimental work is undertaken. Recall several assumptions were made during the derivation:

- Piezoelectric layer electrodes and adhesive layer of negligible thickness
- Perfect bonding between piezoelectric and substrate layers
- Constant uniform electric field through the thickness of the piezoelectric layer
- Proportional damping present across all harvester configurations
- Layer topology is rectangular with constant width and thickness

In order to use Equations (2.44) and (2.46) to calculate the voltage and displacement of the energy harvester the fundamental frequency, ω_1 and fundamental mode shape, W_1 are required. A model for ω_1 and W_1 is presented in the following section.

2.2.4 Transfer matrix model for a segmented unimorph structure

The model presented in so far requires knowledge of the natural frequencies and mode shapes of the harvester. In this section the transfer matrix method [71] is used to obtain this information for a segmented cantilever beam, by taking into account the length and position of the piezoelectric layer. As shown in Figure 2.4 the beam is split into three sections. The substrate material alone makes up sections 1 and 3, while section 2 comprises both piezoelectric and substrate materials. The notation used to define the mechanical forces and deformations at the nodes of each element is shown in Figures 2.4 and 2.5.

The exact beam function for the transverse motion of the i^{th} section of a segmented

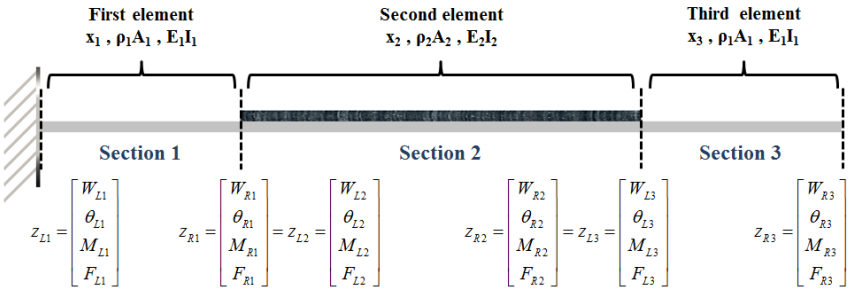

Figure 2.4: Element properties for beam sections. Each nodal joint has an associated displacement (W), rotation (θ), moment (M) and shear force (F).

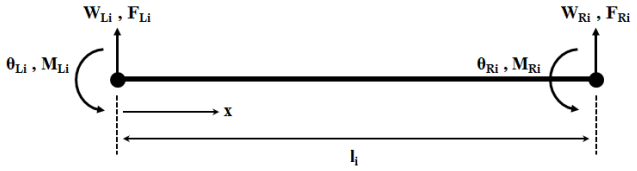

Figure 2.5: Notation adopted for information at nodal points of the ith beam element.

beam is given by:

$$W_i(x) = a\sin\left(\frac{\beta_i x}{l_i}\right) + b\cos\left(\frac{\beta_i x}{l_i}\right) + c\sinh\left(\frac{\beta_i x}{l_i}\right) + d\cosh\left(\frac{\beta_i x}{l_i}\right) \ , \qquad (2.47)$$

where a, b, c and d are constants which are ordinarily determined using boundary conditions, x is the distance from the left side of the beam segment and l_i is the beam segment length. β_i can be defined by:

$$\beta_i = \omega^{0.5} l_i \left(\frac{\rho_i A_i}{E_i I_i}\right)^{0.25} \ , \qquad (2.48)$$

where E_i is the element Young's modulus, I_i is the element area moment of inertia, ρ_i is the element mass density and A_i is the element cross-sectional area. The middle section is a composite piezoelectric/substrate beam and the properties of this element can be calculated using the equivalent flexural rigidity, viz.:

$$(EI)_{\text{composite}} = E_s I_{ys} + E_p I_{yp} \ , \qquad (2.49)$$

where the parallel axis theorem can be used to obtain I_{ys} and I_{yp}, such that:

$$I_{ys} = \frac{b_s {t_s}^3}{12} + b_s t_s \left(\overline{y} - \frac{t_s}{2}\right)^2 , \tag{2.50}$$

$$I_{yp} = \frac{b_p {t_p}^3}{12} + b_p t_p \left(\frac{t_p}{2} + t_s - \overline{y}\right)^2 . \tag{2.51}$$

The mechanical forces and deformations at the right-hand side of any beam element, z_{Ri}, can be related to the left-hand side, z_{Li}, though the use of a transfer matrix, $\mathbf{U_i}(l_i)$ [71], where,

$$\begin{bmatrix} W_{Ri} \\ \theta_{Ri} \\ M_{Ri} \\ F_{Ri} \end{bmatrix} = \mathbf{U_i}(l_i) \begin{bmatrix} W_{Li} \\ \theta_{Li} \\ M_{Li} \\ F_{Li} \end{bmatrix} , \tag{2.52}$$

and $\mathbf{U_i}(l_i)$ is defined by:

$$\mathbf{U_i}(l_i) = \begin{bmatrix} C_0 & -l_i C_1 & -\frac{l_i^2 C_2}{E_i I_i} & -\frac{l_i^3 C_3}{E_i I_i} \\ -\frac{{\beta_i}^4 C_3}{l_i} & C_0 & \frac{l_i C_1}{E_i I_i} & \frac{l_i^2 C_2}{E_i I_i} \\ -\frac{E_i I_i {\beta_i}^4 C_2}{l_i^2} & \frac{E_i I_i {\beta_i}^4 C_3}{l_i} & C_0 & l_i C_1 \\ -\frac{E_i I_i {\beta_i}^4 C_1}{l_i^3} & \frac{E_i I_i {\beta_i}^4 C_2}{l_i^2} & \frac{{\beta_i}^4 C_3}{l_i} & C_0 \end{bmatrix} . \tag{2.53}$$

Constants C_0 to C_3 are defined by:

$$C_0 = \frac{\cosh(\beta_i) + \cos(\beta_i)}{2} , \tag{2.54}$$

$$C_1 = \frac{\sinh(\beta_i) + \sin(\beta_i)}{2\beta_i} , \tag{2.55}$$

$$C_2 = \frac{\cosh(\beta_i) - \cos(\beta_i)}{2{\beta_i}^2} , \tag{2.56}$$

$$C_3 = \frac{\sinh(\beta_i) - \sin(\beta_i)}{2{\beta_i}^3} . \tag{2.57}$$

Please refer to [71] for full details on how the transfer matrix and related constants are derived. For the general case, where piezoelectric material (of length shorter than the substrate layer) is centrally located on the beam, the overall transfer matrix of the system, $\mathbf{U}_{\text{overall}}$, is obtained from:

$$\mathbf{U}_{\text{overall}} = \mathbf{U_3}(x_3)\mathbf{I}_{\text{matrix}}\mathbf{U_2}(x_2)\mathbf{I}_{\text{matrix}}\mathbf{U_1}(x_1) \ , \tag{2.58}$$

where $\mathbf{I}_{\text{matrix}}$ is a 4×4 identity matrix and $\mathbf{U_1}$ through $\mathbf{U_3}$ are the transfer matrices for each section. In some configurations certain sections are not present, i.e. for a conventional energy harvester the piezoelectric layer covers the full length of the beam and sections 1 and 3 are not present. In these cases the corresponding transfer matrices are replaced with 4×4 identity matrices. Since $\mathbf{U}_{\text{overall}}$ relates the clamped end of the structure to the free end, known boundary conditions (in a free vibration situation), $w_{\text{clamped}} = \theta_{\text{clamped}} = M_{\text{free}} = F_{\text{free}} = 0$ can be used to obtain a matrix those determinant yields the natural frequencies of the system. The 2×2 matrix of interest is extracted from the bottom right corner of the $\mathbf{U}_{\text{overall}}$ matrix. Values of ω which produce determinate values of zero provide the natural frequencies of the system. Since mode shapes can be arbitrarily scaled, once natural frequencies are known the corresponding mode shapes are readily obtained by assuming one of the variables, i.e. clamped end shear force F, is unity. Following this the mode shapes are scaled as required, i.e. to the mass of the structure.

2.2.4.1 Preliminary results from the transfer matrix method model

In the following examples the transfer matrix model is used to demonstrate the effects of piezoelectric layer geometry on the fundamental frequency. The substrate and piezoelectric layers are chosen to be aluminium, Al, and PZT respectively. These materials are used to validate the model later, using samples manufactured from Al and PZT, see Chapter 4. The nominal dimensions for the energy harvester used in this investigated study are shown in Table 2.1. Firstly, the effects of changing the piezoelectric layer length are examined. This is achieved, either by removing material from the free end (increasing x_3 on Figure 2.1), or

by removing material from the clamped end (increasing x_1 on Figure 2.1).

Table 2.1: Structural dimensions and mechanical properties of the conventional harvester used throughout this analysis.

Parameter	Value
Substrate length (mm)	50
Substrate width (mm)	5
Substrate thickness (mm)	0.5
PZT length (mm)	50[a]
PZT width (mm)	5[a]
PZT thickness (mm)	0.5
Young's modulus of substrate (GPa)	69
Density of substrate (kg.m^{-3})	2700
Young's modulus of PZT (GPa)	62.1
Density of PZT (kg.m^{-3})	7800

[a] Parameter to be altered during proceeding analysis.

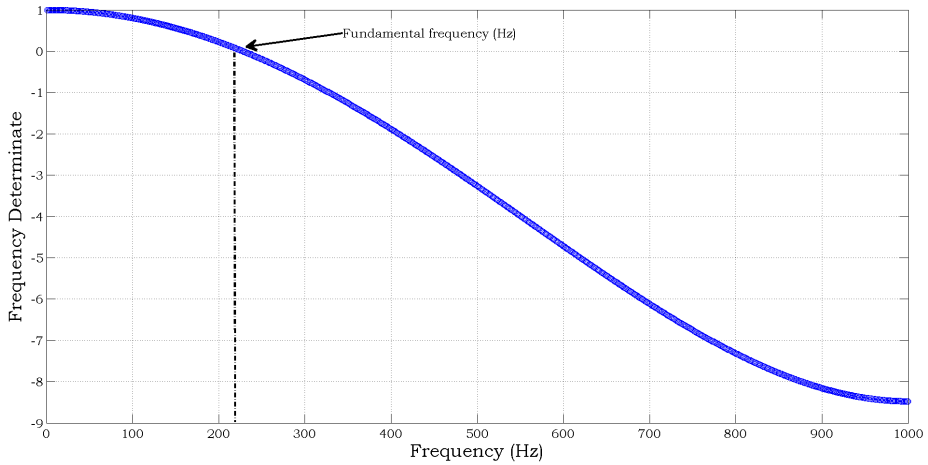

Figure 2.6: Sweeping the frequency to determine the fundamental frequency of a conventional energy harvester whose dimensions can be found in Table 2.1. Fundamental frequency of this design is 228.1 Hz.

Rather than working through the calculation symbolically and obtaining a characteristic equation to solve for the natural frequencies, a numerical approach is adopted here. The solution for the frequency determinant can be obtained efficiently using MATLAB® to perform the matrix calculations. Since the devices considered here are on the macro-scale (micro-scale devices including a tip mass to reduce the natural frequency are considered later) the frequency is swept from 1 Hz to 1000 Hz and interpolation techniques are used to determine the fundamental frequency, see Figure 2.6. The figure shows an example of

sweeping over the whole frequency range, however during implementation in MATLAB® , values are incremented by 1 Hz until the sign of the determinant changes. In this case that would occur at 229 Hz. Interpolation is then used to obtain the value for the frequency, in this case 228.1 Hz, which provides a determinant of zero. This approach provides a more efficient method for obtaining the fundamental frequency.

Figure 2.7 shows how the fundamental frequency changes when piezoelectric material is removed from either end of the beam. The results indicate that the fundamental frequency is significantly affected while altering PZT layer length. In this example, the frequency shifts by over 66%, equivalent to 150 Hz. Any reduction in length will reduce the mass and stiffness of the structure. It is the magnitude by which the stiffness changes which determines the observed trends. Take for example the case where the PZT layer remains coincident with the free end. Initially the reduction in PZT length causes a relatively large reduction in stiffness in comparison to mass, thereby decreasing the fundamental frequency. The piezoelectric layer is effectively acting as a tip mass in this scenario. After a 'critical length', in this case 24 mm, any further reduction in PZT length causes the fundamental frequency to increase. This is due to rate of decrease in mass being faster than stiffness. Similar logic can be applied to the case when the PZT layer remains coincident with the clamped end. Identical effects are also observed when altering the width of the PZT layer, see Figure 2.8. Note in this scenario the substrate width remains constant at 5 mm.

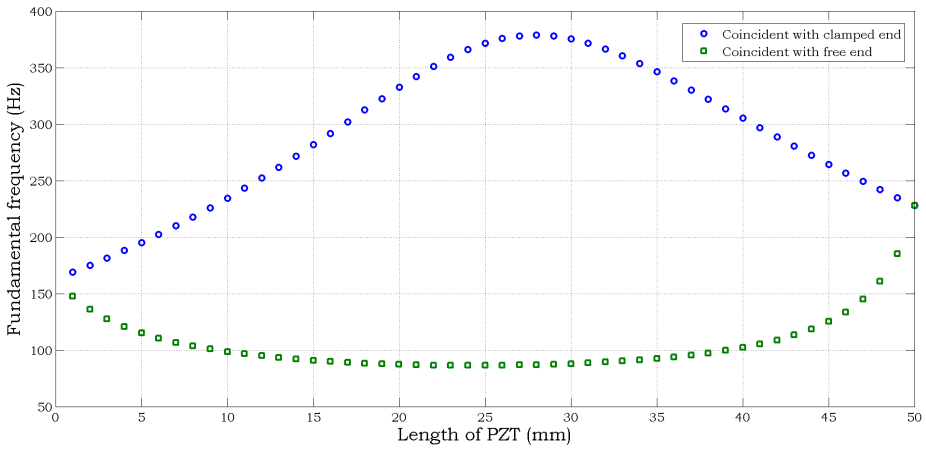

Figure 2.7: Fundamental frequency while altering length of piezoelectric layer.

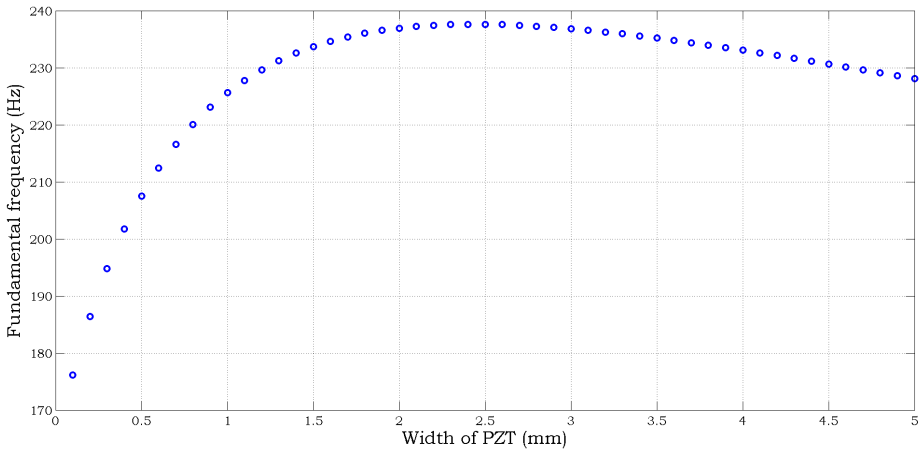

Figure 2.8: Fundamental frequency while altering width of piezoelectric layer.

2.2.5 Numerical study of a conventional energy harvester

In this section a harvester in open and closed circuit conditions is simulated. Open circuit refers to an infinite circuit resistance whereas closed circuit occurs when no resistance is present. The energy harvester, assumed to be of conventional type, is subjected to harmonic base excitation. A low acceleration amplitude is used, i.e. $Y_0\omega^2 = 0.5$ m.s^{-2}, as piezoelectric material is well known to exhibit non-linear behaviour [4, 38, 85, 96] even at moderate acceleration levels, see Chapter 7. The electrical properties of the piezoelectric material, Table 2.2, are taken from supplier data sheet (PCI 255) [72] – this material is used during the experimental tests performed in Chapter 4. The device dimensions are those used in the transfer matrix model study and can be found in Table 2.1.

Table 2.2: Electrical properties of the piezoelectric material used throughout this analysis [1].

Parameter	Value
Piezoelectric constant, d_{31} (m.V^{-1})	-180$\times10^{-12}$
Permittivity, ε_{33}^{S} (F.m^{-1})	1.549$\times10^{-8}$

Figures 2.9 and 2.10 show how the frequency of excitation affects the voltage generated by and tip displacement of a conventional energy harvester respectively. Based on these results the following observations can be made. The energy harvester has a fundamen-

[1] The magnitude of electrical constants are heavy dependant on external conditions i.e. temperature. Values quoted in the table are taken at room temperature (23$\pm$2°C) with variational data available at [73].

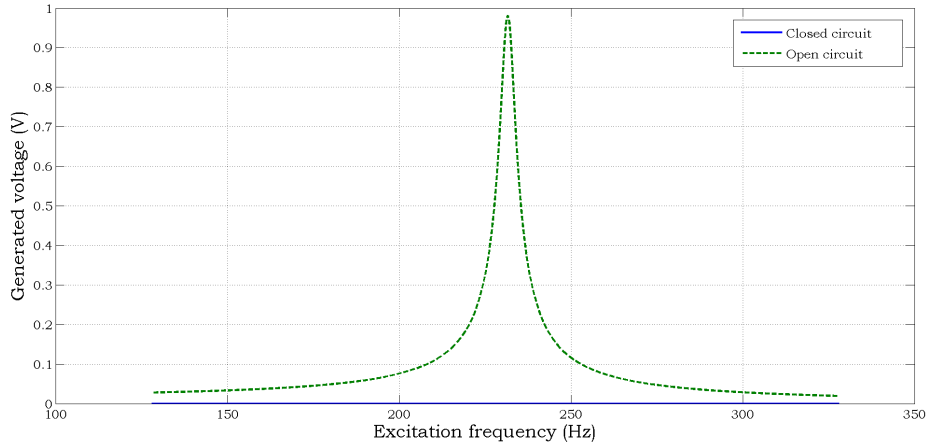

Figure 2.9: Voltage frequency response of conventional harvester in open and closed circuit conditions.

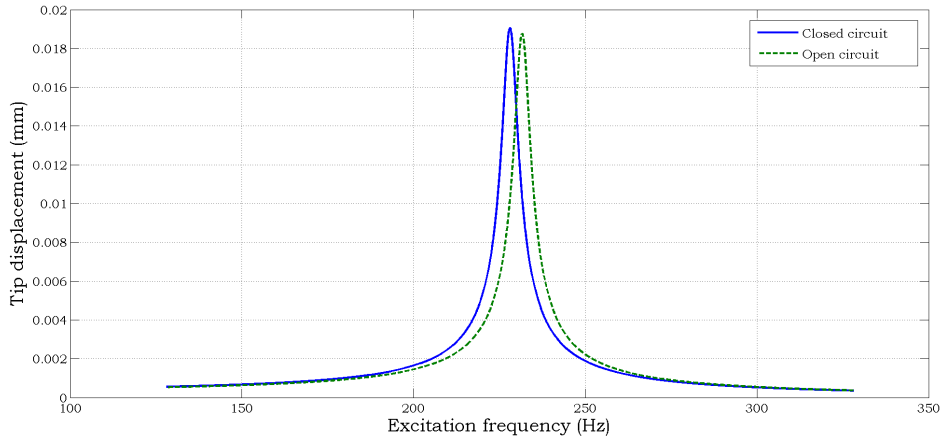

Figure 2.10: Tip displacement frequency response of conventional harvester in open and closed circuit conditions.

tal frequency of 228.1 Hz, which, when used in closed circuit conditions as the frequency of excitation, induces peak tip response. In Figure 2.9 the voltage is zero under closed circuit conditions since no resistor is present. When simulating the harvester in open circuit conditions the peak response, i.e. 0.98 V for the voltage, is seen to occur for an excitation frequency of 231.6 Hz – a 1.5% difference in comparison to the fundamental frequency. This phenomenon is explained later in Chapter 3. Lastly the peak tip displacement in open circuit conditions is smaller than under closed circuit conditions. This is caused, in part, by voltage extracted from the system reducing the forcing magnitude – $(Q_1 - R_1 V_0)$ from Equation (2.46).

2.3 Addition of a tip mass

An integral aspect of cantilever energy harvesters is inclusion of a tip mass, see Figure 2.11. This term refers to mass added to the free end of the cantilever structure and has several important functions. Firstly, the mass acts to increase flexural displacement of the beam equating to a greater strain in the piezoelectric material. The addition of a tip mass also allows for the control and reduction of the fundamental frequency. In the majority of real world applications moderate frequency levels are observed [84], also see Chapter 1, and so reducing the fundamental frequency of energy harvester designs is crucial if they are to be used in practical applications. Controlling the natural frequency is of even greater importance – in particular with mirco-scale devices. For example, imperfection during manufacture, which inevitably occur, can alter the resonant frequency of the structure. A few Hz difference between the resonant frequency and the excitation frequency can cause dramatic reduction in harvester performance. The reason for this is low damping levels (hence small bandwidth) associated with energy harvesters ensuring reduced energy dissipation. This is demonstrated in Chapter 3 and emphasises the importance of having a tip mass for natural frequency control.

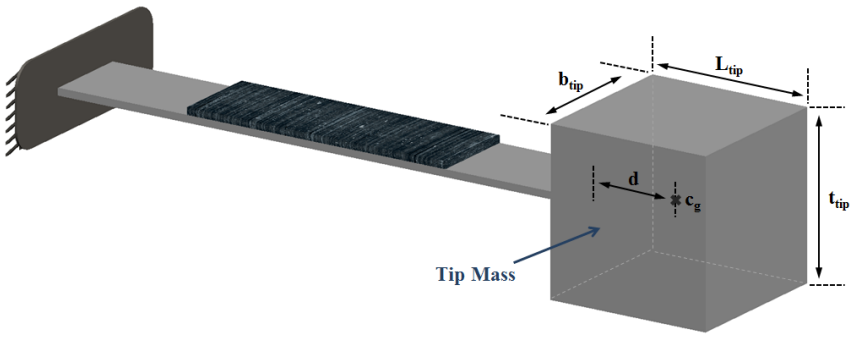

Figure 2.11: Example of a unimorph energy harvester with a tip mass.

2.3.1 Effects of adding a tip mass on the transfer matrix model

The tip mass used in this model is assumed to be a rigid body. The addition of a tip mass affects the boundary conditions (moment and shear force) at the free end of the beam which

are given by: (see Appendix A.1 for full derivation)

$$EI\frac{\partial^2}{\partial x^2}\big(w(x,t)\big) = -m_{\text{tip}}d\frac{\partial^2}{\partial t^2}\big(w(x,t)\big) - (I_G + m_{\text{tip}}d^2)\frac{\partial^3}{\partial x \partial t^2}\big(w(x,t)\big)\big) \ , \tag{2.59}$$

$$EI\frac{\partial^3}{\partial x^3}\big(w(x,t)\big) = m_{\text{tip}}\frac{\partial^2}{\partial t^2}\big(w(x,t)\big) + m_{\text{tip}}d\frac{\partial^2}{\partial x \partial t^2}\big(w(x,t)\big) \ . \tag{2.60}$$

Note, the offset distance from the cantilever free end, d, is also included in the derivation. Although inclusion is necessary to closely represent kinematic effects, numerous previous models i.e. [3], including Erturk and Inman [29], only consider added mass with the centre of mass coincident with the cantilever tip. If the tip mass is a cuboid, d equates to $L_{\text{tip}}/2$. The mass and inertia of the tip mass are represented by m_{tip} and I_G respectively:

$$m_{\text{tip}} = \rho_{\text{tip}} L_{\text{tip}} b_{\text{tip}} t_{\text{tip}} \ , \tag{2.61}$$

$$I_G = \frac{b_{\text{tip}} {t_{\text{tip}}}^3}{12} \ . \tag{2.62}$$

Using Equations (2.59) and (2.60) the following expression for the tip mass transfer matrix, $\mathbf{U}_{\text{tm}}$, can be obtained:

$$\mathbf{U}_{\text{tm}} = \begin{bmatrix} 1 & 0 & 0 & 0 \\ 0 & 1 & 0 & 0 \\ m_{\text{tip}}d & -(I_G + m_{\text{tip}}d^2) & 1 & 0 \\ -m_{\text{tip}} & m_{\text{tip}}d & 0 & 1 \end{bmatrix} \ , \tag{2.63}$$

The overall transfer matrix, Equation (2.58), is modified as follows to include the tip mass:

$$\mathbf{U}_{\text{overall}} = \mathbf{U}_{\text{tm}}\mathbf{U_3}(x_3)\mathbf{I}_{\text{matrix}}\mathbf{U_2}(x_2)\mathbf{I}_{\text{matrix}}\mathbf{U_1}(x_1) \ . \tag{2.64}$$

Due to inclusion of a tip mass, the mode shapes obtained in Section 2.2.4 require the

following normalisation to be satisfied:

$$\int_0^L W_s(x)m(x)W_r(x)\mathrm{d}x + W_s(L)m_{\text{tip}}W_r(L) + 2W_s(L)\Big[m_{\text{tip}}d\Big]W_r'(L) + W_s'(L)\Big[I_G + m_{\text{tip}}d^2\Big]W_r'(L) = \delta_{rs}\ , \tag{2.65}$$

where $W_{s/r}(L)$ and $W'_{s/r}(L)$ are the deflection and rotation respectively at the cantilever tip – $L = x_1 + x_2 + x_3$. For a system without a tip mass the normalisation condition reduces to the conventional expression:

$$\int_0^L W_s(x)m(x)W_r(x)\mathrm{d}x = \delta_{rs}\ . \tag{2.66}$$

2.3.2 Theoretical simulation indicating effects of a tip mass on fundamental frequency

The previously derived model can be used to determine how the tip mass influences previously obtained trends in fundamental frequency while altering piezoelectric material length. Properties of the tip mass simulated in this study are provided in Table 2.3. Tip mass material is assumed to be that used for the substrate layer. The dynamic effects of other materials are examined in Chapter 3. The dimensions and material properties of the cantilever can be found in Table 2.1.

Table 2.3: Structural dimensions and mechanical properties of the tip mass.

Parameter	Value
Tip mass length (mm)	5
Tip mass width (mm)	5
Tip mass thickness (mm)	5
Density of tip mass (kg.m^{-3})	2700

Figure 2.12 shows how the fundamental frequency changes with piezoelectric material length for a conventional energy harvester with and without a tip mass. The results indicate, as expected, that the fundamental frequency reduces with the addition of a tip

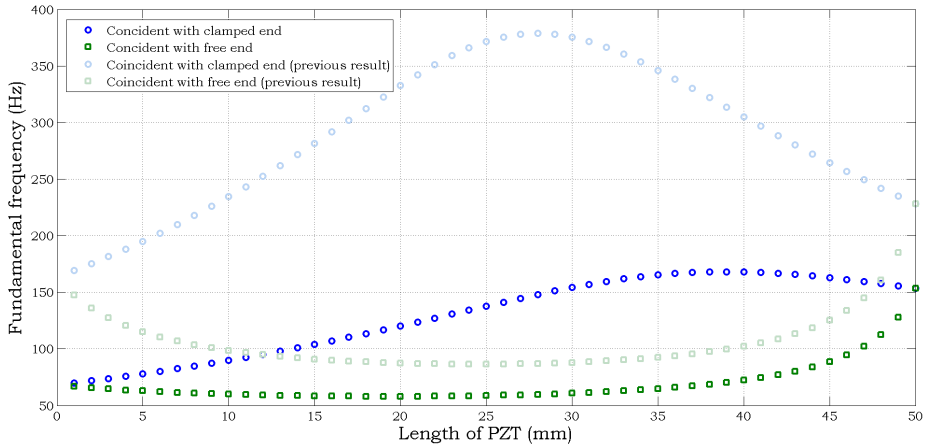

Figure 2.12: Fundamental frequency while altering length of PZT layer. System now includes a tip mass.

mass. Maximum deviation from the fundamental frequency of the conventional design is achieved for designs with shorter PZT layers. The tip mass is the primary reason for this as it is a dominant factor in the overall system mass. Any reduction in PZT length lowers structure stiffness hence a decrease in fundamental frequency is observed.

2.3.3 Effects of adding a tip mass on the forcing magnitude

Addition of a tip mass also affects the mechanical equation of motion in terms of the forcing magnitude. The expression for Q_1 (Equation (2.41)) must be modified to include the translational and rotational effects of the tip mass, and is given by:

$$Q_1 = -Y_0\omega^2\left[\int_0^L m(x)W_1(x)\mathrm{d}x + m_{\text{tip}}W_1(L) + (m_{\text{tip}}d)W_1'(L)\right]. \tag{2.67}$$

Figure 2.13 shows the frequency response for voltage generated by and tip displacement of a conventional energy harvester with and without a tip mass. The results indicate, in comparison to a structure without a tip mass, both peak voltage and peak tip displacement increase. The primary cause for this is an increase in force amplitude, Q_1, experienced by the beam; 0.016 N from 0.014 N. Large deflections produce larger strains thereby creating a structure which can generate more voltage from the same excitation level – 1.79 V compared to 0.981 V, i.e. a 45% increase (in open circuit conditions). Note how the closed and

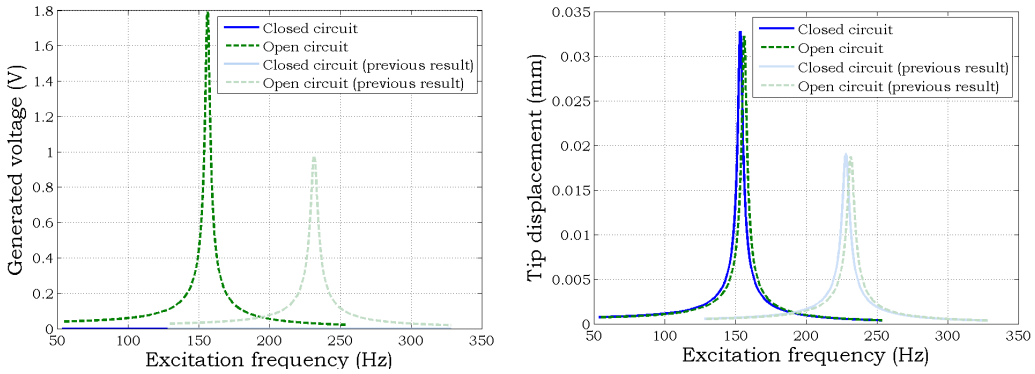

Figure 2.13: Voltage and tip displacement frequency response of conventional harvester with and without a tip mass in open and closed circuit conditions.

open circuit resonance have reduced in comparison to a structure without a tip mass, now occurring at 153.5 Hz and 156.3 Hz respectively. Peak performance occurring at a lower frequency offers greater application possibilities for the energy harvester structure, refer to Chapter 1.

2.4 Equations governing response of a bimorph energy harvester

The previous analysis considered a unimorph energy harvester, in this section a bimorph energy harvester is modelled and simulated. The bimorph energy harvester consists of a substrate layer sandwiched between two layers of piezoelectric material, see Figure 2.14. Again, the assumptions of perfect bonding, negligible adhesive thickness and negligible electrode thickness are made. In addition to this, it is assumed that the geometry and location of the two piezoelectric layers are identical.

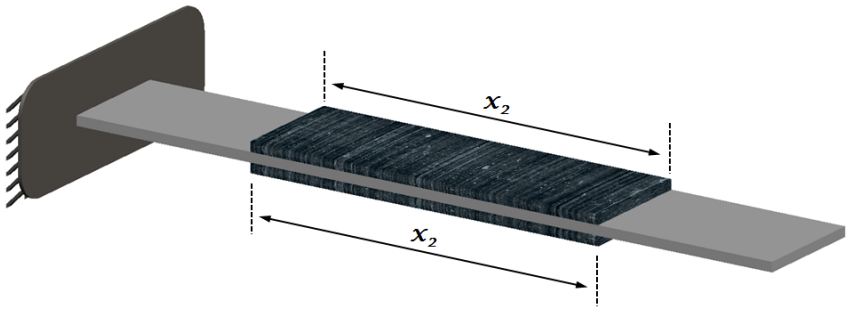

Figure 2.14: Example of a bimorph energy harvester.

The form of equations which govern the response of a bimorph energy harvester are identical to those derived in Section 2.2.3:

$$V(t) = \left[\frac{\dfrac{Q_1 \phi_1 \mathrm{i}\omega}{\left({\omega_1}^2 - \omega^2\right) + \left(2\gamma_1\omega_1\omega\right)\mathrm{i}}}{\dfrac{R_1\phi_1\mathrm{i}\omega}{\left({\omega_1}^2 - \omega^2\right) + \left(2\gamma_1\omega_1\omega\right)\mathrm{i}} + \left(\mathrm{i}\omega + \dfrac{1}{C'_p R_{\text{load}}}\right)} \right] \mathrm{e}^{\mathrm{i}\omega t} \,, \tag{2.68a}$$

$$w_{\text{rel}}(x,t) = W_1(x) \left[\frac{Q_1 - R_1 V_0}{\left({\omega_1}^2 - \omega^2\right) + \left(2\gamma_1\omega_1\omega\right)\mathrm{i}} \right] \mathrm{e}^{\mathrm{i}\omega t} \,, \tag{2.68b}$$

where C'_p is an equivalent capacitance shown in the equivalent circuit, Figure 2.15. The location of the neutral axis, $\overline{y}$, for a bimorph structure is given by:

$$\overline{y} = \frac{\frac{{t_s}^2}{2} b_s + t_s b_s t_p + t_p n b_p t_s + 2{t_p}^2 n b_p}{(t_s b_s + 2 t_p n b_p)} = \frac{t_s}{2} + t_p \,. \tag{2.69}$$

There are also differences in some variables which constitute the above equations and some of these are further dependant on whether the piezoelectric layers are connected in parallel or series, Figure 2.15.

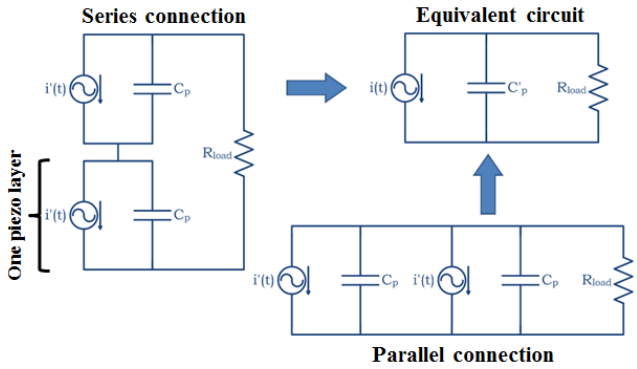

Figure 2.15: Series and parallel piezoelectric layer connections for a bimorph energy harvester.

2.4.1 Series layer connection

If the piezoelectric layers are connected in series the following expressions can be used in Equations (2.68a) and (2.68b).

$$\begin{aligned} \epsilon &= -\frac{E_p b_p d_{31}}{2t_p}\left[\left(2t_p + t_s - \overline{y}\right)^2 - \left(t_p + t_s - \overline{y}\right)^2\right] , \\ C_p' &= \frac{1}{2}\frac{\varepsilon_{33}^S b_p x_2}{t_p} , \\ \phi_1 &= -\frac{E_p d_{31} t_{pc} b_p}{C_p}\Big[W_1'(x_1 + x_2) - W_1'(x_1)\Big] . \end{aligned} \tag{2.70}$$

Recall ϵ occurs in the expression for R_1 (Equation (2.42)).

2.4.2 Parallel layer connection

If the piezoelectric layers are connected in parallel the following expressions can be used in Equations (2.68a) and (2.68b).

$$\begin{aligned} \epsilon &= -\frac{E_p b_p d_{31}}{t_p}\left[\left(2t_p + t_s - \overline{y}\right)^2 - \left(t_p + t_s - \overline{y}\right)^2\right] , \\ C_p' &= 2\frac{\varepsilon_{33}^S b_p x_2}{t_p} , \\ \phi_1 &= -2\frac{E_p d_{31} t_{pc} b_p}{C_p}\Big[W_1'(x_1 + x_2) - W_1'(x_1)\Big] . \end{aligned} \tag{2.71}$$

2.4.3 Modifications to the transfer matrix model for a bimorph configuration

Variables used in the transfer matrix model also require slight modification if a bimorph energy harvester is to be simulated. The expressions for equivalent flexural rigidity and equivalent mass per unit length are shown below:

$$(EI)_{\text{composite}} = E_p I_{yp1} + E_s I_{ys} + E_p I_{yp2} , \tag{2.72}$$

$$(m)_{\text{composite}} = 2\rho_p A_p + \rho_s A_s , \tag{2.73}$$

where I_{yp1}, I_{ys} and I_{yp2}, the second moment of area of individual layers, can be expressed as:

$$I_{yp1} = \frac{b_p {t_p}^3}{12} + b_p t_p \left(\overline{y} - \frac{t_p}{2}\right)^2 , \tag{2.74}$$

$$I_{ys} = \frac{b_s {t_s}^3}{12} + b_s t_s \left(\frac{t_s}{2} + t_p - \overline{y}\right)^2 , \tag{2.75}$$

$$I_{yp2} = \frac{b_p {t_p}^3}{12} + b_p t_p \left(\frac{3t_p}{2} + t_s - \overline{y}\right)^2 . \tag{2.76}$$

2.4.4 Numerical simulations of a bimorph energy harvester

In this section a brief study is performed to compare the performance of unimorph and bimorph energy harvesters. To provide fair comparisons the volume of piezoelectric material is controlled. Each piezoelectric layer in the bimorph design has a thickness of 0.25 mm. All other properties can be found in Tables 2.1 and 2.2.

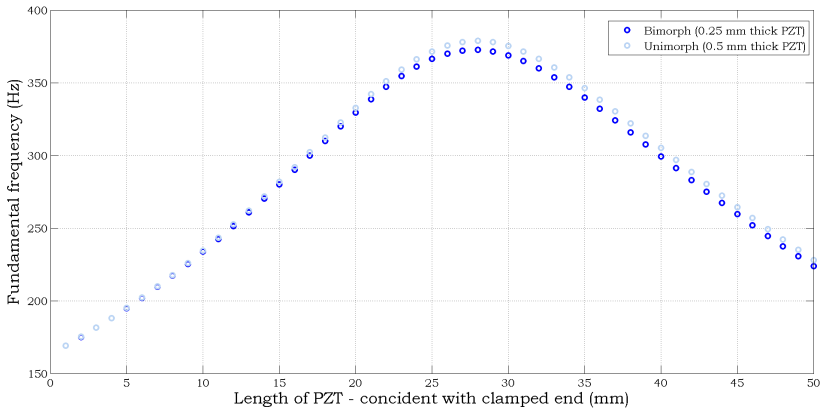

Figure 2.16: Fundamental frequency comparisons between unimorph and bimorph energy harvesters when altering piezoelectric material length.

A brief mention regarding fundamental frequency variations. Figure 2.16 shows changes in fundamental frequency with reductions in PZT length from the free end for both unimorph and bimorph energy harvester designs. The results indicates small differences in fundamental frequency occur between unimorph and bimorph configurations. For shorter lengths these differences are small and these differences gradually reduce to zero as the length reduces to zero. For longer lengths, variations occur due to a difference in

material distribution through the structure which affects the position of the neutral axis and the second moment of area of various layers. For the conventional design, in this particular case, a difference of 1.89% (4.3 Hz) was calculated.

The following performance comparisons between unimorph and bimorph energy harvester are undertaken on a conventional design without a tip mass. Further work is reported in Chapter 3 where results from configurations with reduced PZT material are reported. Figures 2.17 and 2.18 show frequency responses for the voltage generated by and tip displacement of energy harvesters of unimorph and series/parallel bimorph type. From the results one can deduce that voltage generated from a bimorph with layers connected in series is double that of one connected in parallel.

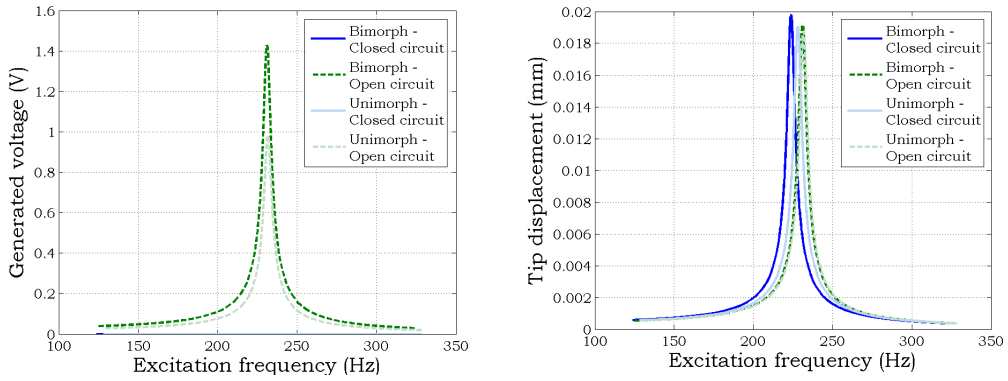

Figure 2.17: Voltage and tip displacement frequency response of a series bimorph energy harvester. Results from a corresponding unimorph harvester included for comparison purposes.

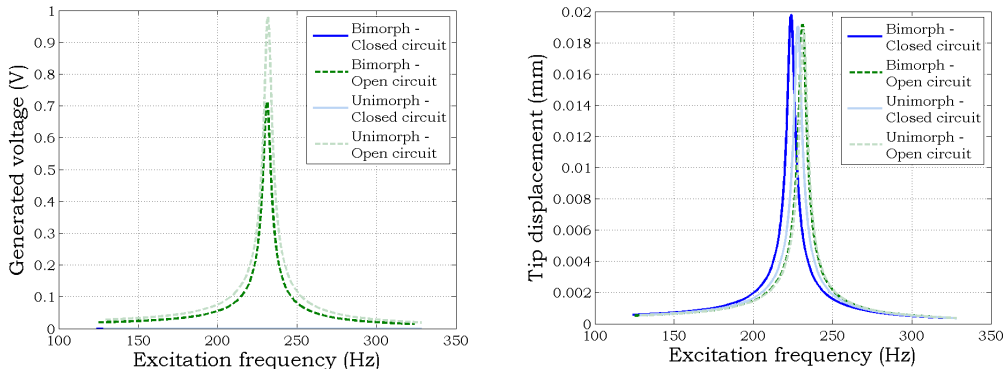

Figure 2.18: Voltage and tip displacement frequency response of a parallel bimorph energy harvester. Results from a corresponding unimorph harvester included for comparison purposes.

This can also be confirmed using Kirchhoff's voltage law. In open circuit conditions a unimorph energy harvester will outperform a parallel configured bimorph in terms of

maximum generated voltage. A maximum voltage of 1.428 V is achievable for a bimorph with a series connection, equating to a 45.6% increase over a unimorph design with the same volume of piezoelectric material.

2.5 Conclusions

In this chapter detailed derivations for a unimorph cantilever piezoelectric energy harvester were presented. The model included proportional damping; in addition to being mathematically convenient it allowed for a means of representing changes in mechanical damping magnitude while altering the geometry of the piezoelectric layer. From the use of exact beam vibration solutions the development of a transfer matrix model provides accurate predictions of both natural frequencies and mode shapes for uniform and non-uniform beam. This, coupled with a distributed-parameter model for the substrate-piezoelectric composite beam allows confident theoretical performance simulations of both uniform and non-uniform samples. Equations of motion for a bimorph energy harvester, with piezoelectric layers connected either in series or parallel, have also been presented in the chapter.

For the tested case, it was found that piezoelectric layer length and width have a significant effect on the fundamental frequency of the structure. Differences in comparison to the conventional design are over 60% (or 150 Hz). Since the density, hence mass, of the piezoelectric layer is large in relation to the substrate layer, it has a significant influence on system dynamics. Preliminary comparisons between a conventional unimorph and bimorph design were also performed. For the tested sample size, it was found that a bimorph with piezoelectric layers connected in series generates twice the voltage of a parallel equivalent. In open circuit conditions, the series bimorph will generate 45.6% more voltage than a unimorph which in turn will outperform a parallel bimorph.

Addition of a tip mass is often considered during energy harvester design. Functions include improving strain distribution along cantilever beams and also fundamental frequency reduction and tuning. Theoretical simulation of a tip mass attached to a unimorph verified this with open circuit voltage increasing from 0.981 V (without tip mass) to

1.79 V and natural frequency reducing from 228 Hz to 156 Hz. The tip mass required extensions and modifications to both the transfer matrix model and the distributed parameter model, in which the offset distance of the tip mass centre of gravity from the cantilever free end was also taken into consideration.

Presented in the following chapter are extensive parametric studies on the piezoelectric layer topology by utilising the developed models. Following this, in Chapter 4, a thorough model validation is presented though extensive experimental works.

CHAPTER 3

ENERGY HARVESTER GEOMETRY OPTIMISATION THROUGH PARAMETRIC STUDIES

3.1 Introduction

In a quest to optimise harvester design and to determine important parameters for maximising the performance of vibrational energy harvesters, this chapter, theoretically investigates how, why, and to what extent, geometrical parameters affect the power generated by the energy harvester. Note that only individual parameters are altered during each unique study with a later chapter, Chapter 6, dealing with multiple simultaneous geometrical parameter changes. Alterations to individual equation variables are extremely difficult to implement in a practical situation. Take as an example the piezoelectric internal capacitance, C_p; varying the permittivity (by using different materials) or dimensions of the piezoelectric layer can indeed alter the magnitude of C_p. However, these changes also affect other variables for example, fundamental frequency and mode shape. It is therefore difficult to gauge the sole effects of C_p on design performance. For this reason, studies and optimisations thorough geometric parameter changes are preferred.

The model which has been derived in Chapter 2 is used here to obtain trends in how the generated power ($P = V^2/R$) is affected by geometric parameters and load resistance – Equation (2.44) is of particular interest here. In addition to designs with or without a tip mass, both macro- and micro-scale devices are considered. A comparison between unimorph designs and their equivalent bimorph configuration will also be performed here. The influence of the following variables on the performance, i.e. power dissipated in a resistive load (Chapter 5 compares the capacitor charging capabilities of harvester configurations), are examined:

- Overall structure geometry, ensuring beam remains uniform
  - Beam length
  - Beam width
  - Substrate layer thickness and piezoelectric layer thickness
- Piezoelectric layer geometry (geometry of substrate layer is fixed)
  - Length from cantilever free or clamped end
  - Width
- Material and size of the tip mass.

Note that during piezoelectric geometry alterations, the topology of the layer will always remain rectangular. The preliminary aim of this chapter is to gain an understanding on how geometric parameters effect the performance of energy harvesters connected to an electrical load. From this the existence and topology of configurations which outperform the conventional energy harvester design can be determined. Questions such as do these optimum topologies also apply to energy harvesters of different scale and do bimorph designs outperform unimorph designs are also addressed in this chapter.

The chapter begins by obtaining constants for the proportional damping expression followed by geometric parameter variations on the first case study. These are performed on macro-scale devices similar in size to those which will be used during experimental

work, refer to Chapter 4. Issues such as how the open-circuit/closed-circuit resonant frequency shift is affected by the magnitude of electro-mechanical coupling and how damping levels influence system bandwidth are also investigated here. Once the effects of the listed geometric parameters have been analysed on the macro-scale device, a second case study is undertaken. This is on a micro-scale device which includes a tip mass to reduce the fundamental frequency and improve strain distribution along the cantilever beam. The penultimate case study deals with the optimisation of piezoelectric material width, length and location on a flexible thin film vibrational energy harvester used to extract power from ocean energy. Lastly, comparisons between unimorph and bimorph harvester configurations are undertaken in an attempt to determine which design is better and whether the outcome is universal. The following experimental matrix provides an overview of the four cases which are considered and their associated parameter variations:

Table 3.1: Table outlining parameter changes to be made for each individual case study.

	Unimorph			Bimorph
	Case study 1	Case study 2	Case study 3	Case study 4
Overall beam length	✓	✓		
Overall beam width				
Substrate layer thickness	✓	✓		
Piezoelectric layer thickness	✓			✓
Piezoelectric layer length	✓	✓	✓	✓
Piezoelectric layer width	✓	✓	✓	
Tip mass parameters		✓		

3.2 Macro-scale device

In this section parametric studies on geometry are undertaken on a macro-scale device with a length of 50 mm. Individual parameters are varied in order to gauge their effects on the performance of a cantilever piezoelectric energy harvesting device. Substrate and piezoelectric

material are assumed to be aluminium (Al) and lead zirconate titanate (PZT), respectively. The nominal structure dimensions, and mechanical and electrical properties, identical to those used in the previous chapter (bar the substrate layer thickness), are repeated here for the convenience of the reader, Table 3.2.

Table 3.2: Structural dimensions, and mechanical and electrical properties of the conventional harvester used throughout this analysis (Note this design does not include a tip mass).

Parameter	Value
Substrate (Al) length (mm)	50
Substrate (Al) width (mm)	5
Substrate (Al) thickness (mm)	0.67
PZT layer length (mm)	50
PZT layer width (mm)	5
PZT layer thickness (mm)	0.5
Young's modulus of Al (GPa)	69
Density of Al (kg.m^{-3})	2700
Young's modulus of PZT (GPa)	62.1
Density of PZT (kg.m^{-3})	7800
Piezoelectric constant, d_{31} (m.V^{-1})	-180$\times$10^{-12}
Permittivity, ε_{33}^{S} (F.m^{-1})	1.549$\times$10^{-8}

In all proceeding studies in this section a constant base acceleration of 0.5 m.s^{-2} is applied to the harvester configurations. Recall the use of proportional damping, Equation (2.31), which allows a change in mechanical damping with geometrical parameter changes. From experimental work, extensive details of with can be found in Chapter 4, the magnitudes of one possible set of α and β values were obtained. A sample with length 49.5 mm and width 5 mm was tested (the piezoelectric and substrate layer thickness was 0.5 mm and 0.67 mm respectively). Natural frequencies of the first two mode of vibration were determined to be 287.04 Hz and 1798.80 Hz. Using the half power point method [80], damping ratios corresponding to these modes were calculated to be 1.07% and 0.43%. Utilising this information and Equation (2.31), the two resulting simultaneous equations can be

solved to obtain the constants α and β.

$$0.0107 = \frac{\alpha}{2 \times (287.04 \times 2 \times \pi)} + \frac{\beta \times (287.04 \times 2 \times \pi)}{2} \tag{3.1}$$

$$0.0043 = \frac{\alpha}{2 \times (1798.80 \times 2 \times \pi)} + \frac{\beta \times (1798.80 \times 2 \times \pi)}{2} \tag{3.2}$$

From the solution to Equations (3.1) and (3.2), α and β are calculated as 37.06 rad.s^{-1} and 4.71×10^{-7} s.rad^{-1}, respectively.

3.2.1 Effects of load resistance on the resonant frequency

It was briefly mentioned in Chapter 2, and shown in Figure 2.10, that the load resistance magnitude affects the resonant frequency of the system. Numerous researchers have also shown this phenomenon [30, 45] with the following equation derived in [30] (presented here in dimensional form) to estimate the open circuit resonant frequency, ω_1^{oc}:

$$\omega_1^{oc} \approx \omega_1 \left(1 + \frac{R_1 \phi_1}{{\omega_1}^2} - 2{\gamma_1}^2\right)^{1/2} \tag{3.3}$$

The equation predicts that for larger differences between electromechanical coupling and mechanical damping magnitude the difference between closed- and open-circuit resonant frequencies is more pronounced. This is demonstrated, for the electromechanical coupling, in Figure 3.1 by comparing two different lengths of piezoelectric material. Note, proportional damping is not utilised here; as a control the damping ratio is kept constant at 0.01. In this example, load resistances of magnitude less than $\approx$1 kΩ produce a system whose resonant frequency and undamped natural frequency are equal, i.e. a situation identical to the closed circuit conditions of a lightly damped system. Open circuit conditions are reached for load resistances greater than $\approx$10 MΩ. The term $\frac{R_1 \phi_1}{{\omega_1}^2}$ is calculated at 0.0347 Q.m^{-2}.s^2 for the 50 mm case and 0.0119 Q.m^{-2}.s^2 for the 10 mm case, equating to a 65.7% difference. Figure 3.1 shows the resonant frequency, for two harvester configurations, plotted against the load resistance. In both cases while sweeping load resistance magnitude the resonant frequency goes from a minimum plateau to a maximum plateau. If the approximate increase from closed- to open-circuit resonant frequencies is compared for the two

designs, from Figure 3.1, a percentage difference of 69% is obtained. This is on par with that calculated using Equation (3.3).

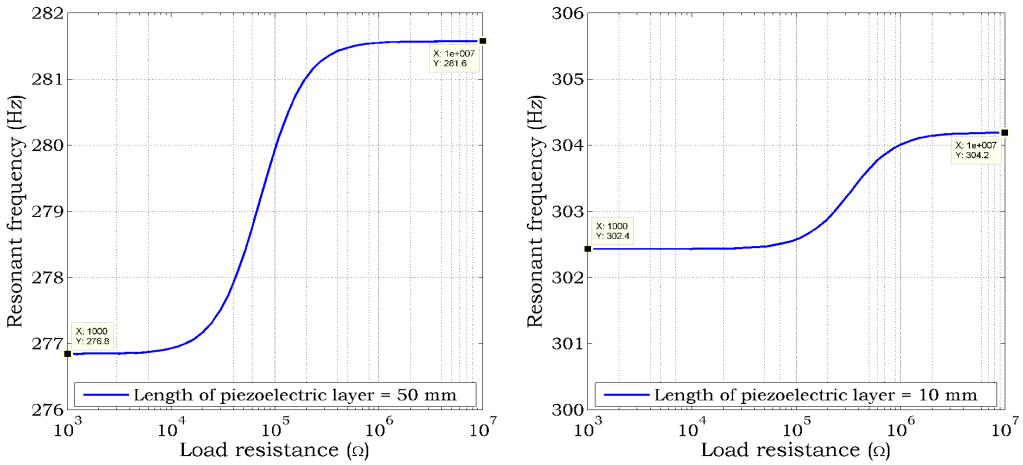

Figure 3.1: Effect of electromechanical coupling on the resonant frequency. Left: longer piezoelectric layer therefore higher electromechanical coupling.

In this chapter, peak power is estimated by taking into account this shift in resonant frequency. Each energy harvester design is simulated over various load resistances, ranging from 100 Ω to 1 MΩ for the first two case studies (Sections 3.2 and 3.3), and from 1 kΩ to 10 MΩ in the final case study (Sections 3.4). In order to determine resonant frequencies and therefore maximum powers, frequency sweeps ($\omega_1 \pm 25$ Hz) are performed for harvester-resistor combinations. The equation used to estimate the power magnitude is shown below:

$$P = \frac{\left[\dfrac{\dfrac{Q_1\phi_1 \mathrm{i}\omega}{\left({\omega_1}^2 - \omega^2\right) + \left(2\gamma_1\omega_1\omega\right)\mathrm{i}}}{\dfrac{R_1\phi_1 \mathrm{i}\omega}{\left({\omega_1}^2 - \omega^2\right) + \left(2\gamma_1\omega_1\omega\right)\mathrm{i}} + \left(\mathrm{i}\omega + \dfrac{1}{C_p R_{\text{load}}}\right)}\right]^2}{R_{\text{load}}}. \tag{3.4}$$

3.2.2 Effects of beam length on harvester performance

The first parameter under investigation is cantilever length, Figure 3.2. In this study, the length of both substrate and piezoelectric layer remain identical. The results indicate that as the length of a short beam is increased, higher power outputs are realised. However, as the length is increased further, the power output decreases. This behaviour can be explained by

considering the influence of beam length on damping, see Figure 3.3. Over the length range of interest, as the beam length increases the mechanical damping increases, suppressing the deflection and reducing the strain acting on the piezoelectric material. This mechanism is responsible for causing a reduction in the dissipated power for increasingly long beams. If a fixed damping ratio was assumed a continual increase in power with beam length would indeed be expected.

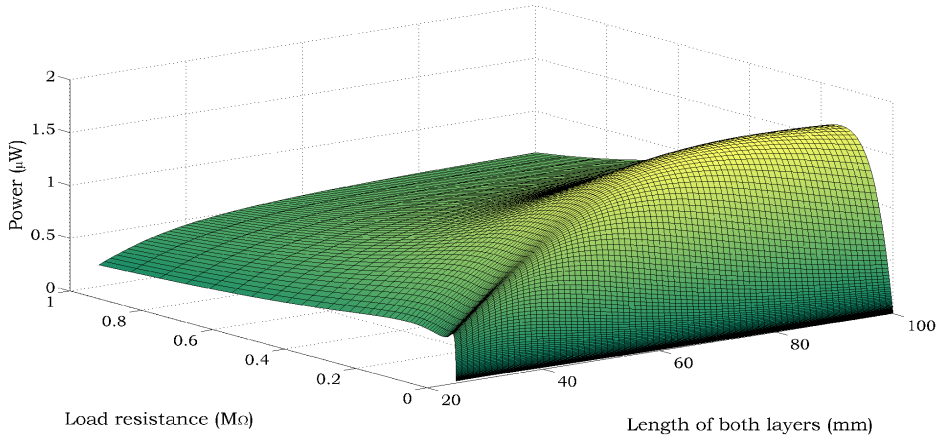

Figure 3.2: Influence of sample length and load resistance on the power dissipated.

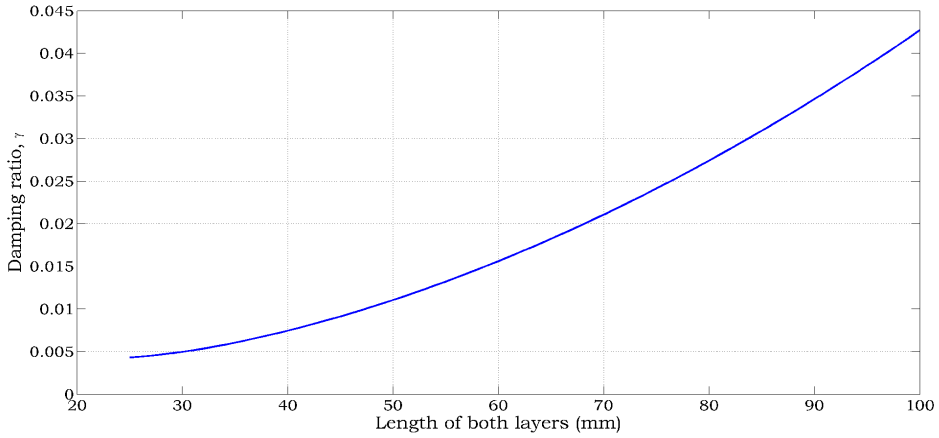

Figure 3.3: Trend between sample length and mechanical damping ratio (obtained using Equation (2.31) – where α=37.06 rad.s^{-1} and β=4.71$\times$10^{-7} s.rad^{-1}.

For this particular combination of materials, beam width and layer thickness the theoretical results indicate a maximum power of 1.682 μW is generated across a 121 kΩ resistor. This is achievable from a beam length of 80 mm. Other researchers who have investigated the effect of beam length include Zhu *et al.* [108]. The group uses finite element software to develop a coupled piezoelectric-circuit finite element model. The main conclusion was

that as the length of the beam reduces, a continual increase in generated power is observed. The results presented in this thesis contradict their observations, and the reason for this is incorrect power normalisation by Zhu *et al.* : their results are obtained whilst maintaining constant base displacement and normalised by dividing with input acceleration. Power should in fact be normalised by dividing with input acceleration squared (not required here since the input acceleration in this study is assumed constant at 0.5 m.s^{-2}). It should also be noted that Zhu *et al.* did not account for how mechanical damping ratio changes with beam length.

3.2.2.1 Bifurcation damping

It is worthwhile mentioning the double peak power phenomenon seen at lower beam lengths. This is due to the relatively low damping levels estimated for these samples. The term 'bifurcation damping ratio' is found in [76] and is used to define a damping ratio below which the double peak phenomenon occurs. For shorter beam lengths the damping magnitude is below the so called bifurcation damping level which causes dissipated power to have two distinct maxima – corresponding to both resonance and anti-resonance. Above a critical value this phenomenon is no longer present and only one peak exists. This concept can be utilised to maintain the bandwidth of the energy harvester while increasing maximum dissipated power by reducing the magnitude of mechanical damping. Damping is notoriously troublesome to control in practical situations. The adhesion of layers, variations in material properties and the clamping of the harvester are but a few factors which contribute to the mechanical damping present in the system. Extensive experimental work on damping is presented in Chapter 4.

System bandwidth is obtained from the power frequency response plots by extracting the difference in frequency at $\frac{P_{\text{peak}}}{\sqrt{2}}$, where P_{peak} is the peak power. Figure 3.4 shows stacked frequency response plots, assuming two different mechanical damping ratios, for load resistances ranging from 100 Ω to 10 MΩ. Stacked refers to the plotting of power frequency responses for various load resistance magnitudes such that plots are superimposed.

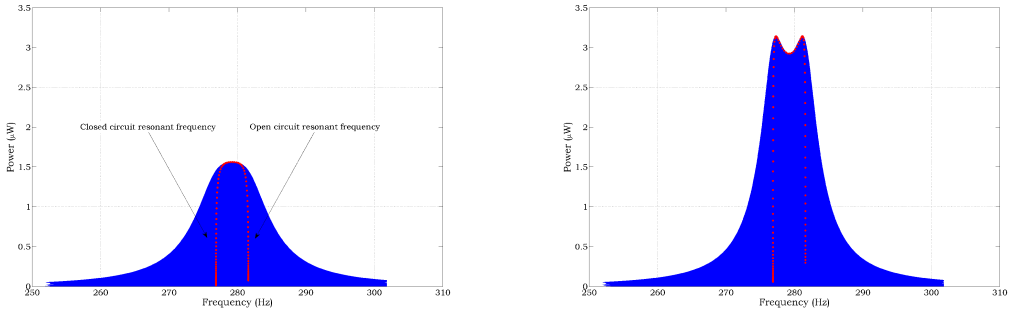

(a) Mechanical damping set at 0.01

(b) Mechanical damping set at 0.005

Figure 3.4: Stacked power frequency response plots for various load resistances. A conventional energy harvester is simulated here with overall length of 50 mm. Red markers show the peak dissipated power for each power frequency response plot.

This provides a 'power envelope' which corresponds to the maximum power generated over a frequency range close to the fundamental frequency. For damping ratios of 0.01 and 0.005 the bandwidth was calculated at 8.6 Hz and 7.4 Hz respectively. Due to a reduction in the damping ratio, the maximum possible power is seen to increase by 26% without greatly affecting the system bandwidth.

3.2.3 Effects of piezoelectric layer length on harvester performance

In this section the effects of piezoelectric layer length are examined. Previous studies, i.e. Friswell and Adhikari [35], have been performed on the piezoelectric layer electrode topology with the correct assumption that the dynamics of the undamped structure do not change. Results from [35] indicate a 115% increase in power output is achievable if the electrodes are made to cover roughly half the piezoelectric material. In their work the load resistance is kept constant at 100 kΩ; if a range of magnitudes had been examined then different trends are likely to occur. This is due to coupling present, ϕ and R – (Equations (2.45) and (2.42)), between mechanical and electric aspects of the system. In the study presented in this thesis, the length of the actual piezoelectric material is altered (in each configuration of harvester, the electrode material is assumed to fully cover upper and lower piezoelectric layer surfaces) and so the dynamics of the undamped structure is affected. Such effects have been accounted for during modelling of the system. In order to assess the effects of piezoelectric layer length on the generated power, the length is reduced from

both the cantilever clamped and free end; results are shown in Figures 3.5 and 3.6. Note that in this work, designs with piezoelectric material longer than the substrate layer are not simulated. This study has been performed by Gao *et al.* [37] with their findings, as expected, showing no real benefit in performance. For such designs the extended section does not contribute to the generated voltage due to alignment between the neutral axis of the overall structure and the neutral axis of the piezoelectric material causing charge cancellation.

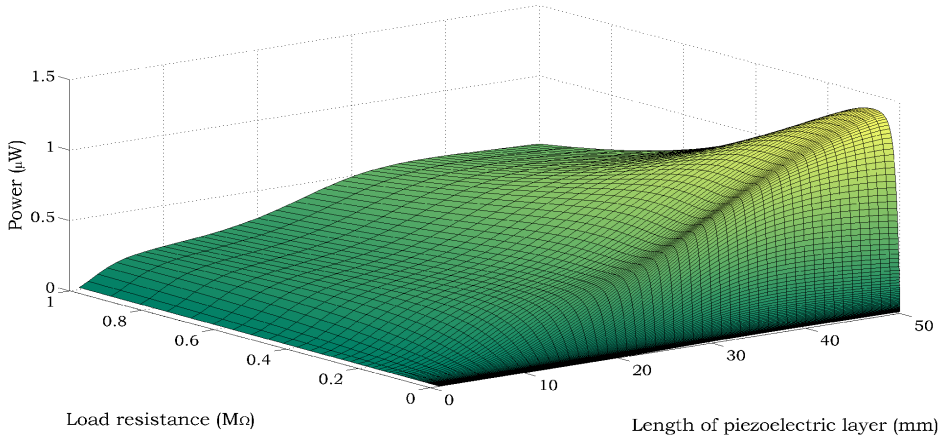

Figure 3.5: Influence of piezoelectric layer length on power dissipated. One end remains coincident with the cantilever clamped end.

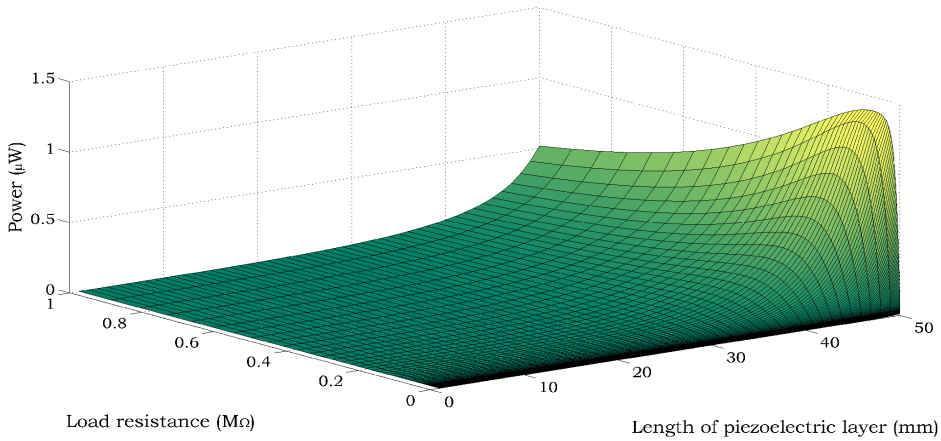

Figure 3.6: Influence of piezoelectric layer length on power dissipated. One end remains coincident with the cantilever free end.

In this particular example the analytical model shows no benefit in maximum generated power for reduced piezoelectric layer lengths. A maximum power of 1.40 μW is achievable over a 73.9 kΩ resistor for a 50 mm layer. The key factor affecting results in this parameter change scenario is the forcing term, Q, which is maximised for longer lengths

of piezoelectric material due to the mass and mode shape of the cantilever. Note, when reducing length from the clamped end the double peak power phenomenon is again present in the region of low mechanical damping levels (≈20 mm to ≈35 mm). If the harvester is connected to an electrical system of high load resistance shortening piezoelectric length from the free end does improve power generated. Over a 1 MΩ resistor the conventional design will generate a power of 0.50 μW, whereas a harvester with a 38 mm long piezoelectric layer will generate 0.53 μW, equating to an increase of 6%.

3.2.4 Effects of thickness ratio on harvester performance

In this section the effects of the thickness ratio are examined. There are two methods for doing this – increasing piezoelectric layer thickness while keeping the substrate layer thickness constant (Figure 3.7), or, increasing the substrate layer thickness while keeping the piezoelectric layer thickness constant (Figure 3.8). Thickness of the variable layer swept from approximately 0.1 mm to 1.5 mm.

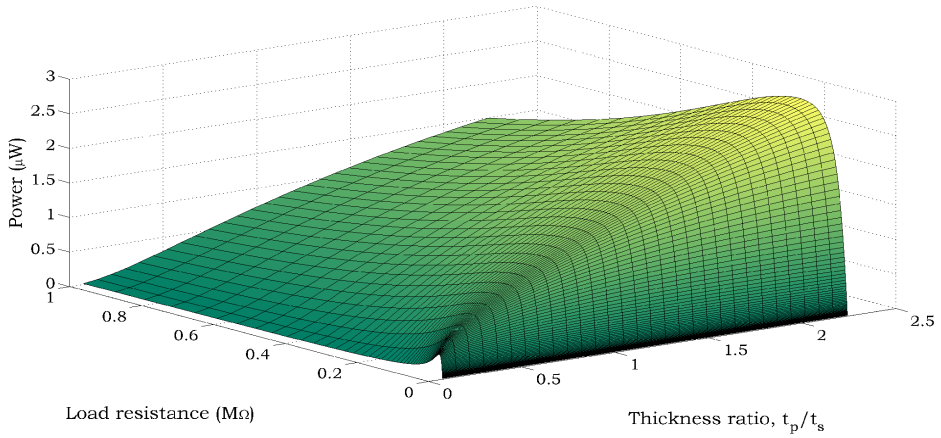

Figure 3.7: Influence of layer thickness ratio on power dissipated. In this case substrate layer length remains constant.

Both Figure 3.7 and Figure 3.8 show that over all resistances there is a continual increase in power with increasing either substrate or piezoelectric thickness. Distance between the neutral axis and the centre of the piezoelectric material increases with an increase in the thickness of either layer. Greater strain is now exerted in the piezoelectric material thereby generating increased voltage. The extent to which the magnitude of this distance is

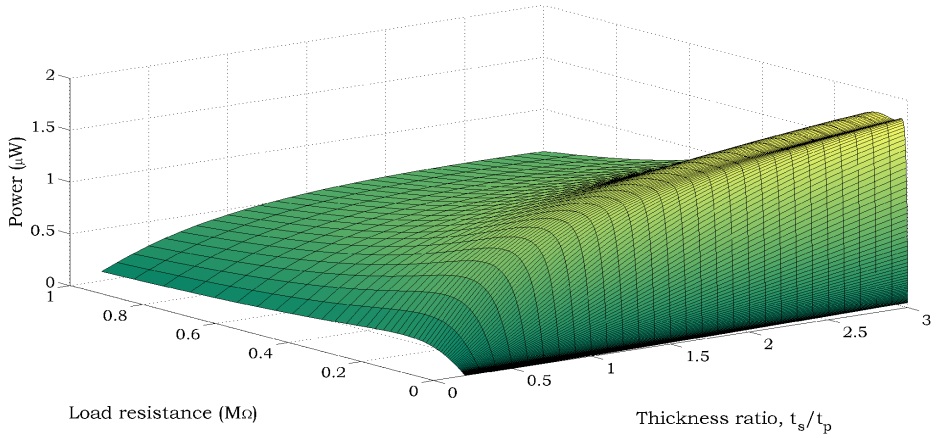

Figure 3.8: Influence of layer thickness ratio on power dissipated. In this case piezoelectric layer length remains constant.

affected by the thickness of either layer is shown in Figure 3.9(a). Observations from this graph would ordinarily lead to the conclusion that increasing the substrate layer thickness while keeping the piezoelectric thickness constant is the preferred option. However, from Figures 3.7 and 3.8 the opposite is true. Other system variables must also be considered as they appear to have a greater effect when considering harvester performance. For example, the piezoelectric internal capacitance, C_p, see Equation (3.5), reduces with increasing piezoelectric thickness and this is beneficial for voltage generation. A 50 mm $\times$ 5 mm layer with thickness 0.5 mm has an internal capacitance of 7.74 nF whereas one with thickness 1.5 mm, 2.58 nF. In addition to this the electro-mechanical coupling is seen to increase while increasing the thickness of either layer which also benefits the voltage generation capabilities of the system. One other variable which has significant importance is the mechanical forcing magnitude, Q_1, see Equation (3.6). For the readers convenience, equations defining C_p and Q_1 are repeated below:

$$C_p = \frac{\varepsilon_{33}^S b_p x_2}{t_p} \,, \tag{3.5}$$

$$Q_1 = -Y_0 \omega^2 \int_0^L m(x) W_1(x) \mathrm{d}x \,. \tag{3.6}$$

Due to differences in layer density and hence mass per unit length the mechanical forcing is seen to be greater for a thicker piezoelectric layer in comparison to a thicker substrate layer,

see Figure 3.9(b). For the largest simulated thickness ratios, mass per unit length for the piezoelectric layer thickening case is 0.40 kg.m^{-1} in comparison to 0.068 kg.m^{-1}.

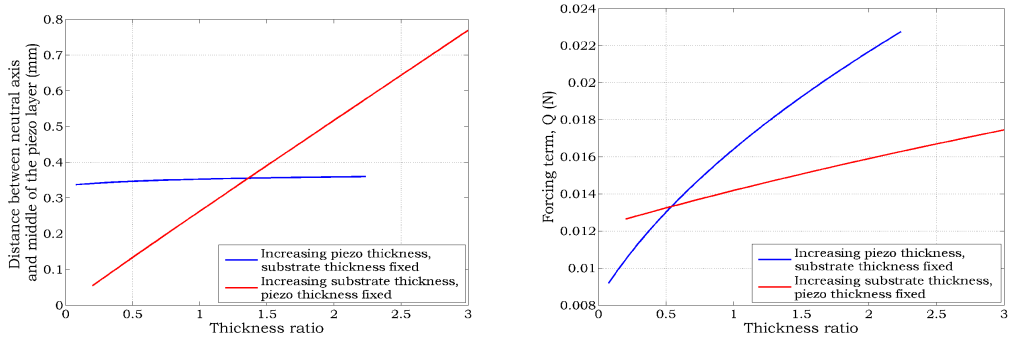

(a) Position of neutral axis in relation to piezoelectric material

(b) Mechanical forcing term

Figure 3.9: The effect of thickness ratio (while altering thickness of piezoelectric layer and substrate layer individually) on certain system variables.

Maximum power of 2.97 μW (dissipated across a 12.9 kΩ load resistance) is seen for a piezoelectric thickness of 1.5 mm in comparison to 1.80 μW (dissipated across a 18.3 kΩ resistor) for a substrate thickness of 1.5 mm. Advantages from increasing layer thickness are countered by an increase in structural stiffness and so one would eventually observe a plateau in the power trends obtained, followed by a decline in performance. So far the dominate factors appear to be the magnitude of forcing and, for higher load resistances, the electro-mechanical coupling term.

3.2.5 Effects of the piezoelectric layer width on harvester performance

Lastly, in this section the effects of the piezoelectric layer width on a macro-scale energy harvester are examined. The substrate layer width is kept constant at 5 mm while the piezoelectric layer width is increased from 0.1 mm to the substrate width, with results shown in Figure 3.10. Over the range simulated, results show that maximum power, 1.40 μW over a 73.9 kΩ resistor, is realised for a configuration with equal substrate and piezoelectric layer thickness. The increase in system mass causes an increase in mechanical forcing, which is the dominant variable, and so an increase in power is observed. The piezoelectric width can be increased further so it overhangs the structure creating devices with improved energy harvesting capabilities. For example, if the piezoelectric layer is 10 mm in width the max-

imum dissipated power is 2.17 μW over a 42.3 kΩ resistor. Caution must be taken when considering such designs since sections of piezoelectric material no longer have the support of the substrate layer so are more susceptible to fracture.

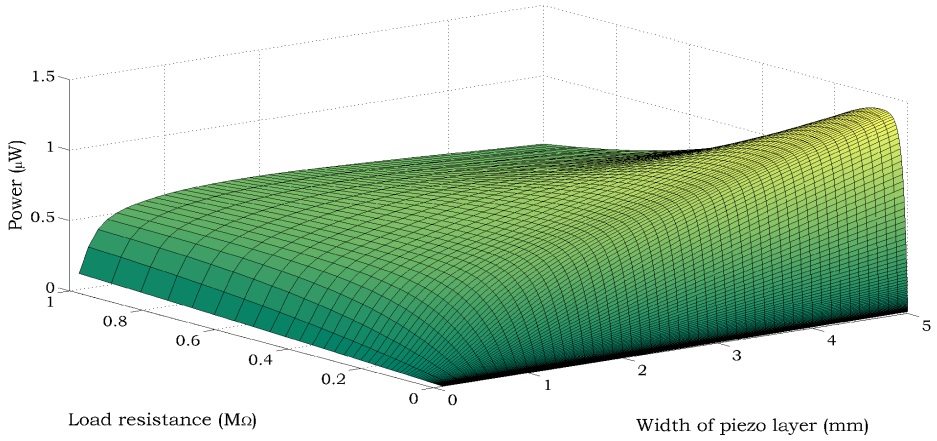

Figure 3.10: Influence of piezoelectric layer width on the power dissipated. Substrate layer width is kept constant at 0.5 mm.

For larger load resistances, i.e. 1 MΩ, the internal capacitance of the piezoelectric layer and the electro-mechanical coupling have greater influence on the trend. A piezoelectric layer with a larger width will have increased internal capacitance and create a system with lower electro-mechanical coupling both of which are detrimental to the power generation capabilities of an energy harvester. For this reason, over a 1 MΩ load resistor, maximum power of 0.6 μW is generated by a harvester comprising of a 1.9 mm wide piezoelectric layer. In the following section comparisons in these power trends with a MEMS-scale device are explored.

3.3 Micro-scale device

In this section the effects of piezoelectric layer dimensions on the performance of a MEMS-scale structure are examined and compared to those obtained for the macro-scale device. This particular MEMS-scale device was manufactured in 2006 by Fang *et al.* [31] using MEMS fabrication techniques; Figure 3.11 shows a schematic representation of the device. The substrate layer is silicon (Si), the piezoelectric material is PZT and the tip mass is nickel. Further details can be found in Fang *et al.* [31]. The actual tip mass was bonded

onto the top of the PZT layer. However, during the following analysis it is assumed that the tip mass overhangs the end of the beam, with its centre of mass coinciding with the neutral axis of the beam. This slight modification is likely to have some influence on the natural frequency and strain acting in the structure compared to the original, results in [31].

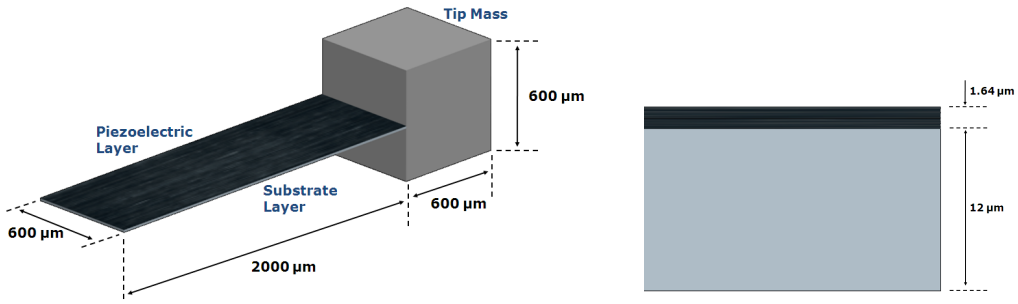

(a) Isometric view

(b) Side view of the two layers

Figure 3.11: Schematic representation of the conventional harvester manufactured by Fang *et al.* [31] with dimensions.

The dimensions and material properties for the structure used in this section are provided in Table 3.3

Table 3.3: Structural dimensions, and mechanical and electrical properties of the conventional harvester used throughout this analysis.

Parameter	Value
Substrate (Si) length (mm)	2
Substrate (Si) width (mm)	0.6
Substrate (Si) thickness (mm)	0.012
PZT layer length (mm)	2
PZT layer width (mm)	0.6
PZT layer thickness (mm)	0.00164
Young's modulus of Si (GPa)	185
Density of Si (kg.m^{-3})	2329
Young's modulus of PZT (GPa)	66
Density of PZT (kg.m^{-3})	7800
Tip mass length (mm)	0.6
Tip mass width (mm)	0.6
Tip mass thickness (mm)	0.6
Density of tip mass (kg.m^{-3})	8908
Piezoelectric constant, d_{31} (m.V^{-1})	-180$\times$10^{-12}
Permittivity, ε_{33}^{S} (F.m^{-1})	1.594$\times$10^{-8}

Due to the size of the device, to get comparable levels of power to the previous study, a constant base acceleration of $2g$ is simulated with the assumption that non-linear behaviour remains negligible.

3.3.1 Effects of beam length and piezoelectric layer length on MEMS-scale harvester performance

In this section the effects of overall beam length and piezoelectric length on the performance of a MEMS scale energy harvester are examined. Firstly, overall beam length; in this study the beam length is increased from 1 mm to 5 mm at 0.1 mm intervals, see Figure 3.12(a).

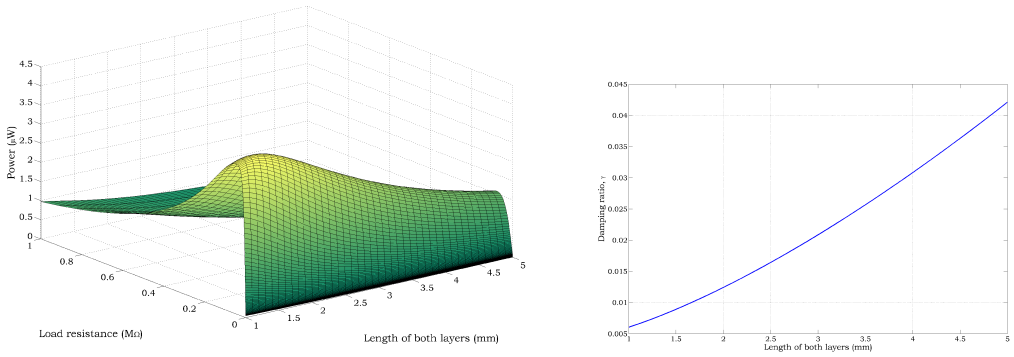

(a) Power (b) Mechanical damping ratio

Figure 3.12: Influence of overall beam length on power dissipated across various load resistances and mechanical damping in the structure.

Similar trends to a macro-scale device are obtained; mechanical damping (which is larger in longer beams, see Figure 3.12(b)) suppresses the deflection and strain acting on the piezoelectric material. This mechanism is responsible for causing a reduction in the generated voltage and power for increasingly long beams. From Figure 3.12(a), maximum power from a sample having a length of 5 mm is 1.57 μW over a 73.9 kΩ resistor. For a sample 1.3 mm in length, maximum power is 4.04 μW dissipated across a 50.9 kΩ which equates to a 157% improvement in performance.

Secondly the effects of piezoelectric material length are examined on a beam comprised of a 2 mm fixed substrate layer length. Figure 3.13(a) and Figure 3.13(b) show the influence of increasing piezoelectric length from the clamped and free end respectively on

the power dissipated over a range of load resistance magnitudes.

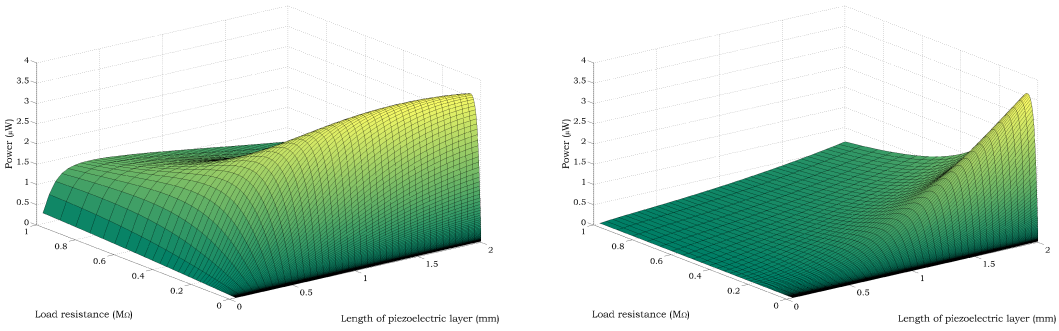

(a) Length incremented with one end remaining coincident with clamped end

(b) Lengh incremented with one end remaining coincident with free end

Figure 3.13: Influence of piezoelectric layer length on power dissipated across various load resistance magnitudes.

From Figure 3.13(b) it is evident, for this particular device, that no improvement in performance is achievable with reductions in piezoelectric material length from the clamped end of the beam. However, Figure 3.13(a) indicates small performance enhancements can be made be removing piezoelectric material from the cantilever free end. The optimum load resistance for the conventional design was found to be 55.9 kΩ, and using this resistance a power of 3.57 μW is dissipated. For this particular device, maximum dissipated power, 3.65 μW across a 67.3 kΩ resistor, was found to occur using piezoelectric material of length 1.6 mm. Recently, Bourisli and Al-Ajmi [12] investigated the influence of geometric parameters on the Electro-Mechanical Coupling Coefficient (EMCC), instead of the power. Their results indicated that a shorter piezoelectric layer is beneficial for increasing the EMCC.

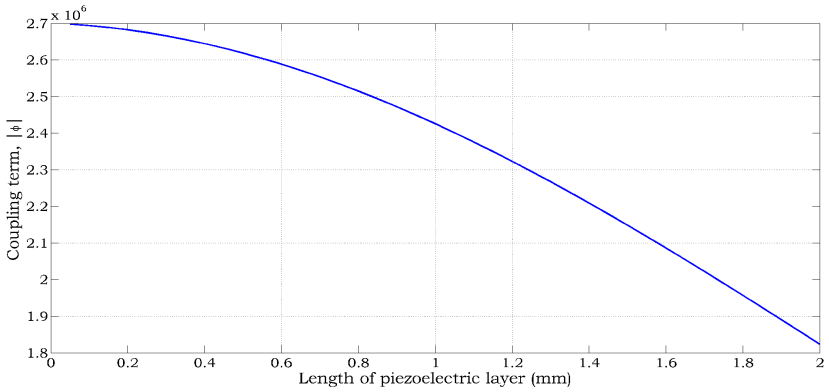

Figure 3.14: Influence of piezoelectric material length on the coupling term, ϕ. One end of the piezoelectric layer remains coincident with the cantilever clamped end.

It had previously been shown by Renno *et al.* [82] that a higher coupling coefficient will not necessarily benefit power generating capabilities of an energy harvester. The results from this model and research concur with this statement. As shown in Figure 3.14, ϕ is maximised when the PZT length is 0.05 mm, which does not correspond to maximum power. The system is however observed to be more reliant on electro-mechanical coupling when the energy harvester is connected to larger load resistances (a similar observation was made for the macro-scale device). Due to the complex interactions between parameters it is difficult to single out and optimise one variable, i.e. ϕ, while keeping all others at an optimum level. This goes some way in justifying the reasoning to adjust physical parameters rather than individual equation variables.

3.3.2 Effects of substrate thickness and piezoelectric width on MEMS-scale harvester performance

In this section the effects of substrate thickness and piezoelectric width will briefly be examined. Initially the result for substrate thickness are presented. Figure 3.15 shows the influence of increasing substrate thickness on the power dissipated across various load resistances.

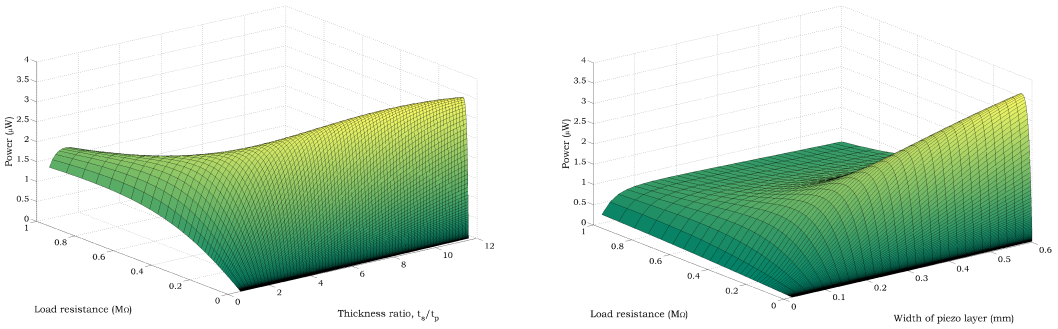

(a) Modifying the substrate layer thickness

(b) Modifying the piezoelectric layer width

Figure 3.15: Influence of two geometric parameter of a MEMS-scale device on power dissipated across various load resistance magnitudes.

Again, similar trends to those obtained for a macro-scale device are observed. However, for the range of thickness ratio tested in this case the plateau for power has been reached. Recall a balance required while increasing substrate thickness due to further dis-

placing piezoelectric material from the neutral axis of the structure counteracted by increasing structure stiffness. A maximum power of 3.62 μW dissipated across a 42.3 kΩ resistor is achievable for a harvester comprising of a 0.0145 mm thick substrate layer ($t_s/t_p = 8.84$). For this structure only minute changes in the forcing term, Q, are observed during substrate thickening and so Q has little effect on the trend obtained. The tip mass, attached to the cantilever free end, is the dominate contributor to overall structure mass and hence dominates the force experienced by the cantilever beam.

In terms of piezoelectric width, again similar trends to a macro-scale device are seen. Across the tested width range, maximum power over all configurations occurs when piezoelectric layer and substrate layer are the same width – 3.57 μW dissipated across a 55.9 kΩ. In the next section the effects of the tip mass material and size will briefly be investigated.

3.3.3 Effects of tip mass size and material on MEMS-scale harvester performance

Inclusion of a tip mass is important for reducing the fundamental frequency, particularly in MEMS-scale devices, and increasing the strain distribution along cantilever structures. The size and material of said tip mass are important factors and govern the performance of a piezoelectric energy harvester. Table 3.4 shows numerical, theoretical, data from altering the tip mass material. Note that all data is for a conventional design with dimensions provided in Table 3.3.

Table 3.4: Numerical data obtained when altering tip mass material.

Tip mass material	Density (kg.m^{-3})	Maximum Power (μW)	Forcing term, Q, (N)	Fundamental Frequency (Hz)	Coupling term, ϕ ($\times 10^6$), (N.C^{-1})
Silicon	2329	1.12	0.014	475.4	3.54
Steel	7900	3.25	0.026	259.4	1.94
Brass	8600	3.47	0.027	248.7	1.86
Nickel	8908	3.57	0.027	244.4	1.82
Tungsten	19250	6.32	0.040	166.4	1.24

A clear trend is recognised from the numerical data in Table 3.4 – increasing the density of the tip mass increases the performance of the energy harvester. The electro-mechanical coupling reduces with increasing density indicating this variable is not the dominate term governing peak power levels. The dominating factors are in fact the fundamental frequency, which reduces with increasing density, and forcing magnitude, which increases with density. As will be explained in Section 3.4 this is not an ideal comparison between harvester designs due to large changes in the fundamental frequency. Results while changing tip mass size were also obtained and are presented here for a conventional energy harvester, with the dimensions again provided in Table 3.3. For this study the nickel tip mass will have a fixed width of 0.6 mm while the length and thickness are incremented from 0.2 mm to 1 mm. By incrementing the thickness not only does the mass increase but so too the offset distance of the tip mass centre of gravity from the beam end thereby exerting greater inertia on the beam. Data is obtained over a range of load resistance magnitudes, with results, provided in Figure 3.16(a), showing greater power levels are achievable by using larger tip masses. The increase in forcing magnitude and reduction in fundamental frequency, Figure 3.16(b), with an increase in tip mass size are again responsible for this outcome. In this case a 400% increase in tip mass length and thickness causes a 550% reduction in the fundamental frequency. Due to this observed sensitivity of tip mass size on fundamental frequency, the use of a tip mass to control the fundamental frequency of an energy harvester is justified. By altering dimensions of the tip mass the fundamental frequency of the structure can be tuned to the targeted frequency of excitation. As was mentioned earlier, this is of particular importance in MEMS-scale applications due to the increased sensitivity of manufacturing defects on the fundamental frequency of devices.

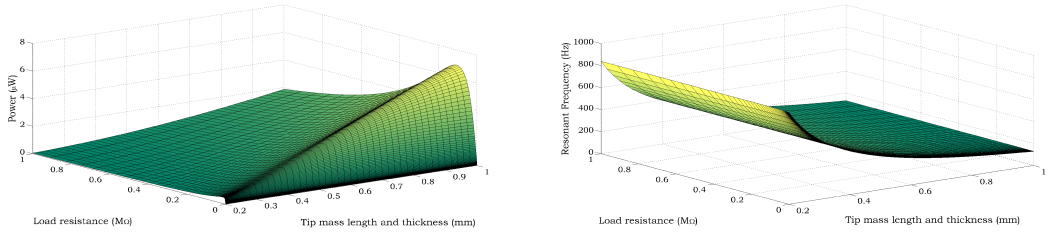

(a) Effect on power generated

(b) Effect on resonant frequency

Figure 3.16: Influence of tip mass length and thickness (equal) on the behaviour of a MEMS-scale piezoelectric energy harvester.

It has been shown in this section that optimisation can too be achieved for MEMS-scale devices and that careful consideration on dimension choices and piezoelectric material location is advisable for improving performance. General trends are similar to those obtained for a macro-scale device with subtle differences due to how size and structure composition effects variable magnitude. The dominate factor during geometrical parameter changes was the fundamental frequency with the influence of electro-mechanical coupling increasing with load resistance magnitude. Examining the effects of tip mass material and size led to the conclusion that increasing either density of size causes power output from the energy harvester to increase. However, this must be taken with caution as the large differences in fundamental frequency reduce the credibility of this test. In the penultimate section of this chapter an optimisation of a larger energy harvester is undertaken.

3.4 Optimisation of a flexible thin film energy harvester

In this section, the design of a thin film harvester developed by a research group at Hiroshima University in Japan [94] is optimised. Their device has been developed to harvest electrical energy from the oceans. It achieves this through fluid-structure interactions e.g. flapping and periodic bending [94]. The harvester comprises of a polyvinylidene fluoride (PVDF) piezoelectric layer bonded to a polyethylene terephthalate (PET) substrate layer. Dimensions and material properties for this system are provided in Table 3.5. In this simulation the previous assumption that each harvester configuration is excited periodically at the frequency at which maximum power can be generated remains. The input acceleration is assumed to be constant at 0.5 m.s^{-2}.

During this optimisation, consideration is also given to the natural frequency of the device. Since this is a low frequency application, designs with fundamental frequencies above 30 Hz will not be considered. For this reason although shortening the device benefits performance, the length of the substrate will remain fixed at 100 mm. Likewise, due to this frequency assumption, adjustments in layer thickness will not be undertaken. In addition, the substrate width will remain fixed at 20 mm as reductions cause decreases in

Table 3.5: Structural dimensions, and mechanical and electrical properties of the harvester manufactured by the group in Japan [94].

Parameter	Value
PET layer length (mm)	100
PET layer width (mm)	20
PET layer thickness (mm)	1
PVDF layer length (mm)	95 [a]
PVDF layer width (mm)	10
PVDF layer thickness (mm)	0.04
Young's modulus of PET (GPa)	3.1 [b]
Density of PET (kg.m^{-3})	1400 [b]
Young's modulus of PVDF (GPa)	8.3 [c]
Density of PVDF (kg.m^{-3})	1780 [c]
Piezoelectric constant, d_{31} (m.V^{-1})	22×10^{-12} [c]
Permittivity, ε_{33}^{S} (F.m^{-1})	1.063×10^{-10} [c]

[a] One end of piezo remains coincident with clamped end.
[b] Material property for PET obtained from [102].
[c] Material property for PVDF obtained from [75].

performance. As is the case in the majority of vibrational energy harvester design, design is tailored to suit characteristics of the excitation source. The dominant excitation frequency is often known and due to resonant behaviour, harvester configurations with fundamental frequencies matching this are designed. Here, a problem is realised while carrying out parametric studies on device geometry – the conventional configuration is designed to operate efficiently at a particular excitation frequency, any subsequent change to configuration geometry will cause a mismatch between fundamental frequency and source frequency. Given that energy harvester performance is very much dependent on this match in frequencies, it is rational to compare different energy harvester configurations having the same natural frequency. This will be undertaken in Chapter 6 by adjusting multiple parameters simultaneously.

Back to the current example, the device manufactured by the group from Japan has a fundamental frequency of 25.68 Hz. From the base acceleration stated above their device can dissipate a maximum power of 0.083 μW over a 2.48 MΩ resistor. Notice how the observed power levels are considerably lower in comparison to the first case study. The reason behind this is clear once examining the magnitude of the piezoelectric material electrical

parameters. The piezoelectric constant d_{31} is a measure of effectiveness of piezoelectric material for energy harvesting and relates force applied to the charge which can be generated. PZT has a d_{31} value which is 8.2 times greater than PVDF. Chapter 10 in Erturk and Inman's book [30] can be referred to for a study on how various piezoelectric materials effect performance of energy harvesters.

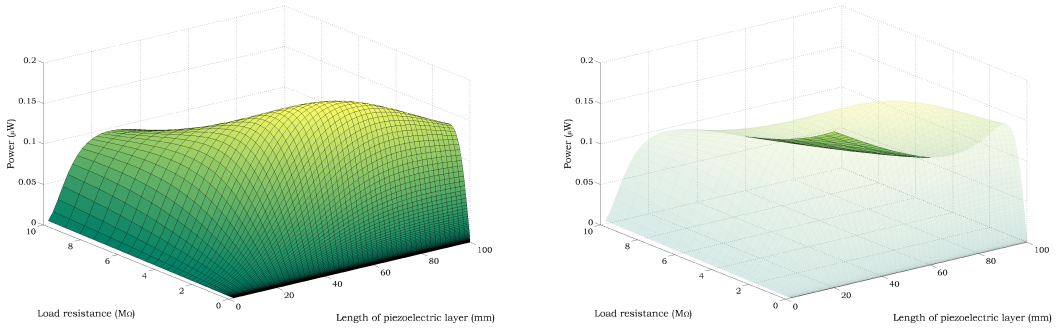

(a) Full power surface plot

(b) Sectioned surface plot of power to show top right corner – cut made at 60 mm length and 5 MΩ resistance

Figure 3.17: Influence of piezoelectric layer length on power dissipated when piezoelectric width equals substrate width. One end remains coincident with the cantilever clamped end.

Benefits in the performance of this device are achievable by increasing PVDF layer width and reducing PVDF length from the free end of the beam, i.e. both layers remain clamped. Maximum power is generated for configurations with PVDF width equal to that of the PET layer, i.e. 20 mm. Recall the reasoning behind this comes from an increase in mechanical forcing due to increased beam mass. Using this width a sweep of PVDF length is undertaken over a range of load resistances with the results presented in Figure 3.17. For a PVDF length of only 55 mm, a maximum power of 0.19 μW is dissipated over a 1.87 MΩ resistor – equating to a 129% increase from the original design. Improvements in performance are more distinct at higher load resistances – across a 10 MΩ resistor, power increase from 0.031 μW for a 100 mm long PVDF layer to 0.096 μW for a 28 mm length (equating to an improvement of over 200%). Due to the low thickness ratio between PVDF and PET layers, only a small difference in the fundamental frequency of the optimised device, 25.86 Hz, exists in comparison to the original design, 25.68 Hz.

3.5 Bimorph macro-scale device

The purpose of this section is to provide comparisons between macro-scale unimorph and series bimorph energy harvester configurations. In order to achieve this in a unbiased manner the volume of piezoelectric material for unimorph and bimorph harvesters must be equal; this is achieved by setting each piezoelectric layer in bimorph designs to half the thickness of that in equivalent unimorph designs, i.e. $t_p = t_p/2$. All other dimensions and material properties can be found in Table 3.2. The first parameter which is considered is the piezoelectric layer length.

3.5.1 Effects of piezoelectric layer length on bimorph design

The length of the piezoelectric layer is increased from the clamped end, i.e. all three layers remain clamped, while ensuring identical top and bottom layer length. Figure 3.18 shows the results for this over various magnitudes of load resistor with the double peak power phenomenon occurring once again. The results indicate a small improvement in maximum power in comparison the unimorph design, see Figures 3.5; occurring for a PZT of 50 mm in length, quantitatively, 1.42 μW is achievable over a 32.0 kΩ or 156 kΩ resistor – in terms of percentage increase this equates to 1.42%.

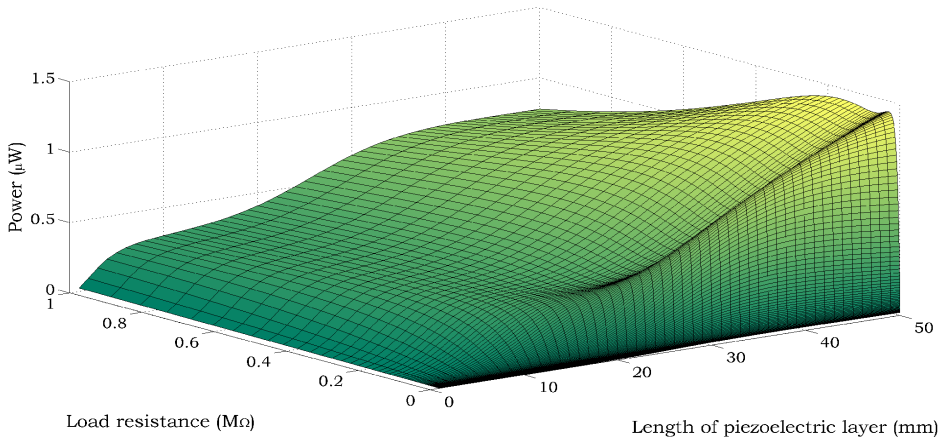

Figure 3.18: Influence of piezoelectric layer length on the power generated by a bimorph energy harvester. Substrate layer length is kept constant at 50 mm.

The advantage of a bimorph over a unimorph is seen when the harvester is connected

to high load resistances. Take for example a 1 MΩ load and configurations comprising of 50 mm PZT layers; the results from Figures 3.5 and 3.18 indicate a power of 0.51 μW and 0.78 μW for a unimorph and bimorph respectively, i.e. a 53% increase. During this particular unimorph-bimorph comparison most of the variables in the voltage equation differ by a fraction of a percent. For example, differences in frequency and mode shapes only arise from differences in the material distribution since material volume between the designs remains identical. Equivalent unimorph and bimorph designs therefore experience similar levels of mechanical damping and forcing. The variable for which the greatest differences are seen is the electro-mechanical coupling term, ϕ, see Figure 3.19.

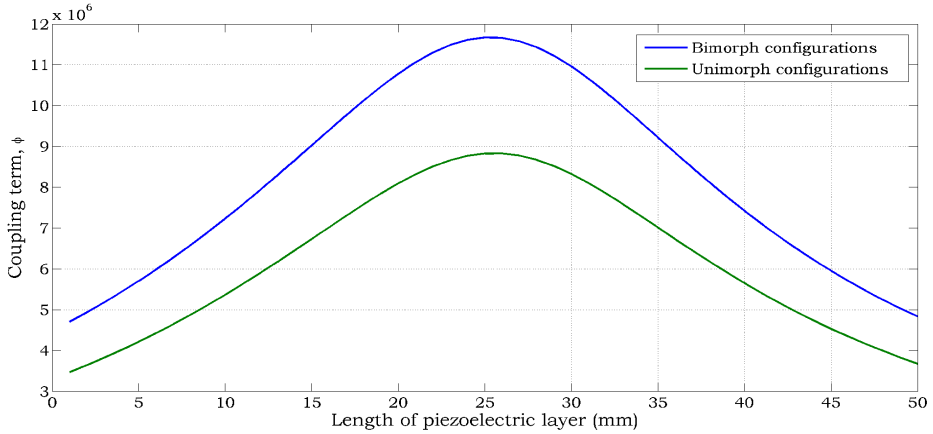

Figure 3.19: Influence of piezoelectric layer length on the magnitude of ϕ for a bimorph and unimorph energy harvester. Substrate layer length is kept constant at 50 mm.

The plot shows that trends between electro-mechanical coupling and PZT length for unimorph and bimorph designs are similar. An increase is initially observed until approximately half the beam length is covered with PZT, this is followed by a gradual decrease. The piezoelectric capacitance, C_p, increases with layer length which would cause a reduction in ϕ, however, this is countered by changes to the mode-shape slope, refer to Equation (2.45) in Chapter 2. These changes were observed, during simulations, to be more distinct for shorter PZT lengths. The importance of and dependence on ϕ when maximising power has already been shown to increase with load resistance magnitude. This is the main reason behind bimorph designs having improved performance levels over unimorph designs for higher resistive loads. In this particular case, for PZT lengths of 50 mm, the percentage increase in ϕ is 31.4%.

3.5.2 Effects of piezoelectric layer thickness on bimorph design

Lastly, the influence of piezoelectric layer thickness on a series bimorph is investigated and compared to results obtained from equivalent unimorph designs, Figure 3.5. The results for a series bimorph are shown in Figure 3.20 with the double peak power phenomenon again present. The plot shows an increase in power with PZT layer thickness over the full load resistor range.

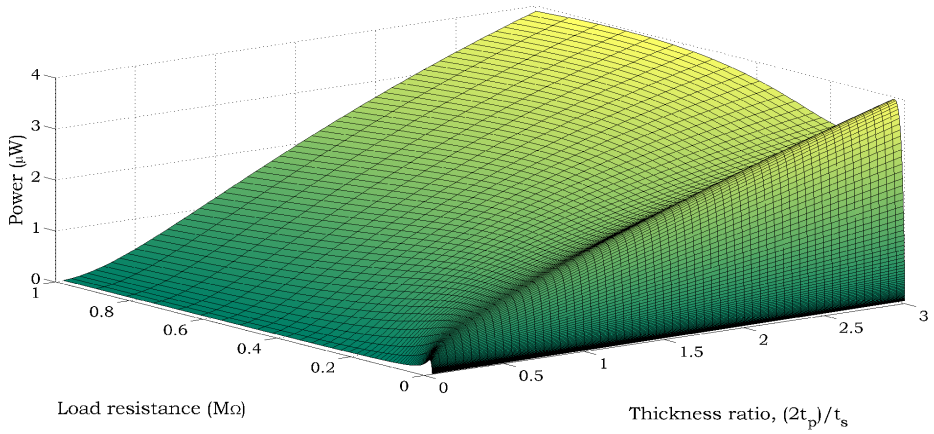

Figure 3.20: Influence of piezoelectric layer thickness on the power generated by a bimorph energy harvester. Substrate layer thickness is kept constant at 0.67 mm.

Numerically, a maximum power of 3.95 μW, across a 29 kΩ or 757 kΩ resistor, can be obtained when the each piezoelectric layer is one-and-a-half times the thickness of the substrate layer. Comparing this maximum power to that obtained for an equivalent unimorph design yields a percentage increase of 13%. The reason behind a greater percentage increase in comparison to that obtain in Section 3.5.1 is evident when considering effects on the neutral axis. For the bimorph case, due to the assumption of identical top and bottom piezoelectric layers, the neutral axis of the cantilever remains coincident with the centre of the substrate layer regardless of the piezoelectric layer thickness. However, for the unimorph case the neutral axis moves up towards the piezoelectric layer when increasing thickness and eventually, for the thicker cases, is found to lie inside the piezoelectric layer, see Figure 3.21. This has an adverse effect on harvester performance due to the upper and lower piezoelectric layer surfaces experiencing opposite charge (i.e. charge cancellation is occurring).

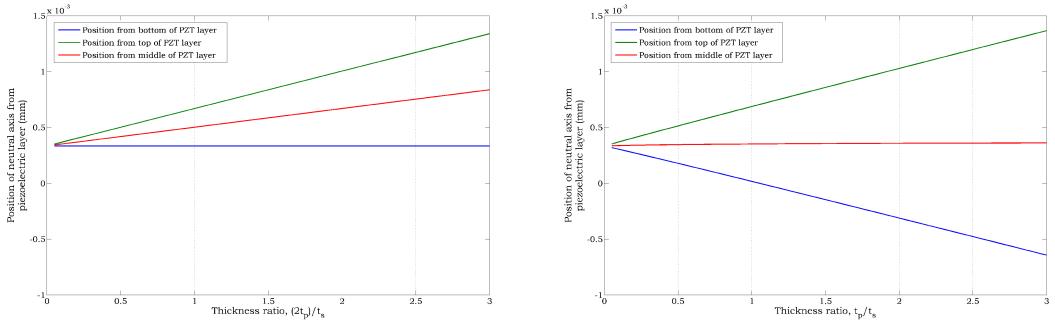

(a) Bimorph configurations

(b) Unimorph configurations

Figure 3.21: Influence of piezoelectric layer thickness on neutral axis location in relation to three different positions through the piezoelectric layer.

In this particular case study, from Figure 3.21(b), the neutral axis for a unimorph, is found to lie within the piezoelectric layer for configurations where the layer thickness approximately exceeds the substrate thickness. Taking the position of the neutral axis from the centre of the PZT layer, the shift in position from the thinnest to thickest simulated case is 0.000026 mm. The equivalent distance for bimorph designs yields a shift of 0.00049 mm, almost 20 times more). This indicates the manufacture of bimorph designs with PZT layers several orders of magnitude thicker than the substrate layer are advisable over equivalent unimorph designs.

3.6 Conclusions

In this chapter the model which was developed in Chapter 2 was utilised to perform parametric studies on device geometry relating to four different case studies. Varied parameters included overall beam length and width, thickness of each layer and lastly the length and width of only piezoelectric material. Each harvester configuration has a unique resonant frequency (a frequency of excitation which provides peak performance) which is obtained through interpolation for each configuration. This resonant frequency was shown to be dependant on the coupling terms, resistance and mechanical damping. The simulated base acceleration applied to each configuration was constant in each case study. It has also been shown that in some situations, when the damping is below a threshold value – known as the bifurcation damping ratio, a double peak phenomenon occurs. This is advantageous since

reductions in mechanical damping will now effect the system bandwidth to a lesser extent.

The first case study was on a macro-scale device similar in size those which will later be used during experimental work, Chapter 4. Variations in beam length showed particularly interesting results. Due to increases in mechanical damping with beam length, longer beams do not necessarily provide performance improvements. For fixed material properties, electrical properties and geometric parameters, with the exception of overall beam length, there exists an optimum structure length which provides maximum power. Increasing the piezoelectric or substrate layer thickness was advantageous; dominant factors contributing to this included the magnitude of mechanical forcing exerted on the beam and, over larger load resistances, the magnitude of electro-mechanical coupling present in the system. The mechanical forcing increases with thickness predominantly due to rises in structure mass. A similar trend is observed for the electro-mechanical coupling, however this is due to reductions in the piezoelectric capacitance and changes in mode shape. Practical implications of this study indicate that the vibrational energy harvester should be designed to maximise both mechanical forcing and electro-mechanical coupling in order to optimise performance.

The second case study was for a micro-scale device which included a tip mass to reduce fundamental frequency and improve strain distribution along the cantilever beam. Similar trends were observed when comparing to the first case study, however, during alterations to the piezoelectric material it was realised that small improvements in power were achievable by removing material from the free end of the beam. During changes in layer geometry of a MEMS-scale device the mechanical forcing term is not as influential due to the tip mass being the dominant factor governing forcing. In this case the trends obtained for power are more dependant on the magnitude of the fundamental frequency and electro-mechanical coupling. Studies on tip mass size and material resulted in the conclusion that a larger denser tip mass will improve the performance of an energy harvester due to reductions in fundamental frequency and increases in mechanical forcing magnitude. This observation should however be considered with care due to the large difference in the fundamental frequency during parametric sweeps.

One major restriction was applied during optimisation of the final case study whereby the fundamental frequency of the device was not to exceed 30 Hz. The target application for this device is to harvest energy from ocean power where high excitation frequencies are unlikely to occur. Overall beam length, width and layer thickness were assumed fixed. A 129% improvement in performance is seen if the device is manufactured with piezoelectric material, of identical width to the substrate layer, covering 55% of the beam rather than the original design – piezoelectric layer half the width of the substrate layer with 95% coverage. Large performance improvements for a practical device highlight the importance of carrying out parametric studies on device geometry during the design process.

Lastly, comparison studies between bimorph designs and their unimorph equivalent were undertaken. During these tests the volume of piezoelectric material for both bimorph and unimorph configurations remained identical (achieved by setting thickness of PZT in bimorph designs to half that of the unimorph design). While considering PZT length, in terms of maximum power achievable, one can expect similar levels for a bimorph and its unimorph equivalent. Advantages of manufacturing a bimorph configuration are evident when the energy harvester is connected to larger load resistances. Electro-mechanical coupling is greater in bimorph designs hence the improved performance over an equivalent unimorph. While increasing the thickness of the piezoelectric layers it was seen that bimorph designs outperform unimorph designs in terms of maximum achievable power. Reasoning behind this became clear when considering material distribution and piezoelectric layer location in relation to neutral axis. Increasing PZT thickness for a unimorph design will eventually result in the neutral axis lying inside the PZT layer. This has a negative affect on performance due to charge cancellation, an issue not observed for the bimorph designs with symmetry ensuring the neutral axis remains coincident with the middle of the substrate layer regardless of PZT layer thickness. The implications of these findings are that bimorph configurations should be considered for harvesters with large piezoelectric to substrate layer thickness ratios and also if the energy harvester is to be connected to a load with high resistance, else a unimorph would suffice.

It is clear that design improvements are possible and that the conventional energy

harvester design is not always the most efficient. Saying that, in this chapter, individual geometric parameters are altered which causes variations in the fundamental frequency of the device. During the design procedure for piezoelectric vibrational energy harvesters the dominant frequency of excitation is usually known hence the conventional energy harvester is designed to resonate at this frequency. Since frequency matching is critical to harvester performance any change in geometry is likely to create a configuration with an inferior performance. To avoid this issue and allow for unbiased comparisons between harvester configurations the fundamental frequency of each design must be identical. This will be achieved in Chapter 6 by systematically altering multiple geometric parameters simultaneously. In the following chapter detailed experimental work is presented in order to validate the derived model and to confirm the observed trends.

CHAPTER 4

EXPERIMENTAL VALIDATION

4.1 Introduction

In Chapter 2 an analytical model for uniform and non-uniform rectangular cantilever energy harvesters was developed. This was followed, in Chapter 3, by theoretical parametric studies to determine how geometric parameters affect the performance of vibrational energy harvesters; trends were obtained relating, for example, PZT length to the power generated. The main aim of this chapter is the validation of both analytical model and theoretical trends, which is attempted through experimental works. Variations in mechanical damping during parametric studies on device geometry is thought to be a key factor in governing performance trends. An experimental study is undertaken with the aim of gauging mechanical damping sensitivity to factors such as clamping condition. The chapter also aims to establish a consistent and reliable in-house sample manufacturing procedure.

The samples used throughout experimental testing require in-house manufacture, allowing for greater flexibility in sample geometry. Experimentation on several methods for cutting PZT sheets is undertaken to determine the most effective cutting method; particular importance is given to heat damage and cutting edge surface finish. Following this, a comprehensive method for sample manufacture is detailed in this chapter.

Individual samples, non-uniform harvesters along with a conventionally designed

harvester, are tested in an attempt to validate the analytical model and the manufacturing method reliability. Frequency responses from both voltage and tip displacement are compared with theoretical results. Voltage is measured with a dynamic signal analyser and tip displacement with a laser vibrometer. Upon completion, attention is turned to the validation of trends between PZT length and voltage generated. Batches of samples with varying lengths of PZT are manufactured for this purpose and reductions of PZT material from both the clamped and free end are investigated. As has been shown in Chapter 3, the overall trend is very much dependant on electric load magnitude and hence data over three different resistors is collected – 1 kΩ, 60 kΩ and 1 MΩ.

The magnitude of mechanical damping will certainly have an effect on results; this is focussed on in the penultimate section of the chapter. As PZT layer length is altered, one would expect the mechanical damping in the system to change. The analytical model developed in Chapter 2 assumes proportional mechanical damping, i.e. a magnitude dependent on the fundamental frequency of the system. Experimental data on mechanical damping are obtained to assess the validity of this assumption. The sensitivity of mechanical damping magnitude to a few other factors, namely the sample width and clamping conditions, is also studied in these works.

4.2 Sample preparation and experimental procedure

Validation of the theoretical model is achieved through the use of samples manufactured in-house. This provides a greater freedom for altering geometric parameters while keeping costs low. The aim is to validate the model in terms of both voltage generated and also the trends shown in Chapter 3. In this section, the sample manufacturing procedure is introduced, followed by an outline of the experimental procedure.

4.2.1 Sample preparation

The manufactured energy harvesters, comprising of Al (Alloy Al 1050) and PZT, are of unimorph type. The PZT (type – PIC 255) was sourced from Physik Instrumente [74] and

delivered as 50 mm $\times$ 50 mm $\times$ 0.5 mm sheets. The square sheets required cutting into strips, each of 7 mm in width. Cutting PZT material is not straightforward due to its brittle natural and so several avenues for achieving this were investigated:

- Water jet cutting machine
  - This method uses abrasion to cut material.
  - The main advantage is that high temperatures are avoided and so temperature sensitive properties, i.e. poling of the PZT, are unaffected. (Recall from Chapter 1 the term 'poling' is used to define the process of domain alignment resulting in piezoelectric properties).
  - The disadvantage of this method is that the resulting samples have rather jagged edges and so equation variables, i.e second moment of area, internal piezoelectric capacitance etc., are not accurately represented. Figure 4.1 shows an example of one sample which was manufactured with this technique. It is evident that the quality of cut is inadequate.

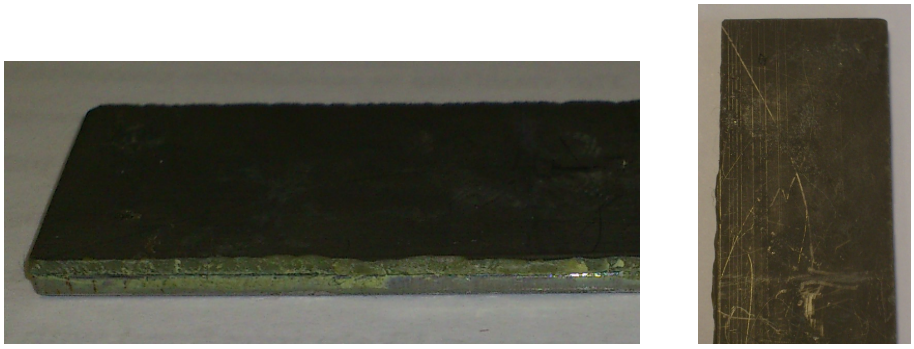

(a) (b)

Figure 4.1: A sample comprising of PZT which is cut using a water jet cutting machine.

- Laser cutting machine
  - This method uses high temperature to cut the material.
  - The main advantage is that the resulting cut surface is of excellent quality, and minimal irregularity is present.
  - The disadvantage of this method is that the high temperatures involved would affect the poling of material, albeit in a localised region. In addition to this,

since material is being melted/burnt, there is a health risk involved due to the lead content of PZT.

- Silicon carbide disk cutting machine
  - This method also uses abrasion to cut material.
  - Advantages and disadvantages are similar to using a water jet cutting machine however the jagged edges in this case are considerably less pronounced. This is due to cutting with a rotating disk as opposed to a high velocity jet of water which disperses on point of impact.

From the three methods outlined above the silicon carbide disk method was decided upon due to its potential for producing the best resulting samples. The setup used to cut the material is shown in Figure 4.2. The PZT sheet is placed on top of a sheet of Al with dimensions 50 mm $\times$ 50 mm $\times$ 0.87 mm or 50 mm $\times$ 50 mm $\times$ 0.67 mm, depending on the sample batch. Both sheets are clamped and cut together which ensures the PZT is supported at all times, thereby preventing premature fracture. The carbide disk remains fixed in translation and rotates at a maximum speed of 3000 rpm, whereas the clamp holding the samples moves along the y-axis at fixed rate. The speed chosen, through a trial and error process, was 0.1 mm.s^{-1}, however for the entry and exit sections a lower speed of 0.05 mm.s^{-1} was used to ensure PZT fracture did not occur.

After strips of 7 mm in width are cut, further preparation must be completed prior to applying adhesive. Since the length of piezoelectric material is required to vary from sample to sample, controlled fractures were performed on the 50 mm long strips, thereby creating layers with the desired lengths. Grit paper was used to remove any jagged edges while ensuring all bonding edges lie at a lower level than the bulk of the strip. This is important for ensuring good surface contact between Al and PZT layers. The next step was to scratch and remove dirt from the Al surface – heavy duty scotch brite paper was used to achieve this. Scratching is important as it creates grooves for the adhesive to flow into. Note, this step was not performed on the PZT since scratching will partly remove the electrode layer hindering the materials ability to collect charge. The last step is to remove dust and debris

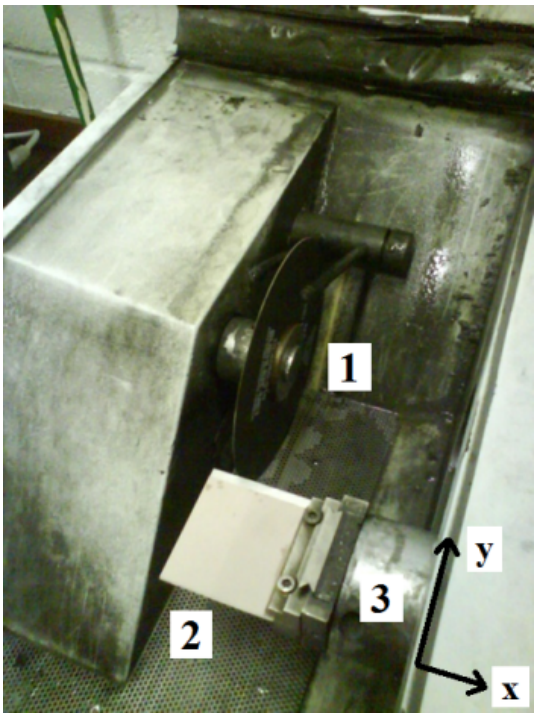

Figure 4.2: Setup of sheets in the cutting machine. (1) Silicon carbide cutting disk (2) 50 mm square sheet of Al and PZT, (3) Motorised, automated movable clamp.

from the bonding surfaces (of both Al and PZT layers) and this was achieved by applying Isopropyl alcohol and wiping using cotton pads.

Two types of adhesive are used in sample manufacture – DP460 epoxy resin [2] and Circuit Works conductive epoxy resin [41]. DP460 is applied to the majority of the bonding area with conductive epoxy applied to a few millimetres of one end. DP460 was chosen due to its superior shear and peel strength in comparison to similar priced products. DP460 is an insulator and so conductive epoxy is essential for creating electrical contact between the PZT bottom electrode and the substrate layer – without this connection voltages generated by the PZT would be immeasurable. Within minutes of the adhesive being applied, samples are placed beneath a weight to create a thin, uniform, bond layer, and remain under these conditions for 48 hours allowing the epoxy to cure fully.

Numerous samples of varying PZT length, ranging from approximately 7.5 mm to 50 mm, (Al length always fixed at 50 mm) were manufactured using this technique, see Figure 4.3. These samples required experimental testing in order to obtain frequency response

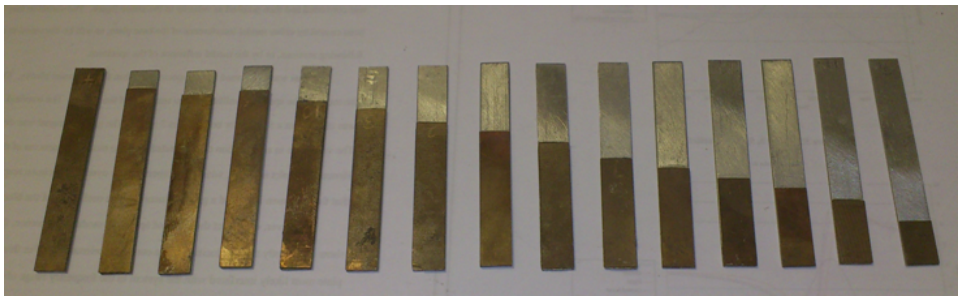

Figure 4.3: One sample batch manufactured in-house.

functions for both tip displacement and voltage generated over various load resistors. The procedure for this is detailed in the following section.

4.2.2 Experimental procedure

Samples manufactured through the procedure outlined above were then tested. In this section an experimental procedure for testing the samples is provided. The following apparatus is required to achieve this:

- Clamp. This is required for mounting samples to the shaker. The design factored in electric insulation between upper and lower inner clamp surfaces. Without this, the energy harvester would remain in a closed circuit electrical condition. Insulation is achieved by bonding 1 mm brass sheets to the inner surfaces of the steel clamp using DP460 epoxy adhesive. Electrical leads are then soldered onto the brass sheets allowing for connections between the energy harvester and electrical circuitry, see Figure 4.4 for a schematic representation of a clamped non-uniform energy harvester.

- PolyTec OFV-055 laser vibrometer. This is used to measure the tip velocity of samples, which is then converted to a displacement.

- PCB Piezotronics accelerometer, model number – 352C23. This is used to measure the base acceleration applied to the samples. Note, a feature of the dynamic signal analyser was occasionally used to ensure base acceleration remained constant to within $\pm 1\%$ of a predefined magnitude.

- Data Physics GW-V4 electromagnetic shaker. This is used for providing a base ex-

citation to samples via the clamp. A schematic of the full assembly is shown in Figure 4.5.

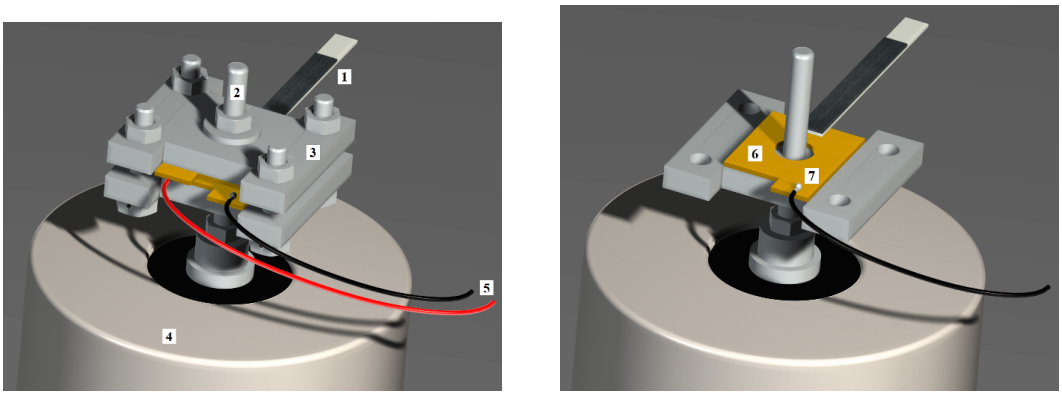

(a) Complete clamp assembly

(b) Upper layer of clamp removed

Figure 4.4: Schematic representation of the clamp assembly. (1) Energy harvester, (2) Spigot attached to shaker, (3) Clamp, (4) Shaker, (5) Leads going to electrical circuitry, (6) Brass sheet electrical insulated from the clamp surface, (7) Lower lead soldered onto brass sheet.

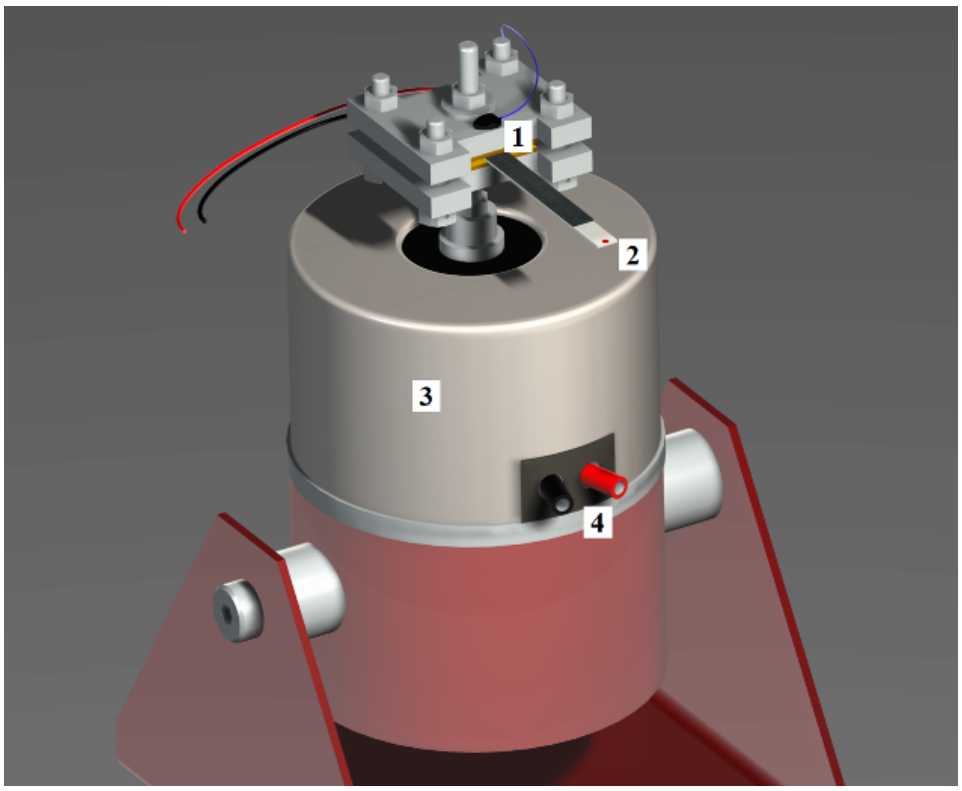

Figure 4.5: Schematic representation of experimental setup. (1) Accelerometer (2) Laser point for vibrometer, (3) Shaker, (4) Power supply input for shaker from amplifier.

- Stanford Research Systems SR785 dynamic signal analyser. This apparatus is used to output a harmonic signal to the shaker via an amplifier. In addition to this, it has

the capability to record two unique signal inputs. One channel was always used to monitor base acceleration while the second channel provided measurement for either voltage across a resistor or tip velocity.

- Electrical equipment, i.e. leads, resistors etc.

The complete setup of apparatus is shown in Figure 4.6. In the next section, validation of the theoretical model is performed. This is achieved by comparing frequency responses obtained from experimental data with theoretical simulations. Both uniform and non-uniform unimorph samples are tested to verify the capabilities of the developed theoretical model and the consistency in the manufacturing procedure.

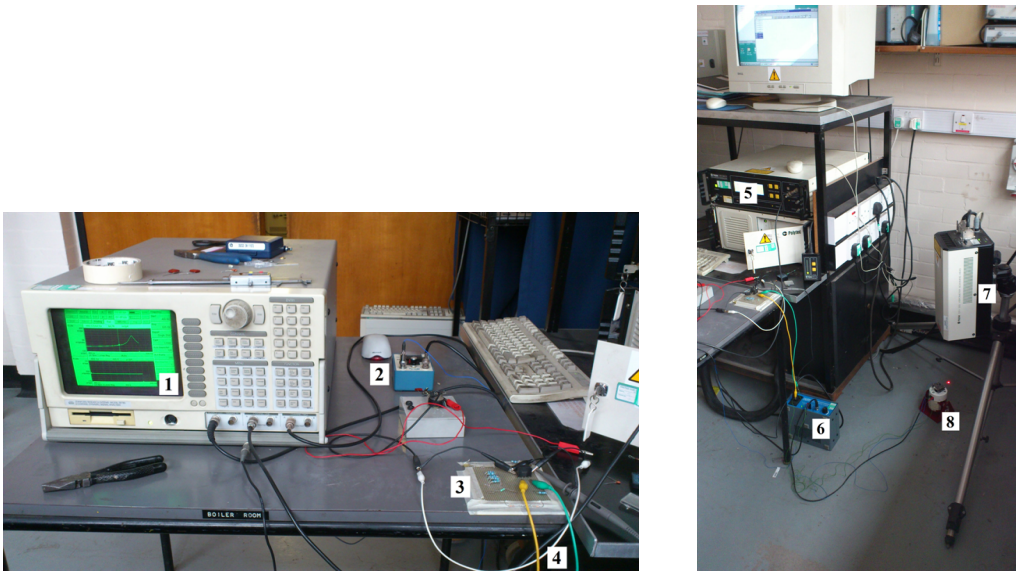

(a) (b)

Figure 4.6: Complete setup of apparatus. (1) Dynamic signal analyser, (2) Accelerometer signal conditioning unit, (3) Circuit board with resistors of various magnitude, (4) Leads from energy harvester, (5) Laser vibrometer signal conditioning unit, (6) Amplifier, (7) Laser vibrometer, (8) Shaker and clamp assembly.

4.3 Validation of theoretical model

In this section the theoretical model is validated for individual energy harvesters. Both generated voltage and tip displacement are of interest with theoretical results obtained from equations presented in Chapter 2, Equation (2.44) and (2.46) respectively. Following this, in Section 4.4, a validation of trends between voltage and PZT length is attempted.

4.3.1 Calibration

The initial step was to ensure the laser vibrometer and accelerometer were calibrated correctly. This was achieved by connecting the accelerometer to the clamp and pointing the laser onto the same point allowing both devices to measure base motion. Figure 4.7 shows results from this test; the base excitation frequency is swept from 335 Hz to 350 Hz at a constant acceleration level of 9.8 m.s^{-2}. The conversion factors provided for the accelerometer and laser vibrometer were 1.022 V.m^{-1}.s^2 and 0.125 m.V^{-1} respectively. The outcome of this simple test shows that both pieces of apparatus are calibrated with each other, to an acceptable degree, with a maximum percentage difference of 0.52%.

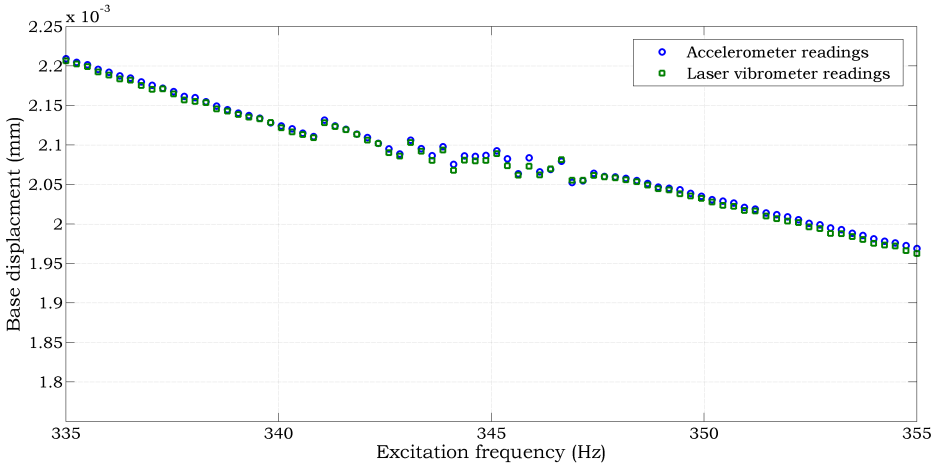

Figure 4.7: Results from the calibration test between the accelerometer and laser vibrometer.

Note, at the time of testing, a sample with fundamental frequency of approximately 343 Hz was mounted in the clamp. Due to vibrational feedback from the sample to the clamp, results in the proximity of 343 Hz are scattered and do not follow the general trend of decreasing base displacement with increasing frequency (required to maintain a constant base acceleration).

4.3.2 Output voltage validation

In this section validation of the theoretical, simulated, voltage generated from various samples is attempted. The first sample tested was a conventional energy harvester with both

Al and PZT layers being identical in length. Dimensions, measured using digital vernier calipers, accurate to 0.01 mm, and material properties can be found in Tables 4.1 and 4.2. During testing, the frequency was swept from 375 Hz to 425 Hz at intervals of 0.5 Hz with base acceleration kept constant at 0.5 m.s^{-2}. Transient response at each frequency is taken into account by applying a settle time of 1 s on the dynamic signal analyser allowing the energy harvester time to reach steady-state oscillations. Sets of data were obtained for two different load resistance magnitudes, 1 kΩ and 60 kΩ. Results from testing are shown in Figure 4.8.

Table 4.1: Structural dimensions of harvesters tested in this section.

Parameter	Sample 1	Sample 12
Al extended length[a] (mm)	46.15	46.02
Al width (mm)	7	7
Al thickness (mm)	0.87	0.87
PZT extended length[a] (mm)	46.15	10.59
PZT width (mm)	7	7
PZT thickness (mm)	0.5	0.5

[a] 'Extended length' refers to the length extruding from the clamp.

Table 4.2: Mechanical properties of harvesters tested throughout experimental work.

Parameter	Magnitude
Young's modulus of Al (GPa)	69
Density of Al (kg.m^{-3})	2700
Young's modulus of PZT (GPa)	62.1
Density of PZT (kg.m^{-3})	7800
Piezoelectric constant, d_{31} (m.V^{-1})	-180$\times$10^{-12}
Permittivity, ε_{33}^{S} (F.m^{-1})	1.549$\times$10^{-8}

Figure 4.8 shows theoretical voltage responses superimposed by experimental data. To obtain theoretical results, information from Tables 4.1 and 4.2 was inserted in the analytical model, Equation (2.44), derived in Chapter 2. Through trial and error a mechanical damping ratio of 0.48% was found in order to match peak response magnitudes. The mechanical damping could also have been found by exciting the harvester in short circuit conditions and measuring the magnitude using, for example, the half power point method

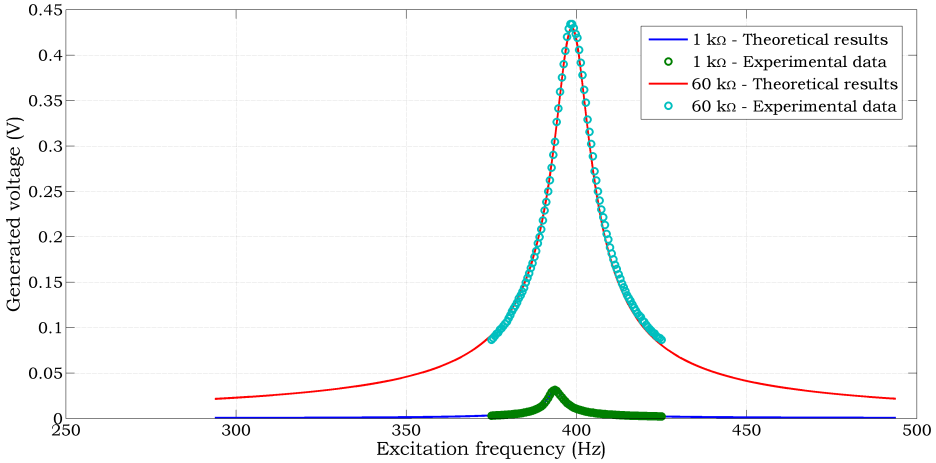

Figure 4.8: Comparison between theoretical and experimental voltage responses, for a conventionally designed energy harvester, across two different load resistances. Mechanical damping magnitude of 0.0048 required to match peak voltage.

[80] (such a procedure is used in Section 4.4). The results in Figure 4.8 indicate an excellent agreement between experimental data and the theoretical model. Shifts in resonant frequency due to changes in load resistance are accurately represented along with peak voltage magnitudes over both resistance. Across a 1 kΩ load, 0.03 V is generated at a resonant frequency of 393.8 Hz, whereas across a 60 kΩ load, 0.43 V is generated at a resonant frequency of 398.7 Hz.

Other samples tested included non-uniform beams. Dimensions of one of these samples, Sample 12, is shown in Table 4.1. The energy harvester is clamped with the PZT layer on the clamped side of the cantilever, i.e. both layers are clamped as shown in Figure 4.4. Again frequency is incremented by 0.5 Hz during the experiment, however, in this case, sweeping ranges from 440 Hz to 490 Hz. Constant base acceleration of 0.5 m.s^{-2} is applied to the sample and a 1 s settle time utilised, results are shown in Figure 4.9 along with theoretical voltage response.

Excellent agreement between theoretical and experimental data is seen when a damping ratio of 0.2% is used in the theoretical model. Saying this, a small discrepancy can be seen when comparing the fundamental frequency. This is most likely due to measurement errors while determining the exact length of extending layers. These errors are taken into account in later sections when experimental and theoretical trends between peak voltage

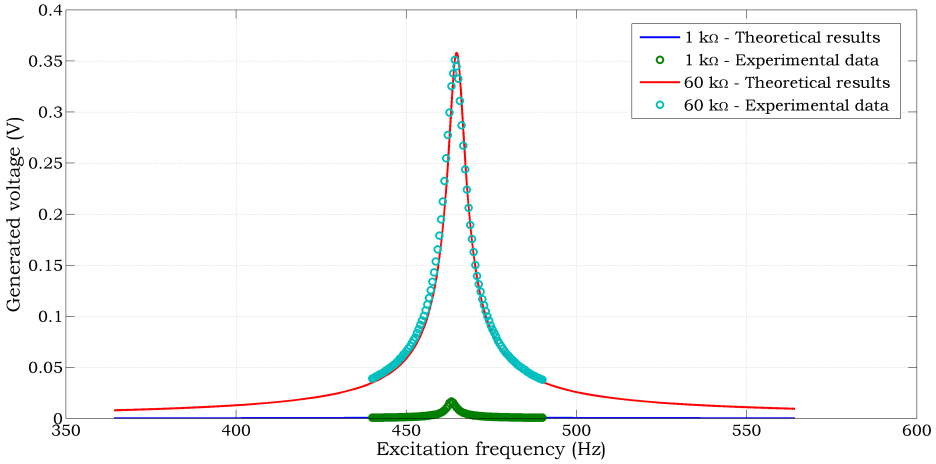

Figure 4.9: Comparison between theoretical and experimental voltage responses, for a non-uniform energy harvester with a PZT layer length of 10.59 mm, across two different load resistances. Mechanical damping magnitude of 0.0020 required to match peak voltage.

and PZT length are compared, see Section 4.4. Across a 1 kΩ load, 0.02 V is generated at a resonant frequency of 464.2 Hz, whereas across a 60 kΩ load, 0.36 V is generated at a resonant frequency of 464.9 Hz. Notice how a PZT length reduction of 77% has only resulted in a 19% peak voltage reduction, for the 60 kΩ case. One of the main reasons behind this is large difference in mechanical damping magnitude between the samples.

4.3.3 Tip displacement validation

In this section validation of the theoretical model in terms of tip displacement is attempted. To illustrate to the reader the reliability of the derived model and manufacturing technique, a second batch of samples comprising of a 0.67 mm thick Al layer are used during this validation. Material properties of Al and PZT remain as before, refer to Table 4.2. Two non-uniform samples are tested here; the first sample comprised of a 31.95 mm $\times$ 5 mm $\times$ 0.67 mm substrate layer and a 12 mm $\times$ 5 mm $\times$ 0.5 mm piezoelectric layer, whereas the second sample was fabricated from a 24 mm $\times$ 5 mm $\times$ 0.67 mm substrate layer and a 21.49 mm $\times$ 5 mm $\times$ 0.5 mm piezoelectric layer. Base acceleration, in the region of 0.1 m.s^{-2}, was not kept constant during these tests and displacement FRFs are used for comparison purposes – $\frac{w_{\text{beam}}}{w_{\text{base}}}$. During these tests both energy harvesters are in closed circuit conditions – $R_{\text{load}} = 0$, see Figure 4.10 for the results.

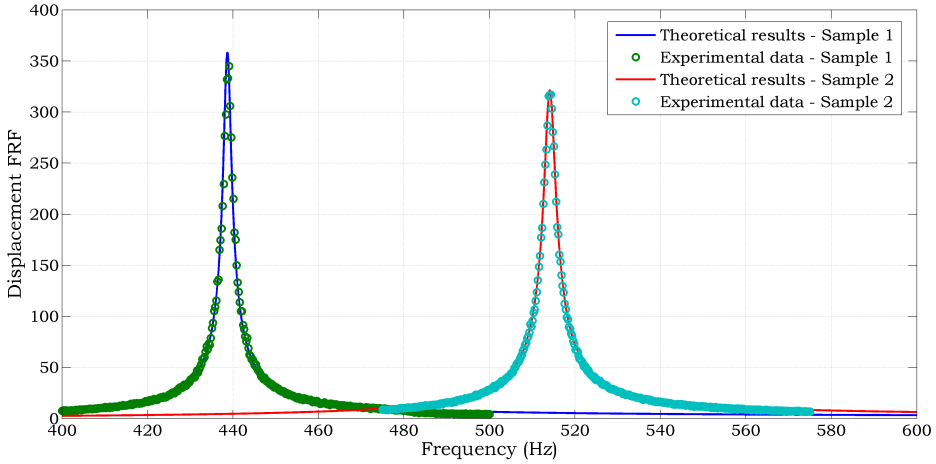

Figure 4.10: Comparison between theoretical and experimental tip displacement responses, for two non-uniform energy harvester in closed circuit conditions.

Once again, the theoretical model and experimental data are in excellent agreement. The estimated damping ratios for the first and second sample where 0.41% and 0.53% respectively. Note that although the samples are smaller in length, width and thickness, the damping ratio is relatively large in comparison to those obtained in Section 4.3.2. Reasons behind this are thoroughly investigated and reported in Section 4.5.

4.4 Validation of voltage vs PZT length trends

Now that validation of the theoretical model for single samples has been completed, attention is turned to the validation of general voltage trends. In addition to this, the fundamental frequencies of all samples are compared to theoretical results. Reducing the piezoelectric material length from both the free and clamped end is investigated in these works.

4.4.1 Reducing PZT length from the free end

In this section reducing piezoelectric layer length from the free end is investigated. 13 samples were manufactured with varying lengths of piezoelectric material (width and thickness constant at 7 mm and 0.5 mm respectively). For all samples the substrate layer dimensions were kept constant at 50 mm $\times$ 7 mm $\times$ 0.67 mm, however, during testing the extended substrate length (length overhanging from the clamp edge) was maintained at 45 mm. Refer to

Table 4.3 for sample dimensions with material properties previously provided in Table 4.2. For each sample, a frequency response plot of the voltage is obtained from which peak voltage and resonant frequency are extracted.

Table 4.3: Piezoelectric layer extended length for samples tested in this section. Note, Al extended length fixed at 45 mm. Al and PZT width identical at 7 mm. Al and PZT thickness fixed at 0.67 mm and 0.5 mm respectively.

Sample	1	2	3	4	5	6	7
PZT extended length (mm)	44.95	39.73	38.34	37.17	33.40	29.59	26.69
Sample	8	9	10	11	12	13	
PZT extended length (mm)	24.32	20.41	17.83	12.54	9.32	4.73	

Figure 4.11 shows a comparison between experimental data and theoretical results for the fundamental frequency of tested samples. Results show an initial increase in fundamental frequency with PZT length followed by a decline starting after the PZT coverage exceeds approximately half the substrate length. A uniform increase in PZT length causes a uniform increase in structure mass which would result in fundamental frequency reduction. However, in conjunction to this there is a gradual increase in structure stiffness. The trend in fundamental frequency is determinant on the magnitude by which both mass and stiffness vary. Horizontal errors bars of $\pm$ 1 mm are added to the plot which factor in small uncertainties, i.e. parallax errors, while measuring extended piezoelectric and substrate layer lengths. There is general agreement between experimental data and theoretical results here with a maximum discrepancy of 2.8%, indicating that the transfer matrix method, refer to Section 2.2.4, is reliable for estimating natural frequencies.

The next stage was an experiment-theory comparison of the peak voltages across various load resistance magnitudes (1 kΩ, 60 kΩ and 1 MΩ) for all 13 samples. Results are shown in Figures 4.12 - 4.14. Notice how two sets of theoretical results have been plotted – one assuming proportional mechanical damping and the other assuming a fixed mechanical damping of 0.004. This damping magnitude was chosen through trial and error in order to provide satisfactory theoretical-experimental data matching. Damping magnitude for the

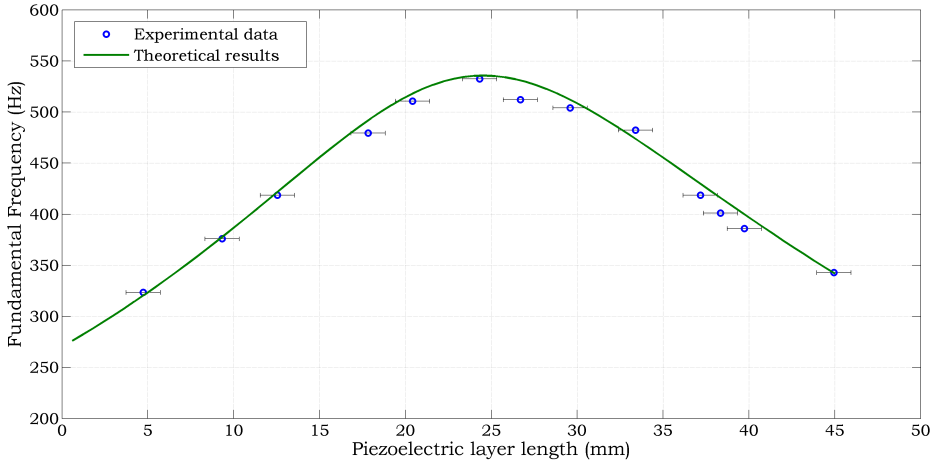

Figure 4.11: Comparison between theoretical and experimental fundamental frequency for the 13 tested samples.

proportional damping case is calculated using:

$$2\gamma_r\omega_r = \alpha + {\omega_r}^2\beta \ , \tag{4.1}$$

with constants α and β equating to 20.13 rad.s^{-1} and 4.71$\times$10^{-7} s.rad^{-1}, respectively. These magnitudes are calculated in a similar manner those in Chapter 3.

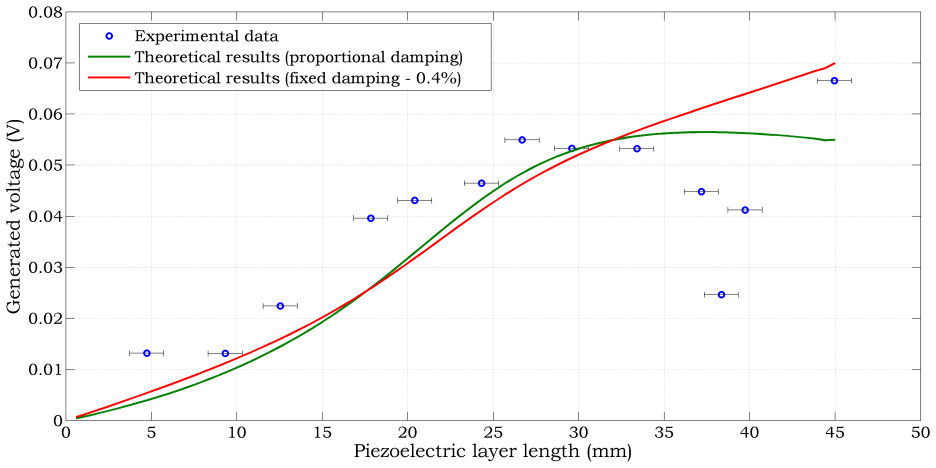

Figure 4.12: Comparison between theoretical and experimental peak voltage across a 1 kΩ load resistor for the 13 tested samples.

The results show that general experimental and theoretical trends are in agreement. For the 1 kΩ case, samples with short PZT layers perform poorly in comparison to those with longer layers. In contrast, across a 60 kΩ or 1 MΩ resistor, shorter layers have compa-

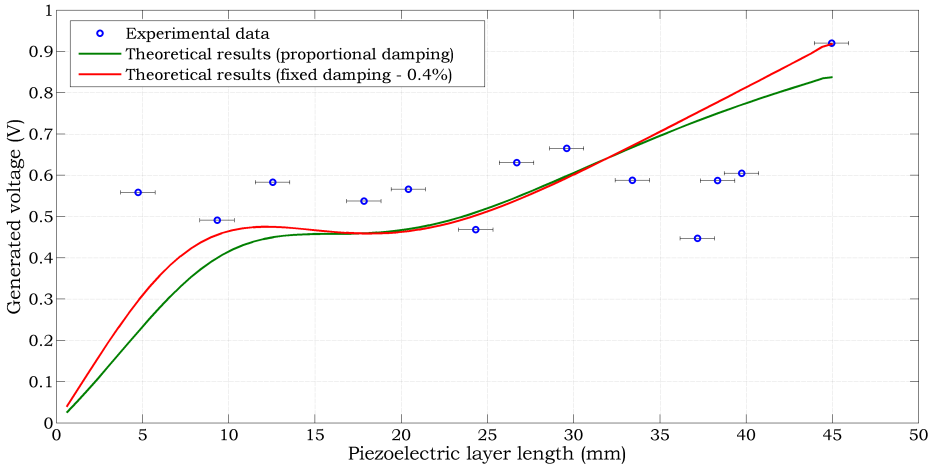

Figure 4.13: Comparison between theoretical and experimental peak voltage across a 60 kΩ load resistor for the 13 tested samples.

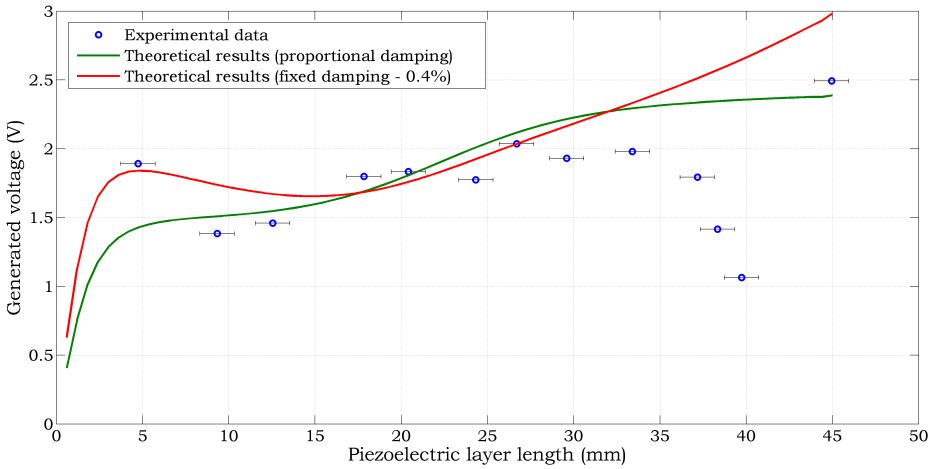

Figure 4.14: Comparison between theoretical and experimental peak voltage across a 1 MΩ load resistor for the 13 tested samples.

rable performance levels to samples comprising of long PZT layers with both experimental data and theoretical results showing this. However, there are several issues which require attention:

- For Sample 1, a fixed mechanical damping level of 0.004 produces results with good agreement for the 60 kΩ case. However, the same cannot be said whilst the sample is connected to a 1 kΩ or 1 MΩ resistor.
- Samples with lengths between 35 mm and 40 mm show poor agreement between experiment and theory.

- Neither assumption of proportional damping or fixed damping is suitable for matching results across the whole sample range.

It was initially thought that the samples manufactured with PZT lengths between 35 mm and 40 mm (Samples 2 - 4) were faulty, either due to structural damage, i.e. micro-cracks, or inconsistency of piezoelectric properties. Further samples in this length range were manufactured and tested with the same outcome – the voltage generated by samples in this range is unusually low across all resistances. Magnitude of the mechanical damping ratio was determined to be the cause for these anomalous results along with providing an explanation for all discrepancies between experimental and theoretical results. Figure 4.15 shows the mechanical damping obtained for each sample in closed circuit conditions. Magnitude of mechanical damping is obtained from individual sample frequency response plots using the half power point method, [80].

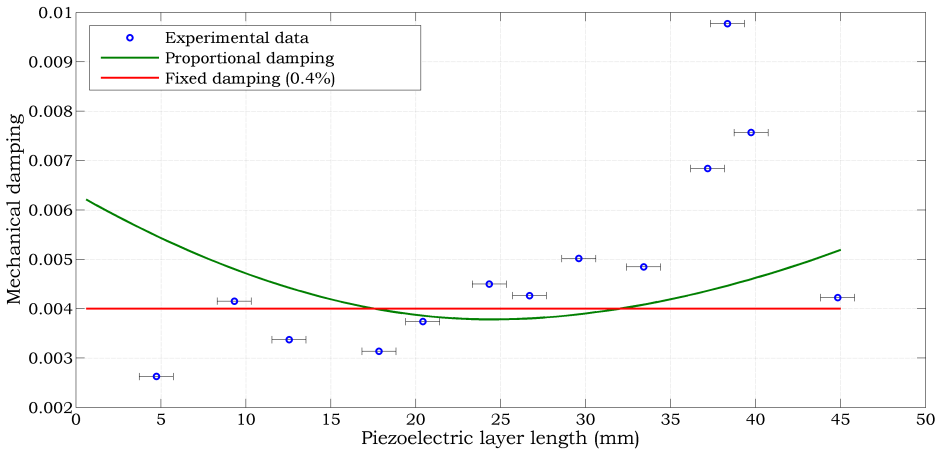

Figure 4.15: Comparison between theoretical (using both proportional and fixed damping) and experimental mechanical damping magnitude for the 13 tested samples.

From the experimental data in Figure 4.15, no clear trend between PZT length and mechanical damping is evident. However, it is clear that samples in the range of 35 mm to 40 mm have a large mechanical damping. This is the reason why Samples 2 - 4 have unusually lower output voltage levels in comparison to other samples. It is also clear that the assumptions of either proportional or fixed damping are not applicable for theoretically estimating the mechanical damping magnitude. Proportional damping assumes mechanical damping is dependant on the fundamental frequency. However, experimental results show

this is not the case in this practical situation. In Section 4.5 the extent to which parameters effect the mechanical damping ratio is determined through further experimental work. Next, theoretical and experimental trends while reducing piezoelectric material length from the clamped end are compared.

4.4.2 Reducing PZT length from the clamped end

In this section reducing piezoelectric layer length from the clamped end is investigated. Nine of the samples manufactured for the previous test were reused here. During testing the extended substrate length (overhanging from the clamp edge) was maintained at 46 mm $\pm$ 1 mm. Refer to Table 4.4 for sample dimensions with material properties provided in Table 4.2. Again, for each sample a frequency response plot of the voltage is obtained from which peak voltage and resonant frequency are extracted. Connections from the PZT top and bottom surface to the load are required to measure generated voltage, however the previous clamp setup is invalid in this case. A separate wire must be attached to the PZT top surface since in all configurations (bar Sample 1), contact between the clamp and PZT top surface is not present. Care must be taken since the wire affects dynamics of the system, see Figure 4.16(a). The plot shows that the wire increases mass, thereby reducing the fundamental frequency, and increases damping, thereby dramatically reducing the response magnitude. Using a single strand of wire is the preferred option, and this resulted in the use of a modified setup for this testing, shown in Figure 4.16(b).

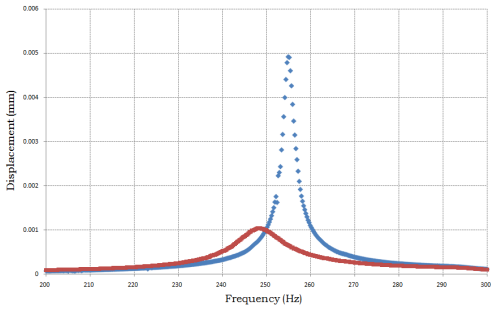

(a) Frequency response when attaching different wires to top surface of PZT. Red – wire bundle. Blue – single strand.

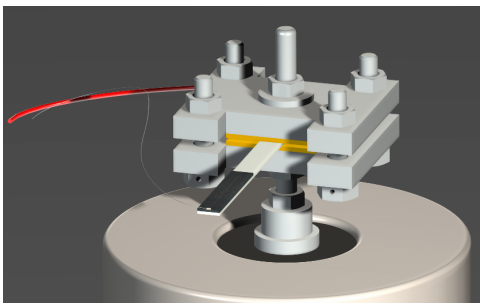

(b) Schematic of setup opted for when taking measurements for this set of samples.

Figure 4.16: Issue with wire connection.

Table 4.4: Piezoelectric layer length for samples tested in this section. Note, Al extended length fixed at 46 mm. Al and PZT width identical at 7 mm. Al and PZT thickness fixed at 0.67 mm and 0.5 mm respectively.

Sample	1	2	3	4	5
PZT length (mm)	46.00	42.20	40.40	39.00	35.50
Sample	6	7	8	9	
PZT length (mm)	30.00	25.50	20.15	14.50	

Figure 4.17 shows a comparison between experimental data and theoretical results for the fundamental frequencies of the tested samples. Trends are again determined by the relative changes in system mass and stiffness. There is again general agreement between experimental data and theoretical results with a maximum discrepancy of 5.6%.

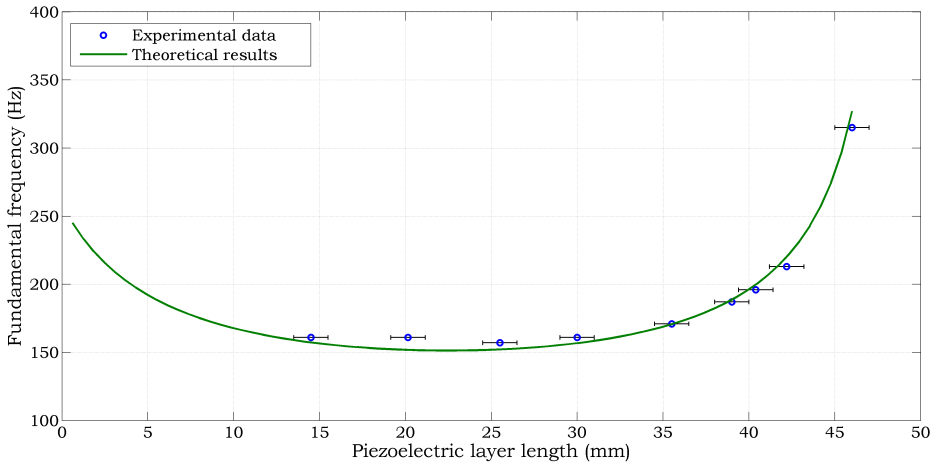

Figure 4.17: Comparison between theoretical and experimental fundamental frequency for the 9 tested samples – reducing length from the clamped end.

The next stage was an experiment-theory comparison of the peak voltages across various load resistance magnitudes (1 kΩ, 60 kΩ and 1 MΩ) for the 9 samples. Results are shown in Figures 4.18 - 4.20. Again, two sets of theoretical results have been plotted – one assuming proportional mechanical damping and the other assuming a fixed mechanical damping of 0.004.

Figures 4.18 - 4.20 indicate good agreement between experimental data and theoretical results, for all resistance magnitudes, when mechanical damping in the theoretical model is fixed at 0.004. This can be explained by comparing the measured mechanical damping

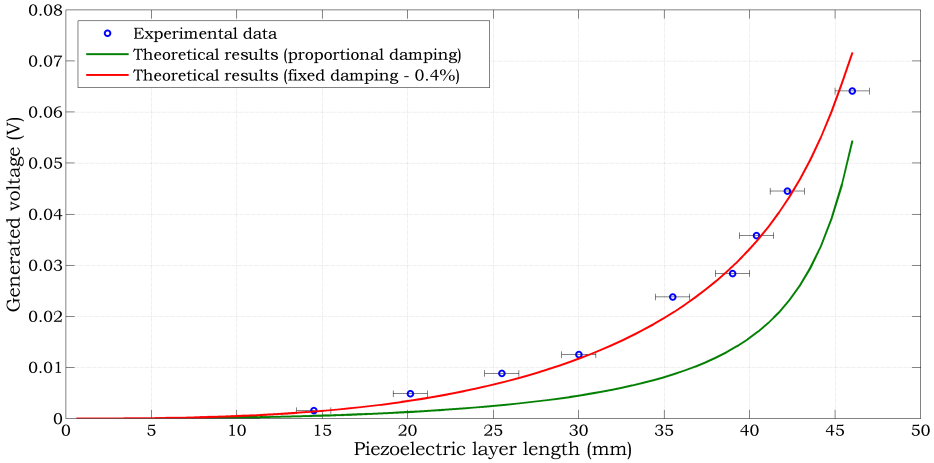

Figure 4.18: Comparison between theoretical and experimental peak voltage across a 1 kΩ load resistor for the 9 tested samples – reducing length from the clamped end.

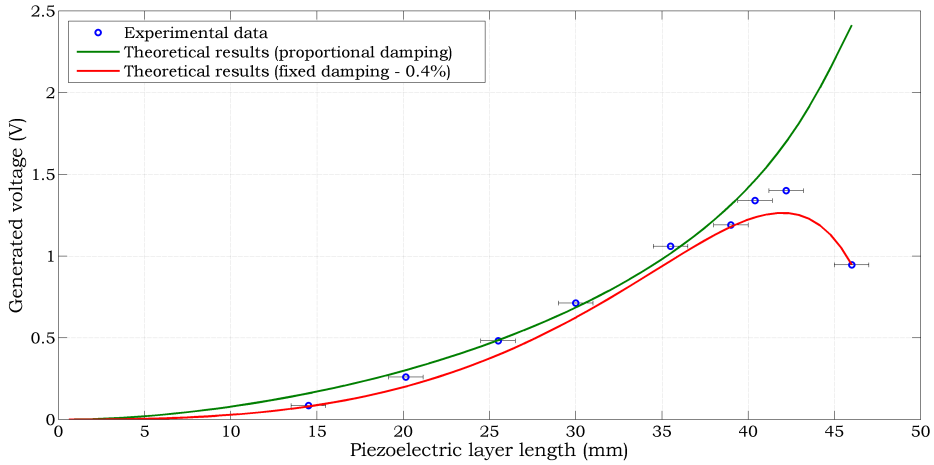

Figure 4.19: Comparison between theoretical and experimental peak voltage across a 60 kΩ load resistor for the 9 tested samples – reducing length from the clamped end.

with theoretical assumptions, Figure 4.21. In this scenario, where PZT length is reduced from the clamped end, mechanical damping remains reasonably constant at approximately 0.0032. The proportional damping assumption is again incorrect confirming a zero correlation between mechanical damping and fundamental frequency while altering PZT length. When the harvester is connected to a 1 kΩ resistor there is a decrease in maximum generated voltage with PZT length. Over 60 kΩ and 1 MΩ resistances both theoretical results and experimental data show maximum voltage is generated when PZT length is several millimetres shorter than in the conventional design.

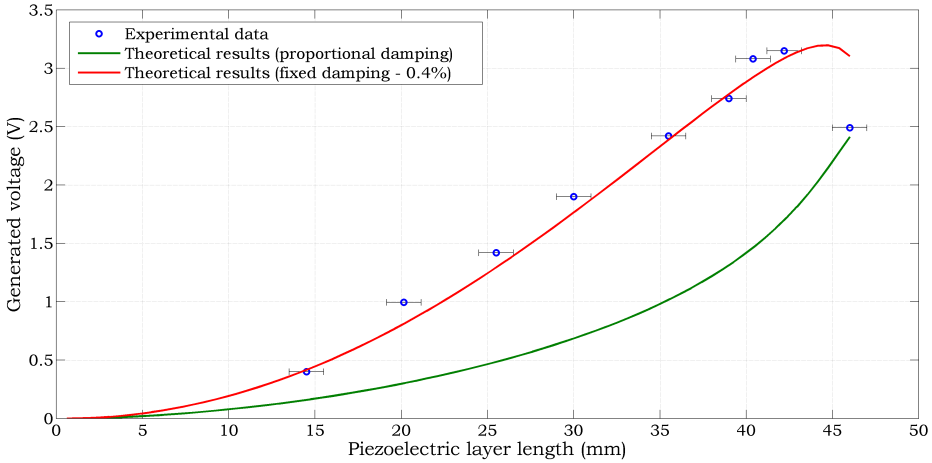

Figure 4.20: Comparison between theoretical and experimental peak voltage across a 1 MΩ load resistor for the 9 tested samples – reducing length from the clamped end.

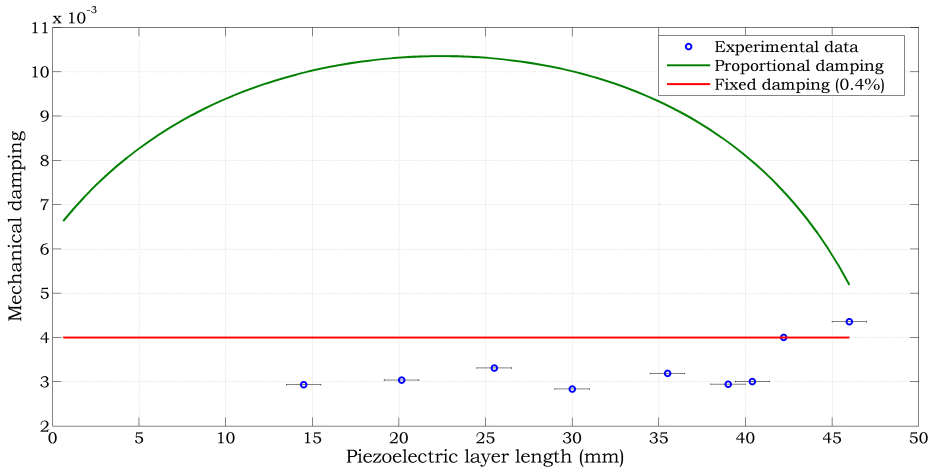

Figure 4.21: Comparison between theoretical (using both proportional and fixed damping) and experimental mechanical damping magnitude for the 9 tested samples – reducing length from the clamped end.

Mechanical damping magnitude has been shown to be pivotal in determining trends between voltage generated and PZT length. It is therefore important to further investigate how the damping magnitude is affected by certain factor and variables. This is presented in the following section.

4.5 Factors affecting the magnitude of mechanical damping

Mechanical damping in structural systems is notoriously troublesome to control and calculate. Mechanical damping is a process of energy loss and can occur through materials, the structure support or to the surrounding environment. More detailed information on these contributors can be found in [5]. In the setup and structure tested in these works the following factors are especially important:

- Sample width.
- Clamping conditions.
- PZT length.

Each of these factor is individually investigated in the following subsections.

4.5.1 Mechanical damping and width

In this section the effects of beam width are examined. 7 samples were manufactured comprising of only Al with widths ranging from 2 mm to 14 mm. The thickness and extended length was kept constant at 0.87 mm and 45$\pm$1 mm respectively. Figure 4.22 shows the extent by which sample width affects mechanical damping. There is a general increase in mechanical damping with beam width. This can be attributed to an increase in material volume and surface area, with surface area increasing the effects of air resistance on the structure. This is seen to become more severe for wider beams. Although width does affect damping it is not the main cause for discrepancies found in Section 4.4.1. The uncertainty in energy harvester width is only $\pm$0.1 mm which equates to a mechanical damping uncertainty of $\approx$0.0001.

It is also worthwhile taking a look at the trend between fundamental frequency and beam width, Figure 4.23. The results show there is a small decrease in frequency with increases width which amplify as the width gets larger. This is due to shear and inertial effects present during vibratory motion. In deriving the theoretical model, Chapter 2, recall

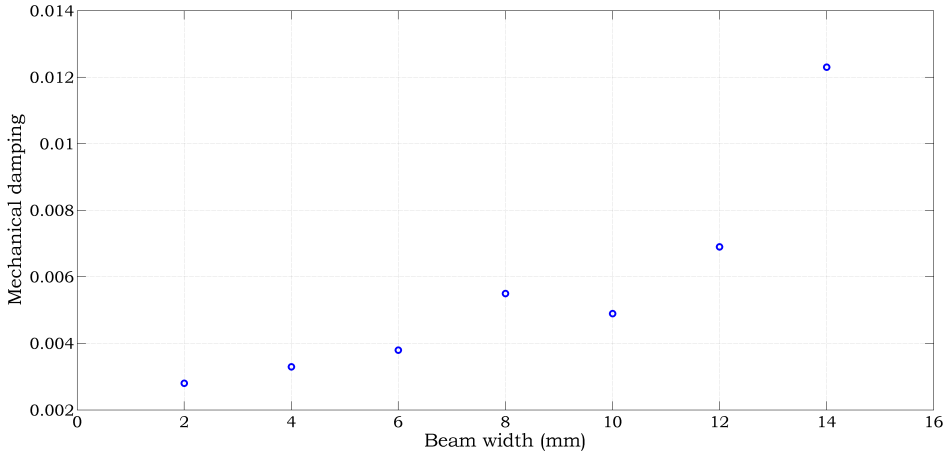

Figure 4.22: Experimental data for the mechanical damping magnitude while increasing beam width.

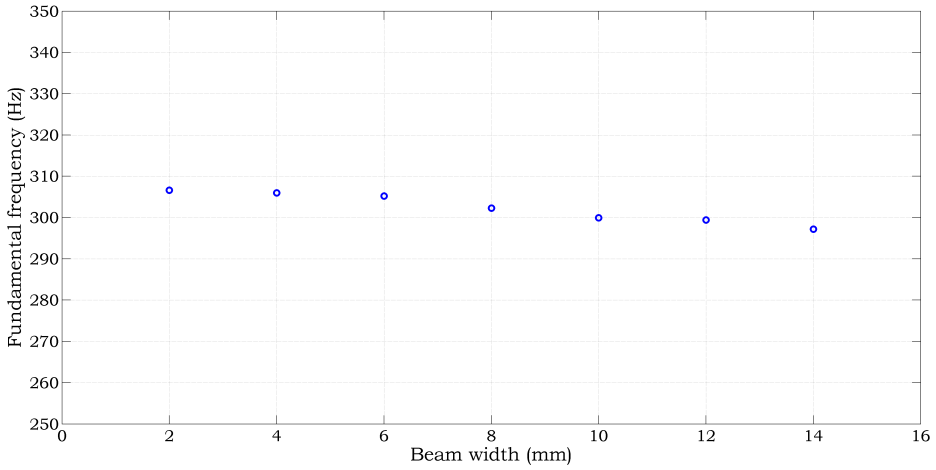

Figure 4.23: Experimental data for the fundamental frequency while increasing beam width.

the Euler-Bernoulli beam assumption is made where the effects of rotational or shear inertia are ignored. For energy harvester dimensions examined in this thesis this is not an issue, however, for harvesters with small length to width aspect ratios more accurate beam models are required, i.e. a Timoshenko beam model [101].

4.5.2 Mechanical damping and clamping conditions

In this section the effects of clamping conditions on the mechanical damping magnitude are investigated. It has previously been shown that mechanical damping is, to a certain degree, dependant on clamping force. Allen [5] demonstrated, through experimental means, that

increasing the torque applied to clamping bolts will decrease mechanical damping. Samples tested comprised of a single titanium layer with dimensions of approximately 115 mm $\times$ 115 mm $\times$ 3 mm. For works in the present thesis a new batch of energy harvester samples was manufactured. The Al substrate layer dimensions are fixed at 50 mm $\times$ 7 mm $\times$ 0.87 mm. The PZT layer thickness and width are 0.5 mm and 7 mm, respectively. The PZT length for each sample is given in Table 4.5 with material properties for both layers remaining identical to prior experimental work, see Table 4.2. Note that these tests are only focused on reducing piezoelectric material length from the cantilever free end.

Table 4.5: Piezoelectric layer extended length for samples tested in this section. Note, Al extended length fixed at 45 mm. Al and PZT width identical at 7 mm. Al and PZT thickness fixed at 0.87 mm and 0.5 mm respectively.

Sample	1	2	3	4	5	6
PZT extended length (mm)	44.96	43.03	41.38	40.03	37.85	33.14
Sample	7	8	9	10	11	12
PZT extended length (mm)	32.95	30.38	26.40	20.62	15.37	10.09

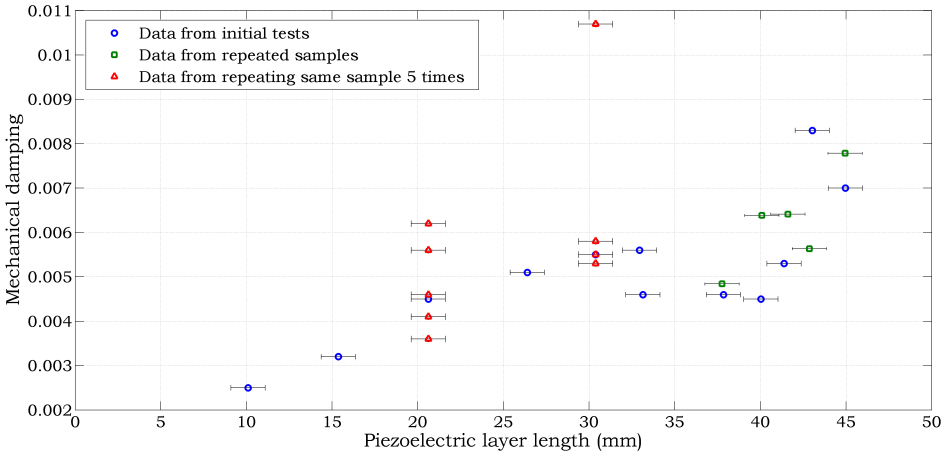

Figure 4.24: Experimental data for mechanical damping while using the steel/brass clamp.

Mechanical damping magnitudes are calculated from the tip displacement frequency response functions while energy harvesters are in closed-circuit conditions, i.e. load resistance and hence electrical damping are equal to zero. Blue data points in Figure 4.24 show the magnitude of mechanical damping obtained from all 12 samples. The difference in PZT length between Samples 6 and 7 is only 0.19 mm (0.5%). However, the difference in the mechanical damping experienced by these samples is 0.001 (17.9%). Mounting of samples

in the clamp is clearly affecting the results here. PZT is brittle so care must be taken not to fracture the material when clamping; an inconsistency exists as there is no control on the magnitude of torque applied to the clamping bolts. The first five samples were mounted in the clamp again and retested. Green data points in Figure 4.24 show the outcome of this. Large differences in the experimental mechanical damping magnitude, for the same samples, were observed with a maximum difference of 0.0027 (32.1%) for Sample 2. The last test was to remount Samples 8 and 10, alternately, five times in order to gauge damping variation over a larger data base, see red data points in Figure 4.24. Again, for both samples, a great uncertainty in the damping ratio is present (Note, the data point at 0.0107 for Sample 8 is classed as an anomaly). In an attempt to improve on this inconsistency, Section 4.5.3 reports test results while using a new clamp.

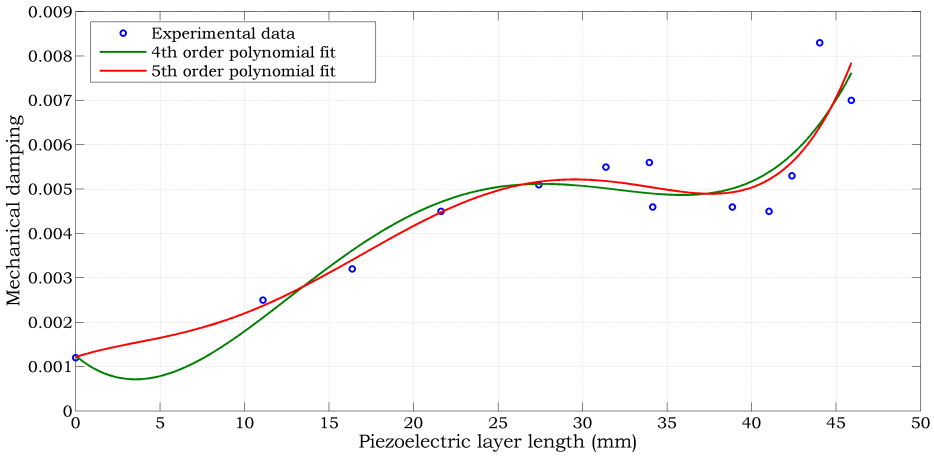

Figure 4.25: Fitting polynomials to experimental data thereby obtain a trend between mechanical damping and PZT length for use in the theoretical model.

Polynomials to the 4th and 5th order were fitted to mechanical damping data obtained during the first test run. This provided two relationships between mechanical damping and PZT length for use in the theoretical model. Note that a sample without a piezoelectric layer was also tested to provide fitting over the full range of PZT lengths. Results from fitting can be found in Figure 4.25. Both 4th and 5th order polynomials provide a reasonable fit to experimental data with a 'dip' in damping magnitude occurring in the range of 40 mm, followed by a slight increase, and finally a linear decrease with PZT length (the 5th order polynomial solution better represents this linear decrease).

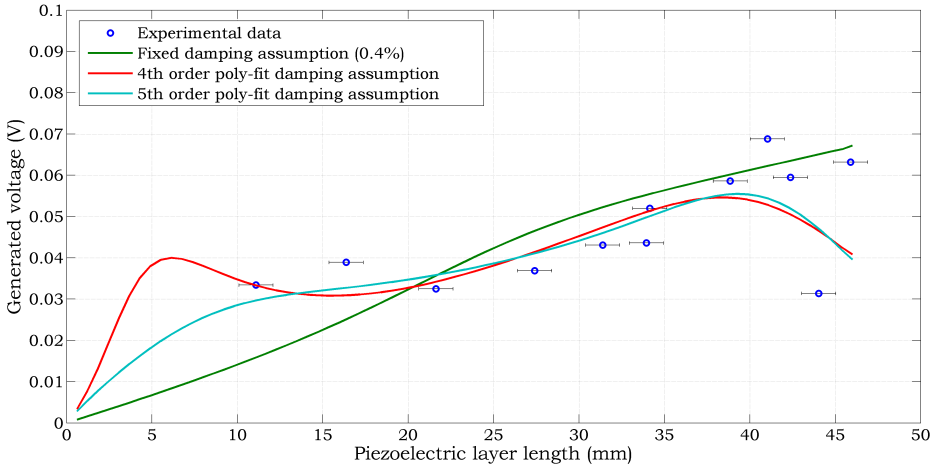

Figure 4.26: Comparison between experimental data and theoretical trends in voltage generated (over a 1 kΩ load) for various length of PZT.

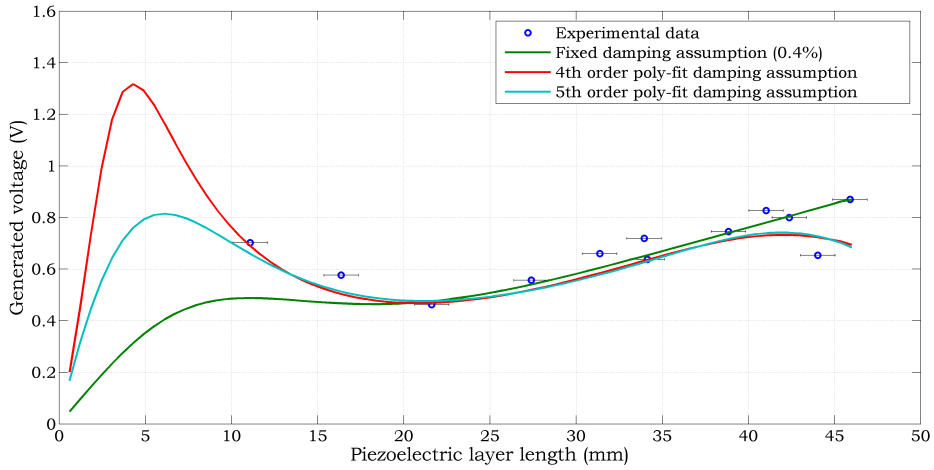

Figure 4.27: Comparison between experimental data and theoretical trends in voltage generated (over a 60 kΩ load) for various length of PZT.

Peak voltages over 1 kΩ and 60 kΩ resistors were obtained for the 12 samples. Trends were also obtained from the theoretical model whilst making three different assumptions in the relationship between mechanical damping and PZT length; namely a fixed 0.004 damping magnitude and a damping magnitude relating to a 4th and 5th order polynomial fit on experimental data. Results for peak voltages can be found in Figures 4.26 and 4.27. Utilising either a 4th or 5th order polynomial fit on experimental damping data provides reasonable agreement between experimental and theoretical peak voltages over the full range of PZT lengths. Figure 4.26 indicates how sensitive the results are to damping magnitude. Peaks and troughs in voltage trends can be superimposed onto troughs and peaks in the damping

trends. Figure 4.27 indicates that samples with shorter PZT layers can outperform the conventional design. This partly results from mechanical damping levels being several orders of magnitude lower in designs with shorter PZT layers.

4.5.3 Mechanical damping and PZT length when using acrylic clamp

In an attempt to overcome the issues with clamping conditions and qualitatively explain how damping is affected by PZT length (reduced from the free end) a new clamp was manufactured solely for the purpose of mechanical damping measurements. The clamp, now made from sheet acrylic, was identical in form to the previous design. The material acrylic was opted for due to its low stiffness properties, reducing risks in fracturing the PZT material while clamping. The batch of samples used in Section 4.5.2 (excluding Samples 2, 3 and 7 due to structural damage sustained in the previous study) were tested twice with results shown in Figure 4.28.

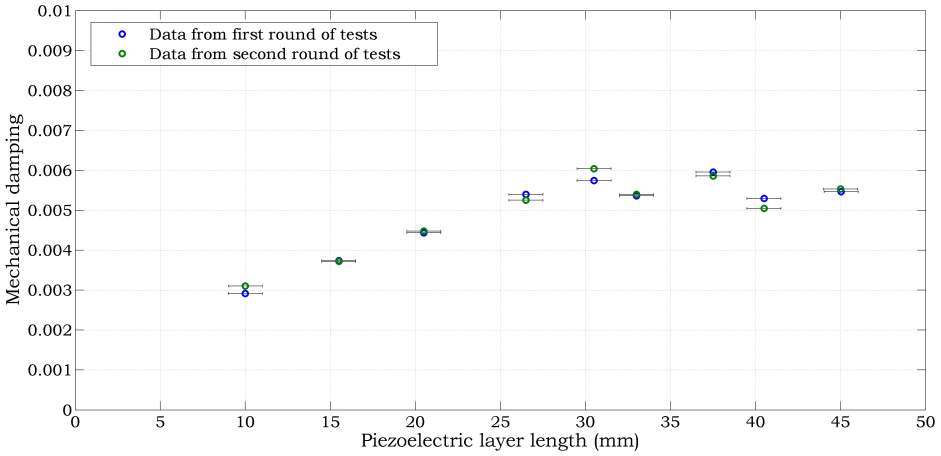

Figure 4.28: Experimental data for mechanical damping while using the acrylic clamp.

Results show that consistency in clamping conditions is improved by using the acrylic clamp with a maximum discrepancy of 0.0003 (4.98%) occurring for Sample 8. A general trend can be seen from the data obtained. At the lower lengths of PZT material (less than half the beam length) damping is seen to reduce linearly with piezoelectric layer length. As the length of piezoelectric material is increased the damping ratio appears to plateau. As has been seen in Section 4.5.2, from both experimental data and theoretical results, harvester

configurations with shortened PZT layers can perform to a similar level as the conventional design, where both substrate and piezoelectric layers are the same length. One key factor for this is the reduced mechanical damping present in shortened PZT configurations; this is due to reduced material volume and epoxy resin which is thought to be a major contributor to the magnitude of mechanical damping. It should also be taken from this testing, that careful consideration ought to be given to the mounting of samples in experimental and practical situations.

4.6 Conclusions

In this chapter, validation of the model derived in Chapter 2 and trends whilst altering the PZT length have been attempted though experimental works. Numerous sample batches comprising of varying PZT lengths were manufactured on site. Through trials of various cutting methods, a silicon carbide disk was decided to be the best option for cutting square PZT sheets into rectangular layers; reasons for this include negligible heat damage to PZT polarisation and even layer edges. The substrate layers, Al, were 50 mm in length with varying lengths of PZT material attached. Bonding was realised through a combination of DP460 and silver conductive epoxy resin.

Initially, individual samples were tested in an attempt to validate the theoretical model with examination of both voltage and tip displacement frequency responses. An excellent agreement with experimental data was achieved for both quantities. In addition to the conventional energy harvester, non-uniform samples also showed good theoretical-experimental agreement. Two batches of samples (comprising of either a 0.67 mm or 0.87 mm substrate layer) were used in this test to verify that the manufacturing technique was reliable.

The next step was to confirm theoretical trends between peak voltage and PZT length with experimental data. Since it has been shown in Chapter 3 that the trend is highly dependent on the load resistance magnitude, experimental data was obtained for 1 kΩ, 60 kΩ and 1 MΩ loads. Firstly, reducing material from the free end was examined. The outcome

showed good theoretical-experimental agreement for sample fundamental frequency indicating suitable reliability of the transfer matrix method model assumption. The results for peak voltage over various load resistances told a rather different story. Neither assumption of proportional damping or fixed damping was adequate for matching voltage data over the full PZT length range. This was due to the existence of large discrepancies between theoretical damping assumptions and the experimental trend between mechanical damping and PZT length. When reduction of PZT material from the cantilever clamped end was examined, theoretical-experimental matching for the peak voltage trends, when assuming a fixed damping, was much better. The reason for this was a rather constant relationship between mechanical damping and PZT length. It can be confirmed however that proportional damping is not an ideal assumption when it comes to making changes to geometrical parameters.

Further work was performed on how various factors affect the mechanical damping ratio. It was seen that beam width does affect the damping magnitude, most probably due to changes in air damping, but not to the extent which would cause the discrepancies witnessed during initial testing. The most important factor was mounting of the cantilever – the clamp itself. Samples were inserted in the clamp and measurements on the damping magnitude made, then samples were retested several times in order to gauge any variation in results. Large variations were seen in mechanical damping measurements for identical samples (0.0027 or 32.1% for one of the samples) and hence it was concluded that the clamping procedure was not consistent. An acrylic clamp was manufactured to provide more consistency between runs for more control on the clamping force applied to samples. Due to the lower material stiffness of acrylic, tightening could be undertaken with less risk to PZT damage. The trend showed that damping increases linearly with PZT length until approximately 66% of the substrate layer is covered thereafter plateauing off for longer PZT lengths. This is evidently beneficial for samples comprising of shorter PZT lengths with performance, in terms of peak generated voltage, exceeding the conventional design. Note, full correction of the clamping issue is not in the scope of these works but can be achieved by using, for example, a transducer to monitor clamping force or torque wrench to monitor torque applied to the clamping bolts.

Power levels output from vibrational energy harvesters are considered rather on the low side in providing for wireless sensor requirements. In addition the majority of practical application situations have intermittent vibrational energy present to harvest with the possibility of energy not being available when required. The inclusion of an energy storage medium, i.e. a capacitor, is therefore advisable. This more realistic scenario will be considered in the next chapter – a theoretical model is created followed by experimental validation and further parametric studies.

CHAPTER 5

STORAGE OF ENERGY CREATED BY ENERGY HARVESTERS

5.1 Introduction

In previous chapters the aim was to develop and validate an analytical model to predict the performance of uniform and non-uniform rectangular cantilever piezoelectric energy harvesters attached to an electrical load, represented by a resistor. Several issues are known to be associated with this type of setup. The low energy levels provided by energy harvesters and the intermittent nature of vibrations occurring in possible application scenarios necessitates the requirement of an energy storage medium, see Chapter 1 for further literature related information.

This chapter is targeted at scenarios where an energy harvester is connected to a capacitor as the means to store energy. A theoretical model is developed in SIMULINK® [59] which predicts the behaviour of such a system in terms of both mechanical and electrical aspects. The transfer matrix method, introduced in Chapter 2, to estimate mechanical behaviour of the cantilever, i.e. fundamental frequency and mode shape, is also used in conjunction with the SIMULINK® model. To represent practical situations more closely, a resistor is included in parallel with the storage capacitor. Inclusion of the resistor is to accommodate losses in electrical components such as diodes. In this case, the advantage of

a SIMULINK® [59] model over an analytical expression is that more complicated electrical circuitry can readily be supplemented to the base model presented here. Note, however, that this is not with the scope of this thesis.

The chapter is laid out as follows. Firstly, the modelling is presented, which includes both a basic analytical model for an energy harvester connected to a storage capacitor (via a diode bridge for rectification) and a base SIMULINK® model for piezoelectric harvesters connected to more complex electrical circuitry. The SIMULINK® model is then used to perform several parametric studies on how topology of an energy harvester effects the performance of devices connected in this electrical scenario. Three of the designs tested in Chapter 3 are again revisited here with the experimental matrix in Table 5.1 outlining parameters which are altered for each case.

Table 5.1: Table outlining parameter changes to be made for each individual case study, see also Chapter 3.

	Case study 1	Case study 2	Case study 3
Piezoelectric layer length	✓	✓	✓
Piezoelectric layer width	✓		
Piezoelectric layer thickness		✓	
Substrate layer thickness		✓	

The final section in this chapter will address the validation of the developed SIMULINK® model through experimental work. The samples used during this study are again manufactured in-house with the manufacturing process detailed in Chapter 4. Once the validation of the theoretical model has been completed, for both uniform and non-uniform samples, voltage trends are obtained for a batch of manufactured samples. Here the aim is to obtain experimental trends for maximum voltage across the storage capacitor against length (altered from either the free or clamped end) and compare with those obtained from the theoretical model. Performance enhancements are expected from topology alterations after observing such outcomes while previously examining the performance of an energy har-

vester connected to a load resistor, see Chapter3.

5.2 Modelling of an energy harvester connected to a storage capacitor

In the following sections, details behind the modelling of an energy harvester connected to a storage capacitor are presented. Initially an analytical model is developed with the assumption that no losses occur in the electrical system. Following this, a more robust SIMULINK® model is developed which takes electrical losses into consideration, for example in the diodes, through the inclusion of a resistor in parallel with the storage capacitor. Analytical modelling for lossless scenarios is readily available in literature with one example provided by Jian-Hui *et al.* [43].

5.2.1 Analytical model

In this section equations governing the mechanical and electrical behaviour of a system allowing for the storage of energy generated by a piezoelectric vibrational energy harvester are developed. The complete system comprises of an energy harvester, diode bridge for full-wave rectification and a means of energy storage, in this case a capacitor, see Figure 5.1.

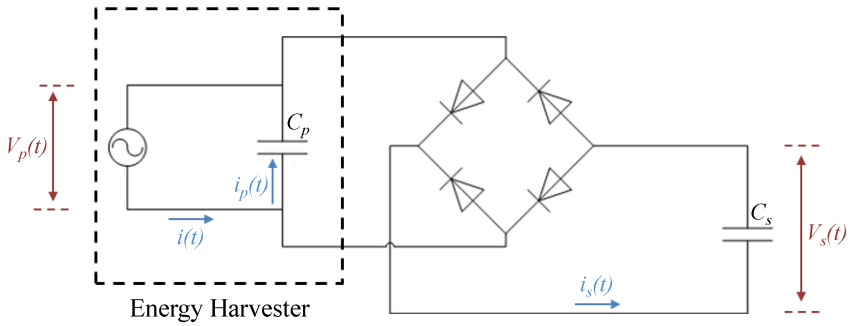

Figure 5.1: Schematic of the charging circuit.

The energy harvester is represented as a current source in parallel with a capacitor,

C_p, with the magnitude of current, $i(t)$, obtained from Equation (2.35) in Chapter 2:

$$i(t) = -E_p d_{31} t_{pc} b_p \left[\frac{\partial W_1(x)}{\partial x}\right]_{x_1}^{x_1+x_2} \dot{\eta}_q(t) \ . \tag{5.1}$$

Recall, performing the analysis with the fundamental mode alone is sufficient due to the frequency of excitation being in close proximity to the fundamental frequency. Equation (5.1) requires the magnitude of the time derivative of the modal co-ordinate, $\dot{\eta}_q(t)$, which can be obtained from solving the following second order differential equation (Equation (2.40)):

$$\ddot{\eta_1}(t) + 2\gamma_1\omega_1\dot{\eta_1}(t) + {\omega_1}^2\eta_1(t) = \Big(Q_1 - R_1 V_p(t)\Big)\mathrm{e}^{\mathrm{i}\omega t} \ , \tag{5.2}$$

with terms such as mechanical forcing, Q_1, and electro-mechanical coupling, R_1, and all other variables previously defined in Chapter 2. Note, the assumption that the harvester is subjected to harmonic base excitation at a frequency of ω rad.s^{-1} remains.

The behaviour of the circuit shown in Figure 5.1, in terms of current and capacitor magnitudes, can be described using the following equations, also see [43], dependant on whether the diode bridge is conducting $\big(V_p(t) \geq V_s(t) + 2V_{th}\big)$ or not $\big(V_p(t) < V_s(t) + 2V_{th}\big)$:

$$i_p(t) = \begin{cases} i(t) & \text{for} \quad V_p(t) < V_s(t) + 2V_{th} \\ i(t)\dfrac{C_p}{C_s + C_p} & \text{for} \quad V_p(t) \geq V_s(t) + 2V_{th} \end{cases} \ , \tag{5.3}$$

$$i_s(t) = \begin{cases} 0 & \text{for} \quad V_p(t) < V_s(t) + 2V_{th} \\ i(t)\dfrac{C_s}{C_s + C_p} & \text{for} \quad V_p(t) \geq V_s(t) + 2V_{th} \end{cases} \ , \tag{5.4}$$

where V_{th} is the diode threshold voltage and C_s is the storage capacitance. i is the current generated by the piezoelectric material, i_p and i_s represent the current flowing through C_p and C_s respectively. V_p is the voltage across the piezoelectric material and V_s is the voltage across the storage capacitor. V_p and V_s are obtained by solving the following first order

differential equations:

$$\dot{V}_p(t) = i_p(t)/C_p \ , \tag{5.5}$$

$$\dot{V}_s(t) = i_s(t)/C_s \ . \tag{5.6}$$

The above set of differential equations, Equations (5.2), (5.5) and (5.6), can be expressed in state-space form allowing the implementation of a MATLAB® [55] ordinary differential equation solver, for example ode45, to obtain the mechanical and electrical behaviour of the system – η, $\dot{\eta}$, V_p and V_s:

$$\begin{bmatrix} \dot{\eta} \\ \ddot{\eta} \\ \dot{V}_p \\ \dot{V}_s \end{bmatrix} = \begin{bmatrix} 0 & 1 & 0 & 0 \\ -{\omega_1}^2 & -2\gamma_1\omega_1 & -R_1 & 0 \\ 0 & 0 & 0 & 0 \\ 0 & 0 & 0 & 0 \end{bmatrix} \begin{bmatrix} \eta \\ \dot{\eta} \\ V_p \\ V_s \end{bmatrix} + \begin{bmatrix} 0 & 0 & 0 \\ Q_1 & 0 & 0 \\ 0 & 1/C_p & 0 \\ 0 & 0 & 1/C_s \end{bmatrix} \begin{bmatrix} \mathrm{e}^{\mathrm{i}\omega t} \\ i_p \\ i_s \end{bmatrix} . \tag{5.7}$$

Although Equation (5.7) provides a means of approximating the behaviour of a piezoelectric energy harvester connected to a storage capacitor, it is not a true representation since electrical losses are experienced in practical situations, for example in circuit components such as diodes. The accommodation of these losses is realised by the addition of a resistor, R_{losses}, in parallel with the storage capacitor, C_s. Due to the increased complexity of electrical equations, which is furthered if more electrical components are included, modelling in SIMULINK® [59] is preferred.

5.2.2 Modelling with SIMULINK®

In this section SIMULINK® [59] is utilised to model the overall electromechanical behaviour of an energy harvester connected to a storage capacitor in parallel with a resistor representing losses. A delay has also been implemented in the model which allows a time lag between applying excitation to the harvester and connection of the harvester to the electrical circuitry; this will be useful during model validation with experimental works. The

mechanical and electrical subsystems are both built using components from Simscape [58] and SimElectronics [56] libraries and coupled together allowing for the electromechanical coupling, and its effects, to remain. By using the presented model as a starting point one could readily expand the electrical circuit on the storage capacitor side to include more sophisticated and practical circuitry – not in the scope of this work. Information regarding such circuits, i.e. synchronous charge extraction, was provided in Chapter 1.

5.2.2.1 Term definitions required as inputs for the SIMULINK® model

Some variables and constants which will appear in the SIMULINK® model are herein defined

$$\text{'xk'} \quad \longrightarrow \quad {\omega_1}^2 \,, \tag{5.8}$$

$$\text{'xc'} \quad \longrightarrow \quad 2\gamma_1 {\omega_1}^2 \,, \tag{5.9}$$

$$\text{'psi'} \quad \longrightarrow \quad -E_p d_{31} t_{pc} b_p \left[\frac{\partial W_1(x)}{\partial x} \right]_{x_1}^{x_1+x_2} \,. \tag{5.10}$$

5.2.2.2 Coupled mechanical and electrical systems of the SIMULINK® model

In this section the SIMULINK® models developed to generate theoretical results are presented to the reader. Figure 5.2 shows the implementation of coupling between mechanical and electrical subsystems. The excitation, in this case mechanical forcing from base motion, Q_1, and the voltage across the piezoelectric material, V_p, is fed into the mechanical subsystem. The delay, if necessary, is realised by means of a switch which disengages the electrical subsystem until desired time has elapsed. Inputs to the electrical system include current generated by the energy harvester, see Equation (5.1), and the magnitude of the additional resistor, R_{losses}. Figure 5.3 shows the mechanical subsystem and requires predefined terms 'xk', 'xc', and electro-mechanical coupling, R_1. Figure 5.4 shows the electrical subsystem and requires predefined terms for piezoelectric and storage capacitance, C_p and C_s respectively. Exponential diode models [57] are used with a saturation current of $1{\times}10^{-14}$ A.

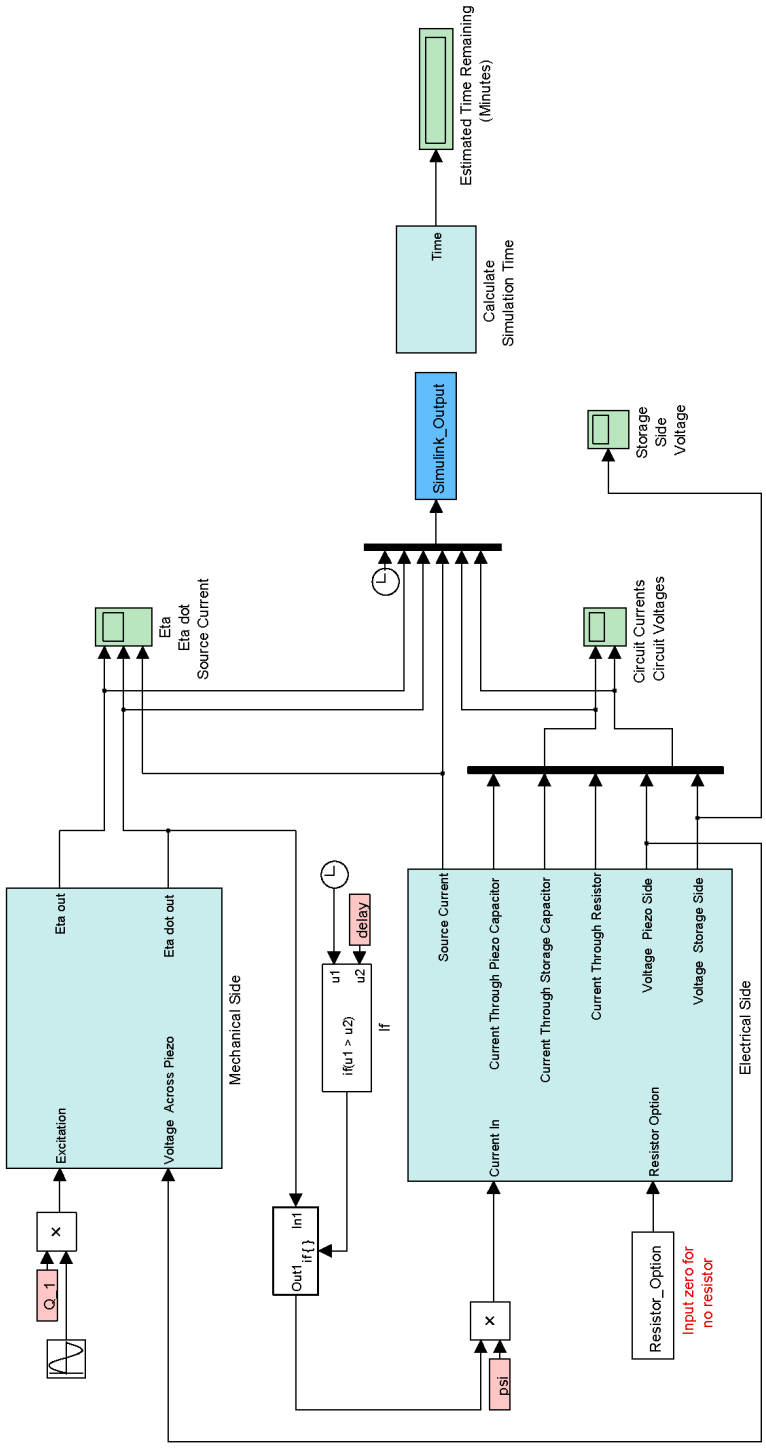

Figure 5.2: The overall SIMULINK® model with individual, but coupled, mechanical and electrical subsystems.

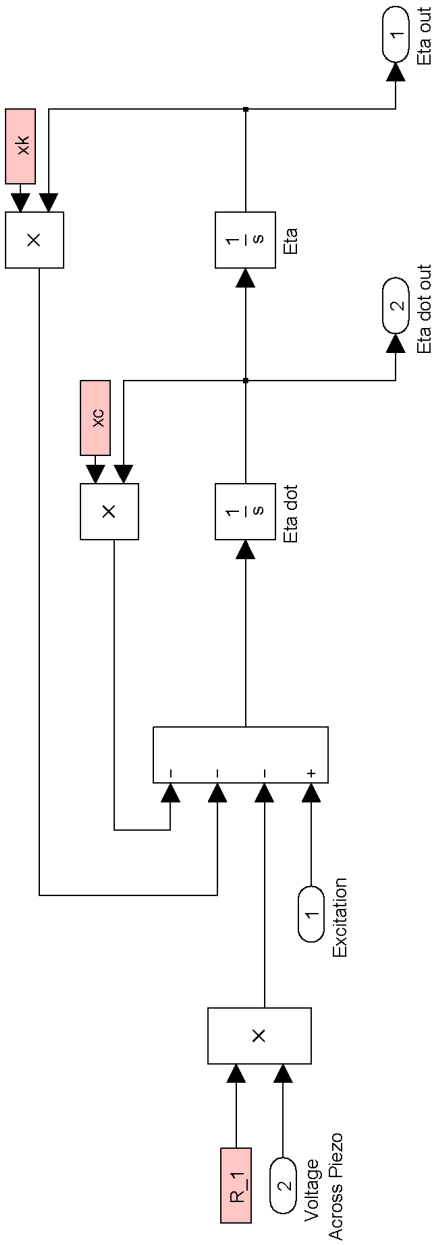

Figure 5.3: SIMULINK® model for the mechanical subsystem.

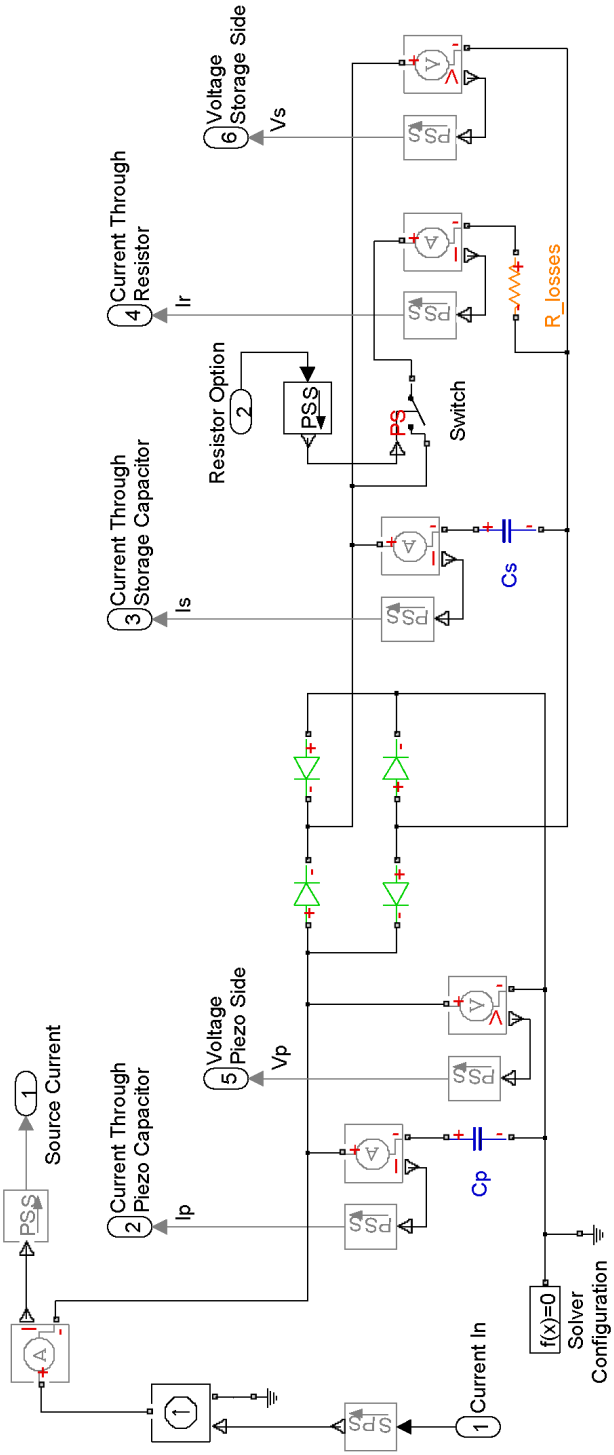

Figure 5.4: SIMULINK® model for the electrical subsystem.

5.3 Parametric studies whilst energy harvester connected to storage capacitor

In this section the effects of how geometrical parameter changes affect the performance capabilities of an energy harvester in the storage of energy scenario are investigated. This is achieved through the use of SIMULINK® models (Figure 5.2-5.4) shown in Section 5.2.2 with the required frequencies and mode shapes obtained from the transfer matrix model, see Chapter 2. The three cases previously examined in Chapter 3 are again used here – a macro-scale device (Case Study 1 in Table 3.1), a micro-scale device (Case Study 2) and a thin film flexible device (Case Study 3). The capacitor size in which energy is stored, for all cases, will remain fixed at 1 μF and a 1 s delay before the start of charging is implemented in-order to allow for the initial transient period. The choice of capacitor size was determined by considering the simulation speed with a 1 μF capacitor allowing for reasonable charging times so that wide ranges of parametric studies can be completed. The charging of a larger capacitor is also briefly investigated during the final case study. A 3 MΩ load resistor is included in the electrical circuit to accommodate losses in the system. Note this value was obtained during the experimental testing of one energy harvester sample, see Section 5.4.2 for further details.

5.3.1 Macro-scaled energy harvester

The dimensions and material properties of the macro-scale device were previously presented in Chapter 3 but are repeated here in Table 5.2 for the convenience of the reader. Recall the choices of material properties and overall structure dimensions in relation to the samples manufactured for experimental validation.

The voltage drop across the diode bridge is approximately 0.8 V which must be exceeded by the energy harvester in-order for energy to be stored in the storage capacitor. For this reason rather than applying a base acceleration of 0.5 m.s^{-2}, as was the case in Chapter 3, an acceleration of 0.75 m.s^{-2} is applied to the energy harvester configurations. It was shown previously in Chapter 4 that the magnitude of mechanical damping has a significant

Table 5.2: Structural dimensions, and mechanical and electrical properties of the conventional harvester used throughout this analysis (Note this design does not include a tip mass), also see Table 3.2

Parameter	Value
Substrate (Al) length (mm)	50
Substrate (Al) width (mm)	5
Substrate (Al) thickness (mm)	0.67
PZT layer length (mm)	50
PZT layer width (mm)	5
PZT layer thickness (mm)	0.5
Young's modulus of Al (GPa)	69
Density of Al (kg.m^{-3})	2700
Young's modulus of PZT (GPa)	62.1
Density of PZT (kg.m^{-3})	7800
Piezoelectric constant, d_{31} (m.V^{-1})	-180$\times 10^{-12}$
Permittivity, ε_{33}^{S} (F.m^{-1})	1.549$\times 10^{-8}$

effect on the trends between geometrical parameter changes and energy harvester performance. Several assumptions are utilised here to represent changes in mechanical damping with geometrical parameters. From extensive experimental work it was observed that either reducing the length of piezoelectric material, increasing the thickness of layers, or reducing the width of layers would generally cause a reduction in mechanical damping. During the following geometric changes it will be assumed this is a linear relation with damping linearly varying from 0.007 to 0.002 for a sweep of the parameter under investigation. The first geometric parameter which is altered is the length of the piezoelectric layer.

5.3.1.1 Length of piezoelectric layer

The piezoelectric material length is here reduced from the clamped end, i.e. both substrate and piezoelectric layer remain coincident at the free end. Figure 5.5 shows the maximum voltage across the storage capacitor while the piezoelectric length is swept from 1 mm to 50 mm in increments of 1 mm. Note, all harvester configurations are excited at their unique open circuit resonant frequency not the undamped natural frequency. Due to the shift in resonant frequency with electrical load, see Chapter 3, excitation at the undamped natural frequency does not provide optimum conditions for maximum voltage generation from the

energy harvester.

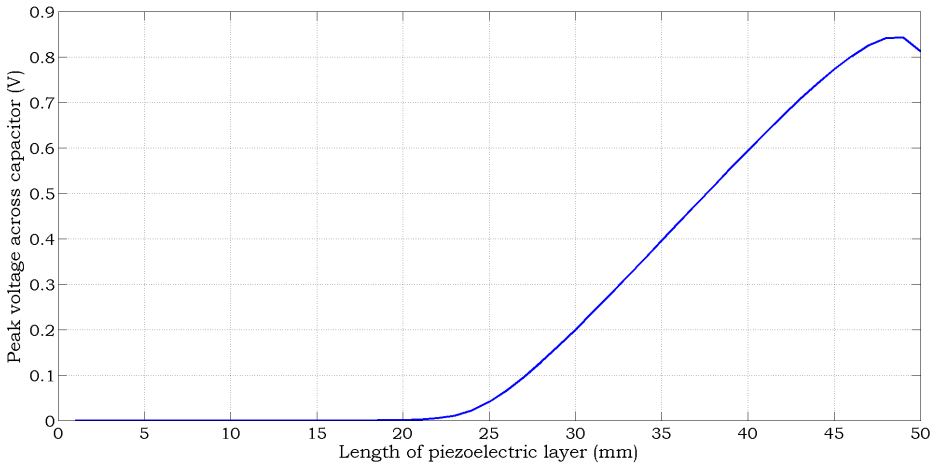

Figure 5.5: Voltage across a storage capacitor for harvester configurations with varying piezoelectric material length. Both layers remain coincident at the free end.

Figure 5.5 shows that the peak voltage across a storage capacitor is zero for configurations with piezoelectric material length below approximately 20 mm and that the peak voltage gradually increases for lengths above 20 mm. The trend can be explained once the effects of piezoelectric layer length on the mechanical forcing, Q, and electro-mechanical coupling, ψ, are examined, see Figure 5.6.

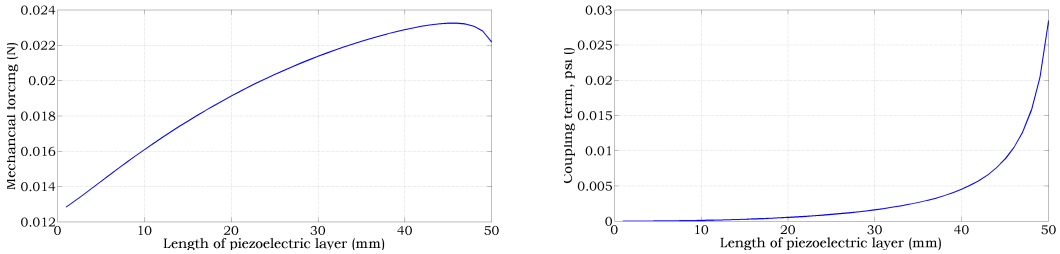

(a) Mechanical forcing (b) Electro-mechanical coupling

Figure 5.6: Effects of piezoelectric material length on equation variables. Both layers remain coincident at the free end.

Figure 5.6(a) shows that the mechanical forcing increases with piezoelectric material length, peaking at 46 mm, followed by a reduction. This is responsible for the maximum voltage occurring when the piezoelectric layer length does not fully cover the substrate layer. The general reduction in ψ and Q with piezoelectric layer length governs the general trend seen in Figure 5.5. For lengths shorter than 20 mm, the voltage generated by the energy harvester is not large enough to overcome the voltage drop across the diode bridge and so

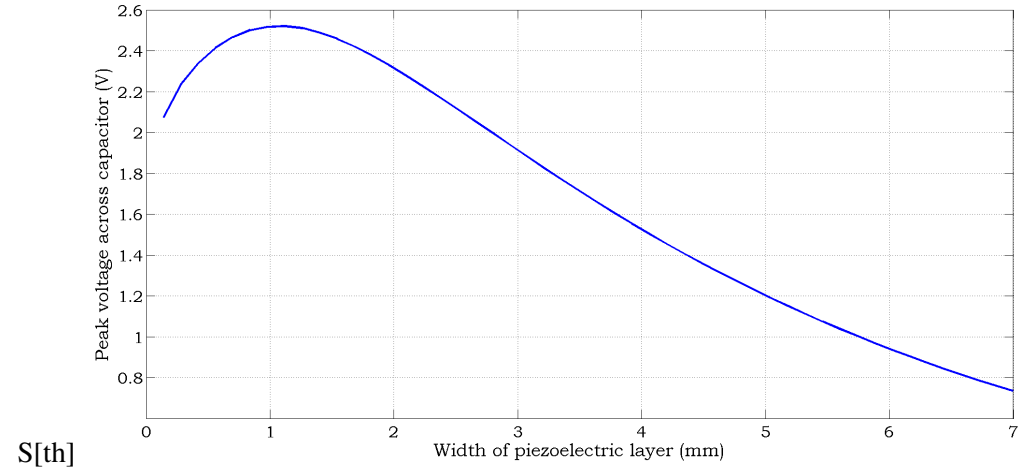

S[th]

Figure 5.7: Voltage across a storage capacitor for harvester configurations with varying piezoelectric material width.

charging of the storage capacitor does not occur. In this particular case, a configuration comprising of a 48 mm long piezoelectric layer provides a peak voltage of 0.84 V across the storage capacitor. This study indicates energy harvester designs which optimise solely Q and ψ are preferred, but it will be shown in later sections that this is not necessarily the case.

5.3.1.2 Width of piezoelectric layer

In this section the effects of piezoelectric layer width on voltage across a storage capacitor are examined. The piezoelectric layer remains centre aligned with the substrate layer (width of 5 mm) and its width is increased incrementally until there is a 1 mm overhang on either side of the substrate layer. Figure 5.7 shows that the conventional design with both layers being of equal width (5 mm) is not an optimum design whereas, in this particular case, manufacturing a device with a width of approximately 1.2 mm generates maximum voltage across the storage capacitor. Numerically, the performance increases by 112% – from 1.19 V for the conventional design to 2.52 V for the optimised design.

This observation cannot be explained by solely examining the effects of geometrical parameter changes on mechanical forcing, Q, and electro-mechanical coupling, ψ, as be-

fore. Increasing the piezoelectric layer width was seen to be beneficial both in terms of Q and ψ during simulations which indicates the wider the piezoelectric layer the better the design. The changes in magnitude of two other variables also need consideration here, namely the mechanical damping ratio and the piezoelectric layer capacitance, see Figure 5.8. Both variables (damping due to the assumption made) reduce with material width and this is beneficial for the current generated by the energy harvester. This one example indicates the complexity in optimising an energy harvester from only equation variables. The magnitude by which all variables change in correspondence to geometrical parameter changes and in relation to each other help determine an optimum configuration and for this reason each case of optimisation must be considered individually.

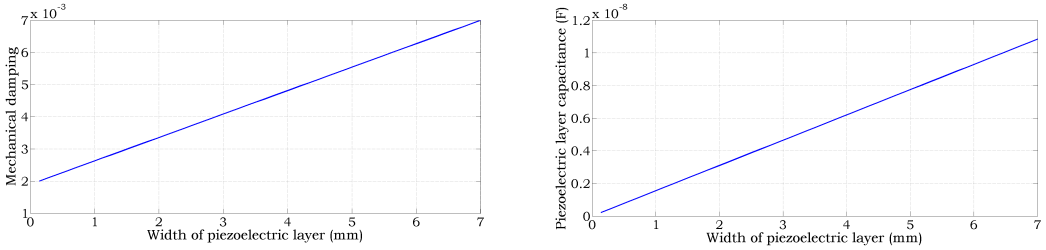

(a) Mechanical damping ratio

(b) Piezoelectric layer capacitance

Figure 5.8: Effects of piezoelectric material width on equation variables.

5.3.2 MEMS-scale energy harvester

In this section the effects of geometric parameters on a MEMS-scale device are examined. Material properties and dimensions are provided in Table 5.3. The resistance magnitude for the losses and the introduced delay are taken as before. In this case, however, the base acceleration applied to the samples is assumed to be a constant $3g$. In addition to this, the magnitude of mechanical damping will instead be varied linearly from 0.004 to 0.007 during parametric sweeps allowing to examine how mechanical damping variations affect the trends obtained.

Table 5.3: Structural dimensions, and mechanical and electrical properties of the conventional harvester used throughout this analysis.

Parameter	Value
Substrate (Si) length (mm)	2
Substrate (Si) width (mm)	0.6
Substrate (Si) thickness (mm)	0.012
PZT layer length (mm)	2
PZT layer width (mm)	0.6
PZT layer thickness (mm)	0.00164
Young's modulus of Si (GPa)	185
Density of Si (kg.m^{-3})	2329
Young's modulus of PZT (GPa)	66
Density of PZT (kg.m^{-3})	7800
Tip mass length (mm)	0.6
Tip mass width (mm)	0.6
Tip mass thickness (mm)	0.6
Density of tip mass (kg.m^{-3})	8908
Piezoelectric constant, d_{31} (m.V^{-1})	-180$\times 10^{-12}$
Permittivity, ε_{33}^{S} (F.m^{-1})	1.594$\times 10^{-8}$

5.3.2.1 Length of piezoelectric layer

The first parameter under investigation is again the piezoelectric material length. The results obtained by reducing the length from either end are shown in Figure 5.9.

Figure 5.9 shows that reducing the piezoelectric material length from the free end, i.e. both layers remain clamped, is beneficial in terms of increasing the energy stored in a capacitor whereas no benefit is observed while reducing material from the clamped end. The results can be explained by considering effects of material removal on the mechanical damping and the magnitude of the coupling term. Changes in the magnitude of mechanical forcing with piezoelectric material length are negligible for MEMS-scale devices due to contributions from the tip mass eclipsing those from the cantilever structure. From the assumption made, mechanical damping reduces with piezoelectric layer length and so one would expect a greater voltage with reduced material length. However, while examining the magnitude of electro-mechanical coupling one observes a detrimental reduction with material length, see Figure 5.10. Although removal of material from either the clamped

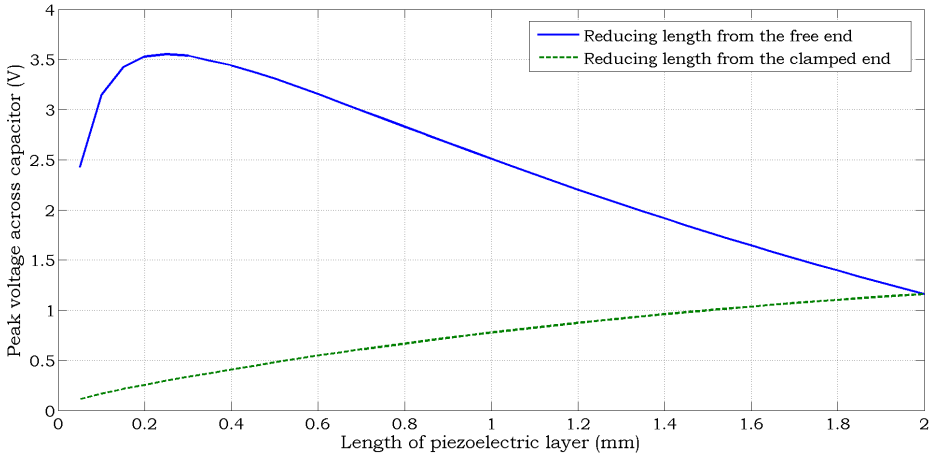

Figure 5.9: Effects of piezoelectric material length on voltage across the storage capacitor.

or free end both cause reductions in the electro-mechanical coupling the magnitude always remains greater for the case where material is removed from the free end of the beam. It is believed that subtle changes and differences in the magnitude of the electro-mechanical coupling parameter is responsible for the different trends obtained. However, a general conclusion can be made – reducing the length of the piezoelectric material from the free end of the beam should be considered when designing piezoelectric energy harvesters for use in such an electrical scenario. Numerically, the benefit observed in this case is a 205% increase in voltage by a configuration comprising of a 0.25 mm long piezoelectric layer in comparison to the conventional design with a piezoelectric layer 2 mm in length.

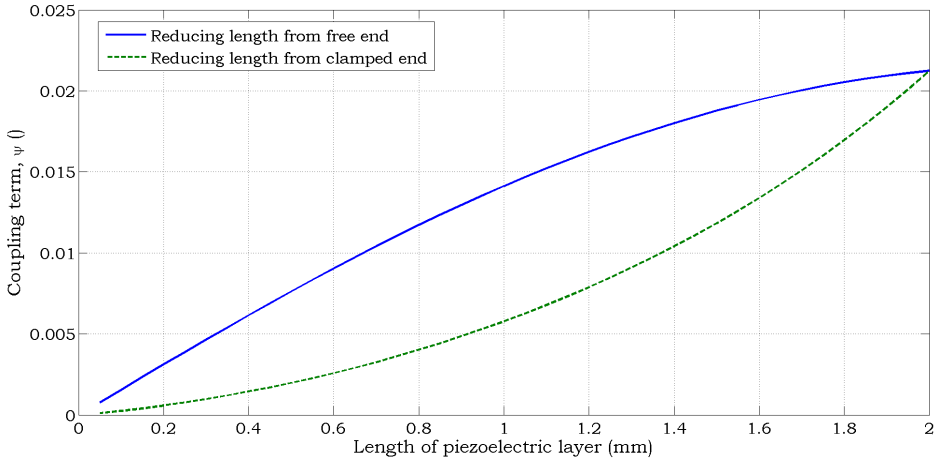

Figure 5.10: Effects of piezoelectric material length on magnitude of electro-mechanical coupling.

5.3.2.2 Thickness of the either substrate or piezoelectric layer

In this subsection the effects of altering either the substrate or piezoelectric layer thickness are discussed briefly; firstly the substrate layer thickness, see Figure 5.11.

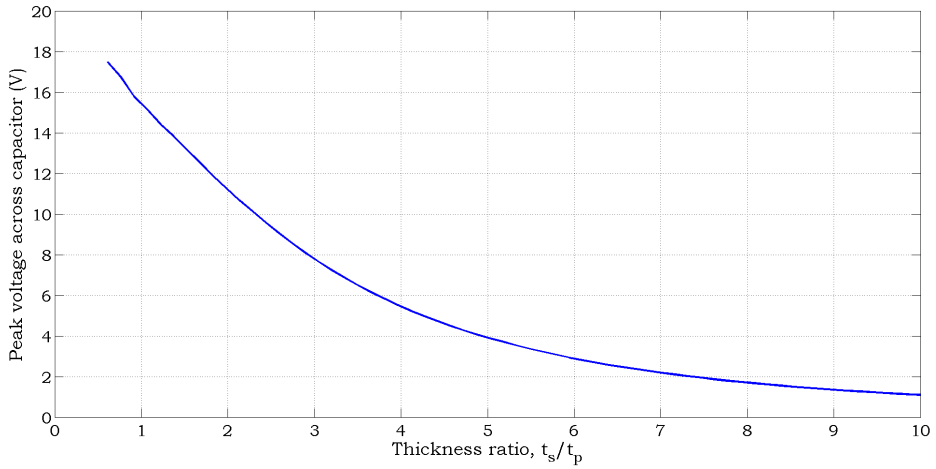

Figure 5.11: Effects of substrate layer thickness on voltage across a 1 μF storage capacitor. Piezoelectric layer thickness remains constant and both layers have identical lengths and widths.

The piezoelectric layer thickness is fixed at 0.00164 mm and the substrate thickness varied from 0.001 mm to 0.0164 mm. Figure 5.11 shows that a thinner substrate layer is beneficial for energy harvester design in terms of maximum voltage across a storage capacitor. The sole reason for this phenomenon being the much lower fundamental frequencies of thinner devices. In practical terms, however, this approach must be applied with caution since thinner devices are, inevitably, more susceptible to failure from increased fragility. In contrast, while altering the piezoelectric layer thickness the theoretical results indicate designs with thicker layers perform better, see Figure 5.12.

The substrate thickness is fixed at 0.012 mm and the piezoelectric layer thickness varied from 0.0001 mm to 0.004 mm. The reason behind improvements in performance with piezoelectric thickness is two fold. Firstly the electro-mechanical coupling term increases with thickness, in the tested range, partly due to the shift in the neutral axis in relation to piezoelectric material location. Secondly, from the assumption made, the magnitude of mechanical damping is reduced in thicker beams. The outlined benefits, in terms of coupling and damping, are also present while increasing the substrate thickness. The fundamental

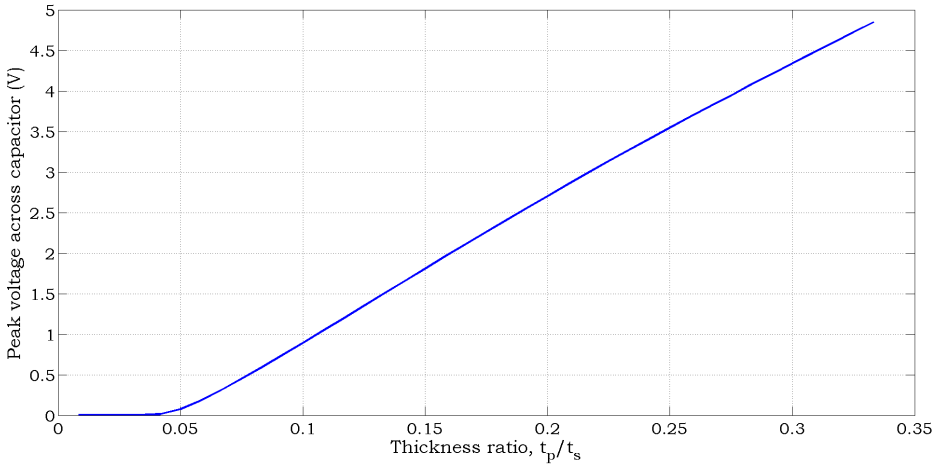

Figure 5.12: Effects of piezoelectric layer thickness on voltage across a 1 μF storage capacitor. Substrate thickness remains constant and both layers have identical lengths and widths.

frequency however does not play as major role in this 'increasing piezoelectric thickness' study as it varies by only 27% over the tested range in comparison to 2000% during the substrate thickness study.

5.3.3 Thin film flexible energy harvester

In this section the optimisation of a thin film flexible device developed at Hiroshima University in Japan [94] to harvest energy from the oceans is undertaken. The dimensions and material properties are provided in Table 5.4. The magnitude of acceleration applied to the samples is fixed at 0.5 m.s^{-2}, a delay of 1 s utilised, and a 3 MΩ resistor included for losses.

Recall from Chapter 3 the restrictions applied in terms of the fundamental frequency for this particular case study. To allow for an impartial comparison between harvester designs one must ensure minimal variation in fundamental frequency. For this reason the thickness of layers will not be altered and only the effects of piezoelectric layer length are examined. Figure 5.13 shows the effects of altering the length of piezoelectric material from either end on the maximum voltage across a 1 μF capacitor.

The results show, for this particular structure size and material combination, that reducing length of piezoelectric material from the clamped end, see green dashed line in

Table 5.4: Structural dimensions, and mechanical and electrical properties of the harvester developed by the group in Hiroshima [94].

Parameter	Value
PET layer length (mm)	100
PET layer width (mm)	20
PET layer thickness (mm)	1
PVDF layer length (mm)	95 [a]
PVDF layer width (mm)	10
PVDF layer thickness (mm)	0.04
Young's modulus of PET (GPa)	3.1 [b]
Density of PET (kg.m^{-3})	1400 [b]
Young's modulus of PVDF (GPa)	8.3 [c]
Density of PVDF (kg.m^{-3})	1780 [c]
Piezoelectric constant, d_{31} (m.V^{-1})	22×10^{-12} [c]
Permittivity, ε_{33}^{S} (F.m^{-1})	1.063×10^{-10} [c]

[a] One end of piezo remains coincident with clamped end.
[b] Material property for PET obtained from [102].
[c] Material property for PVDF obtained from [75].

Figure 5.13, is not beneficial to performance. A maximum voltage of 3.8 V can be stored if using the conventional design consisting of a 100 mm piezoelectric layer. If, however, one was to reduce material length from the free end an improvement in performance is realised as a result of the factors outlined previously. Numerically, subjected to the assumption made in mechanical damping variations, a maximum voltage of 6.4 V can be generated by a harvester with a 32 mm piezoelectric layer in comparison to the conventional design; this equates to a 67.7% increase. The mechanical damping was assumed to decrease linearly from 0.007 at 100 mm length to 0.002 at 0 mm length. The reduction in mechanical damping between the optimal and conventional design is 94%.

It is worthwhile to also consider the time taken to reach maximum charge. Figure 5.14 shows the time history while charging a 1 μF capacitor by both the optimal and conventional designs. The time taken to reach the respective maximum voltage for conventional and optimum designs is 9.3 s and 14.4 s. Although this 55% increase in time taken exists, it is evident from the charging profiles, Figure 5.14, that over the majority of the time span, stored energy is greater when connecting the optimum design in place of the conventional design. It was important to consider these charging profiles since benefits in maximum

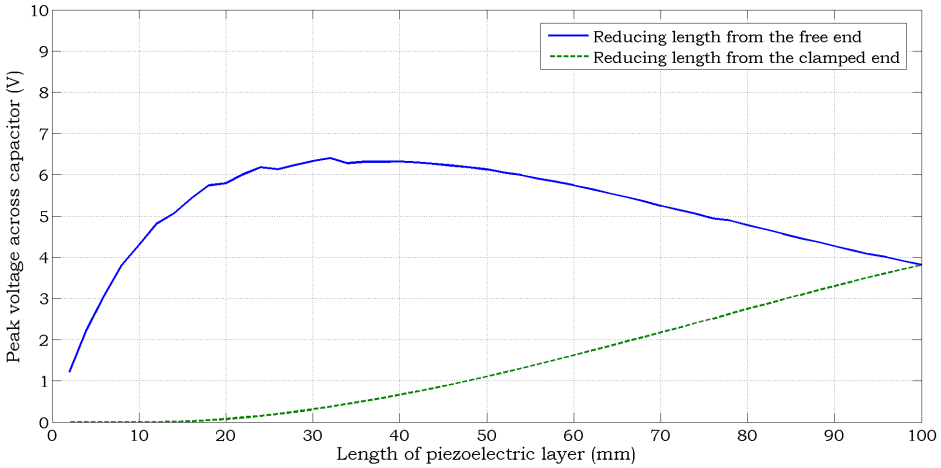

Figure 5.13: Plots showing the effects of removing piezoelectric material from either the free end or clamped end on the maximum voltage across a storage capacitor.

energy stored may have been countered by the increased time taken to reach peak energy level. In this particular study this was found not to be the case, however, the occurrence of such an issue for other harvester sizes/compositions should not be overlooked.

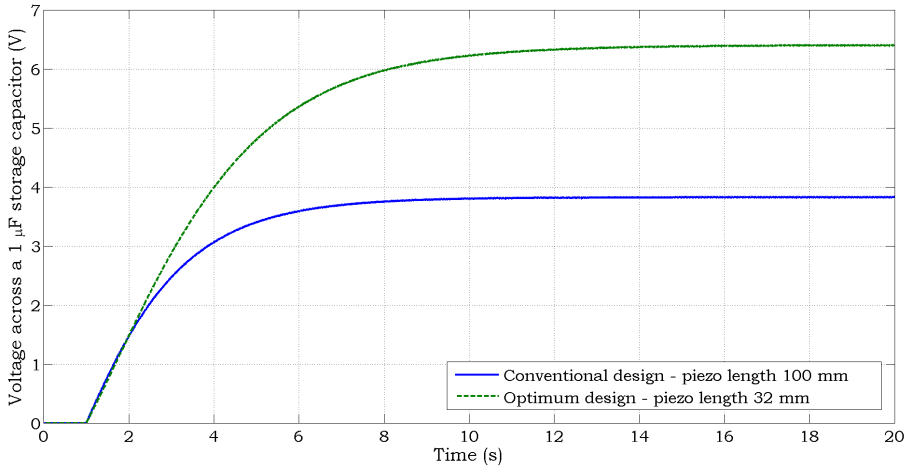

Figure 5.14: The charging profiles of two energy harvester designs.

5.3.3.1 Connecting harvester configurations to larger storage capacitor

It is also worth examining whether the size of the storage capacitor affects the trends obtained: a study is undertaken here by using a 1 mF capacitor. A configuration with varying piezoelectric material length is simulated, ensuring both layers remain clamped, and the

voltage across the storage capacitor after 5 minutes of charging is recorded. Note, this period of time is not enough to fully charge the capacitor. However, a situation where 5 minutes of charging occurs before the stored energy is required is hypothesized. Figure 5.15 shows the variation in voltage after 5 minutes of charging for various lengths of piezoelectric material.

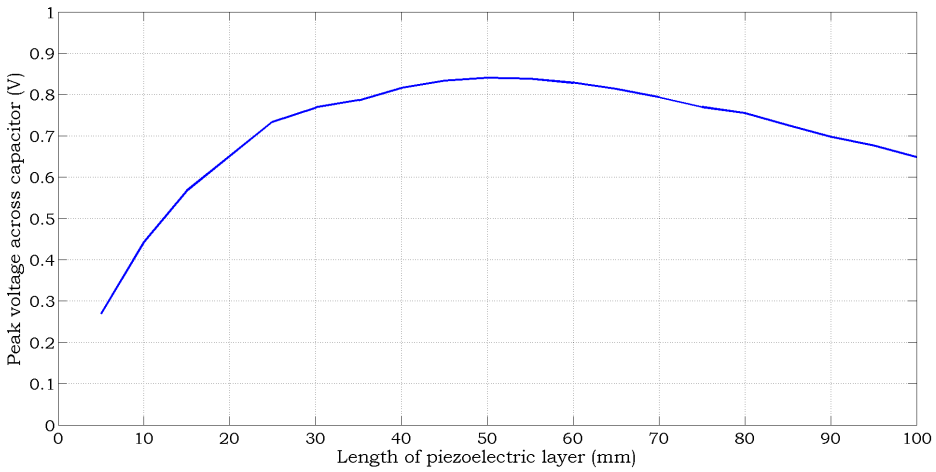

Figure 5.15: Plots showing the effects of piezoelectric material length, when both layers remain clamped, on the voltage across a 1 mF storage capacitor after 5 minutes of charging.

The results show a similar trend to the one seen when fully charging the 1 μF capacitor with the optimum design comprising of piezoelectric material with reduced length. In this particular scenario a 30% improvement in performance is achievable, in comparison to the conventional design, for a harvester configuration consisting of a 50 mm piezoelectric layer. The previous optimum design, comprising of a 32 mm piezoelectric layer, also provides an advantage over the conventional design in this scenario – numerically there exists a 21% increase in the energy stored. From these few case studies it is evident that vast improvements in performance are achievable when careful consideration is given to the topology of the piezoelectric layer particularly in terms of its length from the clamped end of the beam.

5.4 Validation of the SIMULINK® model through experimental work

In the following sections the results obtained using the theoretical model for charging a capacitor are compared with experimental measurements, for the purpose of validation. This is initially performed on individual samples and then experimental trends while varying the length of the piezoelectric layer from either end are presented and explained.

5.4.1 Experimental setup and procedure

The apparatus and experimental setup is similar to that previously used to validate the theoretical model in which an energy harvester is connected to a load resistor, see Chapter 4 – the resistor naturally being replaced with a diode bridge and a capacitor, see Figure 5.16.

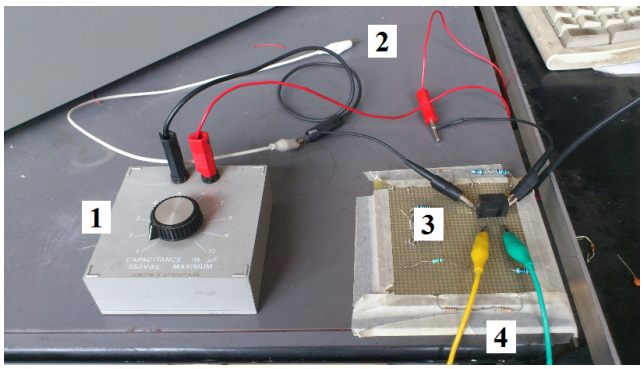

Figure 5.16: Setup of electrical aspect of system. (1) Variable capacitor, (2) Wire to discharge capacitor before data collection begins, (3) Diode bridge, (4) Leads from energy harvester.

The experimental procedure is as follows:

(1) Firstly, the fundamental frequency must be obtained as this will be used for excitation while charging. This is achieved by performing a frequency sweep on the sample under investigation, in open circuit conditions, and measuring tip velocity with the laser vibrometer.

(2) The frequency at which peak velocity occurs is recorded as this will be used as the excitation frequency while charging the capacitor.

(3) The sample is then connected to the electrical circuit containing a diode bridge and a

storage capacitor. A sinusoidal signal at the previously found excitation frequency is applied to the shaker and the system is given a few seconds to reach steady state.

(4) An electrical contact is made between the capacitor terminals thereby discharging it and preventing charging from occurring. A time history recording of the dynamic signal analyser is started and the electrical contact between the capacitor terminals removed allowing charging to occur. The time history data saved includes the voltage across the storage capacitor and the base acceleration experienced by the sample. This acceleration is controlled, between tests, to a reasonable extent, $\pm 1\%$, ensuring a fair comparisons between samples.

(5) Lastly, the energy harvester is removed from any electrical circuitry, connected in closed circuit conditions and a frequency response function of the tip displacement obtained in-order to extract the mechanical damping ratio.

The following section describes and interprets results for two energy harvester samples.

5.4.2 Validation of uniform and non-uniform energy harvesters

The results initially presented are for a conventional sample where both layers have the same length. The sample is made up of a 47.5 mm $\times$ 7 mm $\times$ 0.67 mm Al layer and a 47.5 mm $\times$ 7 mm $\times$ 0.5 mm PZT layer. Material properties can be found in Table 5.2. The magnitude of the capacitor used during experimental data collection was 1 μF and the measured base acceleration was approximately 0.9 m.s^{-2}. Figure 5.17 shows preliminary attempts at theoretical model validation. Blue circles represent data obtained from the experiment with green and red lines representing data from the theoretical model. Experimental-theoretical matching requires slight manipulation, and variables such as mechanical damping and the resistor representing losses in the theoretical model require adjustment. The green line shows data from when losses in the system are ignored and results in a clear conclusion that this assumption is invalid. Time taken to achieve steady state is over estimated if losses are not taken into consideration in the theoretical model. In this particular case, through trial

and error, the inclusion of a 3 MΩ resistor was sufficient to represent such losses, see red line in Figure 5.17.

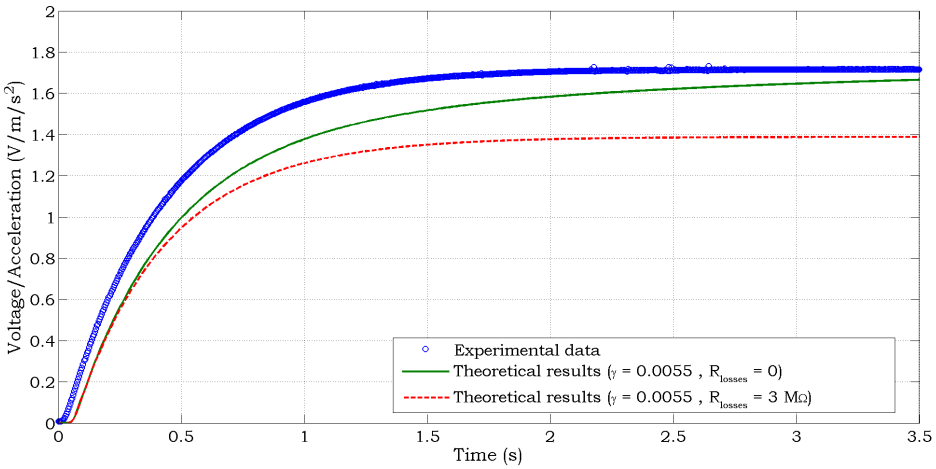

Figure 5.17: Initial attempts to validate the theoretical model with experimental data for a conventional energy harvester.

The next step is to adjust the theoretical results in relation to an accurate magnitude of mechanical damping. From the closed circuit frequency response plot of tip displacement, using the half power point method [80], this was estimated as 0.0048. The green line in Figure 5.18 shows theoretical results utilising this information along with the previously included resistor for losses. The last step is to remove the transient period from the theoretical simulation which introduces a slight time lag as seen in Figure 5.18 more closely resembling experimental conditions. This is accomplished by introducing a 1 s delay before charging of the capacitor begins in the theoretical simulation, see red line in Figure 5.18. After accommodation of the necessary factors outlined above good agreement between experimental data and the developed theoretical model is obtained in terms of predicting both time to steady state and the maximum voltage across the storage capacitor.

Validation for a non-uniform sample was also attempted using the procedure outlined above. The sample, comprising of a 45.5 mm × 7 mm × 0.67 mm Al layer and a 17.88 mm × 7 mm × 0.5 mm PZT layer, was mounted with both layers clamped. Material properties can again be found in Table 5.2. The final comparison plot between theoretical simulation and experimental data is provided in Figure 5.19. A delay of 1 s in the theoretical model was again introduced with damping and the resistor for losses set to 0.0031 and 1.5 MΩ

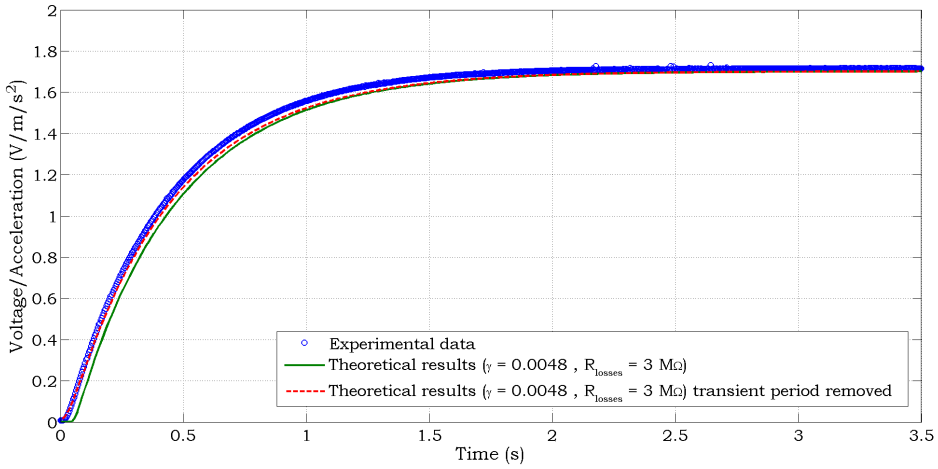

Figure 5.18: Final attempts to validate the theoretical model with experimental data for a conventional energy harvester.

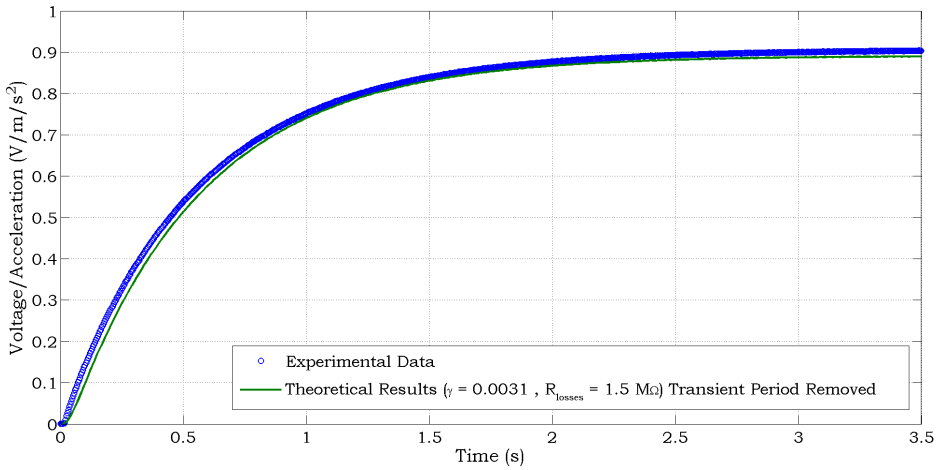

Figure 5.19: Comparison between experimental data and theoretical simulation during the charging of a capacitor by a non-uniform energy harvester.

respectively. It is thought that the magnitude of the resistor representing losses is smaller in this case due to the lower levels of voltage generated by the energy harvester.

Again a good experimental-theoretical agreement is obtained confirming the combined SIMULINK® and transfer matrix model is suitable for predicting the performance of energy harvesters, both uniform and non-uniform, in an electrical scenario consisting of an energy storage medium.

5.4.3 Reduction in length from free end

In this section the effects of the reducing the piezoelectric layer length from the cantilever free end are examined. A new batch containing 10 samples, with extended piezoelectric layer length varying from 9.66 mm to 44.5 mm, were manufactured following the procedure outlined in Chapter 4. The Al substrate layer dimensions were fixed at 50 mm $\times$ 7 mm $\times$ 0.87 mm with length extending from the clamp maintained at 44.5 mm $\pm$ 1 mm. The PZT layer thickness and width was 0.5 mm and 7 mm respectively with material properties available in Table 5.2. The results from testing all samples while charging a 1 μF capacitor are shown in Figure 5.20(a). The trend observed is similar to that seen during theoretical simulations previously preformed. A benefit in the peak voltage across the storage capacitor is observed for harvester configurations comprising of excessively short piezoelectric layers.

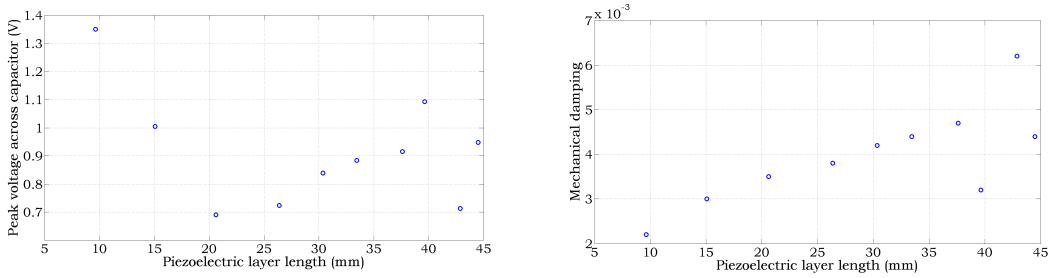

(a) Voltage (b) Damping

Figure 5.20: Experimental data showing the effects of piezoelectric material length on maximum voltage across the storage capacitor and mechanical damping. Both layers remain clamped.

One would ordinarily expect a reduction in performance due to shorter piezoelectric layer lengths generally being detrimental in terms of the electro-mechanical coupling magnitude and the mechanical forcing magnitude. However, as previously explained, shortening the length is favourable in terms of variables such as the piezoelectric capacitance and the mechanical damping, see Figure 5.20(b). The experimental mechanical damping data shows a similar trend to the assumption made during theoretical simulations with an approximate linear decrease with piezoelectric layer length. Sensitivity of the voltage trend to mechanical damping magnitude is evident from examination of data obtained for the longer samples, Figure 5.20. This indicates that controlling and minimising the mechanical damping ratio is beneficial for the performance of energy harvesters with configurations consisting of a short

piezoelectric layer outperforming the conventional design.

5.4.4 Reduction in length from clamped end

In this section an experimental trend for the performance while reducing piezoelectric layer length from the clamped end, i.e. both layers remain coincident at the free end, is presented. The same sample batch used during the previous study is reused here with samples reversed so that only the substrate layer is clamped. Piezoelectric material length is varied over the range 44.5 mm to 14.3 mm. Figure 5.21 shows experimental data obtained for both voltage across the storage capacitor and the mechanical damping ratio. Once again the general trend for voltage, from experimental data, is similar to that obtained from the theoretical model.

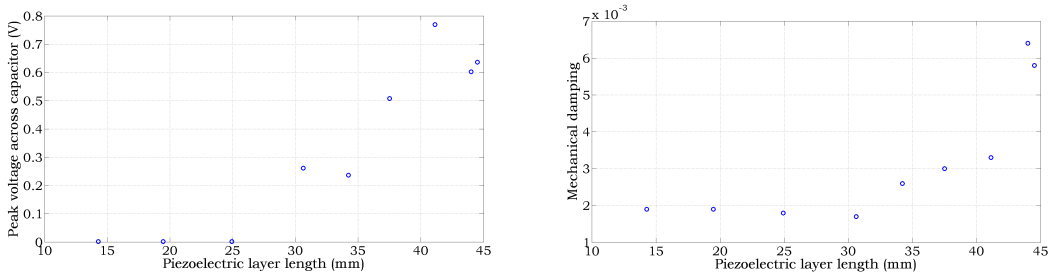

(a) Voltage (b) Damping

Figure 5.21: Experimental data showing the effects of piezoelectric material length on maximum voltage across the storage capacitor and mechanical damping. Both layers remain coincident at the free end.

Figure 5.21(a) indicates a slight reduction in piezoelectric layer length will improve the performance of an energy harvester – recall this is partly due to increases in the mechanical forcing experienced by the cantilever and reductions in mechanical damping. The scatter in experimental data can be explained solely by the damping ratio magnitude, see Figure 5.21(b). The mechanical damping for the sample comprising of a 44 mm piezoelectric layer was measured to be greater than that in the conventional design resulting in a reduction in voltage magnitude where an increase is expected. Similar logic applies when seeking an explanation into why the 30.62 mm sample outperformed the 34.23 mm sample. For lengths shorter than approximately half the substrate length, little or no voltage appears across the storage capacitor. Note how similar findings where obtained from the theoretical model, see Section 5.3.1.1. The reduced mechanical damping ratios, Figure 5.21(b), are

irrelevant here and poor harvester performance partly results from reduced strain levels in a cantilever beam further from the clamped end.

In terms of voltage across a storage capacitor, examination of both sets of experimental data leads to the conclusion that an optimum energy harvester configuration consists of a short piezoelectric layer attached to the clamped end of the cantilever in comparison to the conventional full length design. For the sample size and range tested here, a benefit of 42% was observed when the piezoelectric layer is 9.66 mm. However, this is dependant on the inconsistencies in the mechanical damping experienced by the samples, see Chapter 4.

5.5 Conclusion

This chapter addressed the scenario of piezoelectric energy harvesters connected to a storage medium which is recognised as essential due to the intermittent nature of many vibrational energy sources and low power levels generated from vibrational energy harvesters. Initially a robust model was developed and presented which combined SIMULINK® [59] with the transfer matrix model previously developed. The choice to use SIMULINK® [59] maintained the electro-mechanical coupling present in piezoelectric energy harvesting systems, hence allowing for a base model to be proposed with the ability for users to include more complex circuitry to assess the performance of both uniform and non-uniform energy harvesters in realistic electrical scenarios. The case considered here included a resistor in parallel with the storage capacitor to accommodate losses present in electrical components such as diodes.

The theoretical model was then used to gauge the effects of certain geometric parameters on the performance in terms of maximum voltage across a storage capacitor which directly relates to stored energy. Three distinct cases were examined – a macro-scale device, a micro-scale device and a thin film flexible device. For the macro-scale device, the parameters under investigation were the piezoelectric material length when both layers remain coincident with the free end and the piezoelectric material width. Results showed that variations in factors such as fundamental frequency, forcing, electro-mechanical coupling, piezoelectric capacitance and mechanical damping magnitude governed the trend between geometri-

cal parameters and voltage. Maximum performance was realised by reducing the width of the piezoelectric layer by 78% which lead to a 112% improvement in the energy stored in a 1 μF capacitor. A lower mechanical damping and piezoelectric capacitance are responsible for this outcome countering the lower mechanical forcing and electro-mechanical coupling in configurations with narrow piezoelectric layers.

While performing an optimisation on a MEMS-scale energy harvester the most important observation was that reducing piezoelectric material length from the clamped end can vastly improve performance. Taking into consideration the assumptions regarding variations in mechanical damping magnitude and fixed electrical losses the theoretical model predicted an increase of 205% in terms of energy stored when comparing a configuration comprising of a 0.25 mm long piezoelectric layer with the conventional design (a piezoelectric layer 2 mm in length). In this particular scenario, the effects of any change in piezoelectric material length on the mechanical forcing magnitude can be considered negligible due to the tip mass being the major contributor. The reason behind these vast improvements in performance are again a result of reduced mechanical damping and piezoelectric capacitance; detrimental effects on the electro-mechanical coupling produce a configuration with an optimal material length. Variations in thickness were also examined but the usefulness of these results, particularly associated with substrate thickness, is minimal due to a large variation in fundamental frequency between designs. A general conclusion was that improving the piezoelectric-to-substrate thickness ratio was beneficial to performance however this can result in designs which are more susceptible to failure.

The final case study was for a thin film flexible energy harvester. Alteration in the piezoelectric material length showed improvement in the range of 67%, for reasons outlined above and subjected to the assumptions made, when a design utilising a 32 mm long piezoelectric layer is used in place of the conventional design – note that both layers remain clamped. Time taken by the optimum design to fully charge the capacitor is greater in comparison to the conventional design. However, this is not an issue, since, for the majority of the time span, energy stored whilst charging with the optimum design exceeds energy stored whilst charging with the conventional design. The charging of a larger capacitor was also

undertaken during this case study to investigate whether a similar outcome occurred. While charging a 1 mF capacitor for 5 minutes the optimum design, improving performance by 30%, was observed to consist of a 50 mm piezoelectric layer.

The final section in this chapter was aimed at the experimental validation of the theoretical model through the use of uniform and non-uniform energy harvester samples. Satisfactory agreement was obtained when a resistor accommodating system losses was included in the theoretical model. Without the resistor, the model resulted in an overestimation of the time taken to fully charge the capacitor. While experimentally determining the effects of piezoelectric material length on the maximum stored energy similar trends to those obtained from the theoretical model were obtained highlighting the validity of the developed model. For the sample sizes and range tested, experimental findings showed benefits in performance from manufacturing a harvester with a 9.66 mm piezoelectric layer rather than one of conventional design (where both layers are 44.5 mm). The stored energy in a 1 μF capacitor, whilst utilising the 9.66 mm device, increased by 42%.

In Chapters 2, 3 and 5, while performing geometric optimisations, the fundamental frequency has not been controlled and this is a major drawback to parameter change analyses. In a practical scenario the conventional harvester, with both layers identical in length, will be designed, geometry wise, to have a resonant frequency tuned to the dominant frequency of excitation present from the application surroundings. While performing geometric parameter changes, allowing for design optimisation, an assumption was made whereby each design would be excited at its unique resonant frequency. Herein the problem lies – the new optimised design is unlikely to perform efficiently in the targeted application due to unmatched resonant and excitation frequencies. This issue will be addressed in the following chapter and is eliminated by altering multiple parameters simultaneously in such a manner as to produce numerous energy harvester designs, with varying piezoelectric layer topology, and identical fundamental frequencies.

CHAPTER 6

CONSTANT FUNDAMENTAL FREQUENCY APPROACH

6.1 Introduction

In previous chapters, parametric studies on device geometry were performed in which the fundamental frequency between energy harvester designs was not controlled. In practical situations the dominant excitation frequency is likely to be known, and so materials and dimensions of the energy harvester (conventionally designed with both layers of identical length) are based on creating a configuration with a tuned fundamental frequency. During parametric studies of, for example, the piezoelectric layer geometry and coverage, fundamental frequency of the energy harvester changes. The optimum design obtained from such a study is therefore unlikely to efficiently perform in the targeted application due to a mismatch in the fundamental and dominant excitation frequencies.

In this chapter the above issue is overcome by modifying multiple geometric parameters simultaneously in such a way as to maintain a constant fundamental frequency between energy harvester configurations – thereby providing unbiased design comparisons. Through this the author aims to show that basic alterations in piezoelectric layer dimensions should not be dismissed during the design process. The optimised device will have an identical fundamental frequency to the device with a conventional design and so be suitable for the

targeted application. Erturk and Inman take a similar approach while investigating effects of piezoelectric material on harvester performance [30]. Since material choice affects fundamental frequency they opt to use the bimorph length as the frequency control parameter. From the perspective of the author this was ill-advised as comparisons resulted in piezoelectric material volume doubling (through the increase in length) for certain cases so the purpose of determining how material choice affects the performance was not clearly addressed. Geometry such as substrate layer thickness, length and width, or the dimensions of a tip mass are believed to be better suited for being control parameters. Such parameters are used here while examining the effects of piezoelectric layer geometry on the performance of vibrational energy harvesters.

Table 6.1: Table outlining parameter changes to be made for each individual case study.

	Case study 1		Case study 2		Case study 3	
	R	C	R	C	R	C
Piezoelectric layer length	✓	✓	✓		✓	✓
Piezoelectric layer width						✓
Piezoelectric layer thickness	✓	✓			✓	✓
Control parameter	Substrate thickness		Tip mass dimensions		Substrate thickness	

'R' First electrical scenario – load resistor.
'C' Second electrical scenario – storage capacitor.

The chapter is arranged is the following manner. Firstly the methodology behind a constant fundamental frequency approach is outlined followed by justification of what the author believes to be good, practical, control parameters. In the remaining sections the approach is utilised to generate numerous harvester configurations with identical fundamental frequencies for the three case studies previously examined, see Chapter 5 – a macro-scale device, a micro-scale device and a flexible thin film device. Performance and optimisation of energy harvesters are investigated in the two electrical scenarios previously modelled – power across various load resistors (Chapter 3) and storage of energy in a capacitor (Chap-

ter 5). For each case study, alterations to piezoelectric layer geometry are examined, i.e. the layer length (from both free and clamped end), layer width and layer thickness. For the micro-scale device the tip mass dimensions are used as the control parameter, whereas the fundamental frequency for the other two cases is controlled using the substrate thickness. The experimental matrix shown in Table 6.1 provides an overview of expected parameter change combinations. The chapter will conclude with some closing remarks on findings with emphasise on how best to optimise piezoelectric layer geometry in either electrical scenario.

6.2 Methodology and development of model

In this section the methodology behind the constant frequency method is introduced along with its implementation in MATLAB® [55]. Initially the parameter which is to be examined and its range are selected, i.e. piezoelectric layer length from the free end, varying from 1% coverage to 100% coverage. Following this, a control parameter which can be used to alter the fundamental frequency of the cantilever is selected, i.e. the thickness of the substrate layer. The 'target' fundamental frequency for all configurations is then obtained by calculating the fundamental frequency of the conventional design. All frequency estimations are obtained by using the transfer matrix method outlined in Chapter 2. For each magnitude of the examined parameter a sweep of the control parameter is performed until the target frequency is exceeded and then interpolation is used to estimate the required magnitude for the control parameter. As is shown in the following section some parameters do not perform adequately for frequency control with their implementation being impractical. The MATLAB® code used to obtain these configurations, in the case where piezoelectric length from the clamped end is under examination with substrate thickness as the control, is provided in Appendix B.1.

6.2.1 Control variables

Since the aim is to examine the geometry of the piezoelectric layer, substrate layer dimensions or if applicable, the tip mass dimensions, are used for fundamental frequency control. One example of an adequate control variable is the substrate thickness; this is illustrated in Figure 6.1. For each length of piezoelectric material (removing material from the free end of the beam) the thickness of the substrate layer is swept from 0.16 mm to 0.92 mm. The nominal dimensions and material properties for the macro-scale energy harvester are given in Table 6.2.

Table 6.2: Structural dimensions, and mechanical and electrical properties of the conventional harvester used throughout this analysis (Note this design does not include a tip mass).

Parameter	Value
Substrate (Al) length (mm)	50
Substrate (Al) width (mm)	5
Substrate (Al) thickness (mm)	0.67
PZT layer length (mm)	50
PZT layer width (mm)	5
PZT layer thickness (mm)	0.5
Young's modulus of Al (GPa)	69
Density of Al (kg.m^{-3})	2700
Young's modulus of PZT (GPa)	62.1
Density of PZT (kg.m^{-3})	7800
Piezoelectric constant, d_{31} (m.V^{-1})	-180$\times$10^{-12}
Permittivity, ε_{33}^{S} (F.m^{-1})	1.549$\times$10^{-8}

The effectiveness of a control parameter is characterised by how sensitive any changes to parameter magnitude are on the fundamental frequency of the device. Ideal control parameters can readily alter the fundamental frequency of a device and can be readily implemented in a practical sense, i.e. substrate thickness. As expected, increases in layer thickness cause increases in fundamental frequency resulting from the increase in stiffness-to-mass ratio. Energy harvester designs with various lengths of piezoelectric material can be manufactured with specific substrate thickness thereby producing configurations with the targeted fundamental frequency. Figure 6.2(a) shows the required substrate thickness for the full range of piezoelectric material lengths. After examining how fundamental frequency

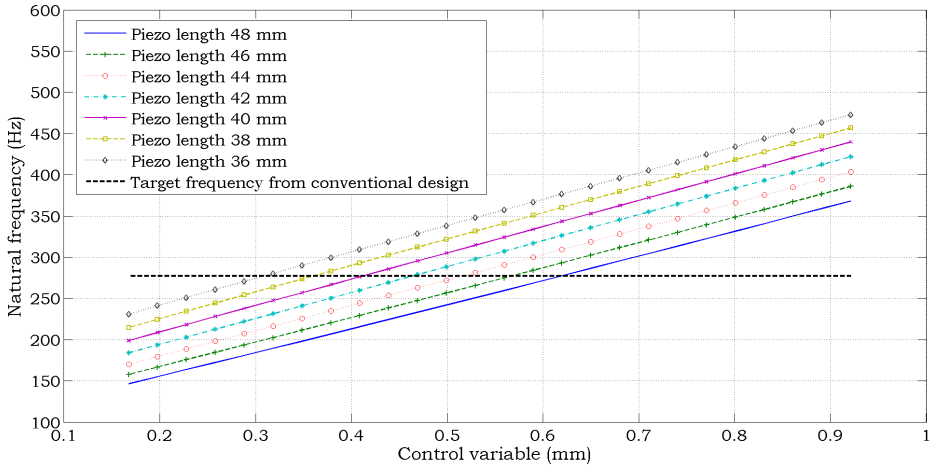

Figure 6.1: Example of good fundamental frequency control. Reducing piezoelectric material length, using substrate thickness as the control parameter.

changes with piezoelectric material length, see Figure 6.2(b), the reasons behind the trend obtained in Figure 6.2(a) is evident.

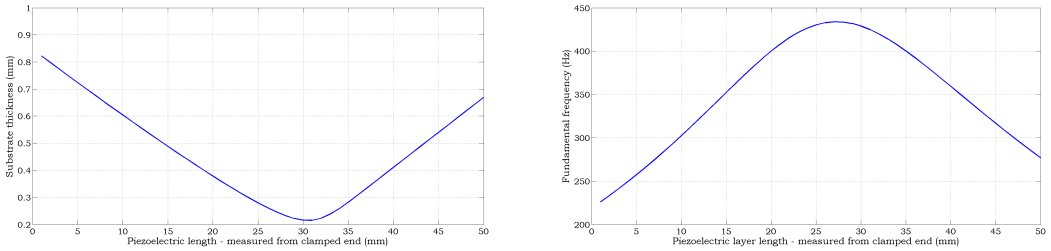

(a) Magnitude of control required to produce configurations with identical fundamental frequencies

(b) Fundamental frequency while altering piezo length with no control

Figure 6.2: Relations between piezoelectric material length with required control and fundamental frequency.

Configurations with higher fundamental frequencies (i.e. a device having a piezoelectric layer length of 27.5 mm in Figure 6.2(b)) naturally require thinner substrate layers (for the 27.5 mm case, Figure 6.2(a) shows a substrate thickness of 0.24 mm is required). This thinning, and after the equilibrium point, subsequent thickening, counters changes in structure dynamics from piezoelectric material length alternations, creating a range of configurations with identical fundamental frequencies. In the remaining sections of this chapter such configurations are tested through theoretical simulations in the two electrical scenarios. Firstly, the power dissipated across a range of load resistors is investigated, and secondly, this is followed by geometry optimisation when energy harvesters are connected to a capac-

itor for energy storage.

6.3 Case studies with energy harvester connected to load resistor

6.3.1 Macro-scale device

In this section, parametric studies on piezoelectric layer geometry are performed on a macro-scaled device while using substrate layer thickness to maintain a constant fundamental frequency of 276.8 Hz. The nominal dimensions of the conventional device were previously provided in Table 6.2. In each case the load resistance is swept from 100 Ω to 1 MΩ (representing a change from closed-circuit to open-circuit conditions) while the base acceleration is maintained at a constant 0.5 m.s^{-2}. The mechanical damping for all tested configurations is assumed fixed at 0.005 (approximately that obtained for the nominal sample during experimental works presented in Chapter 4). The first study considers piezoelectric layer length which is altered from either the free or clamped end.

6.3.1.1 Length of piezoelectric layer

The piezoelectric layer length is swept from 1 mm to 50 mm (substrate length – 50 mm) while the magnitude of the substrate thickness, obtained from procedure outlined in Section 6.2, is used to control fundamental frequency. The substrate thickness corresponding to each piezoelectric layer length can be found in Appendix B.2. Figures 6.3(a) and 6.3(b) show how the dissipated power is affected by both piezoelectric layer length and load resistance. Note how in this case, and all proceeding cases, the energy harvesters are assumed to be excited at the fundamental frequency of the equivalent conventional design. This will not necessarily provide peak power – recall the discussion in Chapter 3 regarding shifts in resonant frequency with load resistance magnitude – however, this assumption provides a means for fairly comparing the performance of energy harvester designs in identical excitation scenarios (same base excitation frequency and magnitude).

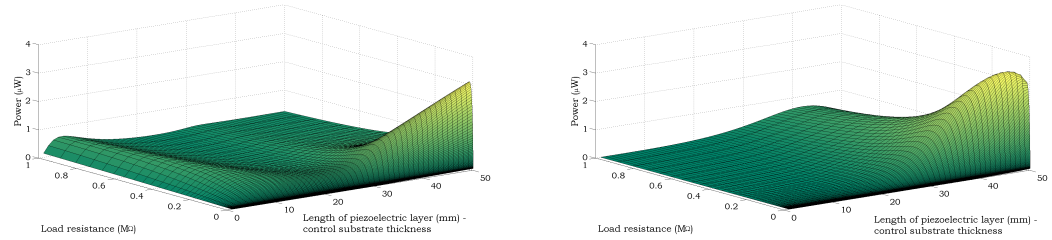

(a) Coincident with clamped end (b) Coincident with free end

Figure 6.3: Plots representing the effects of piezoelectric length on the power generated. Note, all configurations have identical fundamental frequencies.

The figures show that reducing piezoelectric layer length from the clamped end is not favourable in terms of maximum power dissipated, whereas reducing length from the free end indicates a slight improvement in maximum power. Numerically, a 13% increase is possible by reducing the piezoelectric length by 3 mm. This configuration requires a substrate thickness of 0.59 mm rather than the 0.67 mm from the conventional design. The primary reason why an improvement in maximum dissipated power occurs for reduced lengths of piezoelectric material is because there is an increase in mechanical forcing exerted on the cantilever, see Figure 6.4(a).

$$Q_1 = -Y_0\omega^2 \int_0^L m(x)W_1(x)\mathrm{d}x \ . \tag{6.1}$$

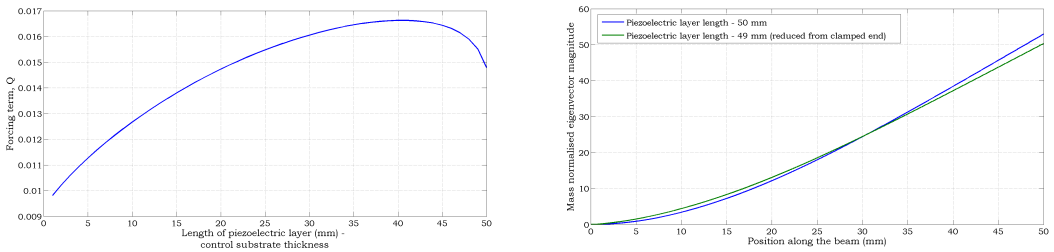

(a) Piezoelectric layer length and forcing magnitude (b) Piezoelectric layer length and mode shape

Figure 6.4: Plots representing the effects of piezoelectric length on various system variables.

Although structural mass has reduced, the increase in mechanical forcing, see Equation (6.1), is a direct result of changes in structural mode shape, $W_1(x)$. Figure 6.4(b) shows mode shapes obtained from configurations with the two longest lengths of piezoelectric material. Subtle differences in the mode shape resulting from variations in material distribution affect Q_1 which directly influences the power generated from energy harvester configura-

tions.

6.3.1.2 Thickness of piezoelectric layer

In this subsection the piezoelectric thickness is swept from 0.25 mm to 1 mm, with substrate thickness again used as the fundamental frequency controlling variable. Figure 6.5 shows the results from such a study with further details on the configuration dimensions provided in Appendix B.3.

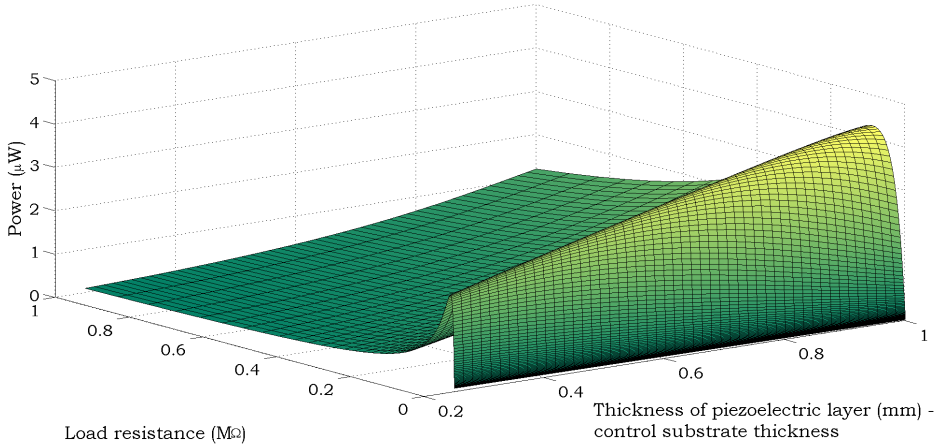

Figure 6.5: Plot representing the effects of piezoelectric layer thickness on the power generated. Note, all configurations have identical fundamental frequencies.

From Figure 6.5 it is evident that, generally, energy harvester performance increases with piezoelectric layer thickness. The primary reason behind this was previously discussed in Chapter 3 – an increase in the forcing magnitude is observed with increases in layer thickness. For this particular type of optimisation, neutral axis location in relation to the position of the piezoelectric layer requires additional consideration. Charge cancellation will occur if the neutral axis lies within the piezoelectric layer which can have detrimental influences on performance. Numerically, over optimum load resistances, a configuration with a piezoelectric layer thickness of 1 mm generates 39% more power than a configuration with the dimensions outlined in Table 6.2. The 100% increase in piezoelectric thickness required a 47.6% reduction in substrate thickness with variations in percentage change arising from differing material properties.

6.3.2 Micro-scale device

In this section a parametric study on the piezoelectric layer length of a micro-scaled device is performed. In this case, the tip mass dimensions are used to maintain a constant fundamental frequency of 244.3 Hz – that of the conventional design. The nominal dimensions of the device are provided in Table 6.3. The tip mass width remains fixed at the beam width, assumed to be a space constraint, while allowing variations in tip mass thickness and length. Load resistance is again swept from 100 Ω to 1 MΩ while the base acceleration is maintained at a constant 2 g. The mechanical damping for all tested configurations is assumed fixed at 0.005, as was assumed in the previous study.

Table 6.3: Structural dimensions, and mechanical and electrical properties of the conventional harvester used throughout this analysis.

Parameter	Value
Substrate (Si) length (mm)	2
Substrate (Si) width (mm)	0.6
Substrate (Si) thickness (mm)	0.012
PZT layer length (mm)	2
PZT layer width (mm)	0.6
PZT layer thickness (mm)	0.00164
Young's modulus of Si (GPa)	185
Density of Si (kg.m^{-3})	2329
Young's modulus of PZT (GPa)	66
Density of PZT (kg.m^{-3})	7800
Tip mass length (mm)	0.6
Tip mass width (mm)	0.6
Tip mass thickness (mm)	0.6
Density of tip mass (kg.m^{-3})	8908
Piezoelectric constant, d_{31} (m.V^{-1})	-180$\times$10^{-12}
Permittivity, ε_{33}^{S} (F.m^{-1})	1.594$\times$10^{-8}

Figure 6.6 shows the effect of length on the power dissipated across various load resistors. Clear improvements in performance are indicated when the length of piezoelectric material is reduced for energy harvesters connected to electrical loads of high resistance. Appendix B.4 can be referred to for comprehensive information regarding each configurations complete dimensions.

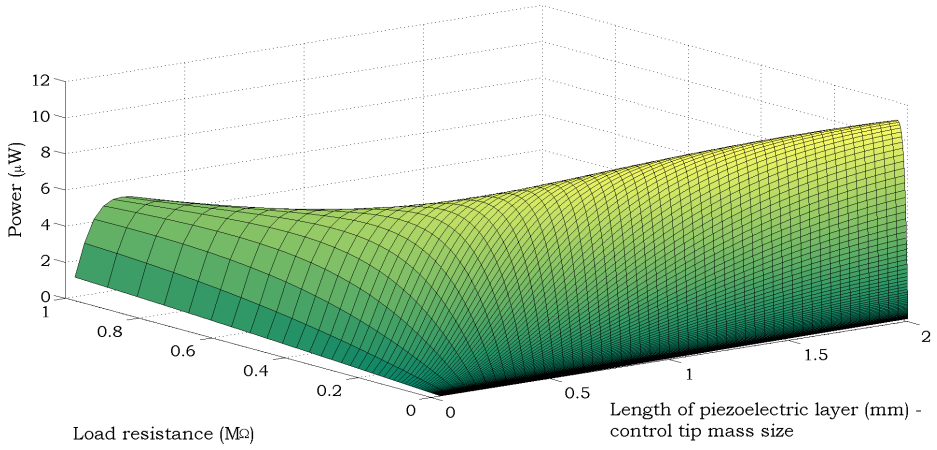

Figure 6.6: Plot representing the effects of piezoelectric layer length on the power generated from a micro-scale device. Note, all configurations have identical fundamental frequencies.

Numerically, over optimum load resistances, generated power can only be increased by a mere 0.2%. However, a 50% reduction in piezoelectric layer length will only cause a 4% reduction in power, allowing for financial saving on material costs with only small detrimental effects on power generated. Substantial improvement is observed when harvesters are connected to the larger load resistances. Over a 1 MΩ resistor an increase of 353% (from 1.12 μW to 5.09 μW) is achievable when reducing piezoelectric length to 0.24 mm in comparison to the 2 mm length in the conventional design. For the optimum design, the tip mass size must be reduced to 0.571 mm $\times$ 0.6 mm $\times$ 0.571 mm to create a configuration with the targeted fundamental frequency of 244.3 Hz. If manufacturing precision is an issue, one could alter one of the tip mass dimensions solely which would indeed increase variability range and reduce sensitivity. The comprise between an increase in mechanical forcing and a reduction in electro-mechanical coupling is again the governing factor for the trends observed.

6.3.3 Flexible thin film energy harvester

In this section, parametric studies on the piezoelectric layer dimensions of a flexible film device developed by the research group at Hiroshima University in Japan [94] are performed, while reverting back to using substrate thickness to maintain a constant fundamental frequency of 26.9 Hz. The nominal dimensions of the device are provided in Table 6.4. In

each case the load resistance is swept from 1 kΩ to 10 MΩ while the base acceleration is maintained at a constant 0.5 m.s^{-2}. The mechanical damping for all tested configurations is assumed fixed at 0.005, as was assumed during previous studies.

Table 6.4: Structural dimensions, and mechanical and electrical properties of the harvester manufactured by the research group at Hiroshima University [94].

Parameter	Value
PET layer length (mm)	100
PET layer width (mm)	20
PET layer thickness (mm)	1
PVDF layer length (mm)	100 [a]
PVDF layer width (mm)	10
PVDF layer thickness (mm)	0.04
Young's modulus of PET (GPa)	3.1 [b]
Density of PET (kg.m^{-3})	1400 [b]
Young's modulus of PVDF (GPa)	8.3 [c]
Density of PVDF (kg.m^{-3})	1780 [c]
Piezoelectric constant, d_{31} (m.V^{-1})	22×10^{-12} [c]
Permittivity, ε_{33}^{S} (F.m^{-1})	1.063×10^{-10} [c]

[a] Material property for PET obtained from [102].
[b] Material property for PVDF obtained from [75].
[c] Note: slightly modified so both layers are the same length, a change which does not drastically affect fundamental frequency of the device.

6.3.3.1 Length of piezoelectric layer

In this section, investigation of the piezoelectric layer length (reduced from the free end only) on performance is undertaken. Figure 6.7 shows the effects of length on the power dissipated across various load resistors. Again, one can see clear improvements in performance from reductions in piezoelectric material length.

Similar behaviour to the previous micro-scale example is obtained with large improvements in performance achievable for energy harvesters connected to larger resistive loads. Numerically, over a 10 MΩ resistor, one can expect a 115% increase in dissipated power for a configuration consisting of a 30 mm piezoelectric layer in comparison to 100 mm. Due to the thickness of the piezoelectric layer in comparison to the substrate layer (25 times smaller), in this particular case, the substrate thickness of the optimal design

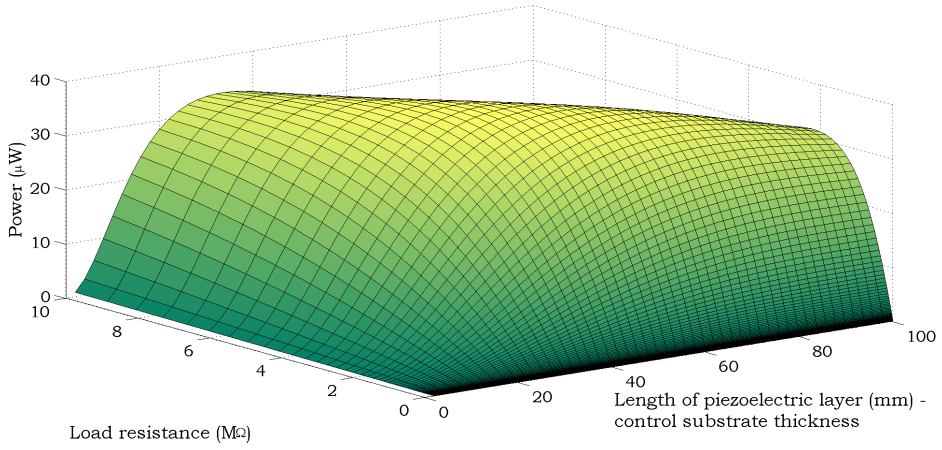

Figure 6.7: Plot representing the effects of piezoelectric layer length on the power generated from the flexible film device. Note, all configurations have identical fundamental frequencies.

can be taken as that of the conventional design.

6.3.3.2 Thickness of piezoelectric layer

In this section piezoelectric layer thickness is the parameter under investigation with substrate thickness remaining as the control parameter. Figure 6.8 shows the influence of thickness on the power dissipated across the load resistance range. Generally, one observes increases in power with thickness across resistor sizes greater than the optimum resistance.

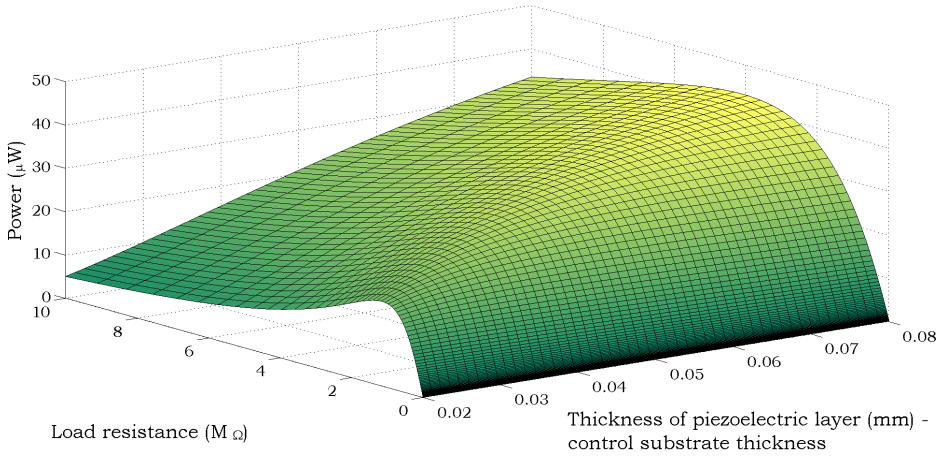

Figure 6.8: Plot representing the effects of piezoelectric layer thickness on the power generated from the flexible film device. Note, all configurations have identical fundamental frequencies.

The increase in electro-mechanical coupling with an increase in thickness can once again explain why over the larger load resistances the generated power increases with length. This trend occurs despite the mechanical forcing reducing with an increase in piezoelectric layer thickness. Once the percentage change of each variable over the examined thickness range is examined one can readily obtain the reason behind the observed trends in dissipated power. The mechanical forcing was found to reduce by 3% compared with a 266% increase in electro-mechanical coupling.

From these studies of configurations with identical fundamental frequencies connected to a load resistance one can conclude that there is a definite benefit to tweaking piezoelectric layer geometry across all scales of energy harvester. It has been shown that optimum lengths of piezoelectric material do exist and these lengths are not in agreement with conventionally designed device. Since the fundamental frequency does not alter between configurations, due to frequency control realised through another geometric parameter, this approach provides a more practical method of design comparison.

6.4 Case studies with energy harvester connected in an energy storage scenario

In this section, case studies of energy harvesters connected to storage capacitors are examined. The SIMULINK® model, which was presented in Chapter 5, is utilised along with configurations of identical fundamental frequencies – already obtained from the procedure outline in Section 6.2. The maximum voltage across a capacitor with magnitude of 1 μF is used as the performance measure. The mechanical damping in all samples is assumed to again be fixed at 0.005 and a resistive load of 3 MΩ, as was the case in Chapter 5, is included within the SIMULINK® model to accommodate losses in electrical components.

6.4.1 Macro-scale device

In this section the macro-scale device is investigated. Dimensions of the nominal sample are provided in Table 6.2 and a base acceleration of 0.75 m.s^{-2} is applied to each configuration. Figures 6.9 and 6.10 show how maximum voltage across the storage capacitor is affected by piezoelectric layer length and piezoelectric layer thickness, respectively, while substrate thickness is used as the control parameter.

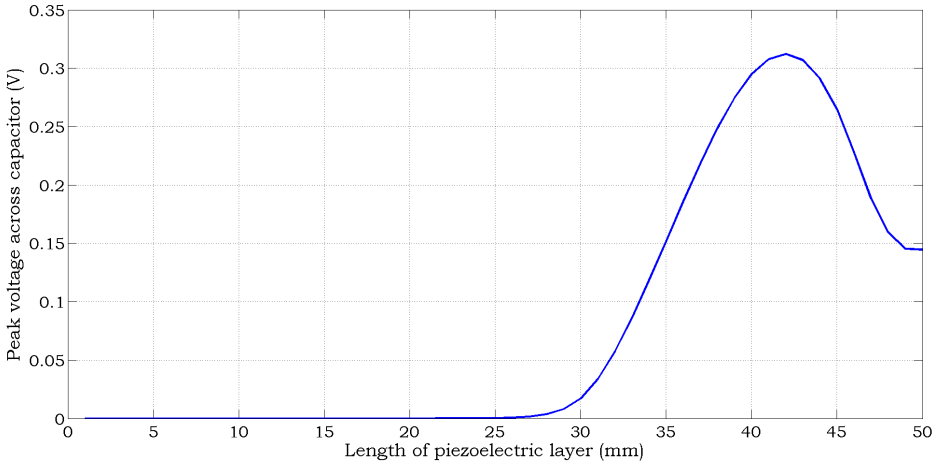

Figure 6.9: Plot representing the effects of piezoelectric layer length on the maximum voltage across a 1 μF capacitor for a device on the macro-scale. Note, all configurations have identical fundamental frequencies.

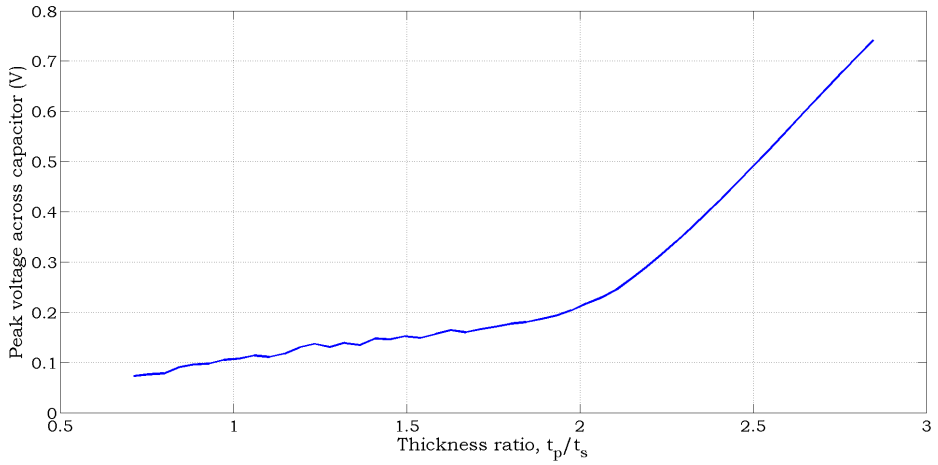

Figure 6.10: Plot representing the effects of piezoelectric layer thickness on the maximum voltage across a 1 μF capacitor for a device on the macro-scale. Note, all configurations have identical fundamental frequencies.

Figure 6.9 shows poor performance of designs with piezoelectric length below approximately half the beam length (25 mm) since in these cases the threshold voltage of the

diode bridge is not overcome. Note that during this study, piezoelectric length was reduced from the clamped end of the beam. Maximum energy storage occurs for a device with a 16% reduction in piezoelectric layer length, which provided a 115% improvement over the conventional design. The optimum design required a 59% increase in substrate thickness to produce a device with the targeted fundamental frequency, see Appendix B.2. Figure 6.10 shows that continuous improvements in performance are achievable while increasing the thickness of the piezoelectric material. Scatter in the simulation data is due to numerical inaccuracies resulting from solver tolerance and rounding errors. The primary cause for both trends was previously described and is due to changes in the mechanical forcing experienced by the samples, see Figures 6.4(a) and Figure 6.11.

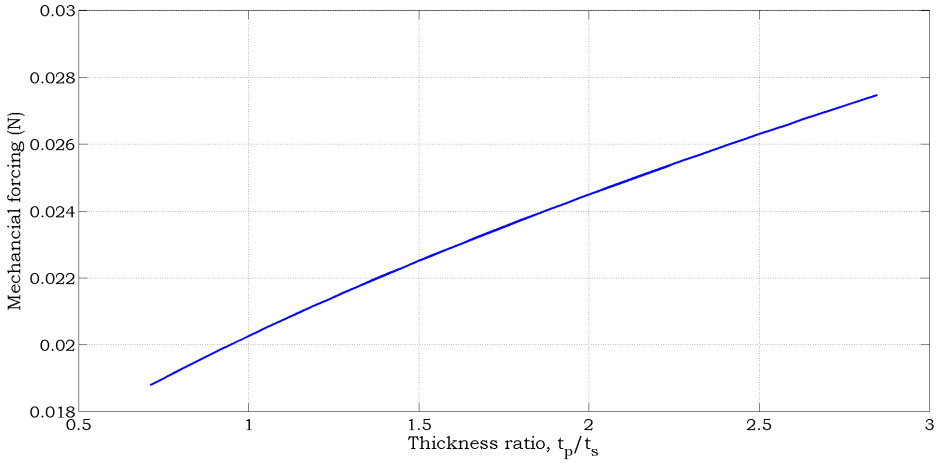

Figure 6.11: Plot representing the effects of piezoelectric layer thickness on the mechanical forcing for a device on the macro-scale. Note, all configurations have identical fundamental frequencies.

For the investigation of piezoelectric layer length, maximum mechanical forcing occurs when the length is 40 mm. However, the maximum voltage occurs for a length of 42 mm. This small shift is due to improved electro-mechanical coupling with piezoelectric layer length, again highlighting the fact that optimisation of one variable, i.e. mechanical forcing, to maximise performance is ill-advised. Geometric changes have been observed not to favour all variables simultaneously and so a balance is required. Figure 6.11 shows a continuous increase in mechanical forcing with piezoelectric thickness directly reflected in the trend between thickness and maximum voltage, Figure 6.10.

6.4.2 Flexible thin film energy harvester

In this final section, investigations on a flexible film device are performed. The base acceleration applied to the configuration is 0.5 m.s^{-2} – this being more than sufficient to overcome the threshold voltage of the diode bridge. The length, width and thickness of the piezoelectric layer are each examined, Figures 6.12 - 6.14 respectively.

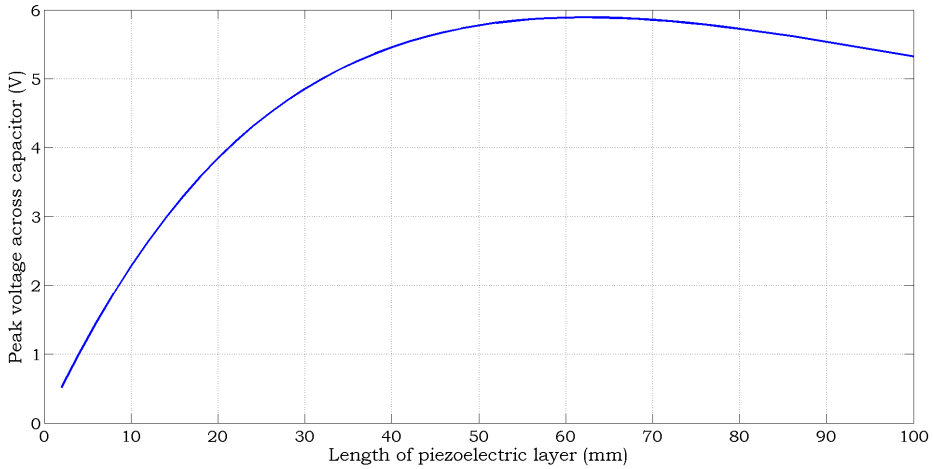

Figure 6.12: Plot representing the effects of piezoelectric layer length on the maximum voltage across a 1 μF capacitor for the thin film device. Note, all configurations have identical fundamental frequencies.

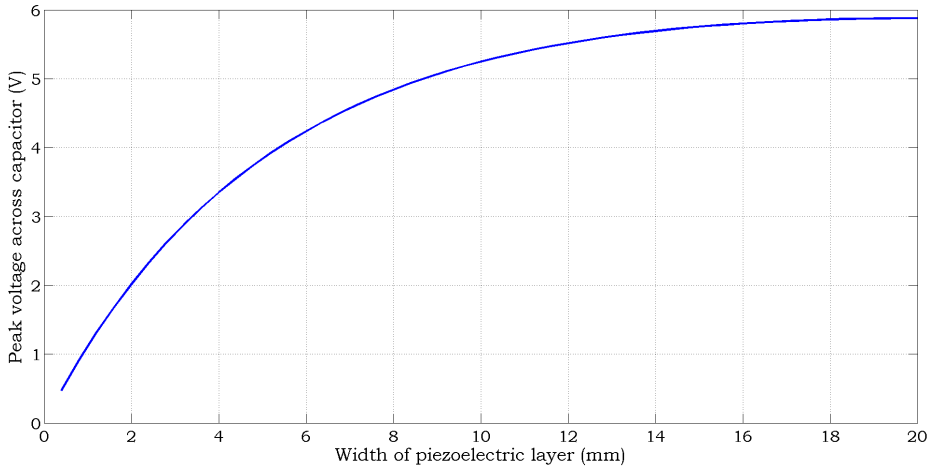

Figure 6.13: Plot representing the effects of piezoelectric layer width on the maximum voltage across a 1 μF capacitor for the thin film device. Note, all configurations have identical fundamental frequencies.

Figure 6.12 shows that slight reductions in piezoelectric layer length can improve the amount of energy stored across the 1 μF capacitor. Numerically, a configuration consisting of a 62 mm piezoelectric layer coincident with the clamped end allows for an 11%

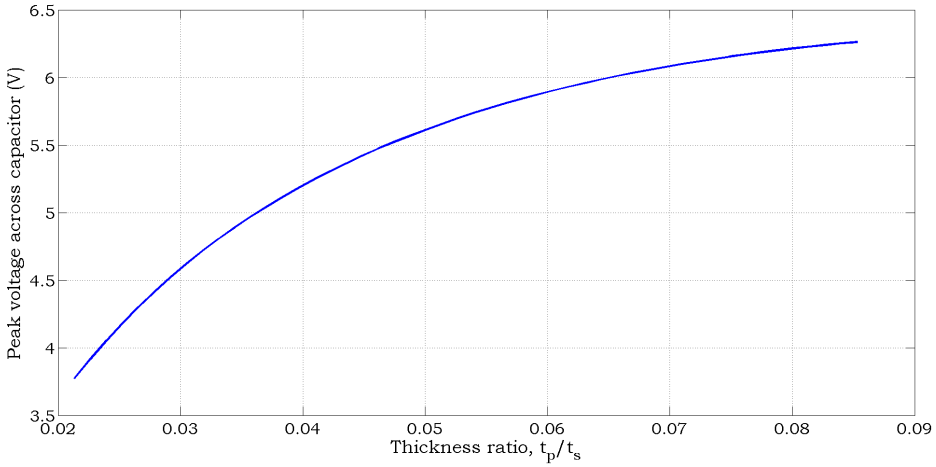

Figure 6.14: Plot representing the effects of piezoelectric layer thickness on the maximum voltage across a 1 μF capacitor for the thin film device. Note, all configurations have identical fundamental frequencies.

increase in stored energy. The substrate thickness of this optimum configuration requires a small alteration (1 mm to 0.99 mm) to produce a design with an identical fundamental frequency to the conventional design. If this change in substrate thickness is not practical then, alternatively, the addition of a small mass to the cantilever tip is proposed. However, this supposedly simple change in control is thought to influence the trend performance, resulting from variation in mode shape from tip mass addition, a study not undertaken here. Figures 6.13 and 6.14 show that increases in both piezoelectric width and thickness have beneficial effects on the amount of stored energy. In terms of width, a configuration with a 20 mm layer, in comparison to the current 10 mm layer, causes increases of over 12%. In terms of thickness (width fixed at 10 mm), having a thickness ratio, t_p/t_s, of 0.085 rather than the current 0.04, will cause energy storage benefits of up to 21%. While altering piezoelectric thickness the optimum configuration, across the tested range, was found to have a 0.94 mm thick substrate layer. Tabulated dimensions of all simulated harvesters can be found in Appendix B.5. A more complete study may possibly involve firstly optimising one parameter, say for example the piezoelectric layer length, and using this new design for further optimisation, for example on piezoelectric layer thickness, again this outside the scope of current work.

6.5 Conclusion

In this chapter an approach which results in a constant fundamental frequency across the energy harvester design range has been presented which involves altering multiple geometric parameters simultaneously. The approach is an improvement on previous energy harvesting parametric studies relating to device geometry as it compares designs with identical fundamental frequencies. Assuming the dimensions and material properties of the conventional energy harvester are chosen to tune fundamental frequency to the application frequency, it is poor practice to compare designs with differing fundamental frequencies. Altering an individual geometric parameter falls into this category, producing an optimum design which can no longer be used in the required application. In these works, the focus has been on examining the influence of piezoelectric layer geometry, using either substrate or tip mass geometry for frequency control purposes. The sensitivity of parameters to the fundamental frequency is determinant on choosing suitable geometric control parameters. The thickness of the substrate layer or dimensions of the tip mass (if applicable, as predominantly only found on micro-scaled devices) are used for fundamental frequency control.

The target frequency is determined from the fundamental frequency of the conventional configuration – both layers identical in length. For each subsequent configuration, resulting from changes made to the length, width or thickness of the piezoelectric layer, one requires the acquisition of a new substrate thickness/tip mass size. This is efficiently achieved through a sweep of the control parameter, until the target frequency is exceeded, followed by interpolation to determine a more precise magnitude, a process implemented in MATLAB® [55]. Through this process geometries of a range of energy harvester configurations are obtained with identical fundamental frequencies.

The three case studies considered throughout this thesis were again revisited – a macro-scale device, a micro-scale device and a flexible device developed at Hiroshima University. The harvester configurations were simulated in both electrical scenarios – firstly, basic attachment to a range of resistive loads, and secondly, connection to a 1 μF capacitor as a means of energy storage. All three cases indicated the piezoelectric geometry can be

modified to improve performance in comparison to the conventional design.

For the first electrical scenario, simulations of the macro-scale device showed improvement in maximum dissipated power from small reduction in piezoelectric length from cantilever clamped end. For the other two case studies, improvements in performance were achieved by reducing piezoelectric layer length from the cantilever free end. Note that this statement will not be valid for all macro-scaled/micro-scaled devices as trends depend on electrical and mechanical material properties along with structure dimensions. The reason behind such differing trends results from how the dynamics of the structure alters while changing piezoelectric layer length which directly affects variables such as the mechanical forcing and electro-mechanical coupling. Although small improvements, 10-20%, are observed in terms of maximum overall power, when considering energy harvesters connected to larger load resistances (greater than 1 MΩ) more substantial improvements in power were observed with increases, over the conventional design, in excess of 100%. All three case studies did show improvements in power with increases in piezoelectric layer thickness, an observation which should be taken with caution due to increased fragility of designs with thicker piezoelectric layers. For fundamental frequency control, reduction in the substrate thickness or increases in the tip mass size (when applicable) were required when increasing piezoelectric layer thickness.

Investigations of energy harvesters in the second electrical scenario whereby generated energy is stored in a capacitor also showed design modifications do indeed improve device performance. It was observed that increases in the thickness and width are both beneficial to the performance of an energy harvester with substrate thickness used for frequency control. In terms of piezoelectric layer length a unique optimum magnitude existed for each case study which differed from the conventional design. Greatest improvements in the level of energy storage occurred for the macro-scale device – in the range of 115%. Although each design case must be addressed individually, these works clearly indicate vast performance improvements are possible from basic alterations to the piezoelectric layer which should not be overlooked during the energy harvester design process. In general, when it comes to optimising the performance of an energy harvester in both energy storage

and direct use applications, both a reduction in piezoelectric layer length and an increase in the piezoelectric layer thickness require consideration. The approach of comparing designs with identical fundamental frequencies is more practical, and along with the robust, experimentally validated, analytical and SIMULINK® models, provides an excellent means for determining optimum energy harvester configurations for the user.

One inherent issue with piezoelectric materials is the non-linear behaviour they exhibit at high acceleration levels [24, 51, 85, 96]. The cases considered thus far have been assumed to experience low levels of excitations resulting in small cantilever deflections thereby avoiding non-linear behaviour. There are however applications where high acceleration levels are unavoidable in which current, linear assumptions, will no longer be valid, leading to an overestimation of energy harvester performance. In an attempt to provide a more complete model, the final chapter in this thesis will consider the issue of non-linearity in energy harvester behaviour with both detailed modelling and experimental validation provided.

CHAPTER 7

NON-LINEAR PIEZOELECTRIC ENERGY HARVESTER MODEL

7.1 Introduction

All work presented thus far has focused on energy harvesters subjected to low acceleration levels (<1 m.s^{-2}). This restriction allowed for and justifies a simplistic linear modelling approach. It is widely known however that piezoelectric material is inherently non-linear [22], the phenomenon also occurring at moderate acceleration levels, and so the currently developed linear model is rather limited. In this final chapter a robust non-linear model for piezoelectric energy harvesters is developed which is expected to provide a means for users to confidently predict the performance of both uniform and non-uniform energy harvesters across a much wider excitation range. Note, details regarding previous models for non-linear piezoelectric energy harvesters were provided in the earlier literature review, see Chapter 1.

The model developed in these works is based on a model developed by Mahmoodi *et al.* [50], for piezoelectric actuation, which was tailored to vibrational energy harvesting scenarios by Mak [51]. As explained by Mak [51] the model in [50] is extended by the addition of an extra degree-of-freedom for the voltage, whose existence is redundant in an actuation scenario as voltage is input as additional forcing. The result of this is two equa-

tions of motion, governing both mechanical and electrical responses. Model extension in regards to work completed by Mak [51] will include the incorporation of dynamic effects from altering piezoelectric layer geometry, i.e. layer length and width, which results in the creation of non-uniform energy harvesters. The transfer matrix approach, detailed in Chapter 2, will again be employed to accurately predict natural frequencies and mode shapes of both uniform and non-uniform energy harvesters. In addition to this extension, an alteration relating to beam curvature is also made. The expression utilised within the presented model is derived through the use of differential geometry [60].

This chapter is laid out in the following manner. Firstly, extensive details regarding model development are presented with the embodiment of non-linearities resulting from both material and geometry. Material non-linearity is introduced in the form of additional terms in the constitutive equations and geometric non-linearity will result from an inextensible beam assumption. The Hamilton Extended Principle along with the calculus of variations are used to obtain equations of motion in the time domain. Following this, results from experimental work on samples manufactured 'in-house' are provided. The aim here is the attempted validation of the theoretical model for both uniform and non-uniform samples. Upon completion, the theoretical non-linear model is used to obtain trends on how voltage is effected by piezoelectric material length when harvester designs are subjected to an acceleration level known to induce non-linear behaviour. The outcomes of scenarios where mechanical damping is either fixed or allowed to vary with piezoelectric layer length along with a case where harvester designs have identical fundamental frequencies are reported. These trends are compared to those produced by a linear model and any similarities or differences are discussed.

7.2 Modelling approach

In this section the detailed modelling of a piezoelectric energy harvester which incorporates both material and geometric non-linearity is presented. The general methodology behind the model development is similar to that undertaken by numerous researchers, i.e.

[50, 51]. A schematic of the structure is shown in Figure 7.1. Recall, x_2 is the length of the piezoelectric layer with x_1 being the distance from the clamped end to the beginning of the piezoelectric layer. Other notations are taken in conjunction with [50], with the inertial co-ordinate system represented by (x,y,z) and the local co-ordinate system represented by (ξ,θ,ζ). The Euler-Bernoulli beam assumption is again used, as was the case during linear model development in Chapter 2, whereby the beam is assumed slender, i.e. its thickness is small in comparison to its length, and so effects of shear deformation and rotary inertia can be neglected. This assumption is reasonable for the vast majority of expected energy harvester geometry with confirmation provided in a study by Dietl *et al.* [25]. Dietl *et al.* show discrepancies in the response between piezoelectric energy harvesters modelled as either Euler-Bernoulli or Timoshenko beams only becoming significant when the structure width surpasses structure length. Material non-linearity, for the piezoelectric layer, is included in the model through the use of non-linear constitutive equations. Whereas, geometric non-linearity is realised by assuming the beam is inextensible, i.e. no elongation occurs along the neutral axis. The effects of this shortening from transverse vibrations, will later be used to relate longitudinal displacements, $u(s,t)$, to the transverse displacements, $v(s,t)$.

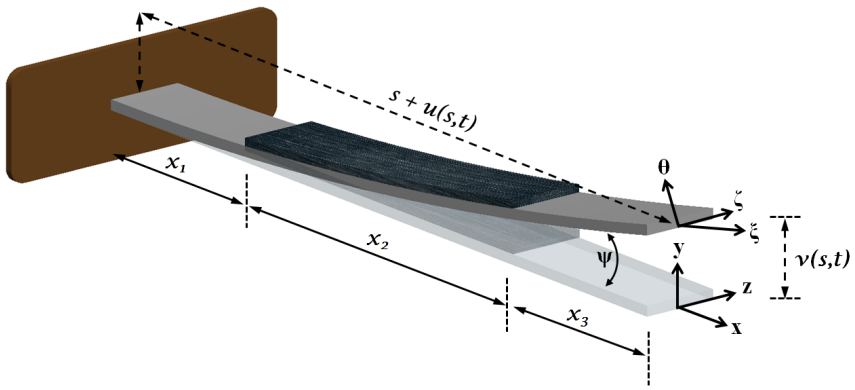

Figure 7.1: A schematic on the notation and displacements used during non-linear model development.

7.2.1 Constitutive equations

The constitutive equation of a material is used to relate axial stress, σ_{11}, to axial strain, ε_{11}, and, in addition for the piezoelectric material, electric displacement, D_3, to axial strain.

Herein, index 3 refers to the y-direction, i.e. through the thickness of the material, and index 1 refers to the x-direction, i.e. parallel to the beam length.

For the substrate material one has

$$\sigma_{11}^{s} = E_s \varepsilon_{11}^{s} \ , \tag{7.1}$$

where superscript s refers to the substrate layer and E_s is the substrate material Young's modulus.

For the piezoelectric material [50] one has

$$\sigma_{11}^{p} = E_p \varepsilon_{11}^{p} + \frac{\mu_1}{2}(\varepsilon_{11}^{p})^2 - E_p d_{31} E_{\text{field}} - \mu_2 \varepsilon_{11}^{p} E_{\text{field}} \tag{7.2}$$

$$D_3 = E_p d_{31} \varepsilon_{11}^{p} + \frac{\mu_2}{2}(\varepsilon_{11}^{p})^2 + \varepsilon_{33} E_{\text{field}} \ , \tag{7.3}$$

where superscript p refers to the piezoelectric layer, E_p is the piezoelectric material Young's modulus, and E_{field} the electric field strength. d_{31} is a piezoelectric material constant and ε_{33} is the material permittivity. The difference between Equations (7.2) and (7.3) and those used during linear modelling, in Chapter 2, is the inclusion of μ_1 and μ_2 which represent coefficients of non-linearity, both specific and unique to a 'batch' of piezoelectric material.

Equations governing the response of the system will be determined through the application of the Hamilton Extended Principle on the Lagrangian of the system in addition to work done on the system. The Lagrangian refers to the difference between kinetic energy, T, and potential energy, U. Expressions for each term are obtained in the following sections.

7.2.2 Potential energy

The potential energy present in the system can be expressed as follows. Note how different segments of the beam are considered individually due to variations in material composition.

$$\begin{aligned} U =& \frac{1}{2}\int_0^{x_1}\iint_{A_s}(\sigma_{11}^s\varepsilon_{11}^s)\mathrm{d}A\mathrm{d}s + \frac{1}{2}\int_{x_1}^{x_1+x_2}\iint_{A_s}(\sigma_{11}^s\varepsilon_{11}^s)\mathrm{d}A\mathrm{d}s \\ &+ \frac{1}{2}\int_{x_1}^{x_1+x_2}\iint_{A_p}(\sigma_{11}^p\varepsilon_{11}^p)\mathrm{d}A\mathrm{d}s + \frac{1}{2}\int_{x_1+x_2}^{L}\iint_{A_s}(\sigma_{11}^s\varepsilon_{11}^s)\mathrm{d}A\mathrm{d}s \\ &+ \frac{1}{2}\int_0^L EA(s)(u'(s,t)+\frac{1}{2}(v'(s,t))^2)^2\mathrm{d}s - \frac{1}{2}\int_{x_1}^{x_1+x_2}\iint_{A_p}E_{\text{field}}(t)D_3\mathrm{d}A\mathrm{d}s\ , \end{aligned} \tag{7.4}$$

where L is the length of the substrate layer – $x_1 + x_2 + x_3$, $\mathrm{d}s$ is the element length, and A_s and A_p are cross-sectional areas for the substrate and piezoelectric material respectively. Figure 7.1 can be referred to for terms $v(s,t)$, the transverse deflection, and $u(s,t)$, the longitudinal deflection, while $(')$ refers to the derivative with respect to arc length, s. Note how, herein, for the deflection terms, dependant variables s and t are excluded for ease in reading. The expression for $EA(s)$ must take into account non-uniform material distribution, realised through the use of Heaviside functions, see Chapter 2.

$$EA(s) = \Big(H(s-0) - H(s-L)\Big)E_s b_s t_s + \Big(H(s-x_1) - H(s-x_1-x_2)\Big)E_p b_p t_p\ . \tag{7.5}$$

An expression for the curvature of a 2D surface can be obtained through the use differential geometry, [60]:

$$\rho = \frac{X'Y'' - X''Y'}{[(X')^2 + (Y')^2]^{1.5}}\ . \tag{7.6}$$

Due to the inextensibility constraint, explained a little later, $(X')^2 + (Y')^2$ is unity. From

Figure 7.1, X and Y are defined as:

$$X = s + u \,, \tag{7.7}$$

$$Y = v \,. \tag{7.8}$$

Using this information the expression for beam curvature becomes:

$$\rho = v'' + v''u' - v'u'' \,, \tag{7.9}$$

and higher powers of beam curvature can be approximated thus (see Appendix C.1.1 for full expressions):

$$\rho^2 \approx (v'')^2 + 2(v'')^2u' - 2v''v'u'' \,, \tag{7.10}$$

$$\rho^3 \approx (v'')^3 \,. \tag{7.11}$$

Assuming the electric field is uniform throughout the constant piezoelectric material thickness, t_p, then $E_{\text{field}}(t)$ in Equation (C.9) can be expressed as:

$$E_{\text{field}}(t) = -\frac{V(t)}{t_p} \,, \tag{7.12}$$

where $V(t)$ is voltage across the piezoelectric layer electrodes.

Manipulation of Equation (7.4) through the use of constitutive relationships, Equations (7.1) - (7.3), utilisation of the strain distribution through beam thickness and expressions for curvature, in addition to performing integration over the cross sectional area of each layer, A_s and A_p, see Appendix C.1.2 for detailed derivations, yields:

$$\begin{aligned} U = \frac{1}{2}\int_0^L \Big\{ & (K_1(s) - K_2(s)V(t))((v'')^2 + 2(v'')^2u' - 2v''v'u'') \\ & + K_3(s)((v'')^3) - K_4(s)(v'' + v''u' - v'u'')V(t) \\ & + EA(s)(u' + \frac{1}{2}(v')^2)^2 - K_5(s)V^2(t) \Big\} \, \mathrm{d}s \,, \end{aligned} \tag{7.13}$$

where the terms K_1 through K_5 are given by:

$$K_1(s) = \Big(H(s-0) - H(s-x_1)\Big)E_sI_s + \Big(H(s-x_1) - H(s-x_1-x_2)\Big)E_sI_{s1} + \Big(H(s-x_1) - H(s-x_1-x_2)\Big)E_pI_{p1} + \Big(H(s-x_1-x_2) - H(s-L)\Big)E_sI_s \ , \tag{7.14}$$

$$K_2(s) = \frac{3}{2}\Big(H(s-x_1) - H(s-x_1-x_2)\Big)\left(\frac{\mu_2 I_{p1}}{t_p}\right) \ , \tag{7.15}$$

$$K_3(s) = \frac{\mu_1}{2}\Big(H(s-x_1) - H(s-x_1-x_2)\Big)I_{p2} \ , \tag{7.16}$$

$$K_4(s) = \Big(H(s-x_1) - H(s-x_1-x_2)\Big)(2E_pd_{31}b_p)\left(t_s + \frac{t_p}{2} - \overline{y}\right) \ , \tag{7.17}$$

$$K_5(s) = \Big(H(s-x_1) - H(s-x_1-x_2)\Big)\left(\frac{b_p\varepsilon_{33}}{t_p}\right) \ . \tag{7.18}$$

$\overline{y}$ is the location of the neutral axis from the bottom of the substrate layer, previously defined in Chapter 2, and I_s, I_{s1}, I_{p1} and I_{p2} are provided by:

$$I_s = \frac{b_st_s^3}{12} \ , \tag{7.19}$$

$$I_{s1} = b_s\left[(t_s)\overline{y}^2 - (t_s^2)\overline{y} + \frac{1}{3}t_s^3\right] \ , \tag{7.20}$$

$$I_{p1} = b_p\left[(t_p)\overline{y}^2 + (-2t_pt_s - t_p^2)\overline{y} + \left(\frac{1}{3}t_p^3 + t_p^2t_s + t_pt_s^2\right)\right] \ , \tag{7.21}$$

$$I_{p2} = b_p\left[\frac{(t_s+t_p-\overline{y})^4}{4} - \frac{(t_s-\overline{y})^4}{4}\right] \ . \tag{7.22}$$

Definitions for remaining variables have also previously been defined in Chapter 2.

Currently the expression for potential energy consists of both longitudinal and transverse deflection terms. However, only transverse vibrations are of interest in this study. At this point the in-extensibility condition can be used to eliminate longitudinal deflection from the energy expression thereby reducing the degrees-of-freedom in the system and simplifying the problem. For the in-extensibility condition to be satisfied, the strain along the neutral axis [50], ε_0, must equate to zero, where ε_0 is given by:

$$\varepsilon_0 = \sqrt{(1+u')^2 + (v')^2} - 1 \ . \tag{7.23}$$

Following expansion and rearrangement one can write:

$$u' = (1 - (v')^2)^{0.5} - 1 \, . \tag{7.24}$$

The use of Taylor's expansion on Equation (7.24) leads to the following approximate relationship between transverse and longitudinal deflections:

$$u' \approx -\frac{1}{2}(v')^2 \, . \tag{7.25}$$

From Equation (7.25), expressions for u, u'', and $\dot{u}$ are trivially obtained:

$$u \approx -\frac{1}{2}\int_0^s (v')^2 \mathrm{d}s \, , \tag{7.26}$$

$$u'' \approx -v''v' \, , \tag{7.27}$$

$$\dot{u} \approx -\frac{1}{2}\frac{\mathrm{d}}{\mathrm{d}t}\int_0^s (v')^2 \mathrm{d}s \approx -\int_0^s v'\dot{v}' \, . \tag{7.28}$$

Using Equations (7.25) and (7.27) in the potential energy expression, Equation (7.13), results in:

$$\begin{aligned} U = \frac{1}{2}\int_0^L \Big\{ & (K_1(s) - K_2(s)V(t))((v'')^2 + (v''v')^2) \\ & + K_3(s)((v'')^3) - K_4(s)(v'' + \frac{1}{2}v''(v')^2)V(t) \\ & - K_5(s)V^2(t) \Big\} \mathrm{d}s \, . \end{aligned} \tag{7.29}$$

7.2.3 Kinetic energy and system Lagrangian

The kinetic energy of such a system can be represented as follows:

$$T = \frac{1}{2}\int_0^L m(s)(\dot{u}^2 + \dot{v}^2)\mathrm{d}s \, , \tag{7.30}$$

and after using the longitudinal-transverse deflection relationship, Equation (7.28), the kinetic energy expression becomes:

$$T = \frac{1}{2}\int_0^L m(s)\left[\left(-\int_0^s v'\dot{v}'\right)^2 + \dot{v}^2\right]\mathrm{d}s\ , \tag{7.31}$$

where the $m(s)$ is the mass per unit length and can be represented as:

$$m(s) = \rho_s A_s + \Big(H(s-x_1) - H(s-x_1-x_2)\Big)\rho_p A_p\ , \tag{7.32}$$

where in turn ρ_s and ρ_p are the substrate and piezoelectric material density respectively. The Lagrangian of the system can be defined as:

$$\mathcal{L} = T - U\ , \tag{7.33}$$

which upon substitution of Equations (7.29) and (7.31) leads to:

$$\begin{aligned}\mathcal{L} = \frac{1}{2}\int_0^L \Bigg\{ & m(s)\left[\left(-\int_0^s v'\dot{v}'\right)^2 + \dot{v}^2\right] \\ & - (K_1(s) - K_2(s)V(t))((v'')^2 + (v''v')^2) - K_3(s)((v'')^3) \\ & + K_4(s)(v'' + \frac{1}{2}v''(v')^2)V(t) + K_5(s)V^2(t)\Bigg\}\,\mathrm{d}s\ .\end{aligned} \tag{7.34}$$

7.2.4 Governing equations of motion

In order to use the Hamilton Extended Principle, the external work acting on the system also requires formulation. External work on the energy harvester results from a combination of base excitation, $\ddot{w}_b(t)$, and the electric potential energy. Note the presence of a negative sign in the following expression is due to the extraction of energy.

$$\mathcal{W} = \left(\iiint_{V_s} \rho_s v \mathrm{d}V_{\text{total}} + \iiint_{V_p} \rho_p v \mathrm{d}V_{\text{total}}\right)\ddot{w}_b(t) - \mathrm{V(t)q(t)}\ , \tag{7.35}$$

where $q(t)$ is the electric charge generated by the energy harvester.

The Hamilton Extended Principle can now be applied to obtain equations of motion which govern the mechanical and electrical response of the energy harvester.

$$\int_{t_1}^{t_2} \delta(\mathcal{L} + \mathcal{W}) \mathrm{d}t = 0 \; . \tag{7.36}$$

Following substitution, and through the application of calculus of variations on each term in the above equation, full details provided in Appendix C.1.3, the following equations of motion are formed:

$$\begin{aligned} & m(s)\ddot{v} + \left[v' \int_L^s m(s) \int_0^s \left(\ddot{v}'' v' + (\dot{v}')^2 \right) \mathrm{d}s \mathrm{d}s \right]' \\ & + \left[\big(K_1(s) - K_2(s) V(t) \big) v'' \right]'' + \left[\Big(\big(K_1(s) - K_2(s) V(t) \big) v'' v' \Big)' v' \right]' \\ & + \left[\frac{3}{2} K_3(s) (v'')^2 \right]'' - \left[\frac{1}{2} K_4(s) V(t) \right]'' + \left[\frac{1}{2} K_4(s) v'' v' V(t) \right]' \\ & - \left[\frac{1}{4} K_4(s) (v')^2 V(t) \right]'' = \left[\iiint_{V_s} \rho_s \mathrm{d}V_{\text{total}} + \iiint_{V_p} \rho_p \mathrm{d}V_{\text{total}} \right] \ddot{w}_b(t) \; , \end{aligned} \tag{7.37}$$

and

$$\begin{aligned} \int_0^L \Bigg\{ & \frac{1}{2} K_2(s) \big((v'')^2 + (v'' v')^2 \big) + \frac{1}{2} K_4(s) \left(v'' + \frac{1}{2} v'' (v')^2 \right) \\ & + K_5(s) V(t) \Bigg\} \mathrm{d}s - q = 0 \; . \end{aligned} \tag{7.38}$$

The boundary conditions associated with Equations (7.37) and (7.38) are:

$$v(0,t) = v'(0,t) = v''(L,t) = v'''(L,t) = 0 \; . \tag{7.39}$$

Classical modal analysis techniques can be used to obtain simplified ordinary differential equations from the existing partial differential equations above. Using this approach the beam deflection, $v(s,t)$, is expressed as an infinite sum of products of normalised eigen-

vectors, $W_r(s)$, and time dependant generalised co-ordinates, $\eta_r(t)$, viz.:

$$v(s,t) = \sum_{r=1}^{\infty} W_r(s)\eta_r(t) \ , \tag{7.40}$$

where 'r' refers the mode number. Substituting this relationship into the equations of motion results in the intermediate equations provided in Appendix C.1.4. The following orthogonality conditions are also utilised on the already mass normalised eigenvectors:

$$\int_0^L W_q(s)m(s)W_r(s)\mathrm{d}s = \delta_{rq} \qquad r,q = 1,2,3,..... \tag{7.41}$$

$$\int_0^L W_q(s)\Big(K_1(s)W_r''(s)\Big)''\mathrm{d}s = \omega_r^2\delta_{rq} \qquad r,q = 1,2,3,..... \tag{7.42}$$

where δ_{rq} is the Kronecker delta function with further details previously provided in Chapter 2. Multiplying the mechanical equation of motion, Equation (7.37), by W_q, integrating over the beam length followed by the rearrangement and collection of terms results in the following modal equation of motion:

$$\begin{aligned}\ddot{\eta}_r(t) + 2\gamma_r\omega_r\dot{\eta}_r(t) + \omega_r^2\eta_r(t) + C_{n1}^r\eta_r^2(t) + C_{n2}^r\eta_r^3(t) + C_{n3}^r\ddot{\eta}_r(t)\eta_r^2(t) \\ + C_{n4}^r\dot{\eta}_r^2(t)\eta_r(t) - C_{n5}^rV(t) - C_{n6}^r\eta_r(t)V(t) \\ + C_{n7}^r\eta_r^2(t)V(t) - C_{n8}^r\eta_r^3(t)V(t) = C_{n9}^r\ddot{w}_b(t)\end{aligned} \tag{7.43}$$

Note how proportional damping, γ_r, has been introduced, as was also the case in Chapter 2, to accommodate for energy dissipation from the system. In Equation (7.43), C_{n1}^r to C_{n9}^r are resulting constants independent of time, provided below:

$$C_{n1}^r = \left[\int_0^L W_q(s)\left[\frac{3}{2}K_3(s)W_r''^2(s)\right]''\mathrm{d}s\right] \tag{7.44}$$

$$C_{n2}^r = \left[\int_0^L W_q(s)\left[\Big(K_1(s)W_r''(s)W_r'(s)\Big)'W_r'(s)\right]'\mathrm{d}s\right] \tag{7.45}$$

$$C_{n3}^r = \left[\int_0^L W_q(s)\left[W_r'(s)\int_L^s m(s)\int_0^s \big(W_r''(s)W_r'(s)\big)\mathrm{d}s\mathrm{d}s\right]'\mathrm{d}s\right] \tag{7.46}$$

$$C_{n4}^r = \left[\int_0^L W_q(s)\left[W_r'(s)\int_L^s m(s)\int_0^s \big(W_r'^2(s)\big)\mathrm{d}s\mathrm{d}s\right]'\mathrm{d}s\right] \tag{7.47}$$

$$C_{n5}^{r} = \left[\int_0^L W_q(s) \left[\frac{1}{2} K_4(s) \right]'' \mathrm{d}s \right] V(t) \tag{7.48}$$

$$C_{n6}^{r} = \left[\int_0^L W_q(s) \Big[\big(K_2(s)\big) W_r''(s) \Big]'' \mathrm{d}s \right] \tag{7.49}$$

$$\begin{aligned} C_{n7}^{r} = & \left[\int_0^L W_q(s) \left[\frac{1}{2} K_4(s) W_r''(s) W_r'(s) \right]' \mathrm{d}s \right] \\ & - \left[\int_0^L W_q(s) \left[\frac{1}{4} K_4(s) W_r'^2(s) \right]'' \mathrm{d}s \right] \end{aligned} \tag{7.50}$$

$$C_{n8}^{r} = \left[\int_0^L W_q(s) \left[\Big(\big(K_2(s)\big) W_r''(s) W_r'(s) \Big)' W_r'(s) \right]' \mathrm{d}s \right] \tag{7.51}$$

$$C_{n9}^{r} = \left[\iiint_{V_s} \rho_s W_q(s) \mathrm{d}V + \iiint_{V_p} \rho_p W_q(s) \mathrm{d}V \right] \tag{7.52}$$

Taking Equation (7.38), following differentiation with respect to time, the rate of change in charge, $\dot{q}(t)$, i.e. current, is expressed by $-V(t)/R_{\mathrm{load}}$. This formulation is acceptable here as investigations only concern voltage across various load resistors. Research on energy harvesters behaving in a non-linear manner connected to storage capacitors is beyond the scope of current work.

$$\begin{aligned} & C_{n10}^{r} \eta_r(t) \dot{\eta}_r(t) + C_{n11}^{r} \eta_r^3(t) \dot{\eta}_r(t) + C_{n12}^{r} \dot{\eta}_r(t) + C_{n13}^{r} \eta_r^2(t) \dot{\eta}_r(t) \\ & \qquad + C_{n14}^{r} \dot{V}(t) + \frac{V(t)}{R_{\mathrm{load}}} = 0 \end{aligned} \tag{7.53}$$

In Equation (7.53), C_{n10}^{r} to C_{n14}^{r} are constants independent of time given by:

$$C_{n10}^{r} = \left[\int_0^L K_2(s) W_r''^2(s) \mathrm{d}s \right] \tag{7.54}$$

$$C_{n11}^{r} = \left[\int_0^L 2K_2(s) \big(W_r''^2(s) W_r'^2(s) \big) \mathrm{d}s \right] \tag{7.55}$$

$$C_{n12}^{r} = \left[\int_0^L \frac{1}{2} K_4(s) W_r''(s) \mathrm{d}s \right] \tag{7.56}$$

$$C_{n13}^{r} = \left[\int_0^L \frac{3}{2} K_4(s) \left(\frac{1}{2} W_r''(s) W_r'^2(s) \right) \mathrm{d}s \right] \tag{7.57}$$

$$C_{n14}^{r} = \left[\int_{0}^{L} K_5(s) \mathrm{d}s \right] \tag{7.58}$$

Equations (7.43) and (7.53) represent the behaviour of unimorph vibrational piezoelectric energy harvesters and can be solved simultaneously to determine transverse vibrations along the structure and voltage generated by the energy harvester. The possibility of non-linear behaviour from high acceleration levels is realised through geometric non-linearity by considering the in-extensibility constraint and material non-linearity in the form of μ_1 and μ_2. Simulations with arbitrary forcing applied to the structure including those with larger acceleration levels can be preformed confidently, with Section 7.3 showing a model validation. Although for the purpose of these works simulations with solely harmonic base excitation are undertaken, steady-state analytical expressions for the equations of motion will not be obtained, i.e. through the use of perturbation techniques such as the method of multiple scales performed in for example [30, 50], allowing for flexibility in future model use. Rather, Equations (7.43) and (7.53) are readily solved numerically, a task undertaken using ode solvers in MATLAB® through the SIMULINK® interface, with the recording of data once steady-state response has been achieved. The SIMULINK® models representing the two equations of motion have been provided in Appendix C.2.

7.3 Experimental work

In this section the attempted validation of the theoretical model presented in Section 7.2 through experimental work is undertaken. New batches of energy harvester samples were manufactured in-house using the techniques outlined in Chapter 4. The dimensions and known material properties for substrate and piezoelectric layers are provided in Table 7.1. The coefficients, μ_1 and μ_2, which represent material non-linearity, are unique for each piezoelectric material batch, see for example [4], and are not provided on the data sheets of material manufacturers. The magnitude of these coefficients, along with the magnitude of mechanical damping, are estimated through curve fitting techniques. All experimental

testing and theoretical simulations will be performed close to the fundamental frequency of the structure. Inclusion of modal information relating to only the first mode of vibrations is therefore required, i.e. $r = 1$ in the equations of motion.

Table 7.1: Structural dimensions and material properties of harvesters used throughout this chapter.

Parameter	Magnitude
Al width (mm)	7
Al thickness (mm)	0.87
PZT width (mm)	7
PZT thickness (mm)	0.5
Young's modulus of Al (GPa)	69
Density of Al (kg.m^{-3})	2700
Young's modulus of PZT (GPa)	62.1
Density of PZT (kg.m^{-3})	7800
Piezoelectric constant, d_{31} (m.V^{-1})	-180$\times$10^{-12}
Permittivity, ε_{33}^{S} (F.m^{-1})	1.549$\times$10^{-8}

Measurements for tip displacement during testing are obtained after conversion of velocity measurements from the laser vibrometer whereas the voltage generated across load resistances is measured using the dynamic signal analyser. All other equipment required during testing and detailed testing procedure have prior been provided in Chapter 4.

7.3.1 Validation when energy harvester is in closed circuit conditions

In this section validation of the non-linear theoretical model for scenarios where energy harvesters are in a closed-circuit electrical condition is attempted. A closed circuit electrical condition has initially been chosen as this eliminates the necessity to estimate one of the non-linear coefficients, namely μ_2, appearing in constant K_2, Equation (7.15), within certain time independent constants, Equations (7.49) and (7.51), which make up the mechanical equation of motion. The process of curve fitting is made simpler through this scenario as only μ_1 and γ require estimation through a trial and error approach. Model validation with a conventional sample, whereby both piezoelectric and substrate lengths are identical, was first attempted with results presented in Figure 7.2. The extended length of each layer is 43.82$\pm$1 mm.

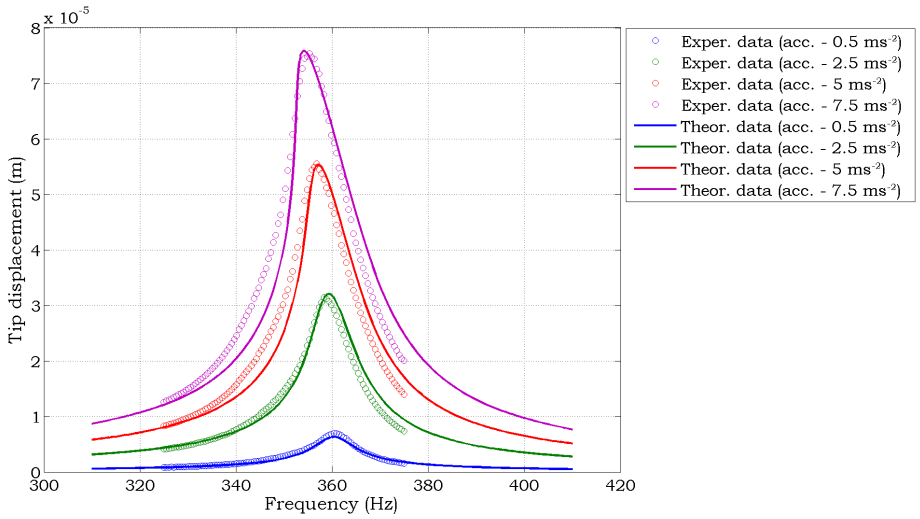

Figure 7.2: Comparison between theoretical and experimental tip displacement responses, for a conventionally designed energy harvester, in closed circuit conditions, subjected to various acceleration levels.

Figure 7.2 shows experimental data superimposed with theoretical results for four different base acceleration levels – 0.5 m.s^{-2}, 2.5 m.s^{-2}, 5 m.s^{-2} and 7.5 m.s^{-2}. Slight discrepancies exist at the tails of the frequency response plots. However, when considering the location of peak tip displacement, a good agreement with experimental data across the acceleration range can be achieved. From the experimental data, one can conclude that non-linearity is present in real situations with the occurrence of 'softening' behaviour. The resonant frequency of the structure was found to be 360.4 Hz at 0.5 m.s^{-2}, shifting to 355.3 Hz at 7.5 m.s^{-2}. Trial and error resulted in the coefficient μ_1 requiring a magnitude of -7$\times$10^{14} Pa in order to replicate this 4.9 Hz shift. The mechanical damping ratio required to fit theoretical trends to experimental data was found to be dependant on the magnitude of base acceleration, an observation also made by previous researchers, e.g. Yao *et al.* [105], and over the range of base accelerations used in these works this relationship was found to be linear, also in agreement with Yao *et al.* [105] along with Mak [51]. The half-power point method, a technique previously outlined in Chapter 3, is used to extracted mechanical damping magnitude from experimental frequency response plots. Figure 7.3 shows the damping ratios obtained in correspondence to Figure 7.2. Details on possible causes for this damping variation phenomenon can be found in a study by Nouira *et al.* [67]. In the experimental setup used during these works, causes are likely to include – air

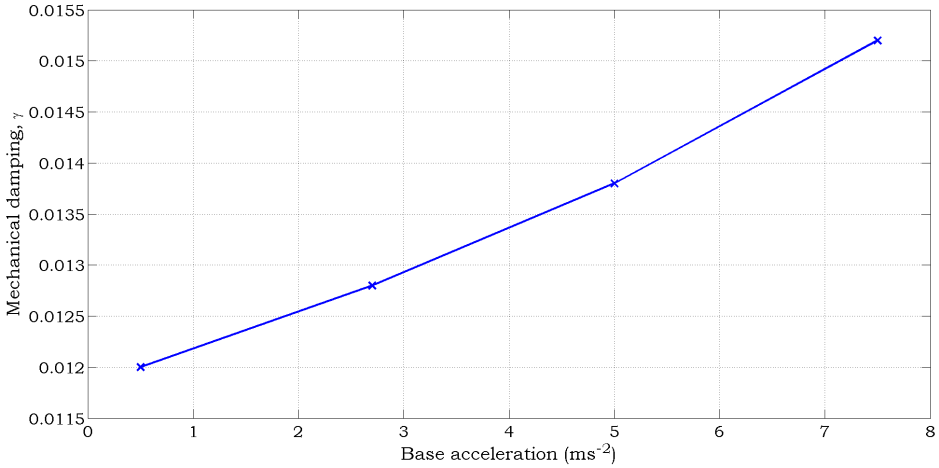

Figure 7.3: Dependency of mechanical damping on base acceleration. Extracted from experimental data using half-power-point method.

flow damping, stick-slip at the clamped end, material damping and thermoelastic damping. In-depth model development incorporating such effects is beyond the scope of these works and since the parametric studies in Section 7.4 are performed at a fixed acceleration level one can correctly assume that the variations in damping magnitude are proportional to the geometric parameter of interest, from Chapter 4, rather than base acceleration.

Model validation using non-uniform energy harvesters was also attempted with the results of two such samples presented in Figures 7.4 and 7.5. For the first sample, substrate and piezoelectric layer length was 43.70$\pm$1 mm and 41.13$\pm$1 mm respectively. Whereas for the second sample, layer lengths were 45.95$\pm$1 mm and 18.15$\pm$1 mm respectively. Note, samples were mounted with both substrate and piezoelectric layers in the clamp, i.e. $x_1 = 0$.

In Figures 7.4 and 7.5, during the generation of theoretical results, the magnitude of μ_1 was assigned a magnitude of -7$\times 10^{14}$ Pa, previously found during conventional design testing. The variation in mechanical damping is again found to increase quasi-linearly with base acceleration across the tested range, see Figure 7.6. Sample 1, with the longer piezoelectric layer yielded good agreement between theoretical and experimental results. Both peak tip displacement amplitudes and the shift in frequency is accurately represented through the developed non-linear theoretical model. Across the acceleration range the resonant frequency shift for this particular sample is 6 Hz. An increase is observed when

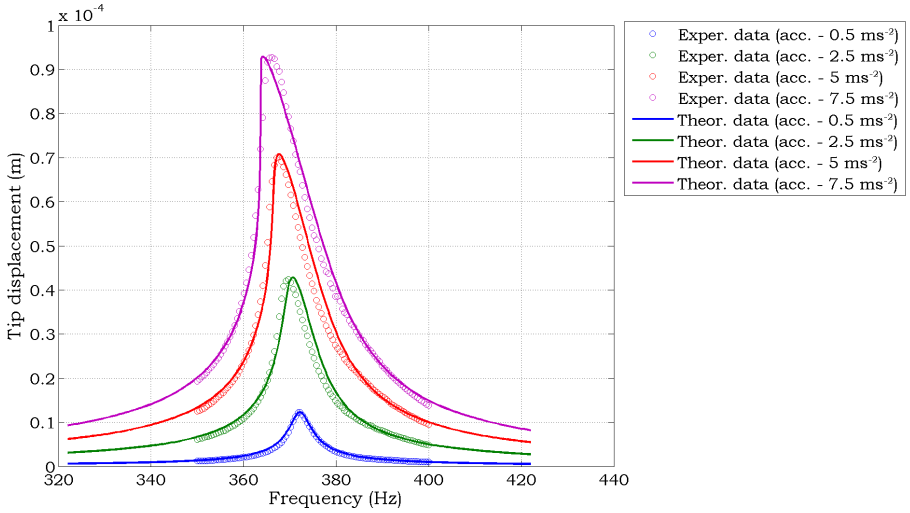

Figure 7.4: Comparison between theoretical and experimental tip displacement responses, for first non-uniform energy harvester, in closed circuit conditions, subjected to various acceleration levels.

comparing with the conventional sample frequency shift due to an increase in deflection. When both samples were subjected to a base acceleration of 0.5 m.s^{-2}, sample 1 exhibited a 74% increase in tip deflection due to improved mechanical forcing and a reduction in mechanical damping. In contrast to the good theoretical-experimental agreement obtained for sample 1, sample 2, see Figure 7.5, with the shorter piezoelectric layer, showed poor theoretical-experimental agreement. There is reasonable agreement for the peak amplitudes through the use of extracted mechanical damping ratios, however, the theoretical model fails to predict the shift in resonant frequency through 'softening'. Across the base acceleration range, experimental data shows a frequency shift of 4 Hz in comparison to the 1.2 Hz observed from the developed non-linear model. An additional form of non-linearity is clearly present during experimental testing, and to gain a deeper insight into the cause, samples comprising of solely aluminium were tested with the outcome presented in Section 7.3.2.

A further note on mechanical damping variations; the result obtained for these two samples in addition to the conventionally designed sample emphasize the complexity and uncertainty involved in regards to mechanical damping. While increasing base acceleration from 0.5 m.s^{-2} to 7.5 m.s^{-2}, mechanical damping for the conventionally designed sample increases by 27%, 102% for the first non-uniform sample, and 94% for the second non-uniform sample. As previously mentioned a detailed insight into the causes of variations in

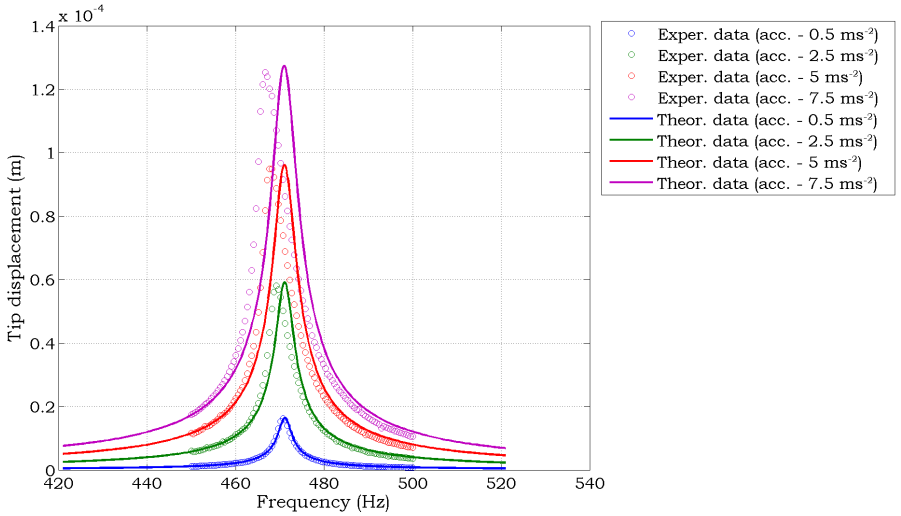

Figure 7.5: Comparison between theoretical and experimental tip displacement responses, for second non-uniform energy harvester, in closed circuit conditions, subjected to various acceleration levels.

mechanical damping and a realistic representation of such variations is beyond the scope of these works. The general trend which was reported in Chapter 4 is still evident however. Mechanical damping reduces with piezoelectric layer length suggesting designs with shorter piezoelectric layers may be beneficial from an energy loss point of view.

7.3.2 Testing aluminium beams in the experimental setup

In this section results from an aluminium beam, tested in the experimental setup, are presented. The purpose of this test was to determine the extent to which non-linearity in the system exists when piezoelectric material is excluded, a hypothesis created after testing samples with short piezoelectric layers. Dimensions of the sample under consideration were chosen to be similar to the substrate layer used in energy harvester composition and are 43 ± 1 mm $\times$ 7 mm $\times$ 0.87 mm. Experimental data obtained for tip displacements at four base acceleration levels, superimposed with theoretical trends from the current non-linear model, are shown in Figure 7.7. In similar fashion to before, the mechanical damping ratios used in the theoretical model are extracted from the experimental frequency response plots, see Figure 7.8. Variation in mechanical damping with base acceleration still occurs for reasons outline in Section 7.3.1.

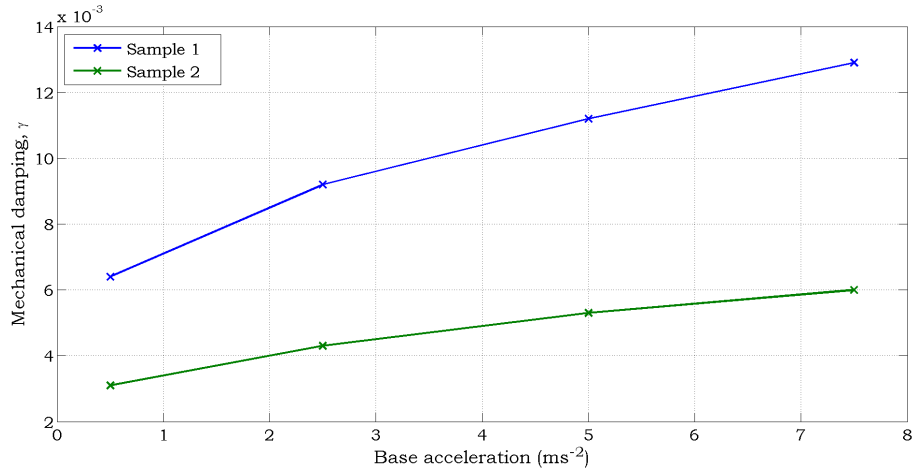

Figure 7.6: Dependency of mechanical damping on base acceleration for two non-uniform samples.

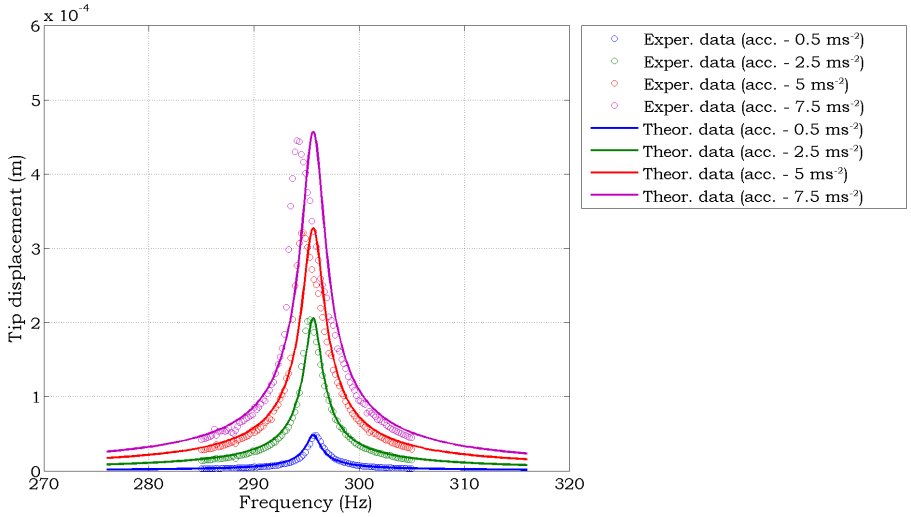

Figure 7.7: Experimental frequency responses of an aluminium beam at varying base acceleration levels.

The experimental data in Figure 7.7 clearly indicates the presence of non-linearity as the base acceleration magnitude is increased. A shift of 1.8 Hz in resonant frequency occurs in the experiment contrasted to a 0 Hz shift for the currently developed non-linear model. It is worthwhile mentioning that geometric non-linearity, factored in during equation of motion derivation, does not have any effect on this particular system. Across the examined base acceleration range, with the chosen sample dimension and material properties, peak deflections are in the range of 0.5 mm which is thought not to be sufficient, on this manufacturing scale, to introduce geometric non-linearity. Moreover, geometric non-linearity results in a 'hardening' effect, and not the 'softening' effect observed here. Mak [51] ob-

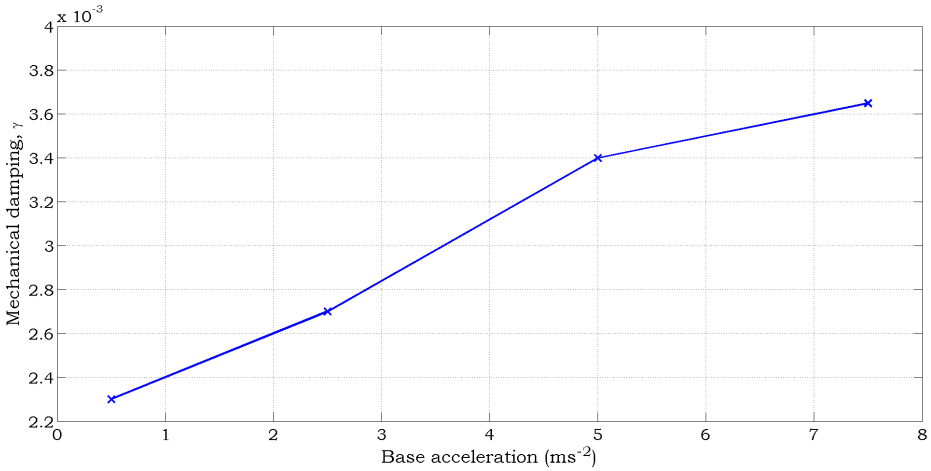

Figure 7.8: Dependency of mechanical damping on base acceleration for aluminium beam.

served similar behaviour whereby geometric non-linearity only became noticeable once his sample was subjected to a base acceleration of $50g$. Although his sample dimensions were on a smaller scale the same reasoning of a low tip displacement causing negligible geometric non-linearity applies. In the following section the author will attempt to theoretically accommodate for the observed additional non-linearity whose influence on the current theoretical model cannot predict.

7.3.3 Accommodation of additional non-linearity

There are numerous studies on the incorporation of non-linearity in vibrating systems with the thesis of Malatkar [53] providing a detailed overview. Briefly, these include, but are not limited to:

- Damping non-linearity. This has already been observed from experimental data and, although detailed modelling is beyond the scope of these works, accommodation in theoretical results takes the form of a linear increase with base acceleration.
- Geometric non-linearity. Already accounted for in the model but essentially irrelevant for this particular case due to small deflections in relation to structure size.
- Material non-linearity. Implemented in material constitutive equations, currently included for the piezoelectric material but could also be present for substrate layers.

- Boundary condition non-linearity. This can be implemented by replacing a 'perfect clamp' boundary condition with one which accounts for torsional flexibility, see for example [92]. The existence of this effect in the present experimental setup was examined through the manufacture of a new clamp. The same outcome was observed with the occurrence of 'softening' behaviour even for aluminium cantilever beams. Additionally, measurements of velocity were taken at various locations on the clamp to determine if a rocking phenomenon was occurring. However, even at the highest used acceleration level of 7.5 m.s^{-2} no significant presence was observed.

In these works the author will make an assumption that the additional non-linearity present in the experimental setup comes from the substrate material itself and manifests itself in the form of a higher order term in the substrate constitutive equation. Adopting a similar symbol convention to that used for piezoelectric material yields the following constitutive equation for substrate material:

$$\sigma_{11}^{s} = E_s \varepsilon_{11}^{s} + \frac{\mu_{s1}}{2}(\varepsilon_{11}^{s})^2 \,, \tag{7.59}$$

where superscript μ_{s1} is the coefficient of non-linearity for the substrate layer. After working this new constitutive equation through the detailed derivation provided in Section 7.2 it is realised that the only affected term is the time-independent constant C_{n1}^{r}, Equation (7.44), in the equation of motion, Equation (7.43). The difference between the previous non-linear model and this current non-linear model can be found in the definition of term $K_3(s)$. The new expression for this constant is provided below:

$$\begin{aligned} K_3(s) = &\frac{\mu_{s1}}{2}\Big(H(s-0) - H(s-x_1)\Big) I_{s2} + \frac{\mu_{s1}}{2}\Big(H(s-x_1) - H(s-x_1-x_2)\Big) I_{s2} \\ &+ \frac{\mu_1}{2}\Big(H(s-x_1) - H(s-x_1-x_2)\Big) I_{p2} + \frac{\mu_{s1}}{2}\Big(H(s-x_1-x_2) - H(s-L)\Big) I_{s2} \,, \end{aligned} \tag{7.60}$$

where I_{s2}, see Appendix C.1.2, is given by:

$$I_{s2} = b_s \left[\frac{(t_s - \overline{y})^4}{4} - \frac{(-\overline{y})^4}{4} \right] \,, \tag{7.61}$$

with all other terms and constants defined in Section 7.2.

Using the new theoretical model, with a trial and error approach to obtain a suitable magnitude for μ_{s1} provides the results presented in Figure 7.9.

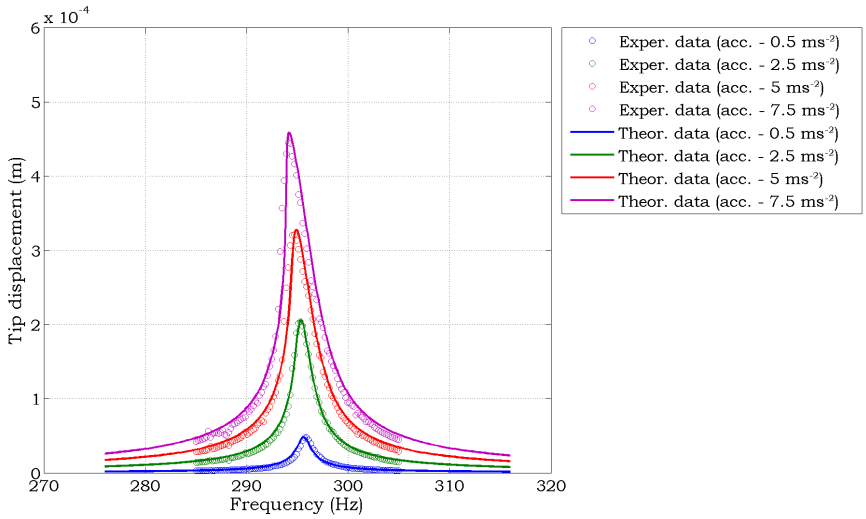

Figure 7.9: Experimental frequency responses of an aluminium beam at varying base acceleration levels with the inclusion of substrate material non-linearity. Theoretical trends shown here can be contrasted to those previously presented in Figure 7.7.

The mechanical damping magnitudes used to produce theoretical results were previously obtained from experimental data and can be extracted from Figure 7.8. The theoretical model requires a μ_{s1} magnitude of -2$\times$10^{13} Pa to represent the desired shift in resonant frequency across the base acceleration range. Note how the non-linearity coefficient is 35 times smaller than that obtained for the piezoelectric material which indicates a large difference in the extent of material non-linearity between piezoelectric and substrate materials as one would ordinarily expect. Non-linear constitutive equations for metals (the substrate layer in these works) can be found in literature but not in the form presented here and are commonly valid in severe operating conditions, i.e. use of the Ramberg-Osgood equation at high temperatures [15]:

$$\epsilon_{11}^{s} = \frac{\sigma_{11}^{s}}{E_s} + \frac{(\sigma_{11}^{s})^{n}}{F_s} \tag{7.62}$$

where superscript n is the strain-hardening exponent and F_s is known as the non-linear modulus. The Ramberg-Osgood was not used due to the conditions in which it is valid not

being present. The model for substrate non-linearity proposed in these works is not ideal, and with more time improvements in modelling would have been made, but, rather, acts as a means to match theoretical results with experimental data.

Two of the cases presented in Section 7.3.1 will now be revisited to verify the addition of substrate material non-linearity in the theoretical model is acceptable across the full range of energy harvester design configurations. The sample with a conventional design, previous results can be found in Figure 7.2, and the second non-uniform sample, previous results can be found in Figure 7.5, are under investigation here. Figures 7.10 and 7.11 show theoretical trends generated from the new non-linear model superimposed onto originally obtained experimental data. The magnitude of mechanical damping for both samples at each base acceleration level has previously been provided in Section 7.3.1 – Figures 7.3 and 7.6. During the generation of all theoretical results presented herein the previously determined μ_{s1} value of -2$\times$10^{13} Pa is used.

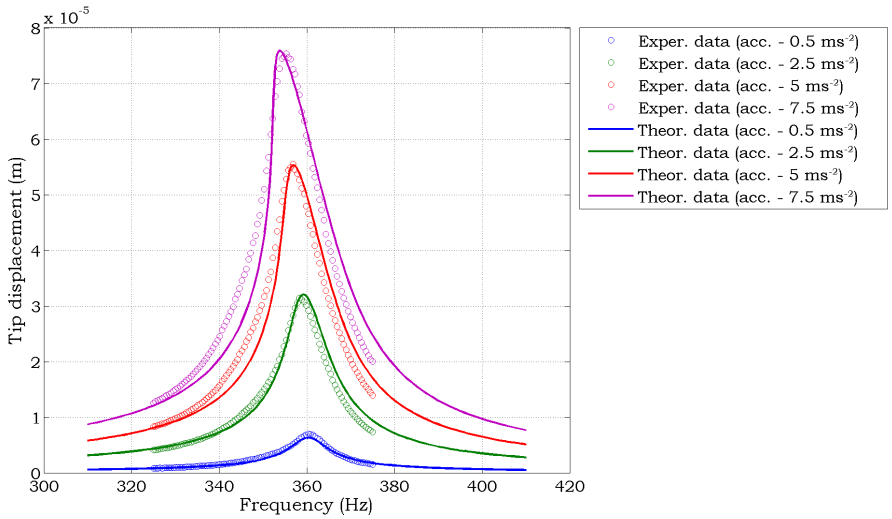

Figure 7.10: Comparison between theoretical and experimental tip displacement responses, for a conventionally designed energy harvester, in closed circuit conditions, subjected to various acceleration levels. Substrate non-linearity also included. Theoretical trends shown here can be contrasted to those previously presented in Figure 7.2.

The conventionally designed sample, Figure 7.10, maintains good agreement between experiment and theory with the inclusion of substrate material non-linearity. The difference in peak tip displacement location between models without and with substrate material non-linearity, while exciting the sample at 7.5 m.s^{-2}, is only 0.2 Hz or 0.06%. The reason behind

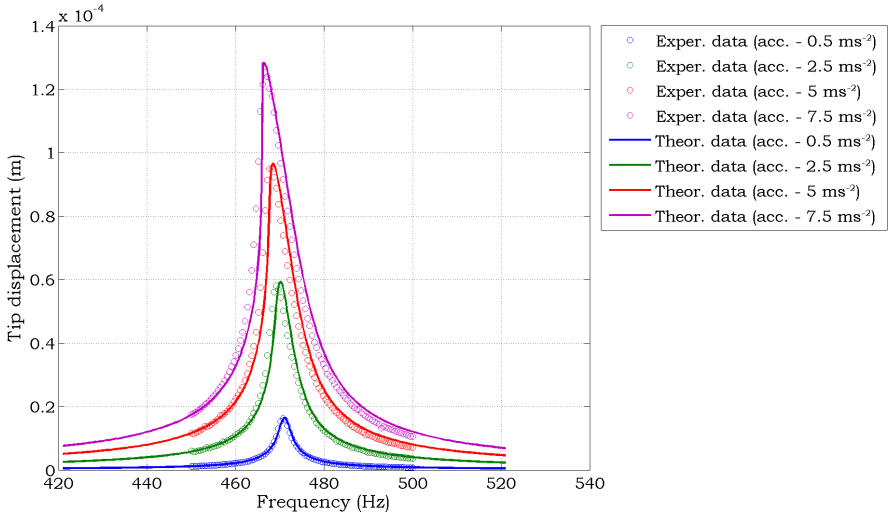

Figure 7.11: Comparison between theoretical and experimental tip displacement responses, for second non-uniform energy harvester, in closed circuit conditions, subjected to various acceleration levels. Substrate non-linearity also included. Theoretical trends shown here can be contrasted to those previously presented in Figure 7.5.

theoretical trends for conventionally designed samples (and samples with large piezoelectric layers) not being effected a great deal by substrate material non-linearity is due to the dominant contribution from piezoelectric material non-linearity, indicated by the magnitudes of μ_1 and μ_{s1}.

For sample 2, comprising of an 18.15$\pm$1 mm piezoelectric layer, poor theoretical-experimental agreement was obtained while using the initially developed non-linear model. Figure 7.11 however shows that the inclusion of substrate material non-linearity rectifies the issue with both theory and experiment in good agreement with one another. The 6 Hz shift in resonant frequency observed during experimental testing is emulated by using the improved non-linear theoretical model with predetermined coefficient magnitudes. Lastly, to conclusively show the model works across the piezoelectric layer length range, Figure 7.12 shows the results from a sample comprising of a 9.77$\pm$1 mm piezoelectric layer attached to a 45.49$\pm$1 mm substrate layer. Information regarding mechanical damping variation is provided in Figure 7.13.

The experimental data in Figure 7.12 shows the presence of slight non-linearity for this particular sample. A small resonant frequency shift of 1.6 Hz is observed. It is believed

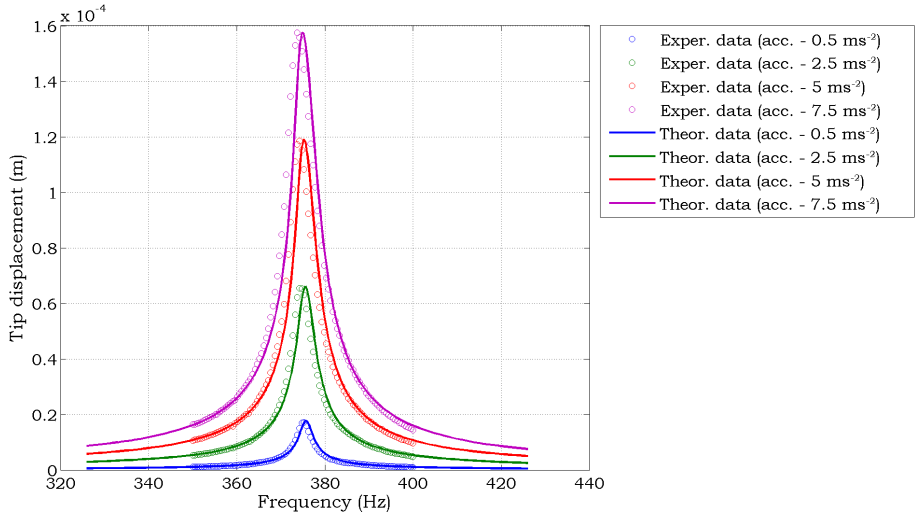

Figure 7.12: Comparison between theoretical and experimental tip displacement responses, for a third non-uniform energy harvester, in closed circuit conditions, subjected to various acceleration levels. Substrate non-linearity also included.

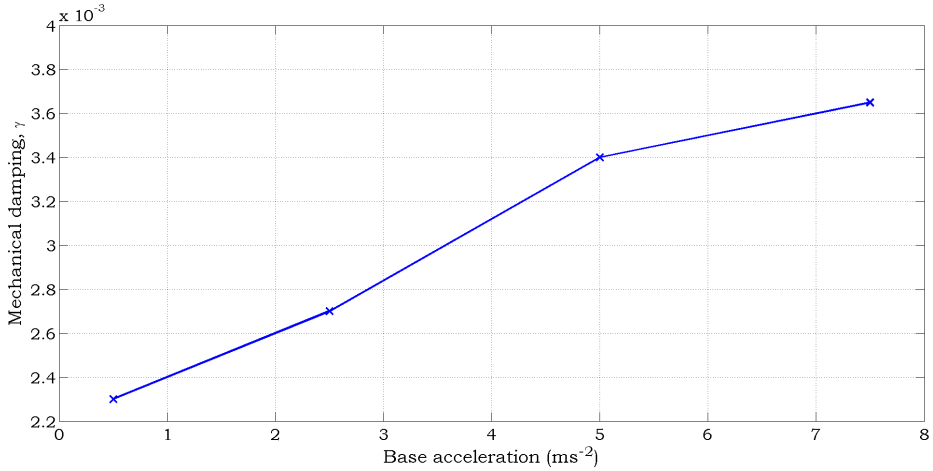

Figure 7.13: Dependency of mechanical damping on base acceleration for a third non-uniform sample.

that sample composition, i.e. having a short piezoelectric layer, (along with the relatively small deflections undertaken by the sample) is responsible for the smaller resonant frequency shifts in comparison to results presented for other samples. Now the theoretical non-linear model has been validated for cases where electrical load is absent, the next step is to introduce a resistor in the experimental setup and determine whether the model can continue to correctly predict dynamic response and, in addition, energy harvester performance.

7.3.4 Inclusion of a resistor representing electrical load

In this section a load resistor is introduced into the experimental setup and results for a conventionally designed sample are presented and discussed. The magnitudes of μ_1 and μ_{s1} (-7$\times$10^{14} Pa and -2$\times$10^{13} Pa respectively) found from previous closed circuit testing are still valid as the energy harvester sample was manufactured from the same 'batch' of sheet piezoelectric material. The two variables which require estimation are μ_2 and γ. Dimensions for the sample under consideration are provided in Table 7.1 with a 45.02 mm$\pm$1 mm extended length. Figure 7.14 shows experimental data superimposed with theoretical trends when no electrical load is present. This was required to determine the mechanical damping magnitude at each excitation level, Figure 7.15, and is further confirmation that the determined magnitudes of μ_1 and μ_{s1} are adequate for this batch of samples.

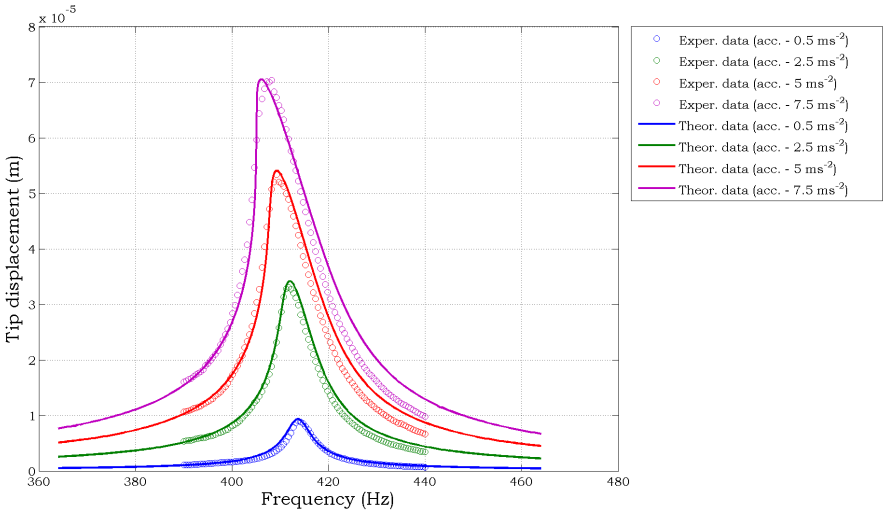

Figure 7.14: Comparison between theoretical and experimental tip displacement responses, for a conventionally designed energy harvester, in closed circuit conditions, subjected to various acceleration levels. Substrate non-linearity also included.

As the base acceleration is ramped up, Figure 7.14, shows expected non-linear behaviour with resonant frequency shifting by 6.5 Hz or 1.57%. Figure 7.16 provides the results obtained when a 150 kΩ resistor is introduced to the system. The first thing to note is that good agreement between experimental and theoretical voltage responses is achievable without the necessity of non-linear coefficient μ_2. The effects of μ_2 on the theoretical model were investigated resulting in the realisation that μ_2 has little influence on the the-

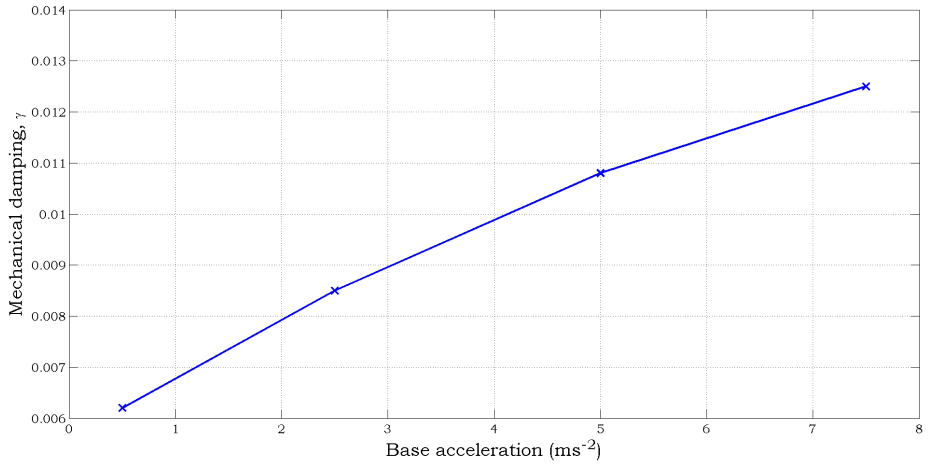

Figure 7.15: Dependency of mechanical damping on base acceleration for the conventionally designed sample.

oretical frequency response. It is believed that this coefficient can be assumed zero in an energy harvesting scenario due to the inherently low voltage levels. Applications utilising piezoelectric material for actuation are subjected to higher voltage levels and in these situations the non-linear coefficient, μ_2, would have a more significant impact on theoretical results.

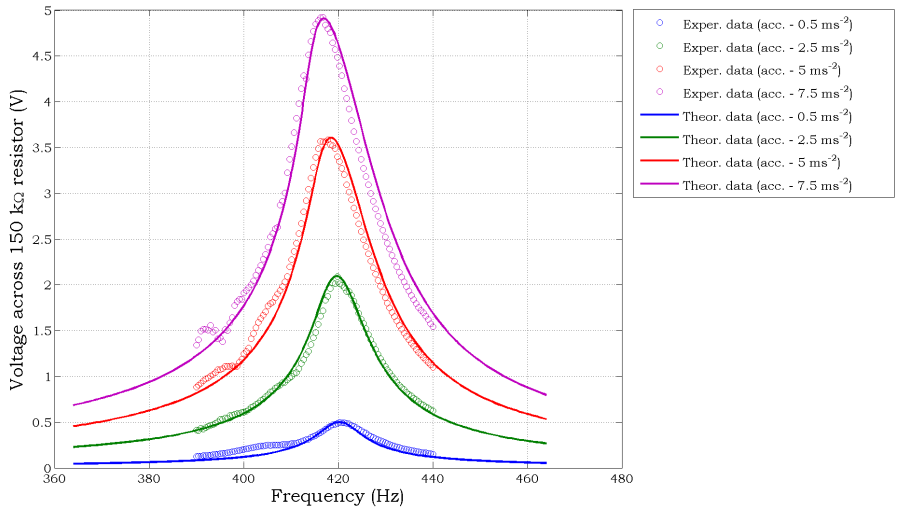

Figure 7.16: Comparison between theoretical and experimental voltage responses, for a conventionally designed energy harvester, connected to a 150 kΩ resistor, subjected to various acceleration levels. Substrate non-linearity also included.

By comparing the frequency shift for cases with and without a resistor, as one would expect, the level of non-linearity reduces when energy is extracted from the system by addi-

tion of an electrical load. This phenomenon has correctly been replicated by the theoretical model. The frequency shift (from an excitation of 0.5 m.s^{-2} to 7.5 m.s^{-2}) reduces to 3.5 Hz or 0.84% from the prior 1.57%. In addition to the correct prediction of a reduced frequency shift, when excited at a low acceleration level to the extent which the system is linear, the theoretical model adequately predicted the overall 6.6 Hz shift in resonant frequency from the inclusion of a load resistor. In the penultimate section the validated theoretical non-linear model, which includes both substrate and piezoelectric material non-linearity in addition to geometric non-linearity, is used to examine how trends in parameter vs. voltage are influenced by base excitation magnitudes.

7.4 Device optimisation while using the non-linear model

In this section comparisons in the trends relating piezoelectric layer length with generated voltage between linear and non-linear energy harvester models are presented and discussed. The dimensions and material properties for the first set of results will remain identical to those used during experimental work in Section 4.3.2 and are provided in Table 7.1. Piezoelectric layer length is the parameter of interest and it is reduced from the free end by increments of 1 mm while the substrate layer length remains fixed at 50 mm. A reduction in length from the free end has been chosen as this modification was previously shown in Chapter 3 to benefit the performance of a rectangular cantilevered energy harvester. Case studies with fixed and varying mechanical damping magnitudes are considered along with single and multiple geometric parameter changes – recall how multiple geometric parameters are modified systematically to create configurations with identical fundamental frequencies, Chapter 6. The base acceleration applied in each case will remain constant at 7.5 m.s^{-2}, a magnitude known to induce non-linear behaviour. The outcome of detailed experimental work, presented in Chapter 4, indicated a general reduction in mechanical damping with piezoelectric layer length. This phenomenon is implemented here by assuming damping magnitude varies linearly from 0.014 (both layers being identical in length) to 0.004 (no piezoelectric material present) with piezoelectric layer length. The reasoning behind the selection for these numbers comes from a desire to remain consistent with assumptions used

in Chapter 5, in addition to an assumption that damping magnitude increases two-fold when base excitation increases fifteen-fold.

7.4.1 Comparison between models when damping magnitude is fixed

Figure 7.17 shows the impact of using a more realistic non-linear model in comparison to a linear model when examining the influence of piezoelectric layer length on the voltage across a 1 MΩ load resistance. Note that the damping is currently assumed fixed at 0.005.

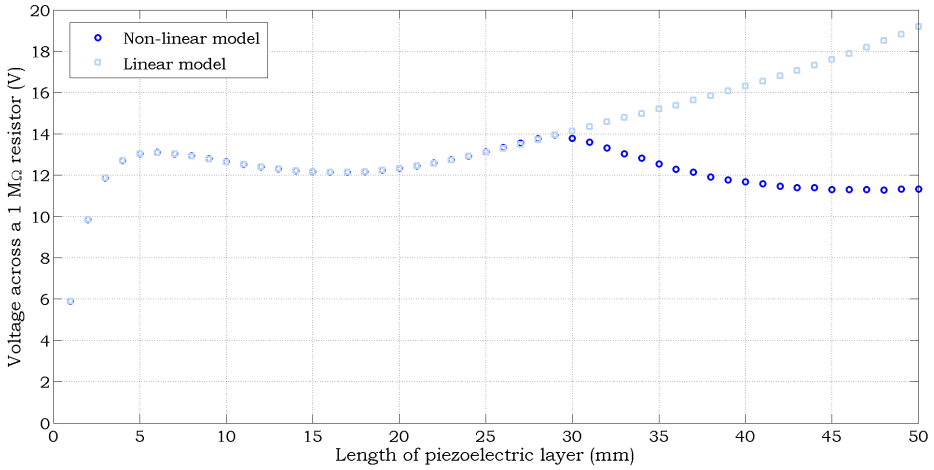

Figure 7.17: Trends between piezoelectric layer length and voltage, generated with linear and non-linear models, when energy harvester connected to a 1 MΩ resistor. Fixed damping of 0.005.

The outcome in Figure 7.17 shows that there are differences between the two models for certain sample configurations. These are seen to materialise for longer piezoelectric layer lengths whereas for shorter lengths any differences can be assumed negligible. It was shown in Section 7.3 that samples with longer piezoelectric layers tend to exhibit a greater degree of non-linearity and the authors believe that this is the root cause of differences between the two sets of results. Recall how a balance between the optimisation of mechanical forcing and electromechanical coupling governs the general trend for the linear model. In terms of discrepancies for this particular case, with the assumptions made regarding damping magnitude, the linear model (while considering the conventional design) over-predicts the voltage by 7.9 V or 70%.

7.4.2 Comparison between models when damping magnitude is not fixed

The next set of results, see Figure 7.18, shows the same comparison, however, on this occasion the damping magnitude is assumed linearly proportional to the piezoelectric layer length.

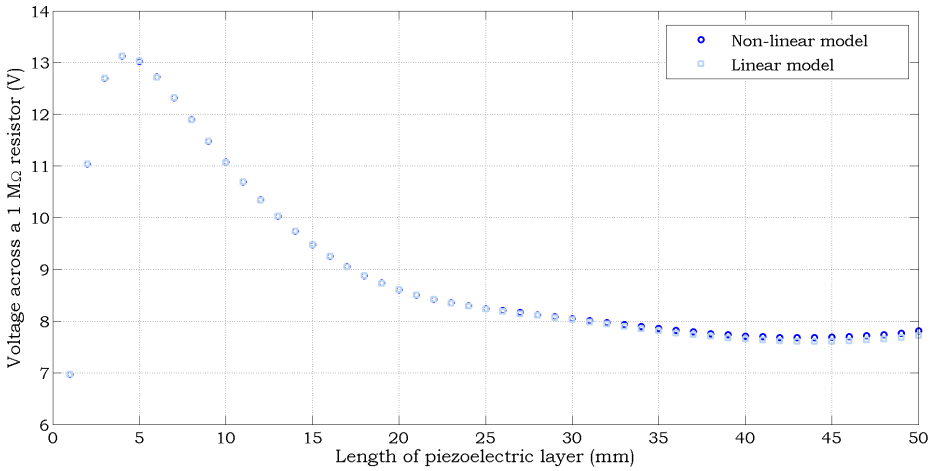

Figure 7.18: Trends between piezoelectric layer length and voltage, generated with linear and non-linear models, when energy harvester connected to a 1 MΩ resistor. Damping varies depending on length.

This set of results provides an entirely different outcome. Figure 7.18 shows that both linear and non-linear models predict similar voltage levels across the full range of piezoelectric layer lengths. Since samples with shorter piezoelectric layers have lower mechanical damping the reduced energy loss is beneficial and results show an optimum device consisting of a rather short piezoelectric layer. Maximum discrepancy between the models is approximately 1.2% which occurs for the conventional design. Magnitude of damping for samples with longer piezoelectric layers (in the most extreme case, 0.014 rather than 0.005 used prior) acts to restrain deflections which in turn is limiting the magnitude of non-linearity experienced by these samples, i.e. the increase in non-linearity from an increase in piezoelectric material is being countered by an increase in damping. On the face of it, it may now appear that the newly developed non-linear model is surplus, however, it is important to also examine the frequency responses generated by the model, see Figure 7.19.

Figure 7.19 compares frequency response plots obtained by both linear and non-linear models for a sample comprising of a 44 mm piezoelectric layer. A 6.2 Hz difference in

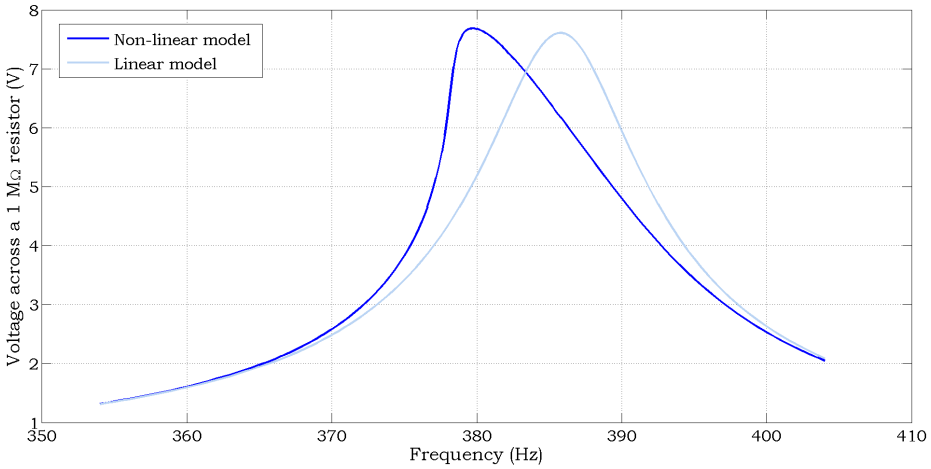

Figure 7.19: Frequency response plots, generated with linear and non-linear models, when energy harvester connected to a 1 MΩ resistor.

resonant frequency is present between the two models and if a designer was using the linear model to predict performance, an overestimation of 23% in voltage would have occurred (at the resonant frequency predicted the linear model). These examples here highlight the necessity and desirability of a non-linear model to approximate the frequency at which peak performance is expected and the level of performance one would expect if the harvester is subjected to a range of excitation amplitudes.

7.4.3 Simulations for harvester designs with a constant fundamental frequency

Lastly, results from a study on how performance trends from linear and non-linear models differ when comparing harvester with identical fundamental frequencies are presented, see Figure 7.20. Dimensions of each configuration are generated through the constant fundamental frequency approach outlined in Chapter 6, where substrate thickness was used as the control parameter, and can be found in Appendix B.2. Material properties can be found in Table 7.1 and as aforementioned in the previous chapter, damping magnitude during this type of case study is assumed constant due to difficulties in predicting damping magnitude during multiple geometric parameter changes.

Figure 7.20 indicates the linear model follows a similar trend to that obtained when layer length was examined while not maintaining a constant fundamental frequency, Fig-

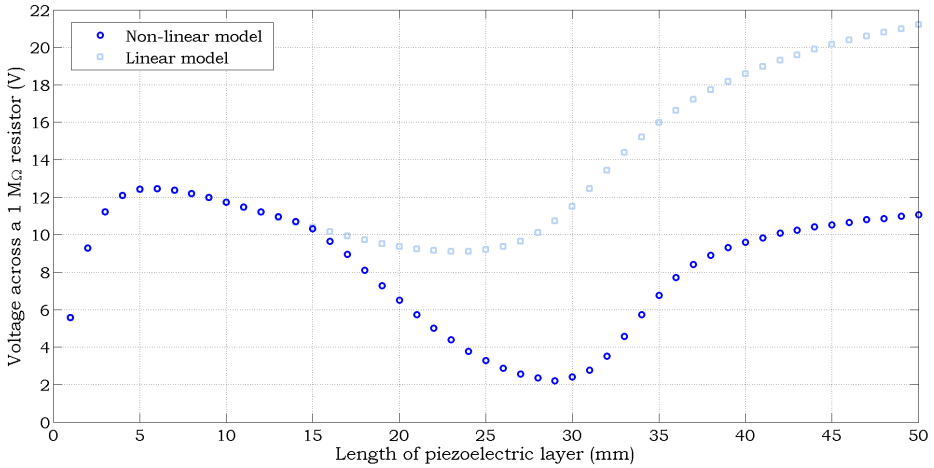

Figure 7.20: Trends between piezoelectric layer length and voltage, generated with linear and non-linear models, when energy harvester connected to a 1 MΩ resistor. Fixed damping of 0.005.

ure 7.17. During this case study, however, deviation of the non-linear model trend begins at a much shorter piezoelectric layer length. The reason behind this is evident when also considering substrate layer thickness as the control variable. From the changes in dynamic response while shortening piezoelectric layer length it has already been shown in Chapter 6 that samples with piezoelectric layers around the 25 mm mark have the largest fundamental frequencies. These samples naturally require the thinnest substrate layers and so beam deflections occurring for these samples are greatly increased. This induces an elevated level of non-linear behaviour thereby resulting in the rather low voltage levels seen in Figure 7.17.

7.5 Conclusion

A robust model allowing for predictions in dynamic response of rectangular, uniform and non-uniform, piezoelectric energy harvesters in non-linear behaviour inducing conditions has been presented in this chapter. Also presented was detailed theoretical model validation through experimental testing on samples manufactured 'in-house'. Lastly, a parametric study indicating how the performance of energy harvesters is affected by piezoelectric material length was undertaken. Scenarios whereby the increased acceleration levels resulted in the presence of non-linearity were studied and discussed.

Piezoelectric materials inherently behave in a non-linear fashion, even when sub-

jected to moderate levels of excitation, and therefore a model which encompassed this was developed. In addition to material non-linearity, the developed model also incorporated geometric non-linearity. Although simulations and testing undertaken in these works caused geometric non-linearity to be redundant (resulting from a combination of sample dimensions, material properties and excitation levels), inclusion ensures the model can be utilised in situations where inducing conditions are present. As an example, the thin-film flexible device on which parameter changes were performed in previous chapters, is expected to experience geometric non-linearity as a result of the larger bending deformations occurring for this structure. Piezoelectric material non-linearity was considered in the form of coefficients, hence additional terms, in the constitutive equation whereas geometric non-linearity presented itself from the assumption that there is no elongation along the neutral axis of the beam (the inextensible beam condition).

Closed-circuit testing was initially undertaken as this results in the omission of one of the piezoelectric non-linear coefficients, μ_2, thereby requiring trial and error curve fitting to obtain magnitudes of only μ_1 and γ. For this 'batch' of piezoelectric material a μ_1 magnitude of -7$\times10^{14}$ Pa was ideal in providing good theoretical-experimental agreement in terms of 'softening' behaviour. For all samples the magnitude of γ was observed to increase with base acceleration amplitude in a quasi-linear manner across the current excitation range (0.5 m.s^{-2} to 7.5 m.s^{-2}). In the present experimental setup this is likely due to phenomena such as stick-slip damping and air damping. Unpredictability and variation in the rate of increase between samples caused detailed modelling of damping variations with a combination of length and base acceleration to be beyond the scope of these works. Following preliminary experimental work it was discovered that the initially developed theoretical non-linear model, although reliable for devices with long piezoelectric layers, fell short when predicting the response of shorter layered devices. Samples with the absence of piezoelectric material were also tested and data showed the presence of non-linearity, albeit small, remained. Due to low deflections amplitudes experienced by macro-scaled samples at the maximum excitation level, geometric non-linearity was ruled out, and following a study into further causes of non-linearity in vibrating beams it was decided that material non-linearity for the substrate layer be included. This was to take a similar form to that used for

the piezoelectric material. Upon inclusion, the new theoretical non-linear model provided good agreement with experimental data across the full range of samples. The coefficient of non-linearity for the substrate layer was estimated having a magnitude of -2×10^{13} Pa. Validation when a resistive load is included in the circuit was also completed and it was found that the second piezoelectric non-linear coefficient, μ_2, can be assumed zero in energy harvesting systems due to the expectancy of low voltage levels. Both theoretical model and experimental data showed a reduced degree of non-linear behaviour through the introduction of an electrical load; this phenomenon is a direct result of reduced beam displacement from the extraction of energy.

While comparing results from the linear energy harvester model developed in Chapter 2 and the non-linear model developed here, some differences were evident. Trends on how the performance of an energy harvester is affected by the piezoelectric layer length were investigated. The magnitude of damping was seen to play an important role in determining how closely linear and non-linear models behaved. For the case in which damping magnitude was modelled to vary proportionally with piezoelectric layer length, linear and non-linear models were in close agreement in terms of peak voltages across the full range of samples. This resulted from increased non-linearity, expected from an increase in piezoelectric material, countered by higher levels of damping suppressing deflection of the structure. However, the non-linearity affects the resonant frequency of the system, a phenomenon not predicted by the linear model. For the case study in which damping was considered as a constant of 0.005, deviation of the non-linear model trend, from the linear model trend, occurred for samples with longer piezoelectric layer lengths. The linear model in the most extreme case was seen to over-predict the performance of the system by 70%. Confidence in results from the linear model depreciate with the level of acceleration applied and as was seen in the experiment even moderate levels of acceleration induce non-linear behaviour. When developing an optimisation tool, particularly for robust parametric studies, non-linearity in vibrating systems must not be overlooked as over-predictions in expected performance of the energy harvester are a likely result.

Further work in this particular area would be a detailed analysis for other causes of

non-linearity since the addition of material non-linearity in the substrate layer, albeit providing reasonable correction across the entire sample range, requires more evidence of its existence. In addition, the combination of this non-linear model with the energy storage model is advisable. This will help determine the extent to which non-linear behaviour affects energy harvester performance in a more realistic electrical scenario.

CHAPTER 8

CONCLUSIONS AND FUTURE WORK

8.1 Conclusions and summary of findings

This section provides an overview of the work undertaken and reports the key findings of the thesis.

Chapters 2 and 3

The development and use of a linear theoretical model for both uniform and non-uniform rectangular cantilever piezoelectric energy harvesters can be found in these two chapters. The modelling in Chapter 2 incorporated a crude method by which damping magnitude varied proportionally with fundamental frequency along with the possibility of tip mass inclusion. The transfer matrix method has been utilised to accurately calculate the natural frequencies and mode shapes of the energy harvester. In Chapter 3, in-depth parametric studies on device geometry have been undertaken for three distinct harvesters – two macro-scale (one with increased flexibility from material choice) and one micro-scale. In addition to this, a performance comparison between biomorph and unimorph designs has been completed. The outcome of these tests can be summarised as follows:

- A double peak phenomenon occurs for devices with damping below a threshold value, providing scenarios whereby the increased quality factor has reduced detrimental effects on system bandwidth.
- Resulting from increased levels of mechanical damping present in longer beams (also

observed experimentally), an optimal overall beam length exists, with excessively long beams showing reduced levels of power.

- As a result of electro-mechanical coupling the magnitude of electrical load resistance has been seen to highly influence trends in performance.

- Increasing the thickness of the piezoelectric layer on both macro- and micro-scale devices, across the tested range, resulted in improvements in performance. Firstly, electro-mechanical coupling, whose influence on trends increases with load resistances, increases from changes in mode shape and reductions in piezoelectric capacitance. Secondly, the increase in structure mass results in improvements in mechanical forcing. This is more significant for macro-scale devices since mechanical forcing in micro-scale devices is predominately from the tip mass. However, such a conclusion regarding thickness optimisation should be taken with caution, as resulting designs are more susceptible to failure. In addition, it has since been found that this observation is dependant on energy harvester composition.

- Increasing the size/density of the tip mass will improve the performance of devices as a result of lower fundamental frequencies and higher magnitudes of mechanical forcing. However, large variations in fundamental frequency make such studies biased.

- For all three case studies, when harvesters are connected to optimal load resistances, increasing the piezoelectric width will benefit harvester performance. Alterations to the thin film macro-scale flexible device, when connected to a 1 MΩ load, resulted in a performance increase of 129% through a reduction in piezoelectric layer length to 55% coverage and an adjustment which made both layers identical in width.

- If the energy harvester is connected to electrical loads with high resistance or the thickness ratio between piezoelectric and substrate layers is large (slightly ambiguous as 'large' is highly dependant on harvester material composition) a biomorph design should be selected over an equivalent unimorph.

Chapter 4

In this chapter the reader has been provided with detailed information regarding the sample

manufacturing process, experimental testing procedure and numerous results from testing. The aim here has been to extensively validate the theoretical model. Variations in magnitude of mechanical damping were observed to be a key issue in data reliability. Details on investigating and tackling issues in mechanical damping and other important findings are outlined below:

- In terms of sample manufacture, use of a silicon carbide disk is advised for cutting PZT sheets with the utilisation of both DP460 and silver conductive epoxy resin in bonding PZT material to a metal substrate.
- Experimental-theoretical comparisons for individual samples, uniform and non-uniform, showed excellent agreement (magnitude of mechanical damping adjusted in each case to match peak response), indicating the reliability of the manufacturing procedure.
- The assumption of mechanical damping being proportional to frequency has been found to be invalid.
- Experimental trends in piezoelectric layer length (adjusted from the free end) against voltage across resistors of various magnitudes were found to be in agreement with those obtained theoretically. Note the assumption that mechanical damping magnitude is fixed. This assumption is seen to be acceptable after estimating damping levels extracted from experimental data, indicating the validity of the theoretical model.
- Sample mounting has been observed to be the main factor in mechanical damping variations. In the most extreme case, mechanical damping measurements varied by 32% – a finding which naturally has huge implications in trend validation. Consistency in clamping was realised through the use of an acrylic clamp.
- The trend between mechanical damping and piezoelectric layer length from the clamped end showed a linear proportional increase followed by saturation after approximately 66% coverage.
- Fitting a polynomial to the experimental data on mechanical damping for use in the theoretical model allowed for good experimental-theoretical agreement to be obtained. In addition to having similar fundamental frequencies, both theoretical and

experimental findings indicated that devices manufactured with short piezoelectric layers have similar performance capabilities to the conventional design. The implications of such findings suggest that investigating piezoelectric layer coverage can assist in determining optimum designs and cost-cutting avenues, i.e. from a view point of reduction in material quantity.

Chapter 5

Optimisation of geometry whilst connecting energy harvesters to more realistic electrical circuitry has been presented in this chapter. Modelling and theoretical simulations, validated experimentally, were completed using SIMULINK® . The decision to use SIMULINK® allowed for the effects of electro-mechanical coupling to remain while providing the possibility of future model extensions on the electrical side to be made readily. Key findings from this chapter are:

- On a macro-scale device, reducing the width of the piezoelectric layer (substrate width remains fixed) indicated impressive performance improvements, increases of over 100% in the magnitude of stored energy, in comparison to a design with both layers having identical widths.
- Reductions in mechanical damping (from the assumption made) and piezoelectric capacitance were the primary cause for the improved performance by devices consisting of narrow piezoelectric layers.
- The above two factors were also responsible for improvements in performance of over 200% when optimising piezoelectric layer length on a micro-scale device. The optimised device had a piezoelectric-to-substrate length ratio of 1/8.
- One must be wary of charging profiles, as, although an optimised design allows for a greater level of energy to be stored, an increase in time taken to reach this peak value could be an issue. Note however, no detrimental effects were observed here for the thin film flexible device.
- Validation of the theoretical model through experimental testing highlighted the essential nature of including a resistor in the modelling to accommodate electrical

losses. A satisfactory outcome for validation was achieved for both uniform and non-uniform devices.

- Experimental data indicated a similar outcome to theoretical trends. Experimentally, a device consisting of a 9.66 mm piezoelectric layer outperformed the conventional design by 42%.

Chapter 6

This chapter tackled one of the main issues with parametric studies on device geometry – a non-constant fundamental frequency between designs. Overcoming this issue has been realised through the simultaneous change of multiple geometric parameters. Performed in a systematic manner this approach can be used to generate sets of energy harvesters with identical fundamental frequencies allowing for unbiased geometric optimisations to be made. Key findings from this chapter are outlined below:

- The effectiveness of a control parameter is related to how sensitive changes in the control parameter are to changes in fundamental frequency.
- Good control parameters were found to be the substrate thickness and, when applicable, tip mass dimensions.
- In similar fashion to previous parametric studies performed in Chapter 3, improvements in the power dissipated in a load resistor, from reducing piezoelectric length, were observed. Although the determined optimised piezoelectric layer lengths differ when using the constant fundamental frequency approach, the general trends were observed to remain similar to those obtained during the non-controlled case.
- For the macro-scale device, performance improvements have been observed by reducing length from the free end. For the remaining two cases, improvements have been realised through length reductions from the free end. This highlights the importance of addressing each case individually and the impossibility of a universal design template.
- As opposed to the previous study in Chapter 5, in this constant fundamental frequency scenario, increases in performance were linked to an increase in width when consid-

ering the level of energy stored. The fixed mechanical damping assumption is thought to be the cause of this observed difference.

Chapter 7

Due to limitations in linear modelling when considering scenarios with moderate to high levels of acceleration, particularly when concerning piezoelectric materials, the final step has been to develop a non-linear model for uniform and non-uniform cantilever piezoelectric energy harvesters. Both material and geometric non-linearities have been included in model development, with material non-linearity residing in additional terms in material constitutive equations, and geometric non-linearity resulting from an inextensible beam assumption. An outline of key findings from this chapter are provided below:

- Experimental testing demonstrated that material non-linearity dominates over geometric non-linearity in cantilever piezoelectric energy harvesters. This was seen in the form of softening behaviour with a reduction in resonant frequency occurring for increased base excitation.

- Theoretical model validation using a conventional energy harvester was readily achieved and resulted in the non-linear coefficient, μ_1, requiring a magnitude of -7$\times 10^{14}$ Pa.

- Testing of substrate layers only (i.e. aluminium cantilever beams) across the base acceleration range of 0.5 m.s^{-2} to 7.5 m.s^{-2} also gave rise to non-linearity in the form of softening. This has been accommodated through the inclusion of a higher order term in the substrate constitutive equation in similar fashion to piezoelectric material non-linearity.

- A non-linear coefficient, μ_{s1}, of -2$\times 10^{13}$ Pa was required to theoretically replicate experimental results. Using the determined values for μ_1 and μ_{s1} the theoretical model has been shown to provide reasonable agreement with experimental findings across the full sample range (harvesters with various piezoelectric layer lengths while substrate length is fixed).

- The magnitude of mechanical damping was found to increase in a quasi-linear manner across the tested base excitation range. This indicates a reduction in the efficiency of

energy harvesters operating at high acceleration levels.

- As a result of electrical energy extraction from the system, the inclusion of a load resistor reduces the extent of non-linear behaviour.

- Using the assumption whereby damping increases quasi-linearly with piezoelectric layer length, small differences between the linear and non-linear models were observed in terms of peak voltage across a 1 MΩ resistor while varying piezoelectric length. However, the importance of a non-linear model has been witnessed when observing voltage FRFs with the occurrence of significant shifts in resonant frequency. Without knowledge of such shifts during the design/optimisation of an energy harvester the resulting device may have inefficient operation.

8.2 Closing remarks

Work completed in this thesis has shown the importance of parametric studies on geometry during the design process of cantilever piezoelectric energy harvesters. Vast improvements in harvester performance resulted from alterations to piezoelectric layer coverage. It was also shown that complete modelling of the system, particularly in relation to the electrical system to which the energy harvester is connected, is highly important and influences the dimensions of an optimised device. The geometry optimisation of energy harvesters in a more realistic electrical scenario by using SIMULINK® , while ensuring electro-mechanical coupling remains in the model, is seen to be a major step forward in this regard. The magnitude of mechanical damping had significant effects on the trends generated throughout this work and is identified as a key variable during parametric studies. The inclusion of variations in mechanical damping with geometric parameter changes, during theoretical simulations, was attempted in an approximate manner. Experimental findings showed that reducing the length of piezoelectric material reduces mechanical damping which is favourable in terms of energy harvester performance. A common theme observed throughout this work was that devices manufactured using shorter piezoelectric layers (substrate length fixed at x mm) can outperform, or at least compete with, the conventional design which is common in past

literature. This naturally has positive practical implications particularly when concerning manufacturing/material costs.

By systematically altering multiple geometric parameters simultaneously to maintain a constant fundamental frequency between designs, unbiased design comparisons can be made. The methodology provided in the thesis is seen as essential when considering the optimisation of an energy harvesting device. The development of a robust non-linear model, for both uniform and non-uniform piezoelectric energy harvesters, is also seen as an essential step in the energy harvester optimisation field of research. Knowledge on resonant frequency shifts is vital in order to design and optimise devices so they will operate efficiently at the excitation conditions. Trends and observations from the developed theoretical models have continually been replicated by extensive experimental work which should instil confidence in the reliability of the models and the potential for future utilisation. Admittedly, until a deeper understanding is gained of how mechanical damping varies with geometric changes, experimental work will still be required. However, by using the general findings and theoretical models from the thesis, it is believed experimental work is required to a far reduced extent. Naturally, significant savings on time and money can be ensured by performing detailed optimisations through computation rather than experimental means.

8.3 Future work

In this section, the recommendation of areas in which further work can be undertaken is outlined. Firstly, and possibility most importantly is an in-depth study into mechanical damping. It has been seen throughout this thesis that variations in the magnitude of mechanical damping greatly influence theoretical model validation when related to trends in performance. Rectifying the inconsistencies in clamping procedure can be examined in greater detail here. It was experimentally observed, for one macro-scale harvester case, that damping increased from 0.002 (substrate layer only) to 0.007 (when the piezoelectric layer length was equal to the substrate length). This factor of 3.5 was assumed to universally apply to the other two case studies. However, work needs to be performed in determining the

extent to which the magnitude of variation in mechanical damping is affected by device size and composition. Experimental data for other devices would be useful in achieving this. Predictions of changes in mechanical damping with other geometric changes (i.e. piezoelectric layer thickness), which was beyond the scope of current work, is also advised. Two other areas in which further information regarding mechanical damping variations would be useful is while altering multiple geometric parameters, where in this work the mechanical damping was assumed fixed during such parametric studies, and for situations where devices are subjected to higher acceleration levels (recall the mechanical damping magnitude was seen to increase with base excitation, and the rate of this increase varied from sample to sample). Detailed insight and knowledge on the variation of mechanical damping would further increase the reliability of the developed theoretical models.

Further model validation is also suggested as an avenue of future work. This is partially in progress with the manufacture and testing of flexible thin film devices. The outcome is looking promising for unimorph structures as theoretical results from the developed nonlinear model are in good agreement with experimental data. It is recommended that the theoretical model also be validated using devices manufactured on the micro-scale in addition to devices with various material composition. The testing of such differing devices will help towards gaining an understanding behind the limitation of the current theoretical model.

The majority of optimisations performed in the thesis were on unimorph devices. Future work on investigating the optimisation of bimorph devices is also recommended. Significant differences in the trends between performance and geometric parameters are expected, particularly whilst examining the effects of layer thickness. Reasons behind this hypothesis come from differences and tendencies in neutral axis location when comparing unimorph and bimorph devices.

It has comprehensively been shown that the electrical aspects of an energy harvesting system have a significant influence on the geometry of an optimised device. In Chapter 5, the optimisation of harvesters connected to a storage capacitor in parallel with a resistor was

presented. Utilisation of more efficient circuits, i.e. those briefly described in Section 1.4.4, is recommended for further work. This can be readily achievable with foundations, in form of SIMULINK® models, provided in the thesis.

The non-linear energy harvester model presented in Chapter 7 required the addition of substrate material non-linearity in order to effectively simulate cantilever substrate beams vibrating at elevated acceleration levels. However, since the substrate material used during testing was aluminium, at the acceleration levels applied, one would not expect material non-linearity to have occurred. Further work is recommended here to determine the root cause of the observed 'softening' behaviour. Note however that the addition of substrate material non-linearity has turned out to be useful for simulating flexible thin film energy harvesters as the substrate layer in such devices is comprised of silicone rubber. Even at moderate acceleration levels (0.2 m.s^{-2}) this material is seen to exhibit a non-linear stress-strain relationship indicating the essential nature to include substrate material non-linearity. In addition, utilisation and validation of the non-linear energy harvester model when harvesters are simulated in a more realistic electrical scenario is advised.

LIST OF PUBLICATIONS

1. R. Patel, S. McWilliam and A. A. Popov, 'A geometric parameter study of piezoelectric coverage on a rectangular cantilever energy harvester', *Smart Materials and Structures*, **20**, 085004 (12 pp), 2011.

2. R. Patel, S. McWilliam and A. A. Popov, 'Improved parameter study of a piezoelectric energy harvester with experimental validation', *10th International Workshop on Micro and Nanotechnology for Power Generation and Energy Conversion Applications*, Leuven, Belgium, 4 pages, 2010.

3. A. A. Popov, B. Chouvion, O. J. Bakker and R. Patel, 'Some recent trends and contemporary applications of structural dynamics', *International Conference UACEG 2009: Science & Practice*, Sofia, Bulgaria, 12 pages, 2009.

4. R. Patel, A. A. Popov and S. McWilliam, 'Parametric study of a cantilevered piezoelectric energy harvester', *9th International Workshop on Micro and Nanotechnology for Power Generation and Energy Conversion Applications*, Washington DC, USA, 4 pages, 2009.

5. R. Patel, A. A. Popov and S. McWilliam, 'Vibrational energy harvesting devices', *Recent Patents on Mechanical Engineering*, **2**, pp. 80–92, 2009.

BIBLIOGRAPHY

[1] 'IEEE standard on piezoelectricity', *IEEE Ultrasonics, Ferroelectrics, and Frequency Control Society*, p. (74 pp), 1987.

[2] 3M Scotch-Weld, website last accessed on 04–03–2012, URL:http://www.3m.com/intl/kr/img/adh/adhesives/dpseries/DP460.pdf.

[3] J. Ajitsaria, S. Y. Choe, D. Shen and D. J. Kim, 'Modeling and analysis of a bimorph piezoelectric cantilever beam for voltage generation', *Smart Materials and Structures*, **16**, pp. 447–454, 2007.

[4] A. Albareda, P. Gonnard, V. Perrin, R. Briot and D. Guyomar, 'Characterization of the mechanical nonlinear behavior of piezoelectric ceramics', *IEEE Transactions on Ultrasonics, Ferroelectrics, and Frequency Control*, **47**, pp. 844–853, 2000.

[5] K. S. Allen, *Evaluation Techniques for Determining Damping Mechanisms on Titanium Plates*, Ph.D. thesis, Air Force Institute of Technology, Department of the Air Force, Air University, Wright-Patterson Air Force Base, Ohio, 2005.

[6] Americian Piezo, website last accessed on 15–11–2008, URL:http://www.americanpiezo.com/piezo_theory/piezo_theory.pdf.

[7] M. Arafa and A. Baz, 'On the nonlinear behavior of piezoelectric actuators', *Journal of Vibration and Control*, **10**, pp. 387–398, 2004.

[8] Y. W. Bai and M. Y. Yang, 'An improved design of a wireless keyboard powered by solar cells and a large capacitor', *IEEE Transactions on Consumer Electronics*, **54**, pp. 1355–1359, 2008.

[9] S. Beeby and N. White, *Energy Harvesting For Autonomous Systems*, Norwood, Massachusetts: Artech House, 2010.

[10] S. P. Beeby, M. J. Tudor and N. M. White, 'Energy harvesting vibration sources for microsystems applications', *Journal of Measurement Science and Technology*, **17**, pp. 175–195, 2006.

[11] S. Belouettar, L. Azrar, E. M. Daya, V. Laptev and M. Potier-Ferry, 'Active control of nonlinear vibration of sandwich piezoelectric beams: A simplified approach', *Computers and Structures*, **86**, pp. 386–397, 2008.

[12] R. I. Bourisli and M. A. Al-Ajmi, 'Optimization of smart beams for maximum modal electromechanical coupling using genetic algorithms', *Journal of Intelligent Material Systems and Structures*, **21**, pp. 907–914, 2010.

[13] J. D. Bronzino, *The Biomedical Engineering Handbook - Third Edition*, New York, USA: CRC Press Taylor & Francis Group, 2006.

[14] G. P. Carman and D. G. Lee, 'Non-contact mechanical energy harvesting device and method utilizing frequency rectification', *WO2008079321A2*, 2008.

[15] J. Chakrabarty, *Theory of Plasticity*, Oxford, UK: Butterworth-Heinemann, 2006.

[16] C. Y. K. Chee, L. Tong and G. P. Steven, 'A review on the modelling of piezoelectric sensors and actuators incorporated in intelligent structures', *Journal of Intelligent Material Systems and Structures*, **9**, pp. 3–19, 1998.

[17] C. J. Chen, *Physics of Solar Energy*, Hoboken, New Jersey: John Wiley & Sons, Ltd, 2011.

[18] Y. Chiu, C. T. Kuo and Y. S. Chu, 'MEMS design and fabrication of an electrostatic vibration-to-electricity energy converter', *Journal of Microsystem Technologies*, **13**, pp. 1663–1669, 2007.

[19] D. L. Churchill and S. W. Arms, 'Slotted beam piezoelectric composite', *US20070114890A1*, 2007.

[20] R. W. Clough and J. Penzien, *Dynamics of Structures*, United States of America: McGraw-Hill, 1975.

[21] K. A. Cook-Chennault, N. Thambi and A. M. Sastry, 'Powering MEMS portable devices – a review of non-regenerative and regenerative power supply systems with special emphasis on piezoelectric energy harvesting systems', *Journal of Smart Materials and Structures*, **17**, p. 043001 (33 pp), 2008.

[22] E. F. Crawley and E. H. Anderson, 'Detailed models of piezoceramic actuation of beams', *Journal of Intelligent Material Systems and Structures*, **1**, pp. 4–25, 1990.

[23] M. F. Daqaq, 'Response of uni-modal duffing-type harvesters to random forced excitations', *Journal of Sound and Vibration*, **329**, pp. 3621–3631, 2010.

[24] M. F. Daqaq, C. Stabler, Y. Qaroush and T. Seuaciuc-Osório, 'Investigation of power harvesting via parametric excitations', *Journal of Intelligent Material Systems and Structures*, **20**, pp. 545–557, 2009.

[25] J. M. Dietl, A. M. Wickenheiser and E. Garcia, 'A timoshenko beam model for cantilevered piezoelectric energy harvesters', *Smart Materials and Structures*, **19**, p. 055018 (12 pp), 2010.

[26] A. Erturk, *Electromechanical Modeling of Piezoelectric Energy Harvesters*, Ph.D. thesis, Virginia Polytechnic Institute and State University, Blacksburg, Virginia, USA, 2009.

[27] A. Erturk and D. J. Inman, 'A distribution parameter electromechanical model for cantilever piezoelectric energy harvesters', *Journal of Sound and Acoustics*, **130**, p. 041002 (15 pp), 2008.

[28] A. Erturk and D. J. Inman, 'Issues in mathematical modeling of piezoelectric energy harvesters', *Smart Materials and Structures*, **17**, p. 065016 (14 pp), 2008.

[29] A. Erturk and D. J. Inman, 'An experimentally validated bimorph cantilever model for piezoelectric energy harvesting from base excitations', *Smart Materials and Structures*, **18**, p. 025009 (18 pp), 2009.

[30] A. Erturk and D. J. Inman, *Piezoelectric Energy Harvesting*, Chichester, UK: John Wiley & Sons, Ltd, 2011.

[31] H. B. Fang, J. Q. Liu, Z. Y. Xu, L. Dong, L. Wang, D. Chen, B. C. Cai and Y. Liu, 'Fabrication and performance of MEMS-based piezoelectric power generator for vibration energy harvesting', *Microelectronics Journal*, **37**, pp. 1280–1284, 2006.

[32] M. Ferrari, M. Bau, M. Guizzetti and V. Ferrari, 'A single-magnet nonlinear piezoelectric converter for enhanced energy harvesting from random vibrations', *Sensors and Actuators A: Physical*, **172**, pp. 287–292, 2011.

[33] M. Ferrari, V. Ferrari, M. Guizzetti, B. Ando, S. Baglio and C. Trigona, 'Improved energy harvesting from wideband vibrations by nonlinear piezoelectric converters', *Sensors and Actuators A: Physical*, **162**, pp. 425–431, 2010.

[34] Ferro Solutions, website last accessed on 15–11–2008, URL:`http://www.ferrosi.com`.

[35] M. I. Friswell and S. Adhikari, 'Sensor shape design for piezoelectric cantilever beams to harvest vibration energy', *Journal of Applied Physics*, **108**, p. 014901 (6 pp), 2010.

[36] X. Gao, W. H. Shih and W. Y. Shih, 'Induced voltage of piezoelectric unimorph cantilevers of different nonpiezoelectric/piezoelectric length ratios', *Journal of Smart Materials and Structures*, **18**, p. 125018 (8 pp), 2009.

[37] X. Gao, W. H. Shih and W. Y. Shih, 'Vibration energy harvesting using piezoelectric unimorph cantilevers with unequal piezoelectric and nonpiezelectric lengths.', *Applied Physics Letters*, **97**, p. 233503 (3 pp), 2010.

[38] F. Goldschmidtboeing, M. Wischke, C. Eichhorn and P. Woias, 'Nonlinear effects in

piezoelectric vibration harvesters with high coupling factors', Washington DC, USA: PowerMEMS, 1–4th December 2009, 2009.

[39] F. Goldschmidtboeing and P. Woias, 'Characterization of different beam shapes for piezoelectric energy harvesting', *Journal of Micromechanics and Microengineering*, **18**, p. 104013 (7 pp), 2008.

[40] M. Hagiwara, S. Takahashi, T. Hoshina, H. Takeda and T. Tsurumi, 'Analysis of nonlinear transient responses of piezoelectric resonators', *IEEE Transactions on Ultrasonics, Ferroelectrics and Frequency Control*, **58**, pp. 1721–1729, 2011.

[41] ITW Chemtronics, website last accessed on 04–03–2012, URL:`http://docs-europe.electrocomponents.com/webdocs/0031/0900766b80031a13.pdf`.

[42] Y. B. Jeon, R. Sood, J. H. Jeong and S. G. Kim, 'MEMS power generator with transverse mode thin film PZT', *Journal of Sensors and Actuators*, **122**, pp. 16–22, 2004.

[43] L. Jian-Hui, W. Xiao-Ming, C. Hao, L. Xi, R. Tian-Ling and L. Li-Tian, 'Analyses of vibration-based piezoelectric power generator in discontinuous operation mode', *Sensors and Actuators A: Physical*, **152**, pp. 48–52, 2009.

[44] S. P. Joshi, 'Non-linear constitutive relations for piezoceramic materials', *Smart Materials and Structures*, **1**, pp. 80–83, 1992.

[45] M. A. Karami and D. J. Inman, 'Equivalent damping and frequency change for linear and nonlinear hybrid vibrational energy harvesting systems', *Journal of Sound and Vibration*, **330**, pp. 5583–5597, 2011.

[46] Kelsius, website last accessed on 08–01–2013, URL:`http://www.kelsius.com/markets/healthcare-cold-chain-monitoring/`.

[47] H. Kulah and K. Najafi, 'Energy scavenging from low-frequency vibrations by using frequency up-conversion for wireless sensor applications', *Sensors Journal, IEEE*, **8**, pp. 261–268, 2008.

[48] S. Kulkarni, E. Koukharenko, R. Torah, J. Tudor, S. Beeby, T. O'Donnel and S. Roy, 'Design, fabrication and test of integrated micro-scale vibration-based electromagnetic generator', *Journal of Sensors and Actuators*, **145–146**, pp. 336–342, 2008.

[49] J. Q. Liu, H. B. Fang, Z. Y. Xu, X. H. Mao, X. C. Shen, D. Chen, H. Liao and B. C. Cai, 'A MEMS-based piezoelectric power generator array for vibration energy harvesting', *Journal of Microelectronics*, **39**, pp. 802–806, 2008.

[50] S. N. Mahmoodi, N. Jalil and M. F. Daqaq, 'Modeling, nonlinear dynamics, and identification of a piezoelectrically actuated microcantilever sensor', *IEEE Transactions on Mechatronics*, **13**, pp. 58–65, 2008.

[51] K. H. Mak, *Vibration Modelling and Analysis of Piezoelectric Energy Harvesters*, Ph.D. thesis, University of Nottingham, University Park, Nottingham, UK, 2011.

[52] K. H. Mak, A. A. Popov and S. McWilliam, 'Experimental model validation for a nonlinear energy harvester incorporating a bump stop', *Journal of Sound and Vibration*, **331**, pp. 2602–2623, 2012.

[53] P. Malatkar, *Nonlinear Vibrations of Cantilever Beams and Plates*, Ph.D. thesis, Virginia Polytechnic Institute, Blacksburg, Virginia, USA, 2003.

[54] B. P. Mann and N. D. Sims, 'Energy harvesting from the nonlinear oscillations of magnetic levitation', *Journal of Sound and Vibration*, **319**, pp. 515–530, 2007.

[55] MathWorks - MatLab, website last accessed on 05–08–2010, URL:`http://www.mathworks.com/help/matlab/index.html`.

[56] MathWorks - SimElectronics, website last accessed on 05–08–2010, URL:`http://www.mathworks.com/help/physmod/elec/index.html`.

[57] MathWorks - SimElectronics-Diode, website last accessed on 05–08–2010, URL:`http://www.mathworks.com/help/physmod/elec/ref/diode.html`.

[58] MathWorks - Simscape, website last accessed on 05–08–2010, URL:`http://www.mathworks.com/help/physmod/simscape/index.html`.

[59] MathWorks - Simulink, website last accessed on 05–08–2010, URL:http://www.mathworks.com/help/simulink/index.html.

[60] J. McCleary, *Geometry From A Differentiable Viewpoint*, Cambridge, UK: Cambridge University Press, 1995.

[61] C. R. McInnes, D. G. Gorman and M. P. Cartmell, 'Enhanced vibrational energy harvesting using nonlinear stochastic resonance', *Journal of Sound and Vibration*, **318**, pp. 655–662, 2008.

[62] C. Metzger, F. Michahelles and E. Fleisch, 'Ambient energy scavenging for sensor-equipped RFID tags in the cold chain', Kendal, England: EuroSSC, 23–25th October 2007, 2007.

[63] MicroStrain, website last accessed on 15–11–2008, URL:http://www.microstrain.com.

[64] P. D. Mitcheson, T. C. Green, E. M. Yeatman and A. S. Holmes, 'Architecture for vibration-driven micropower generators', *Journal of Microelectromechanical Systems*, **13**, pp. 429–440, 2004.

[65] P. D. Mitcheson, E. M. Yeatman, A. S. Holmes and T. C. Green, 'Energy harvesting from human and machine motion for wireless electronic devices', *Proceedings of The IEEE*, **96**, pp. 1457–1486, 2008.

[66] H. Mutsuda, R. Watanabe, M. Hirata, Y. Doi and Y. Tanaka, 'Elastic floating unit with piezoelectric device for harvesting ocean wave energy', Rio de Janeiro, Brazil: OMAE, 10–15th June 2012, 2012.

[67] H. Nouira, E. Foltête, L. Hirsinger and S. Ballandras, 'Investigation of the effects of air on the dynamic behavior of a small cantilever beam', *Journal of Sound and Vibration*, **305**, pp. 243–260, 2007.

[68] K. B. Oldham and J. Spanier, *The Fractional Calculus*, New York, America: Academic Press, 1974.

[69] R. Patel, A. A. Popov and S. McWilliam, 'Vibrational energy harvesting devices', *Recent Patents on Mechanical Engineering*, **2**, pp. 80–92, 2009.

[70] Perpetuum, website last accessed on 15–11–2008, URL:`http://www.perpetuum.com`.

[71] E. C. Pestel and F. A. Leckie, *Matrix Methods in Elasto Mechanics*, New York, America: McGraw-Hill, 1963.

[72] Physik Instrumente, website last accessed on 04–11–2008, URL:`http://www.piceramic.com/piezo_materials_2.php`.

[73] Physik Instrumente, website last accessed on 04–11–2008, URL:`http://www.piceramic.com/piezo_materials_3.php`.

[74] Physik Instrumente, website last accessed on 04–09–2011, URL:`http://www.piceramic.com/piezo_materials_1.php`.

[75] PrecisionAcoustics, website last accessed on 21–02–2012, URL:`http://www.acoustics.co.uk/static/pdf/PVdF-properties.pdf`.

[76] S. Priya and D. J. Inman, *Energy Harvesting Technologies*, New York, USA: Springer Science + Business Media, 2009.

[77] S. Priya and R. D. Myers, 'Piezoelectric energy harvester', *US 20080074002A1*, 2008.

[78] J. Qiu, H. Jiang, H. Ji and K. Zhu, 'Comparison between four piezoelectric energy harvesting circuits', *Frontiers of Mechanical Engineers in China*, **4**, pp. 153–159, 2009.

[79] R. Ramlan, M. J. Brennan and B. R. Mace, 'Improving the performance of an energy harvesting device using nonlinearity', Leuven, Belgium: ISMA, 15–17th Sep 2008, 2008.

[80] S. S. Rao, *Mechanical Vibration - Fourth Edition*, Upper Saddle River, New Jersey: Pearson Prentice Hall, 2004.

[81] M. Renaud, P. Fiorini, R. van Schaijk and C. van Hoof, 'Harvesting energy from the motion of human limbs: the design and analysis of an impact-based piezoelectric generator', *Smart Materials and Structures*, **18**, p. 035001 (16 pp), 2009.

[82] J. M. Renno, M. F. Daqaq and D. J. Inman, 'On the optimal energy harvesting from a vibration source', *Journal of Sound and Vibration*, **320**, pp. 386–405, 2009.

[83] S. Roundy, E. S. Leland, J. Baker, E. Carleton, E. Reilly, E. Lai, B. Otis, J. M. Rabaey, P. K. Wright and V. Sundararajan, 'Improving power output for vibration-based energy scavengers', *Journal of Pervasive Computing, IEEE*, **4**, pp. 28–36, 2005.

[84] S. Roundy, P. K. Wright and J. Rabaey, 'A study of low level vibrations as a power source for wireless sensor nodes', *Journal of Computer Communication*, **26**, pp. 1131–1144, 2003.

[85] G. Sebald, H. Kuwano, D. Guyomar and B. Ducharne, 'Simulation of a Duffing oscillator for broadband piezoelectric energy harvesting', *Smart Materials and Structures*, **20**, p. 075022 (17 pp), 2011.

[86] S. M. Shahruz, 'Design of mechanical band pass filters for energy scavenging', *Journal of Sound and Vibration*, **292**, pp. 987–998, 2005.

[87] D. Shen, J. Ajitsaria, S. Y. Choe and D. J. Kim, 'The optimal design and analysis of piezoelectric cantilever beams for power generation devices', *MRS Proceedings*, **888**, pp. 0888–V03–04, 2005.

[88] Y. C. Shu, I. C. Lien and J. W. Wu, 'An improved analysis of the SSHI interface in piezoelectric energy harvesting', *Smart Materials and Structures*, **16**, pp. 2253–2264, 2007.

[89] H. A. Sodano, D. J. Inman and G. Park, 'A review of power harvesting from vibration using piezoelectric materials', *The Shock and Vibration Digest*, **36**, pp. 197–205, 2004.

[90] H. A. Sodano, G. Park and D. J. Inman, 'Estimation of electric charge output for piezoelectric energy harvesting', *Strain*, **40**, pp. 49–58, 2004.

[91] S. C. Stanton, A. Erturk, B. P. Mann, E. H. Dowell and D. J. Inman, 'Nonlinear nonconservative behavior and modeling of piezoelectric energy harvesters including proof mass effects', *Journal of Intelligent Material Systems and Structures*, **23**, pp. 183–199, 2012.

[92] M. Tabaddor, 'Influence of nonlinear boundary conditions on the single-mode response of a cantilever beam', *International Journal of Solids and Structures*, **37**, pp. 4915–4931, 2000.

[93] Y. Tanaka, K. Matsumura and H. Mutsuda, 'An experimental study of power generation and storage using a flexible piezoelectric device', *International Journal of Applied Electromagnetics and Mechanics*, **18**, pp. 1–6, 2003.

[94] Y. Tanaka, Y. Michinaka and H. Mutsuda, 'An experimental study of a submerged power generator that uses flexible power generation devices', Kaohsiung, Taiwan: MAGDA, 14–16th November 2011, 2011.

[95] R. Tashiro, N. Kabei, K. Katayama, E. Tsuboi and K. Tsuchiya, 'Development of an electrostatic generator for a cardiac pacemaker that harnesses the ventricular wall motion', *Journal of Artificial Organs*, **5**, pp. 239–245, 2008.

[96] A. Triplett and D. D. Quinn, 'The effect of non-linear piezoelectric coupling on vibration-based energy harvesting', *Journal of Intelligent Material Systems and Structures*, **20**, pp. 1959–1967, 2009.

[97] F. S. Tse, I. E. Morse and H. R. T., *Mechanical Vibration Theory and Applications - Second Edition*, Boston, Massachusetts: Allyn and Bacon, 1978.

[98] Veryst Engineering, website last accessed on 15–11–2008, URL:`http://www.veryst.com/publications.html`.

[99] T. Wacharasindhu and J. W. Kwon, 'A micromachined energy harvester from a keyboard using combined electromagnetic and piezoelectric conversion', *Journal of Micromechanics and Microengineering*, **18**, p. 104016 (8 pp), 2008.

[100] Q. Wang and N. Wu, 'Optimal design of a piezoelectric coupled beam for power harvesting', *Smart Materials and Structures*, **21**, p. 085013 (9 pp), 2012.

[101] W. J. Weaver, S. P. Timoshenko and D. H. Young, *Vibration Problems In Engineering*, Canada: John Wiley & Sons, Ltd, 1990.

[102] Wikipedia, website last accessed on 21–02–2012, URL:`http://en.wikipedia.org/wiki/Polyethylene_terephthalate`.

[103] C. B. Williams and R. B. Yates, 'Analysis of a micro-electric generator for microsystems', *Journal of Sensors and Actuators*, **52**, pp. 8–11, 1996.

[104] M. Wischke, M. Masur, M. Kroner and P. Woias, 'Vibration harvesting in traffic tunnels to power wireless sensor nodes', *Smart Materials and Structures*, **20**, p. 085014 (8 pp), 2011.

[105] L. Q. Yao, J. G. Zhang, L. Lu and M. O. Lai, 'Nonlinear dynamic characteristics of piezoelectric bending actuators under strong applied electric field', *Journal of Micro-ElectoMechanical Systems*, **13**, pp. 645–652, 2004.

[106] Q. Zheng, Z. Wang and Y. Xu, 'Symmetric air-spaced cantilevers for strain sensing', *Journal of Sensors and Actuators*, **147**, pp. 142–149, 2008.

[107] D. Zhu, M. J. Tudor and B. S. P., 'Strategies for increasing the operating frequency range of vibration energy harvesters: a review', *Measurement Science and Technology*, **21**, p. 022001 (29 pp), 2010.

[108] M. Zhu, E. Worthington and A. Tiwari, 'Design study of piezoelectric energy harvesting devices for generation of higher electrical power using a coupled piezoelectric-circuit finite element method', *IEEE Transactions on Ultrasonics Ferroelectrics and Frequency Control*, **57**, pp. 427–437, 2010.

APPENDIX A

TIP MASS MODELLING

A.1 Detailed derivation for the effects of tip mass addition

In this section the boundary conditions for a beam with a tip mass offset from the end of the beam are derived. Figure A.1 shows a schematic of the tip mass outlining relevant variables.

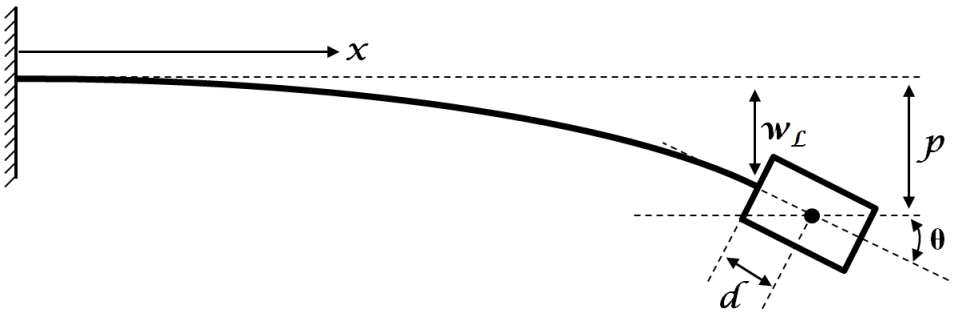

Figure A.1: Schematic of tip mass addition.

From Figure A.1 one can readily deduce:

$$\sin\theta = \frac{p - w_L}{d} = w'_L \,, \tag{A.1}$$

or

$$p = w'_L d + w_L \,. \tag{A.2}$$

The total kinetic energy from tip mass addition (translational and rotational) can be defined as:

$$KE = \frac{1}{2} m_{\text{tip}} \dot{p}^2 + \frac{1}{2} I_G \left(\dot{w}'_L\right)^2 , \tag{A.3}$$

$$KE = \frac{1}{2} m_{\text{tip}} \left(\dot{w}'_L d + \dot{w}_L\right)^2 + \frac{1}{2} I_G \left(\dot{w}'_L\right)^2 . \tag{A.4}$$

The Lagrangian for the beam can be defined as:

$$\mathcal{L}_B = \frac{1}{2} \left[\rho A \left(\dot{w}\right)^2 - EI \left(w''\right)^2 \right] . \tag{A.5}$$

The application of the Hamilton Extended Principle:

$$\int_{t_1}^{t_2} \delta(\mathcal{L}_B + KE) \mathrm{d}t = 0 , \tag{A.6}$$

and using the calculus of variations, shown below, will provide the required boundary conditions.

At $x = L$, and taking $w(L,t)$:

$$\frac{\partial (KE)}{\partial w} - \frac{\partial}{\partial t}\left(\frac{\partial (KE)}{\partial \dot{w}}\right) + \left| \frac{\partial \mathcal{L}_B}{\partial w'} - \frac{\partial}{\partial x}\left(\frac{\partial \mathcal{L}_B}{\partial w''}\right) - \frac{\partial}{\partial t}\left(\frac{\partial \mathcal{L}_B}{\partial \dot{w}'}\right) \right|_{x=L} = 0 . \tag{A.7}$$

At $x = L$, and taking $w'(L,t)$:

$$\frac{\partial (KE)}{\partial w'} - \frac{\partial}{\partial t}\left(\frac{\partial (KE)}{\partial \dot{w}'}\right) + \left| \frac{\partial \mathcal{L}_B}{\partial w''} \right|_{x=L} = 0 . \tag{A.8}$$

After performing the differentiations in Equations (A.7) (A.8) one obtains the following

boundary conditions for the free end:

$$-\frac{\partial}{\partial t}\left(m_{\text{tip}}\dot{w}\right)-\frac{\partial}{\partial t}\left((m_{\text{tip}}d)\dot{w}'\right)+\frac{\partial}{\partial x}\left(EIw''\right)=0\ ,$$

$$\Longrightarrow \boxed{EI\frac{\partial^3}{\partial x^3}\big(w(x,t)\big)=m_{\text{tip}}\frac{\partial^2}{\partial t^2}\big(w(x,t)\big)+m_{\text{tip}}d\frac{\partial^2}{\partial x\partial t^2}\big(w(x,t)\big)}\ . \tag{A.9}$$

$$-\frac{\partial}{\partial t}\left((m_{\text{tip}}d)\dot{w}'\right)-\frac{\partial}{\partial t}\left((m_{\text{tip}}d^2)\dot{w}\right)-\frac{\partial}{\partial t}\left((I_G\dot{w}'\right)-\left(EIw''\right)=0\ ,$$

$$\Longrightarrow \boxed{EI\frac{\partial^2}{\partial x^2}\big(w(x,t)\big)=-m_{\text{tip}}d\frac{\partial^2}{\partial t^2}\big(w(x,t)\big)-(I_G+m_{\text{tip}}d^2)\frac{\partial^3}{\partial x\partial t^2}\big(w(x,t)\big)\big)}\ . \tag{A.10}$$

APPENDIX B

CONSTANT FREQUENCY APPROACH TO PARAMETER CALCULATIONS

B.1 Example code for obtaining one set of harvester dimensions

Provided below is a copy of the MATLAB® script used in obtaining and recording dimensions for energy harvesters with identical fundamental frequencies in a scenario where piezoelectric layer length from the clamped end is the parameter of interest and substrate thickness is used as the control parameter. The user is required to define the dimensions of the conventional design along with the range of piezoelectric layer lengths for which a substrate thickness is required.

```
%-------------------------------------------------------------------------
%-------------------------------------------------------------------------

close all
clear all
clc
format short e


%% Defining Structure Properties
[tp_norm,ts_norm,L_norm,x1_norm,x2_norm,x3_norm,bp_norm,bs_norm,Ep,Es, ...
    rhop,rhos,Input_Acceleration,d_31,e_S_33,gamma,R_load, ...
    add_mass,rhom,Lm_norm,bm_norm,tm_norm,res] = z_properties_thesis;
```

```
%% Run Transfer Matrix Model To Get Target Natural Frequency
unimorph=1;
[Stage_intermediate_out,x,omega_n,z,m_x,mass,cg,norm,diff_slope] = ...
    TM_method_function(L_norm,x1_norm,x2_norm,x3_norm,bs_norm, ...
    bp_norm,ts_norm,tp_norm,Ep,Es,rhop,rhos,add_mass,rhom, ...
    Lm_norm,bm_norm,tm_norm,res,unimorph);

Target_Freq=omega_n(1)/2/pi;
Target_Freq_Rounding=rounding(Target_Freq,5);      % function to round numbers


%% Defining The Parameter Under Investigation And The Control Parameter
total=50;
x3_matrix=L_norm/total:L_norm/total:L_norm-L_norm/total;

difference=50/100*ts_norm;
total=50;
control_variable_min=ts_norm-difference;
control_variable_max=ts_norm+difference;
control_variable_inc=(control_variable_max-control_variable_min)/total;

control_variable=control_variable_min:control_variable_inc:control_variable_max;

Constant_Freq_Parameters=zeros(length(x3_matrix)+1,12);
Constant_Freq_Parameters(1,:)=[L_norm x1_norm x2_norm x3_norm tp_norm ...
    ts_norm bp_norm bs_norm Lm_norm bm_norm tm_norm 1];

% Predefining matrices to optimise code performance
L=zeros(length(x3_matrix),length(control_variable));
x1=zeros(length(x3_matrix),length(control_variable));
x2=zeros(length(x3_matrix),length(control_variable));
x3=zeros(length(x3_matrix),length(control_variable));
tp=zeros(length(x3_matrix),length(control_variable));
ts=zeros(length(x3_matrix),length(control_variable));
bp=zeros(length(x3_matrix),length(control_variable));
bs=zeros(length(x3_matrix),length(control_variable));
Lm=zeros(length(x3_matrix),length(control_variable));
bm=zeros(length(x3_matrix),length(control_variable));
tm=zeros(length(x3_matrix),length(control_variable));
Freq_matrix=zeros(length(x3_matrix),length(control_variable));


sp=cell(size(x3_matrix*2));
```

```
%% Sweep Of Parameter Under Investigation
for loop1=1:length(x3_matrix)


    %% Sweep Of Control Variable
    for loop2=1:length(control_variable)


        %% Defines Trial Configuration Geometry
        L(loop1,loop2)=L_norm;
        x1(loop1,loop2)=x1_norm;
        x2(loop1,loop2)=L_norm-x3_matrix(loop1);
        x3(loop1,loop2)=x3_matrix(loop1);
        tp(loop1,loop2)=tp_norm;
        ts(loop1,loop2)=control_variable(loop2);
        bp(loop1,loop2)=bp_norm;
        bs(loop1,loop2)=bs_norm;
        Lm(loop1,loop2)=Lm_norm;
        bm(loop1,loop2)=bm_norm;
        tm(loop1,loop2)=tm_norm;

        if x1(loop1,loop2)==0 && x2(loop1,loop2)==0
            error('Check Lengths Of Sections - NOTE: Cannot Have Just x3');
        end

        if x1(loop1,loop2)+x2(loop1,loop2)+x3(loop1,loop2)>=L+1e-10
            error('Check Lengths Of Sections');
        end


        %% Run Transfer Matrix Model To Get Natural Frequency Of Trial Device
        [Stage_intermediate_out,x,omega_n,z,m_x,mass,cg,norm,diff_slope] = ...
            TM_method_function(L_norm,x1_norm,x2(loop1,loop2),x3(loop1,loop2), ...
            bs_norm,bp_norm,ts(loop1,loop2),tp_norm,Ep,Es,rhop,rhos,add_mass,rhom, ...
            Lm_norm,bm_norm,tm_norm,res,unimorph);

        Freq_matrix(loop1,loop2)=omega_n(1)/2/pi;
        Freq_matrix(loop1,loop2)=rounding(Freq_matrix(loop1,loop2),5);

        disp({['Loop number ',num2str(loop2),'- ',num2str(loop1)];
            ['Target loop number ',num2str(length(control_variable)), ...
            '- ',num2str(length(x3_matrix))]});

    end

    sp{loop1*2-1}= ...
        sprintf('Length of Piezo = %s %s',num2str(x2(loop1,loop2)*1e3),'mm');
```

```
    sp{loop1*2}= ...
        sprintf('TARGET FREQUENCY (Full Length Piezoelectric Layer)');

    plotting=1;
    if plotting==1

        h1=figure(1);
        set(h1,'OuterPosition',[0 150 160*8 90*8])
        figure(1)
        plot(control_variable*1e3,Freq_matrix(loop1,:))
        xlabel('Control Variable (mm)','FontName','Bookman Old Style','FontSize',14)
        ylabel('Natural Frequency (Hz)','FontName','Bookman Old Style','FontSize',14)
        hold all
        plot([control_variable(1)*1e3 control_variable(end)*1e3], ...
            Target_Freq_Rounding*[1 1],'k','LineWidth',2)
        hold all

        if loop1==1
            RemoveWhiteSpace(h1,0)
        end

        if loop1==length(x3_matrix)
            saveas(gcf,[pwd,filesep,'Vary x3 - Control ts'])
        end

    end

    if Target_Freq<min(Freq_matrix(loop1,:)) || Target_Freq>max(Freq_matrix(loop1,:))
        save('Vary x3 - Control ts','Constant_Freq_Parameters')
        error('Does not reach target frequency')
    end


    %% Use Interpolation To Determine Exact Value Of Control Parameter
    required_control=interp1(Freq_matrix(loop1,:),control_variable,Target_Freq);
    disp(['Required Control - ',num2str(required_control*1e3),'mm']);
    Constant_Freq_Parameters(loop1+1,:)=[L_norm;x1_norm;x2(loop1,loop2); ...
        x3(loop1,loop2);tp_norm;required_control;bp_norm;bs_norm; ...
        Lm_norm;bm_norm;tm_norm;1];

end

save('Vary x3 - Control ts', 'Constant_Freq_Parameters')

%-------------------------------------------------------------------------
%-------------------------------------------------------------------------
```

B.2 Dimensions for macro-scale energy harvesters (1)

In this section energy harvester dimensions are provided which will result in configurations with identical fundamental frequencies for the macro-scale device. Piezoelectric length is the parameter of interest and substrate thickness used as the control parameter.

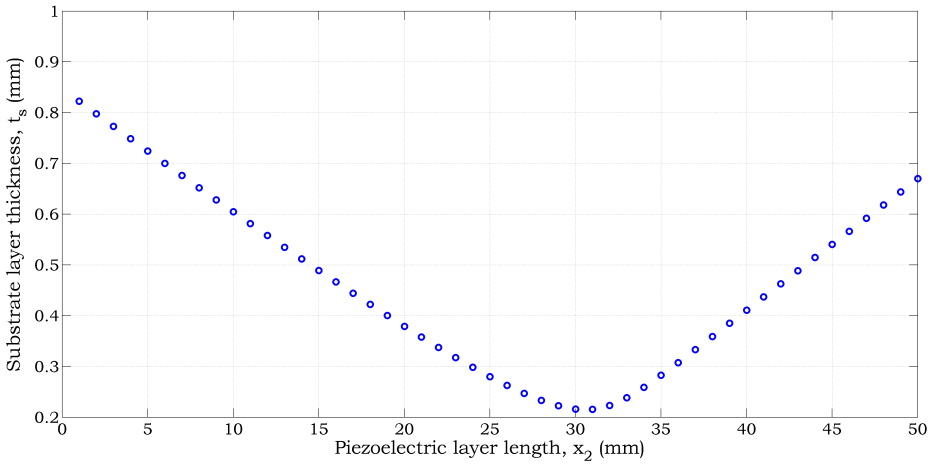

Figure B.1: Plot indicating the substrate thickness required for designs of various piezoelectric lengths. Piezoelectric layer remains coincident with clamped end. Constant parameters – $L = 50$ mm, $x_1 = 0$ mm, $t_p = 0.5$ mm, $b_p = 5$ mm, $b_s = 5$ mm, $L_m = 0$ mm, $t_m = 0$ mm, $b_m = 0$ mm.

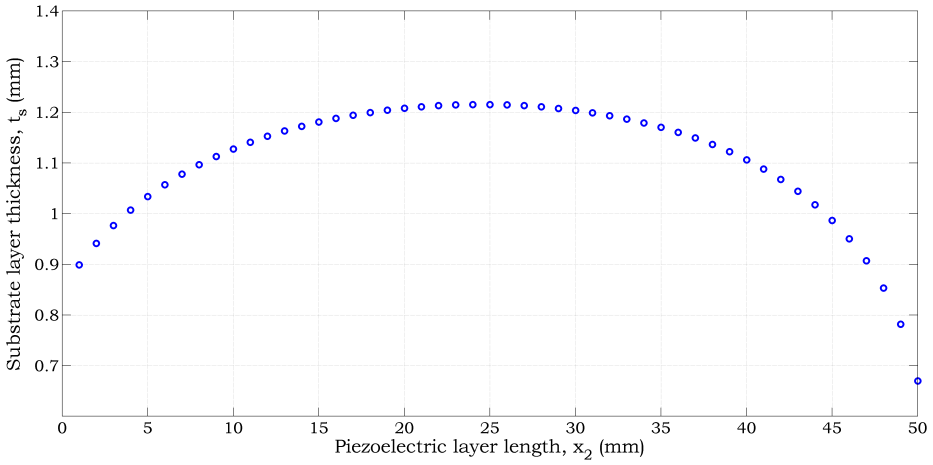

Figure B.2: Plot indicating the substrate thickness required for designs of various piezoelectric lengths. Piezoelectric layer remains coincident with free end. Constant parameters – $L = 50$ mm, $x_3 = 0$ mm, $t_p = 0.5$ mm, $b_p = 5$ mm, $b_s = 5$ mm, $L_m = 0$ mm, $t_m = 0$ mm, $b_m = 0$ mm.

B.3 Dimensions for macro-scale energy harvesters (2)

In this section energy harvester dimensions are provided which will result in configurations with identical fundamental frequencies for the macro-scale device. Piezoelectric thickness is the parameter of interest and substrate thickness used as the control parameter.

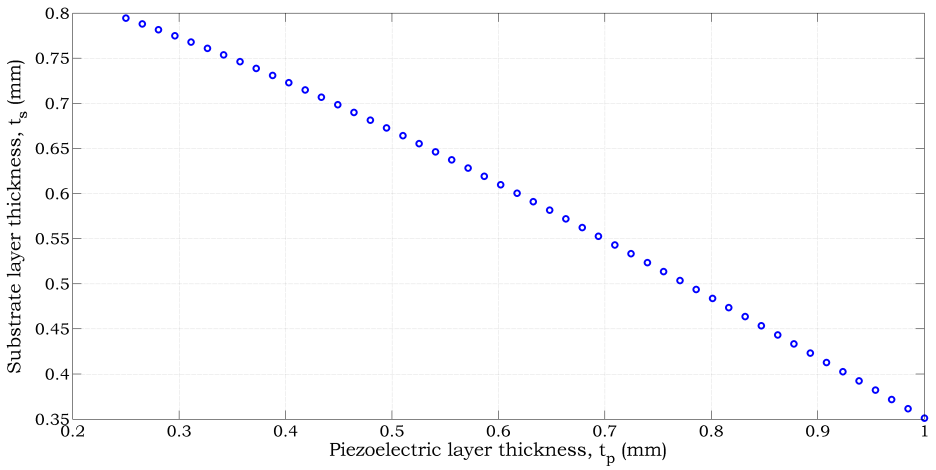

Figure B.3: Plot indicating the substrate thickness required for designs of various piezoelectric thickness. Constant parameters – $L = 50$ **mm,** $x_1 = 0$ **mm,** $x_2 = 50$ **mm,** $x_3 = 0$ **mm,** $b_p = 5$ **mm,** $b_s = 5$ **mm,** $L_m = 0$ **mm,** $t_m = 0$ **mm,** $b_m = 0$ **mm.**

B.4 Dimensions for micro-scale energy harvesters

In this section energy harvester dimensions are provided which will result in configurations with identical fundamental frequencies for the micro-scale device. Piezoelectric length from the clamped end is the parameter of interest and tip mass dimensions are used as the control parameter.

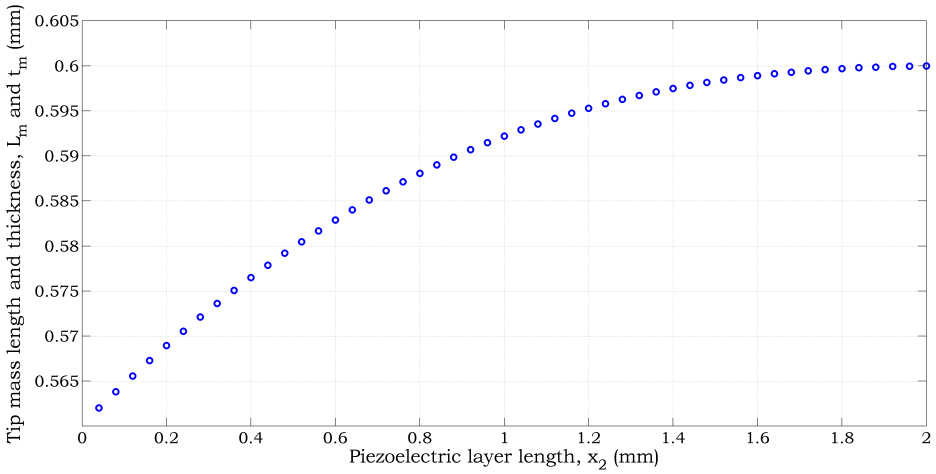

Figure B.4: Plot indicating the tip mass length and thickness required for designs of various piezoelectric length. Piezoelectric layer remains coincident with clamped end. Constant parameters – $L = 2$ mm, $x_1 = 0$ mm, $t_p = 0.002$ mm, $t_s = 0.012$ mm, $b_p = 0.6$ mm, $b_s = 0.6$ mm, $b_m = 0.6$ mm.

B.5 Dimensions for thin film energy harvesters

In this section energy harvester dimensions are provided which will result in configurations with identical fundamental frequencies for the thin film flexible device. Piezoelectric length from the clamped end, piezoelectric width and piezoelectric thickness were the parameters of interest with frequency control in each case provided by substrate thickness.

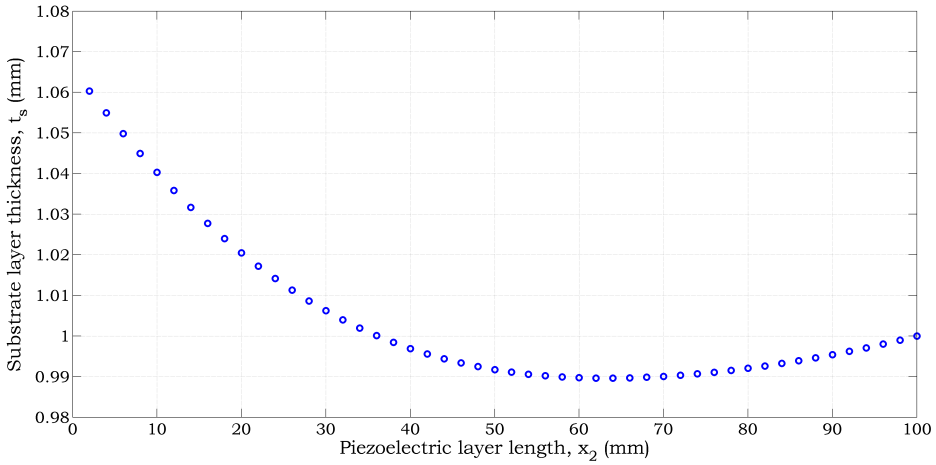

Figure B.5: Plot indicating the substrate thickness required for designs of various piezoelectric lengths. Piezoelectric layer remains coincident with clamped end. Constant parameters – $L = 100$ **mm,** $x_1 = 0$ **mm,** $t_p = 0.04$ **mm,** $b_p = 10$ **mm,** $b_s = 20$ **mm,** $L_m = 0$ **mm,** $t_m = 0$ **mm,** $b_m = 0$ **mm.**

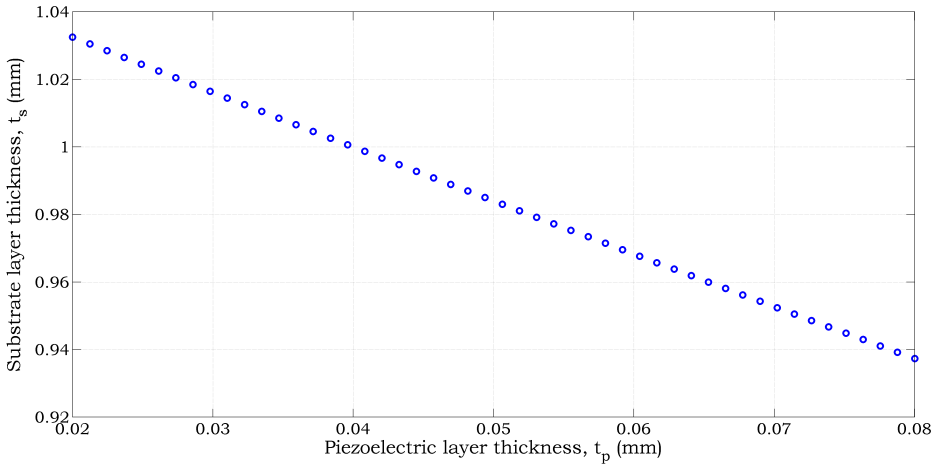

Figure B.6: Plot indicating the substrate thickness required for designs of various piezoelectric thickness. Constant parameters – $L = 100$ **mm,** $x_1 = 0$ **mm,** $x_2 = 100$ **mm,** $x_3 = 0$ **mm,** $b_p = 10$ **mm,** $b_s = 20$ **mm,** $L_m = 0$ **mm,** $t_m = 0$ **mm,** $b_m = 0$ **mm.**

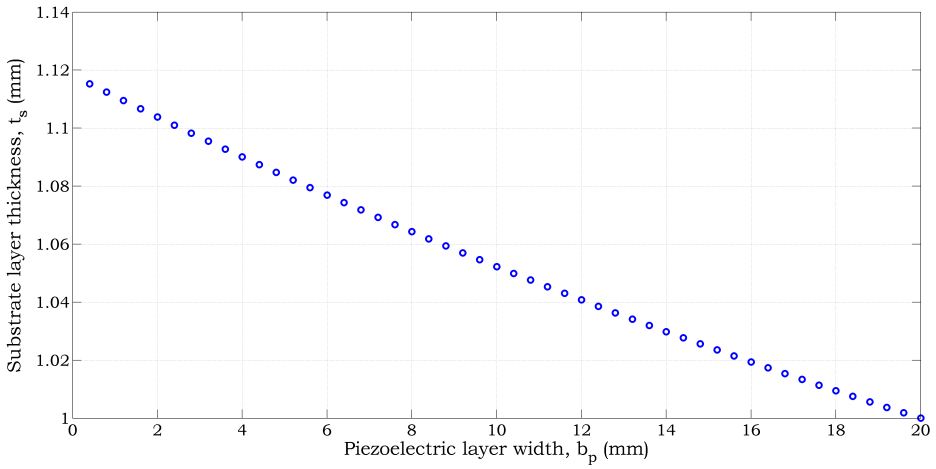

Figure B.7: Plot indicating the substrate thickness required for designs of various piezoelectric widths. Constant parameters – $L = 100$ **mm,** $x_1 = 0$ **mm,** $x_2 = 100$ **mm,** $x_3 = 0$ **mm,** $t_p = 0.04$ **mm,** $b_s = 20$ **mm,** $L_m = 0$ **mm,** $t_m = 0$ **mm,** $b_m = 0$ **mm.**

APPENDIX C

NON-LINEAR MODELLING OF PIEZOELECTRIC ENERGY HARVESTERS

C.1 Detailed derivation of non-linear model

C.1.1 Higher order curvature expressions

ρ, ρ^2 and ρ^3 can be expressed as:

$$\rho = v'' + v''u' - v'u'' \,, \tag{C.1}$$

$$\rho^2 = (v'')^2 + 2(v'')^2u' - 2v''v'u'' + (v'')^2(u')^2 - 2v''u'v'u'' + (v')^2(u'')^2 \,, \tag{C.2}$$

$$\begin{aligned}\rho^3 =& (v'')^3 + 3(v'')^3u' - 3(v'')^2v'u'' + 3(v'')^3(u')^2 - 6(v'')^2u'v'u'' \\ &+ 3v''(v')^2(u'')^2 + (v'')^3(u')^3 - 3(v'')^2(u')^2v'u'' + 3v''u'(v')^2(u'')^2 \\ &- (v')^3(u'')^3 \,.\end{aligned} \tag{C.3}$$

Once the higher order terms are neglected the above terms can be approximated as:

$$\rho = v'' + v''u' - v'u'' \,, \tag{C.4}$$

$$\rho^2 \approx (v'')^2 + 2(v'')^2u' - 2v''v'u'' \,, \tag{C.5}$$

$$\rho^3 \approx (v'')^3 \,. \tag{C.6}$$

C.1.2 Full details on obtaining potential energy expression

Substituting the constitutive equations, Equations (7.1)-(7.3), into Equation (7.4) yields:

$$\begin{aligned} U =& \frac{1}{2}\int_0^{x_1} \iint_{A_s} (E_s(\varepsilon_{11}^s)^2)\mathrm{d}A\mathrm{d}s + \frac{1}{2}\int_{x_1}^{x_1+x_2} \iint_{A_s} (E_s(\varepsilon_{11}^s)^2)\mathrm{d}A\mathrm{d}s \\ &+ \frac{1}{2}\int_{x_1}^{x_1+x_2} \iint_{A_p} (E_p(\varepsilon_{11}^p)^2)\mathrm{d}A\mathrm{d}s + \frac{1}{2}\int_{x_1}^{x_1+x_2} \iint_{A_p} (\frac{\mu_1}{2}(\varepsilon_{11}^p)^3)\mathrm{d}A\mathrm{d}s \\ &- \int_{x_1}^{x_1+x_2} \iint_{A_p} (E_p d_{31} E(\varepsilon_{11}^p))\mathrm{d}A\mathrm{d}s - \frac{3}{4}\int_{x_1}^{x_1+x_2} \iint_{A_p} (\mu_2 E_{\text{field}}(\varepsilon_{11}^p)^2)\mathrm{d}A\mathrm{d}s \\ &+ \frac{1}{2}\int_{x_1+x_2}^{L} \iint_{A_s} (E_s(\varepsilon_{11}^s)^2)\mathrm{d}A\mathrm{d}s + \frac{1}{2}\int_0^L (EA(s)(u' + \frac{1}{2}(v')^2)^2)\mathrm{d}s \\ &- \frac{1}{2}\int_{x_1}^{x_1+x_2} \iint_{A_p} ((\varepsilon_{33}){E_{\text{field}}}^2(t))\mathrm{d}A\mathrm{d}s \,. \end{aligned} \tag{C.7}$$

Strain in the beam can be expressed in terms of distance from the neutral axis, y, and beam curvature, ρ, viz.:

$$\varepsilon_{11} = y\rho \,. \tag{C.8}$$

Utilising this relationship in conjunction with Equation (C.7) yields:

$$\begin{aligned}U =& \frac{1}{2}\int_0^{x_1}\iint_{A_s}(E_s(y^2\rho^2))\mathrm{d}A\mathrm{d}s + \frac{1}{2}\int_{x_1}^{x_1+x_2}\iint_{A_s}(E_s(y^2\rho^2))\mathrm{d}A\mathrm{d}s \\ &+ \frac{1}{2}\int_{x_1}^{x_1+x_2}\iint_{A_p}(E_p(y^2\rho^2))\mathrm{d}A\mathrm{d}s + \frac{1}{2}\int_{x_1}^{x_1+x_2}\iint_{A_p}(\frac{\mu_1}{2}(y^3\rho^3))\mathrm{d}A\mathrm{d}s \\ &- \int_{x_1}^{x_1+x_2}\iint_{A_p}(E_p d_{31}E(y\rho))\mathrm{d}A\mathrm{d}s - \frac{3}{4}\int_{x_1}^{x_1+x_2}\iint_{A_p}(\mu_2 E_{\text{field}}(y^2\rho^2))\mathrm{d}A\mathrm{d}s \\ &+ \frac{1}{2}\int_{x_1+x_2}^{L}\iint_{A_s}(E_s(y^2\rho^2))\mathrm{d}A\mathrm{d}s + \frac{1}{2}\int_0^L(EA(s)(u' + \frac{1}{2}(v')^2)^2)\mathrm{d}s \\ &- \frac{1}{2}\int_{x_1}^{x_1+x_2}\iint_{A_p}((\varepsilon_{33})E^2_{\text{field}}(t))\mathrm{d}A\mathrm{d}s\ . \end{aligned} \tag{C.9}$$

Performing integration over the cross sectional area of the beam gives the following expressions (note, $\overline{y}$ is the neutral axis location from the bottom of the substrate layer):

$$\iint_{A_s} y^2 dA = \int_{-t_s/2}^{t_s/2}\left(\int_{-b_s/2}^{b_s/2} y^2\mathrm{d}b\right)\mathrm{d}y$$

$$\therefore \quad \Big[b\Big]_{-b_s/2}^{b_s/2}\int_{-t_s/2}^{t_s/2} y^2\mathrm{d}y$$

$$\therefore \quad b_s\left[\frac{y^3}{3}\right]_{-t_s/2}^{t_s/2}$$

$$\therefore \quad \frac{b_s t_s^3}{12} = I_s\ , \tag{C.10}$$

$$\iint_{A_s} y^2 dA = \int_{-\overline{y}}^{t_s-\overline{y}}\left(\int_{-b_s/2}^{b_s/2} y^2\mathrm{d}b\right)\mathrm{d}y$$

$$\therefore \quad \Big[b\Big]_{-b_s/2}^{b_s/2}\int_{-\overline{y}}^{t_s-\overline{y}} y^2\mathrm{d}y$$

$$\therefore \quad b_s \left[\frac{y^3}{3}\right]_{-\overline{y}}^{t_s-\overline{y}}$$

$$\therefore \quad b_s \left[(t_s)\overline{y}^2 - (t_s^2)\overline{y} + \frac{1}{3}t_s^3\right] = I_{s1} \ , \tag{C.11}$$

$$\iint\limits_{A_s} y^3 dA = \int_{-\overline{y}}^{t_s-\overline{y}} \left(\int_{-b_s/2}^{b_s/2} y^2 \mathrm{d}b\right) \mathrm{d}y$$

$$\therefore \quad \left[b\right]_{-b_s/2}^{b_s/2} \int_{-\overline{y}}^{t_s-\overline{y}} y^3 \mathrm{d}y$$

$$\therefore \quad b_p \left[\frac{y^4}{4}\right]_{-\overline{y}}^{t_s-\overline{y}}$$

$$\therefore \quad b_p \left[\frac{(t_s-\overline{y})^4}{4} - \frac{(-\overline{y})^4}{4}\right] = I_{s2} \ , \tag{C.12}$$

$$\iint\limits_{A_p} y^2 dA = \int_{t_s-\overline{y}}^{t_p+t_s-\overline{y}} \left(\int_{-b_p/2}^{b_p/2} y^2 \mathrm{d}b\right) \mathrm{d}y$$

$$\therefore \quad \left[b\right]_{-b_p/2}^{b_p/2} \int_{t_s-\overline{y}}^{t_p+t_s-\overline{y}} y^2 \mathrm{d}y$$

$$\therefore \quad b_p \left[\frac{y^3}{3}\right]_{t_s-\overline{y}}^{t_p+t_s-\overline{y}}$$

$$\therefore \quad b_p \left[(t_p)\overline{y}^2 + (-2t_pt_s - t_p^2)\overline{y} + (\frac{1}{3}t_p^3 + t_p^2t_s + t_pt_s^2)\right] = I_{p1} \ , \tag{C.13}$$

$$\iint\limits_{A_p} y^3 dA = \int_{t_s-\overline{y}}^{t_p+t_s-\overline{y}} \left(\int_{-b_p/2}^{b_p/2} y^2 \mathrm{d}b\right) \mathrm{d}y$$

$$\therefore \quad \Big[b\Big]_{-b_p/2}^{b_p/2} \int_{t_s-\overline{y}}^{t_p+t_s-\overline{y}} y^3 \mathrm{d}y$$

$$\therefore \quad b_p \left[\frac{y^4}{4}\right]_{t_s-\overline{y}}^{t_p+t_s-\overline{y}}$$

$$\therefore \quad b_p \left[\frac{(t_s+t_p-\overline{y})^4}{4} - \frac{(t_s-\overline{y})^4}{4}\right] = I_{p2}\,. \tag{C.14}$$

C.1.3 Full details on utilising the calculus of variations

Using the calculus of variations on terms in the Equation (7.36):

$$\begin{aligned} & K_1(s)(v'')^2 \\ \text{Using} \Longrightarrow \quad & \frac{\partial F}{\partial v} - \frac{\mathrm{d}}{\mathrm{d}s}\frac{\partial F}{\partial v'} + \frac{\mathrm{d}^2}{\mathrm{d}s^2}\frac{\partial F}{\partial v''} \\ \therefore \quad & \frac{\mathrm{d}^2}{\mathrm{d}s^2}\big(2K_1(s)v''\big) \\ \therefore \quad & \big[2K_1(s)v''\big]''\,, \end{aligned} \tag{C.15}$$

$$\begin{aligned} & K_1(s)(v''v')^2 \\ \text{Using} \Longrightarrow \quad & \frac{\partial F}{\partial v} - \frac{\mathrm{d}}{\mathrm{d}s}\frac{\partial F}{\partial v'} + \frac{\mathrm{d}^2}{\mathrm{d}s^2}\frac{\partial F}{\partial v''} \\ \therefore \quad & -\frac{\mathrm{d}}{\mathrm{d}s}\big((2K_1(s)v''v')v''\big) + \frac{\mathrm{d}^2}{\mathrm{d}s^2}\big((2K_1(s)v''v')v'\big) \\ \therefore \quad & -\frac{\mathrm{d}}{\mathrm{d}s}\big((2K_1(s)v''v')v''\big) + \frac{\mathrm{d}}{\mathrm{d}s}\big((2K_1(s)v''v')'v'\big) \\ & + \frac{\mathrm{d}}{\mathrm{d}s}\big((2K_1(s)v''v')v''\big) \\ \therefore \quad & \big[(2K_1(s)v''v')'v'\big]'\,, \end{aligned} \tag{C.16}$$

$$\text{From the above} \Longrightarrow \quad \big[2K_2(s)V(t)v''\big]''\,, \tag{C.17}$$

$$\text{Likewise} \implies \left[(2K_2(s)V(t)v''v')'v'\right]', \tag{C.18}$$

$$\begin{aligned} & K_3(s)(v'')^3 \\ \text{Using} \implies \quad & \frac{\partial F}{\partial v} - \frac{\mathrm{d}}{\mathrm{d}s}\frac{\partial F}{\partial v'} + \frac{\mathrm{d}^2}{\mathrm{d}s^2}\frac{\partial F}{\partial v''} \\ \therefore \quad & \frac{\mathrm{d}^2}{\mathrm{d}s^2}\left(3K_3(s)v''^2\right) \\ \therefore \quad & \left[3K_3(s)v''^2\right]'', \end{aligned} \tag{C.19}$$

$$\begin{aligned} & K_4(s)v''V(t) \\ \text{Using} \implies \quad & \frac{\partial F}{\partial v} - \frac{\mathrm{d}}{\mathrm{d}s}\frac{\partial F}{\partial v'} + \frac{\mathrm{d}^2}{\mathrm{d}s^2}\frac{\partial F}{\partial v''} \\ \therefore \quad & \frac{\mathrm{d}^2}{\mathrm{d}s^2}\big(K_4(s)V(t)\big) \\ \therefore \quad & \big[K_4(s)V(t)\big]'', \end{aligned} \tag{C.20}$$

$$\begin{aligned} & K_4(s)\frac{1}{2}v''(v')^2V(t) \\ \text{Using} \implies \quad & \frac{\partial F}{\partial v} - \frac{\mathrm{d}}{\mathrm{d}s}\frac{\partial F}{\partial v'} + \frac{\mathrm{d}^2}{\mathrm{d}s^2}\frac{\partial F}{\partial v''} \\ \therefore \quad & -\frac{\mathrm{d}}{\mathrm{d}s}\big(K_4(s)v''v'V(t)\big) + \frac{\mathrm{d}^2}{\mathrm{d}s^2}\big(0.5K_4(s)v'^2V(t)\big) \\ \therefore \quad & -\big[K_4(s)v''v'V(t)\big]' + \big[0.5K_4(s)v'^2V(t)\big]'', \end{aligned} \tag{C.21}$$

$$\begin{aligned} & m(s)\dot{v}^2 \\ \text{Using} \implies \quad & \frac{\partial F}{\partial v} - \frac{\mathrm{d}}{\mathrm{d}t}\frac{\partial F}{\partial \dot{v}} \\ \therefore \quad & -\frac{\mathrm{d}}{\mathrm{d}t}\big(2m(s)\dot{v}\big) \\ \therefore \quad & -\big[2m(s)\ddot{v}\big], \end{aligned} \tag{C.22}$$

$$m(s)\left(-\int_0^s v'\dot{v}'\right)^2$$

$$\begin{aligned}
\text{Using} \Longrightarrow \quad & \frac{\partial F}{\partial v} - \frac{\mathrm{d}}{\mathrm{d}s}\frac{\partial F}{\partial v'} + -\frac{\mathrm{d}^2}{\mathrm{d}s\mathrm{d}t}\frac{\partial F}{\partial \dot{v}'} \\
\therefore \quad & \left[2v' \int_L^s m(s) \int_0^s \left(\ddot{v}''v' + \dot{v}'^2\right)\mathrm{d}s\mathrm{d}s\right]', \qquad \text{(C.23)}
\end{aligned}$$

$$\begin{aligned}
& K_2(s)V(t)(v''^2 + (v''v')^2) \\
\text{Using} \Longrightarrow \quad & \frac{\partial F}{\partial V} \\
\therefore \quad & \left[K_2(s)(v''^2 + (v''v')^2)\right], \qquad \text{(C.24)}
\end{aligned}$$

$$\begin{aligned}
& K_4(s)V(t)(v'' + \frac{1}{2}v''(v')^2) \\
\text{Using} \Longrightarrow \quad & \frac{\partial F}{\partial V} \\
\therefore \quad & \left[K_4(s)(v'' + 0.5v''v'^2)\right], \qquad \text{(C.25)}
\end{aligned}$$

$$\begin{aligned}
& K_5(s)V^2(t) \\
\text{Using} \Longrightarrow \quad & \frac{\partial F}{\partial V} \\
\therefore \quad & \left[2K_5(s)V(t)\right], \qquad \text{(C.26)}
\end{aligned}$$

$$\begin{aligned}
& qV(t) \\
\text{Using} \Longrightarrow \quad & \frac{\partial F}{\partial V} \\
\therefore \quad & \left[q\right]. \qquad \text{(C.27)}
\end{aligned}$$

C.1.4 Utilisation of classic modal approach

Substituting the modal summation expression, Equation (7.40) into current equations of motion, Equations (7.37) and (7.38), yields:

$$
\begin{aligned}
& m(s)W_r(s)\ddot{\eta}_r(t) \\
& + \left[W_r'(s)\eta_r(t)\int_L^s m(s)\int_0^s \big(W_r''(s)\ddot{\eta}_r(t)W_r'(s)\eta_r(t) + W_r'^2(s)\dot{\eta}_r^2(t)\big)\mathrm{d}s\mathrm{d}s\right]' \\
& + \Big[\big(K_1(s) - K_2(s)V(t)\big)W_r''(s)\Big]''\eta_r(t) \\
& + \left[\Big(\big(K_1(s) - K_2(s)V(t)\big)W_r''(s)W_r'(s)\Big)'W_r'(s)\right]'\eta_r^3(t) \\
& + \left[\frac{3}{2}K_3(s)W_r''^2(s)\right]''\eta_r^2(t) - \left[\frac{1}{2}K_4(s)V(t)\right]'' \\
& + \left[\frac{1}{2}K_4(s)W_r''(s)W_r'(s)V(t)\right]'\eta_r^2(t) - \left[\frac{1}{4}K_4(s)W_r'^2(s)V(t)\right]''\eta_r^2(t) \\
& = \left[\iiint_{V_s}\rho_s\mathrm{d}V + \iiint_{V_p}\rho_p\mathrm{d}V\right]\ddot{w}_b(t)\ , \qquad \text{(C.28)}
\end{aligned}
$$

and

$$
\begin{aligned}
\int_0^L \Big\{ & \frac{1}{2}K_2(s)\big(W_r''^2(s)\eta_r^2(t) + (W_r''^2(s)W_r'^2(s)\eta_r^4(t))\big) \\
& + \frac{1}{2}K_4(s)\left(W_r''(s)\eta_r(t) + \frac{1}{2}W_r''(s)W_r'^2(s)\eta_r^3(t)\right) \\
& - K_5(s)V(t)\Big\}\mathrm{d}s - q = 0\ . \qquad \text{(C.29)}
\end{aligned}
$$

C.2 SIMULINK® models representing non-linear equations of motion

The following three figures show the SIMULINK® models used in solving the set of equations which govern mechanical and electrical response, Equations (7.43) and (7.53).

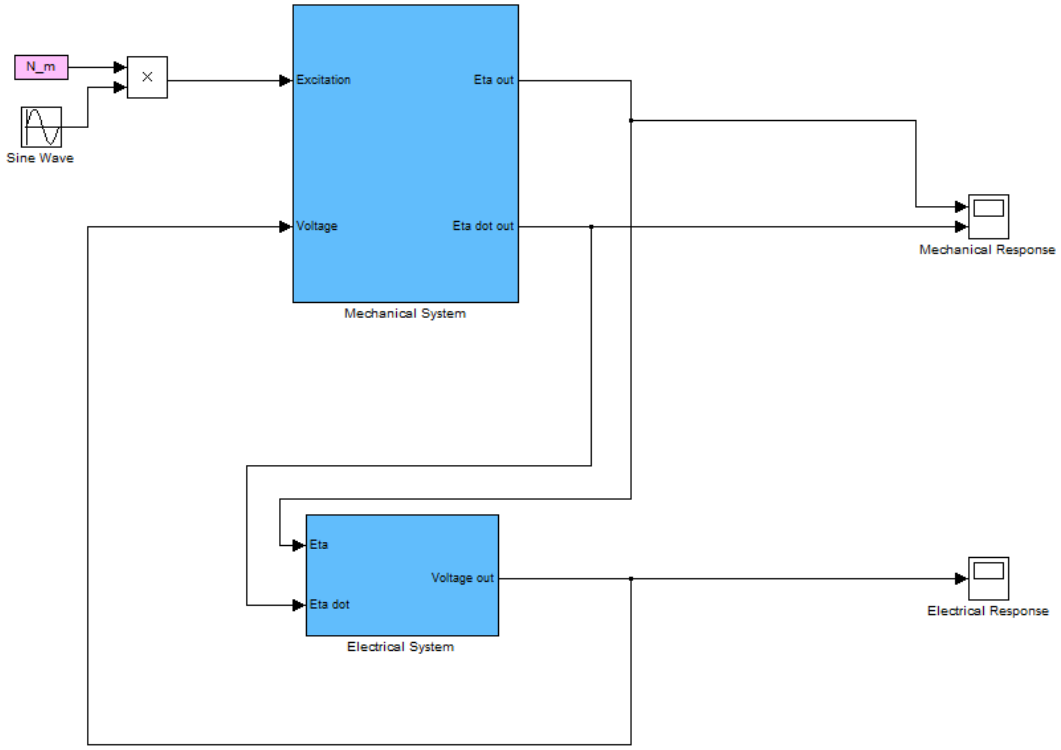

Figure C.1: Overall SIMULINK® model for the non-linear set of equations with individual, but coupled, mechanical and electrical subsystems.

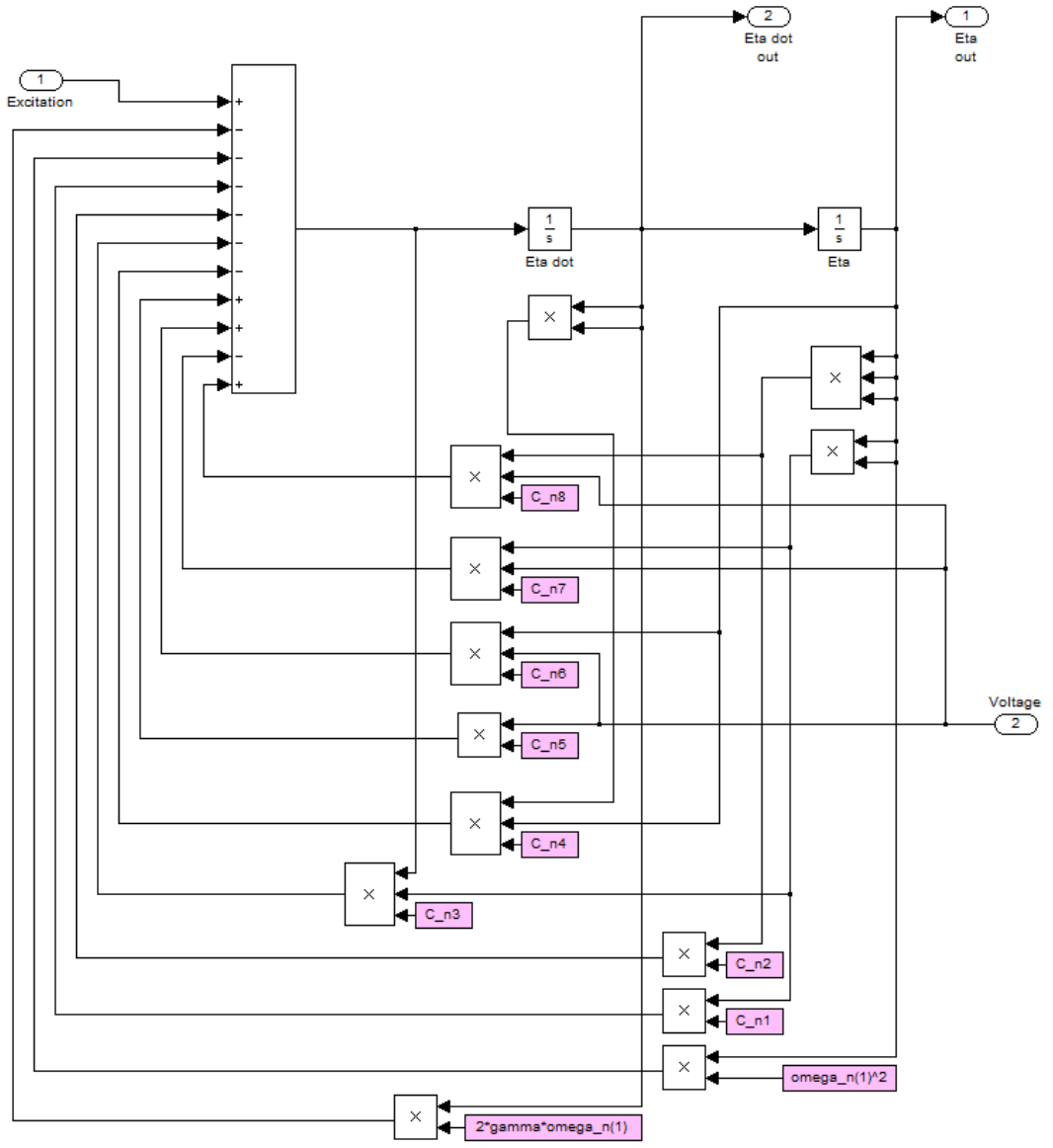

Figure C.2: SIMULINK® model for the modal equation of motion.

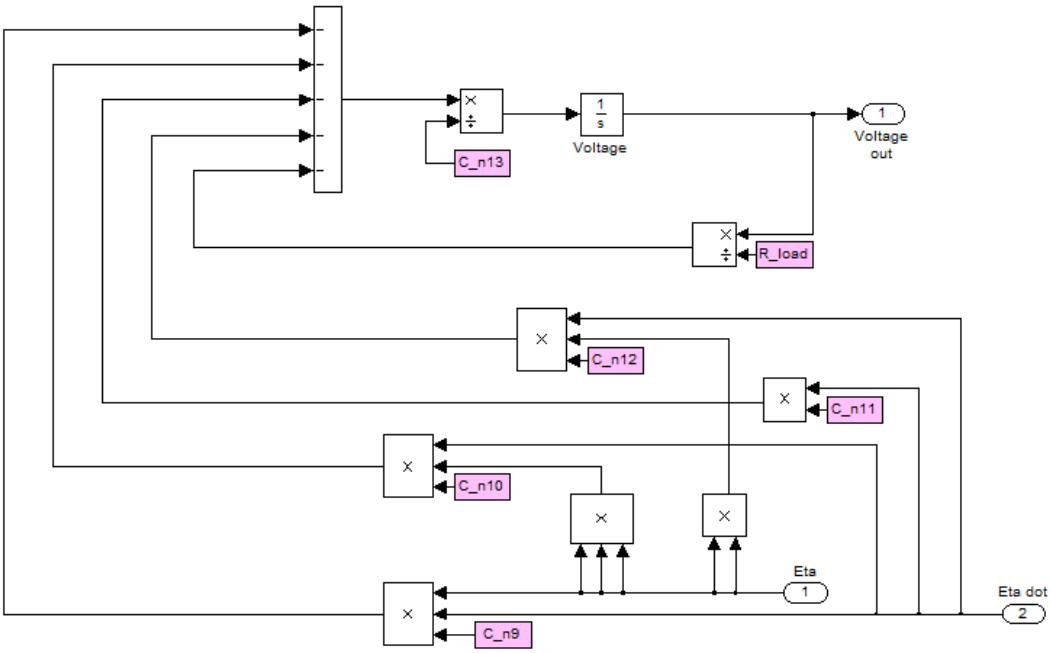

Figure C.3: SIMULINK® model for the electrical equation of motion.